

N A63-61

1N-34

158855

1928

Experimental and Numerical Investigation of the Effect of Distributed Suction on Oblique Shock Wave/Turbulent Boundary Layer Interaction

Driss Benhachmi and Isaac Greber
Case Western Reserve University
Cleveland, Ohio

and

Warren R. Hingst
Lewis Research Center
Cleveland, Ohio

(NASA-TM-101334) EXPERIMENTAL AND NUMERICAL
INVESTIGATION OF THE EFFECT OF DISTRIBUTED
SUCTION ON OBLIQUE SHOCK WAVE/TURBULENT
SECONDARY LAYER INTERACTION Ph.D. Thesis
(NASA) 192 p

N88-30084

Unclas
0158855

CSCI 20D G3/34

August 1988

NASA

ACKNOWLEDGEMENTS

I would like to thank Thomas Benson for his assistance and contribution to the numerical calculations of this research. Special thanks are given to Kirk Seablom and the staff of the 1 ft \times 1 ft supersonic wind tunnel for their contribution to the experimental work.

This work was performed at NASA Lewis Research Center in Cleveland, Ohio, through NASA Grant NAG 3-61.

TABLE OF CONTENTS

	Page
ACKNOWLEDGEMENTS	i
NOMENCLATURE	v
CHAPTER 1 : INTRODUCTION	1
CHAPTER 2 : EXPERIMENTAL PROCEDURE	6
2.1 Wind Tunnel Facility	6
2.2 Test Plate Models	6
2.3 Suction Equipment	8
2.4 Shock Generator	8
2.5 Instrumentation	9
2.5.1 Wall Pressure and Temperature	9
2.5.2 Pitot Probe	10
2.5.3 Hot-Wire Probe and Anemometer	10
2.5.4 Documentation of two-dimensionality	11
2.6 Experimental Procedure	12
2.7 Test Conditions	14
2.8 Data Reduction	15
CHAPTER 3 : EXPERIMENTAL RESULTS	16
3.1 Properties of the Incoming Boundary Layer	16
3.1.1 Percentage of Boundary Layer Bleed	18
3.2 Flow in the Absence of Shock Waves	19
3.2.1 Rough Wall Results	19
3.2.2 Porous Wall Results	23
3.2.3 Porous Plate Calibration	27
3.3 Shock Wave/Boundary Layer Interaction Results	27
3.3.1 Interactions on the Rough Plate	28
3.3.2 Interactions on the Porous Plate	30
3.4 Two-Dimensionality	35
3.4.1 Rough Wall	35

3.4.2 Porous Wall	37
3.5 Comparison of Rough and Porous Plate Results	38
3.5 Comparison with Other Work	39
CHAPTER 4 : NUMERICAL CALCULATIONS	40
4.1 Governing Equations	40
4.2 Turbulence Model	41
4.3 Coordinate Transformation	43
4.4 Numerical Procedure	44
4.5 Computational Domain and Grid	46
4.6 Boundary and Initial Conditions	47
CHAPTER 5 : NUMERICAL RESULTS	50
5.1 Interactions on a Solid Wall	50
5.1.1 Mach number 2.46	50
5.1.2 Mach number 2.98	52
5.2 Interactions on a Porous Wall	53
5.2.1 Mach number 2.46	53
5.2.2 Mach number 2.98	55
CHAPTER 6 : CONCLUSIONS AND RECOMMENDATIONS	58
REFERENCES	62
APPENDIX A : DATA REDUCTION	66
APPENDIX B : HOT-WIRE CALIBRATION AND CORRECTION	69
APPENDIX C : POROUS MATERIAL CALIBRATION	74
TABLE I	76
TABLE II	77
FIGURES	78

NOMENCLATURE

a	Sonic speed
A	Constant in porous wall equation
A^+	Variable in damping term
b	Span of rough and porous plate
B	Constant in porous wall equation
c	Constant used in the logarithmic law of the wall = 5.1
C_p	Specific heat at constant pressure
C_f	Skin friction coefficient
D	Damping factor
e	Total energy per unit volume
F	Suction factor
J	Transformation Jacobian
k	RMS roughness height
\dot{m}_s	Total suction mass flow
p	Thermodynamic pressure
p^+	Nondimensionalised pressure gradient
P_r	Molecular Prandtl number = 0.72
$P_{r,t}$	Turbulent Prandtl number = 0.9
R	Gas constant
R_e	Reynolds number
$R_{e,k}$	Reynolds number based on RMS roughness height
t	Time
T	Temperature
u	Velocity in x-direction
u^*	Van Driest's generalized velocity
u_τ	Friction velocity = $\sqrt{\tau_w/\rho_w}$
u^+	Inner velocity in x-direction = u^*/u_τ
U_ξ	Contravariant velocity along ξ -Direction
U_η	Contravariant velocity along η -Direction
v	Velocity in y-direction

v_w^+	Nondimensionalized normal velocity at the wall = v_w/u_τ
x	Streamwise cartesian coordinate
x_{sh}	x location of shock wave in computational domain
X_G	x location of shock generator leading edge
y	Normal cartesian coordinate
y^+	Inner distance from the wall = yu_τ/ν_w
Y_G	y location of shock generator leading edge
z	Lateral cartesian coordinate
α	Shock generator angle
α	CFL number
β	Costant used in damping terms
δ	Boundary layer thickness
δ^*	Displacement thickness
δ_i^*	Kinematic displacement thickness
ϵ	Turbulent eddy viscosity
η	Transformed coordinate normal to the surface
κ	Von Karman costant = 0.4
μ	Dynamic viscosity
ν	Kinematic viscosity
ρ	Density
σ_{xx}, σ_{yy}	Normal shear stress
σ	Constant in equation (3-6)
τ	Tagential shear stress
θ	Momentum thickness

Subscripts

aw	Adiabatic wall condition
BL	Boundary layer
CL	Centerline
CFL	Courant Fredirik Lewis
e	Boundary layer edge
P	Pitot pressure
PL	Bleed plenum chamber

<i>s</i>	Suction
<i>sh</i>	Shock
<i>T</i>	Stagnation conditions
<i>w</i>	Wall conditions
1	Conditions of first pitot profile

Superscripts

*	Compressibility transformation
+	Non-dimensionalized by inner variables
.	Quantity per unit time

CHAPTER 1

INTRODUCTION

The investigation of the interaction between oblique shock waves and turbulent boundary layers is an important problem in the design of supersonic inlets of airbreathing propulsion systems. These interactions are known to induce changes in the thickness of the boundary layer and the shape of the velocity profiles. If the pressure rise associated with the incident and reflected shocks is of sufficient strength, separation of the boundary layer may occur and this in turn will affect the inlet performance. If not controlled, these effects will result in lower inlet total pressure recovery and increased flow distortion. A common method of boundary layer control involves bleeding a portion of the low momentum boundary layer flow through porous walls, slots, or scoops. Mass removal for boundary layer control reduces the thickness of the boundary layer, increases its ability to withstand higher pressure gradients without separating, and changes the shape of the velocity profiles.

Control of oblique shock wave/turbulent boundary layer interactions with suction have been investigated experimentally both in two-dimensional and axysimmetric configurations in a number of studies. Among these experiments were those of Strike and Rippey [1], Hingst and Tanji [2], Seebaugh and Childs [3], and Sun and Childs [4], who used perforated walls to control the interaction. There have also been experiments incorporating bleed in supersonic inlets by Hingst and Johnson [5], and Fukuda, Hingst and Reshotko [6]. The suction in these experiments was applied through discrete holes. An experimental investigation using continuous suction through a porous material was performed by Lee [7], and Lee and LeBlanc [8]. A recent review of the literature on the subject of shock wave/turbulent boundary layer interactions and their control is presented in reference [9].

The use of continuous suction through porous materials for shock wave/boundary layer interaction control has not been studied extensively most likely for the following reasons. The surface roughness of porous materials causes thickening of the boundary layer which can negate the effect sought from suction. The porous

plate may have to be quite thick or reinforced to sustain the pressure difference on its two sides without deforming. This can cause a high pressure drop through the porous material requiring a lower pressure in the bleed system, which may be expensive to implement. Porous materials, however, present some advantages over surfaces with discrete holes or slots. A porous surface gives approximately a continuous distribution of mass transfer and allows a better approximation of the normal velocity boundary condition at the wall. Their study remains interesting at least for theoretical purposes and numerical code verification.

When an oblique shock wave interacts with a turbulent boundary layer on a porous surface the pressure rise associated with the incident and reflected shocks may cause a variation in mass flow through the surface. This variation is not known a priori and depends on the strength of the shock, the nature of the porous material, and the bleed system. Experimental measurements of bleed distribution through the boundary layer control area have been limited to the work of Hingst and Tanji [2] who used a hot-wire probe to measure the flow rate through discrete holes. In the work of Lee and LeBlanc [8], no local bleed measurements were made; instead the Darcy equation was used to compute the flow distribution through the porous material from the difference between the measured wall pressure and the pressure inside the bleed plenum chamber. Both studies found a bleed distribution very similar to the pressure distribution.

Continuing advances in computational fluid dynamics and computer capabilities have provided the opportunity to calculate the interaction of oblique shock waves impinging on a boundary layer. Numerical solutions of the mass averaged Navier-Stokes equations for these interactions on a flat plate and in a compression corner [10-13], and in high speed inlets [14] have produced convincing results and reached favorable agreement with experimental measurements. Unfortunately, for interactions with suction the numerical solutions and experiments have not always been in good agreement [15,16]. The major difficulty can be easily identified as the lack of accurate turbulence models and adequate boundary conditions on porous walls.

Turbulence modeling for flows involving compressibility effects, strong pressure gradients, and suction is a very difficult task, and among the many models that have been tested, none has been found to be general and accurate. Of the eddy viscosity

type models, the Cebeci-Smith model [17] and the Baldwin and Lomax model [11] are the most commonly used for the computations of shock wave/turbulent boundary layer interactions. Shang [10] used the former model for the the computation of shock wave/boundary layer interactions on a flat plate and in a compression corner and found it to predict the mean flow characteristics reasonably well. Cebeci [18] extended his basic model to include the effects of pressure gradient and mass transfer and verified its capabilities for subsonic conditions. Its application for shock wave/turbulent boundary layer interactions with suction have been made by Knight [16]. The Baldwin and Lomax model was patterned after that of Cebeci-Smith with modifications that avoid the necessity for finding the edge of the boundary layer. It has been verified in adverse pressure gradient flows for shock wave/turbulent boundary layer interactions [11,12], but no extension has been made to include the effect of bleed. A critical review of this model and its deficiencies are given by Visbal [19]. Most recently, Abrahamson [15] performed numerical computations on the control of an oblique shock wave with suction using the Baldwin and Lomax model modified for bleed. The modification employs the additional terms proposed by Cebeci [18] for flows with pressure gradients and mass transfer.

Numerical computations that must account for mass transfer at the wall are limited by the lack of suitable boundary conditions for modeling boundary layer bleed. In general the bleed is assumed to be a continuous flow of mass through a porous wall, whereas experiments are made with perforated walls or slots. A variety of methods of defining the bleed mass flux distribution have been employed. For example, Tassa and Sankar [20] and Hanin, Wolfstein, and Landau [21] used a constant suction rate within the the interaction region to eliminate separation in laminar cases. For turbulent flows, Knight [16] specified a constant bleed distribution throughout the interaction region. The specified bleed was taken equal to the average of the experimentally measured total suction mass flow rate. Recently, Abrahamson [15] modeled the flow through discrete holes as an isentropic process. The flow rate was then computed from the ratio of local wall total pressure and a specified bleed plenum pressure. A constant was introduced in the bleed equation and adjusted so that the total mass bled would match the value reported in the experiment of Hingst and Tanji [2].

It appears from the literature that detailed experimental information on the

effects of continuous suction on the boundary layer properties in the region of interaction with an oblique shock wave is not currently available. Such data are essential for the verification of computational methods that must account for suction to control shock wave/boundary layer interactions. There is also a need to develop bleed models to predict mass flux through the wall. The present investigation is both an experimental and a numerical study of the effect of continuous suction through a porous material on the interaction of a two-dimensional oblique shock wave with a turbulent boundary layer. The primary objective of the experimental program was to investigate the effects of suction on the interaction behavior and provide quantitative data for the verification of computational methods and turbulence models that are based on the assumption of continuous suction through porous walls. A secondary objective was to derive an empirical equation that correlates the mass flow with the pressure drop through the porous plate. This model equation was used in the numerical computations as a boundary condition on the porous wall to determine the bleed distribution. Since any porous material has some degree of surface roughness, a series of measurements were made on a rough plate to examine the effect of roughness on the interaction and establish a baseline data for bleed comparisons.

The experimental investigation was carried out in the NASA-Lewis Research Center 30.5 cm×30.5 cm (1ft×1ft) supersonic wind tunnel, using the naturally occurring boundary layer on the tunnel walls. The interaction was studied on a porous plate and a rough plate. The porous plate was made from a screen type material called Dynapore, backed by a hexagonal cell honeycomb material for structural support. The rough plate insert was made by epoxying a Dynapore sheet with a solid aluminum plate underneath, in this way the porous and rough plate will have the same surface roughness. The porous and rough plates were 12.7 cm (5.0 in) long and 15.24 cm (6.0 in) wide spanning half the tunnel sidewall. Tests were conducted on both plates at free stream mach numbers 2.5 and 3.0, and total pressure of 172.3 kpa (25.0 psia) and 241.2 kpa (35.0 psia), respectively. Data are reported for a unit Reynolds number of $1.66 \text{ E}7/\text{m}$ ($5.0 \text{ E}6/\text{ft}$) for $M = 2.5$ and $1.85 \text{ E}7/\text{m}$ ($5.6 \text{ E}6/\text{ft}$) for $M = 3.0$. Flow deflection angles were varied from 0° to 8° .

Wall static pressure measurements were made both along the test plate centerline and off the centerline. Boundary layer pitot pressure surveys were made upstream

of, within, and downstream of the interaction region using a pitot probe. The local bleed rates through the porous plate were measured with a hot-wire probe mounted in the bleed plenum chamber. An oil film visualization technique was used primarily to check for two-dimensionality of the flow. The results are presented in the form of wall pressure distributions and pitot pressure profiles. For the tests with suction, the local mass flow distributions through the porous wall are also reported.

The goal of the numerical study was to compute the flowfield characteristics of a two-dimensional oblique shock wave/turbulent boundary layer interaction on a porous wall with suction. The computations were made using a modified version of the Navier-Stokes code developed by Shang [22]. The numerical code solves the unsteady, compressible, mass averaged Navier-Stokes equations using the explicit time marching scheme of MacCormack [23] to obtain a steady state solution. Two modifications were made to the numerical code used herein. The first one was the use of the empirical bleed model that relates the mass flux through the porous wall to the difference between the local wall static pressure and a specified bleed plenum pressure. The empirical bleed model offers the advantage of being able to account for variable bleed distribution produced by the streamwise pressure gradient caused by the shock wave. The Cebeci turbulence model, which accounts for the effects of pressure gradient and suction, was implemented instead of the Baldwin and Lomax model.

Numerical results are first verified by comparison with the experimental measurements of wall static pressure, total pressure profiles, and bleed distribution through the porous wall. Then the flowfield structure is delineated by presenting pressure and Mach number contours. The turbulence model and bleed model boundary condition were found to give results that are in fairly good agreement with experimental data in spite of the fact that the effect of plate roughness was not modeled.

CHAPTER 2

EXPERIMENTAL PROCEDURE

2.1 Wind Tunnel Facility

The experimental investigation was performed in the 30.5 cm×30.5 cm (1 ft×1 ft) supersonic wind tunnel of the NASA-Lewis Research Center. The facility is of the open circuit type, providing continuous operation through availability of separate upstream high pressure air supply and downstream sub-atmospheric pressure to achieve necessary pressure ratios for generation of supersonic flows. An overall view of the wind tunnel is shown in Figure 1.

Mach number is established by selection of one of six fixed nozzle blocks designed for nominal Mach numbers of 1.6, 2.0, 2.5, 3.0, 3.5, and 4.0. The tunnel has the capability of achieving total pressures in the plenum chamber up to 345.0 kpa (50.0 psia) and unit Reynolds numbers of 3.3 E6/m to 3.6 E7/m (1.0 E6/ft to 1.1 E7/ft). Reynolds number control is obtained by adjustment of the stagnation pressure in the plenum chamber through manipulation of throttling valves. Air temperature is not adjustable and is typically near the ambient value with neither condensation nor liquefaction occurring. In the present experiments, the tunnel was operated at nominal Mach numbers 2.5 and 3.0 with stagnation pressures of 172.3 kpa (25.0 psia) and 241.2 kpa (35.0 psia) respectively. The unit Reynolds number was 1.66 E7/m (5.0 E6/ft) for $M = 2.5$ and 1.85 E7/m (5.6 E6/ft) for $M = 3.0$. The sidewalls of the test section are interchangeable and can be replaced with removable inserts that provide the necessary instrumentation and equipment for any particular test requirement. A photograph of the tunnel test section, with the suction plate, shock generator, and pitot probe mounted in it, is shown in Figure 2. This facility has been used for many shock wave/boundary layer interaction studies in the past and its capabilities are well documented [24-26].

2.2 Test Plate Models

The experiments were conducted on one of the sidewalls of the tunnel test section. An aluminum plate of 30.5 cm (12.0 in) span and 40.6 cm (16.0 in) length was

fabricated to match the tunnel test section wall. It can accommodate interchangeable plate inserts, which are removable from outside the tunnel. A rubber O-ring around the perimeter creates an air tight compression seal. A sketch of the configuration used in the present experiment is presented in Figure 3. Two insert plates were tested, a porous plate and a rough non-porous plate. The porous plate was made from a 2-layer Dynapore material (Model 407570, manufactured by Michigan Dynamics), which is a stainless steel woven material used commercially as a filter material. A photograph of the porous material is shown in Figure 4. The flattened surfaces are due to the calendering process (done by the manufacturer), which squeezes the woven material to a specified thickness, reducing its porosity and improving its smoothness. The thickness of the sheet used was 1.5 mm (0.06 in). This type of material or similar ones have been used by other researchers for boundary layer studies [27-30].

The strength of the Dynapore sheet is inadequate without backup. To provide structural support as well as air ducting a hexagonal cell stainless steel honeycomb structure, of 0.48 cm (0.19 in) cell size and 1.9 cm (0.75 in) thickness, was bonded to the porous sheet. The bonding was done all around the edges of the porous plate and on some spots along two lines each one 5.08 cm (2.0 in) off the plate centerline. These spots were carefully selected so as not to affect the wall static pressure measurements. No check was made to evaluate the effects of the honeycomb structure or of the bonding on the flow uniformity through the porous plate. The bonding was done in a controlled temperature furnace under vacuum at the NASA-Lewis fabrication shop. The porous sheet-honeycomb assembly was then epoxied into an aluminum frame. A cross section of the porous plate insert is shown in Figure 5-a. Two sets of porous plate inserts were constructed, one was instrumented with static taps and thermocouples for surface pressure and temperature measurements and boundary layer surveys, the other was left blank for local bleed distribution surveys. A rough plate was fabricated by epoxying a solid aluminum plate to the porous sheet (Fig. 5-b). The plate was instrumented with static taps only. Both rough and porous plates have a screen mesh type of roughness.

Knife-edged fences were mounted along the porous and rough plate inserts to isolate the region of study from the three-dimensional flow in the test section corners. Similar fences were used by Hingst and Tanji [2] for the same purpose mentioned

above. No tests without the fences were made in the present study to demonstrate their effect; however, an oil film visualization was made on the plate surface, in the region between the fences, and showed that they did not disturb the incoming boundary layer (see section 3.1). The fences were 5.08 cm (2.0 in) high extending beyond the boundary layer edge of approximately 3.0 cm (1.18 in) and were mounted 7.62 cm (3.0 in) to either side of the plate centerline. A plane view of the test plate which houses either the rough or porous plate insert is presented in Figure 6. When the porous plate insert and fences were installed on the test plate the porous area open to the flow was 15.24 cm (6.0 in) wide and 12.7 cm (5.0 in) long.

2.3 Suction Equipment

In order to supply boundary layer suction through the porous plate, a bleed vacuum system was attached to the test section. This system consisted of a bleed plenum chamber, a vacuum pump, and an exhaust system (Figure 1). The bleed plenum chamber, having a rectangular cross section 40.64 cm by 30.5 cm and a height of 37.0 cm (16.0×12.0×14.5 in), was bolted to the outer side of the test section sidewall on which the experiment was conducted. A vacuum boost pump was used in the bleed line to provide greater bleed rates than could otherwise be obtained simply by bleeding directly to the tunnel exhaust system. The bleed rate was not controlled in the present experiments; however, the pump maintained sufficiently low pressures in the bleed chamber, on the order of 3.5 kpa (0.5 psia), for suction to occur. The exhaust system is a long pipe of 15.24 cm (6.0 in) ID, which houses an orifice plate to measure the total bleed flow rate. The local bleed rate through the porous plate was measured by a single hot-wire probe mounted on a traversing mechanism inside the bleed plenum chamber as will be explained in section 2.5.

2.4 Shock Generator

A sharp leading edge, full span, flat plate shock generator, having continuously variable incidence and independent axial location, was mounted to the sidewall opposite the test plate. Teflon strips affixed to each side of the plate provided sliding seals at the tunnel upper and lower walls, preventing leakage from one side of the plate to the other. The shock generator was 40.64 cm (16.0 in) long so that the expansion fan originating from its trailing edge reached the test wall well downstream of the instrumented area. The shock generator was fixed on the forward end (close to the

leading edge) to a pair of sharp edged legs (struts), each one 5.08 cm (2.0 in) from the plate centerline, thereby removing torsional displacement of the plate if held only on one leg. The struts were attached to pivots, bolted on the outside of the tunnel wall to reduce blockage effect. The rotation of the generator was provided by a driving shaft attached to the back end of the plate. Three slots were machined in the mounting sidewall to allow passage of the struts and driving shaft. The mounting of the shock generator allowed the plate to be moved to different axial locations so that the shock wave produced would impinge near the center of the porous and rough plate inserts.

Generator angle (and hence the shock strength) was varied by a remotely activated drive unit attached to the end of the generator plate and the mounting wall. The value of the shock generator angle with respect to the test plate surface was inferred from the voltage output of a potentiometer, linked to the drive unit, which was calibrated against the unloaded shock generator angles.

2-5 Instrumentation

The measurements consisted of wall static pressures and temperatures, pitot pressure distributions through the boundary layer, and local bleed surveys through the porous plate. The pitot pressures were obtained with a pitot probe and the bleed flow rate with a single hot-wire anemometer. A detailed discussion of the instrumentation is given below.

2.5.1 Wall Pressure and Temperature

The surface static pressure distribution was obtained with 75 pressure taps of 0.5 mm (0.02 in) ID arranged in six rows parallel the plate centerline. The two rows with 35 taps staggered 0.457 cm (0.18 in) from the centerline were combined to plot the axial wall static pressure distribution. The remaining four rows were used to check the extent of uniformity of the flow in the spanwise direction, as will be explained later. The taps were closely spaced in the interaction region and spread out farther away. The details of the arrangement and spacing of the taps is shown in Figure 7. All tubes on the rough and porous plates were mounted flush with the flow surface. The tubes mounted on the smooth wall and rough plate insert were fixed as shown in Figures 8-a and 8-b. The ones mounted on the porous plate insert were epoxied to the honeycomb structure as illustrated in Figure 8-c.

Surface temperature was measured by five chromel-constantan thermocouples

placed along a line parallel to and offset 4.32 cm (1.7 in) from the centerline. The first thermocouple was mounted on the solid test plate upstream of the plate insert, and the next four were on the porous plate (Fig. 7). No thermocouples were installed on the rough plate insert. The static taps and thermocouples locations are referenced to the farthest upstream static tap on the solid plate (tap 38).

2.5.2 Pitot Probe

Pitot pressure measurements through the boundary layer were obtained using a pitot probe designed as shown in Figure 9. The tip of the probe was made of 0.508 mm (0.02 in) stainless steel tube with 0.0635 mm (0.0025 in) wall thickness, flattened to a height of 0.41 mm (0.016 in). The probe was mounted on an automatic traversing mechanism capable of moving axially (x-direction) and perpendicularly (y-direction) to the test plate by two stepping motors remotely actuated by a stepping motor driver/control unit. The driving motors and gear assembly were mounted on the outside of the tunnel diffuser sidewall. Probe surface contact was determined by an electrical 'touch' circuit. The location of the probe when off the plate surface was indirectly determined from voltage outputs of encoders linked to the stepping motors, which were previously calibrated against probe positions. Since the traversing mechanism does not provide spanwise movements (z-direction) an extension arm was used to hold the probe 3.66 cm (1.44 in) from the plate centerline for additional boundary layer surveys that will serve to check the two-dimensionality of the flow. A Fluke microcomputer instrument controller, Model 1752A, was interfaced with the stepping motor driver/control unit through an IEEE port and a BASIC program was written to automatically move the probe to preselected positions.

2.5.3 Hot-Wire Probe and Anemometer

Local bleed mass flow through the porous plate insert was measured by a single hot-wire probe operated by a TSI-IFA 100 constant-temperature anemometer. The hot-wire probe, of the plug-in type, was constructed at the NASA-Lewis instrumentation shop. A schematic diagram of the probe is shown in Figure 10-a. The wire used was a tungsten wire of 5 μm (0.00019 in) diameter and 0.19 cm (0.075 in) length yielding an $l/d \simeq 400$ (wire length to diameter ratio). The tungsten wire was welded to two conically shaped supports (prongs) which were epoxied to a ceramic holder. Small lead wires were used to connect the probe to the anemometer coaxial

cable. Two probes were used in the present investigation; the first one lasted for one hour of testing, the other was run for the remainder of the test, approximately four hours. The hot-wires were calibrated for mass flow prior to measurements in a TSI calibrator unit, model 1125. The calibration was done at atmospheric conditions. Because measurements were carried out at low flow densities (low pressure conditions in the bleed plenum chamber), a correction for the effect of Knudsen number was made to the measured values as outlined in Appendix B. The probes were operated at an overheat ratio of 1.8 for both calibration and measurements.

The hot-wire probe in its holder was mounted on an actuator inside the bleed plenum chamber as sketched in Figure 10-b. The actuator was driven in two perpendicular directions (x- and z-directions) by two stepping motors remotely controlled. A translation stage, to which the probe holder was attached, served to position the probe at a certain height above the honeycomb.

2.5.4 Documentation of Two-Dimensionality

The oblique shock wave/turbulent boundary layer interaction experiments were intended to be "two-dimensional" in this study. This was sought because it offers a simple flow configuration useful as a simple test case for analytic and numerical computations. Previous studies of these interactions have always indicated the existence of three-dimensional effects [31-34]. Suction is believed to reduce or eliminate three-dimensionality effects. In order to verify two-dimensionality, spanwise wall pressure measurements, boundary layer pitot surveys at a lateral location off the plate centerline, and oil film visualizations were made.

a) Static pressures

Two lines of eight static taps each, located 1.32 cm (0.52 in) above and below the plate centerline, were used for comparison with the centerline pressure distribution. The taps were installed on both the rough plate and porous plate in the region where the shock boundary layer was to occur. Six rows of five taps each were used in the spanwise direction to check further the uniformity of the flow. Two rows were located on the solid wall, one upstream and one downstream of the insert plate, and four on the porous and rough plates (Figures 6 and 7).

b) Off-axis pitot profiles

Additional pitot pressure profiles were measured along a line parallel to the plate centerline and offset from it a distance of 3.66 cm (1.44 in). A total of nine profiles were obtained at the same axial locations as the first nine profiles measured along the centerline. The extension arm on which the probe was mounted for these surveys did not permit taking additional measurements downstream.

c) Off-axis hot-wire measurements

During tests with suction, hot-wire measurements were made along two additional lines 3.0 cm (1.19 in) above and below the porous plate centerline. This was used to verify the uniformity of the plate porosity and check for the spanwise variation in bleed that might result from the presence of three-dimensional effects.

d) Flow visualization

A qualitative investigation of the flow on the plate surface was attempted using an oil film visualization technique as outlined by Jurkovitch [25]. The oil film visualizations were made on the same plates used for measurements after all tests were completed. The technique had little success for the interactions on the rough and porous plate inserts because the oil was either absorbed by the pores or by the suction equipment.

2.6 Experimental Procedure

Before the tunnel start-up, the pitot pressure probe was moved to the farthest downstream position and away from the wall, and the shock generator was set at zero angle. A leak check of the static taps and the bleed system was made under vacuum. The wind tunnel was then started and let run for at least 15 minutes before taking data to ensure steady state conditions. After the warm-up period, the shock generator was set at the desired angle and the vacuum pump, for suction cases, was started and let warm up for five minutes. The pump warming time was short because it heated up quickly at low bleed flow rates. For the empty tunnel runs, the shock generator was removed from the test section and the plate to which it was attached was replaced by a plexiglass plate insert. For $M = 3.0$ tests, the nozzle block was replaced and the shock generator moved forward in the test section for the shock wave to impinge on the rough plate and the porous plate insert at approximately the same

location as in the $M = 2.5$ case.

The measurements encompassed the tunnel operating conditions (stagnation pressure and temperature), wall pressures, and wall temperatures. For tests with bleed, the pressure and temperature inside the bleed plenum chamber were recorded as well as the pressure and temperature upstream of the orifice plate and pressure drop across it. The latter data were used to determine the total suction mass flow rate. To eliminate probe interference on the above measurements, the pitot probe was moved downstream of the wall instrumentation. During boundary layer surveys, the pitot pressure probe was moved through the boundary layer starting from the free stream toward the wall in a series of predetermined steps. The steps were decreased as the probe moved closer to the wall. When the probe touched the wall, the driving unit stopped. The reading at the touch position was subtracted from, and half the probe tip height was added to all y-positions, assuring that the distances are referenced from the wall zero position.

The local bleed surveys were made on the non-instrumented porous plate. To check that the tunnel running conditions were the same as the ones with the instrumented porous plate, tunnel stagnation conditions, wall pressure on the smooth part of the test plate, and conditions in the bleed plenum chamber were recorded. Duplication of test conditions was good; however, the total suction mass flow removed was lower by as much as 8% with respect to tests during which the boundary layer was surveyed. This reduction in bleed is probably due to changes in hardware in the bleed plenum chamber. During wall pressure measurements and boundary layer surveys, Tygon tubes, connecting static taps to the pressure measuring equipment, were ducted through the bleed plenum chamber, while during bleed surveys, the hot-wire traversing mechanism was mounted inside the chamber (see Figure 10). The hot-wire probe was positioned approximately at the center of each honeycomb cell along the centerline, 0.32 cm (0.125 in) above the surface, and the voltage reading and probe position were recorded. During measurements, it was noticed that the hot-wire output voltage was stable and the average of two readings only was taken at each position. A total of 25 equally spaced points were surveyed. The spacing between points was equal to the size of the honeycomb cell, that is 0.48 cm (0.19 in). Similar measurements were repeated with the probe moved 3.0 cm (1.19 in) to either side of

the plate centerline.

All pressure data were measured using an Electronically Scanned Pressure (ESP) system having a range of ± 206.7 kpa (30 psia). The accuracy of the ESP system is $\pm 0.1\%$ of the full scale. The tunnel stagnation pressure was controlled typically to within $\pm 0.1\%$ of the nominal value during any given run. Temperature data were measured by chromel-constantan thermocouples accurate to $\pm 0.5^\circ\text{K}$ (1.0°F). The temperatures were determined from thermocouple EMF voltage outputs and an oven reference temperature of 339°K (150°F). The OMEGA data tables were used for their conversion. The axial pitot probe position was accurate to ± 0.5 mm (0.02 in), while the y-position to ± 0.25 mm (0.01 in). The shock generator angle setting is accurate to $\pm 0.1^\circ$. The mean value of the anemometer voltage was converted to mass flow using the calibration curve after correction for Knudsen number effect. The accuracy of the hot-wire position was ± 0.25 mm (0.01 in) in both axial and spanwise positions. The hot-wire readings were accurate to $\pm 5\%$. The total bleed mass flow accuracy is estimated to be better than $\pm 5\%$.

2.7 Test Conditions

The investigation was conducted at free stream nominal Mach numbers of 2.5 and 3.0. The tunnel stagnation pressure was held at 172.3 kpa (25.0 psia) for $M = 2.5$, and 241.2 kpa (35.0 psia) for $M = 3.0$. The total temperature in the plenum remained between 299°K and 301.5°K (538°R and 543°R) for all tests. The unit Reynolds number was 1.66 E7/m and 1.85 E7/m (5.0 E6/ft and 5.6 E6/ft) for $M = 2.5$ and $M = 3.0$, respectively. The boundary layer was turbulent in the test section, and the boundary layer thickness of the first profile measured on the smooth wall was approximately 3.0 cm (1.18 in).

The rough plate was tested first to establish the non-suction baseline data before performing tests on the porous plate. Each plate was tested at the two Mach numbers with shock generator deflections of 0° , 4° , 6° , and 8° . The no shock case was conducted with the shock generator plate removed from the test section to eliminate any possible disturbances. The coordinates of the shock generator leading edge, with respect to the reference station, are sketched in Figure 11. For each condition (Mach number and shock angle), the mass flow rate bled through the porous plate was the maximum obtainable by the suction system. The experimental test conditions are

summarized in Table I.

Pitot pressure profiles along the centerline and off the centerline were measured on the porous plate for all test conditions, except for the no shock case for which only centerline surveys were made. No off-centerline pitot pressure surveys were made on the rough plate. For the 6° and 8° flow deflection angles, the boundary layer was separated on the rough plate. No pitot pressure surveys were made for these cases because of insufficient tunnel time. In the zero deflection case, five pitot pressure profiles were measured along the centerline, three of which were on the porous and rough plate inserts and two on the smooth wall. On the porous plate, a total of 12 profiles were taken along the centerline and 9 off the centerline, for the non zero deflection angles. The location of the pitot pressure surveys are referenced to the first static tap along the centerline. This zero reference was 12.85 cm (5.06 in) downstream of the beginning of the test plate or alternatively 24.54 cm (9.66 in) downstream of the beginning of the tunnel test section. The positions at which the profiles were taken are indicated in Figure 7.

2.6 Data Reduction

The pitot data were reduced using the measured wall static pressure and the Rayleigh pitot formula to calculate the Mach number distribution. The static pressure throughout the boundary layer was assumed constant and equal to the wall value. This assumption may not be completely valid in the presence of suction and oblique shock waves (see Appendix A) and an experimental check should be done. The temperature was obtained from the Crocco-Busemann relation, assuming that the wall temperature was adiabatic. With these assumptions, then, the velocity profiles, for the zero flow deflection angle, were obtained and relevant integral properties were calculated using standard formulas and integration techniques. No velocity profiles were deduced for the shock wave/boundary layer interaction cases because the static pressure is not constant normal to the wall within the interaction region.

CHAPTER 3

EXPERIMENTAL RESULTS

Mean flow measurements of incident oblique shock wave/turbulent boundary layer interactions on a rough plate and a porous plate with suction were made at nominal Mach numbers 2.5 and 3.0. The total pressure was 172.3 kpa (25.0 psia) and the unit Reynolds number 1.66 E7/m (5.0 E6/ft) for $M = 2.5$ conditions. For $M = 3.0$, the total pressure and unit Reynolds number were 241.2 kpa (35.0 psia) and 1.85 E7/m (5.6 E6/ft), respectively. Stagnation temperature remained at near 300°K (540°R), and wall temperature near adiabatic condition. A no-shock case was run to establish the empty tunnel baseline data. A total of three shock strengths, generated by plate angles of 4° , 6° , and 8° were tested. A summary of the test conditions is given in Table I.

Experimental results are presented in the form of surface static pressures and temperatures, and pitot pressure surveys at various axial stations along the plate centerline and 3.66 cm (1.44 in) off the centerline. In the tests with bleed, the local mass flow distributions through the porous plate are also reported.

3.1 Properties of the Incoming Boundary Layer

The boundary layer under investigation grows on the sidewall of the test section, which is a continuation of the nozzle wall. Its origin is effectively at the nozzle throat and its thickness at the first survey station is approximately 3.0 cm (1.18 in) compared to the 30.5 cm (12.0 in) test section height and width. An oil film visualization was used to check the uniformity of the incoming boundary layer and the effect of the fences. Figure 12 shows that the streamlines on the smooth wall, upstream of the rough or porous plate insert, are virtually straight and parallel to the plate centerline. The use of fences did not seem to introduce any disturbances in the region of study. Additional documentation on the two-dimensionality of the flow on the rough plate and porous plate will be presented in section 3.4.

Typical incoming velocity profiles for the tests conducted at nominal Mach numbers 2.5 and 3.0 are presented in Figure 13-a. The pitot pressure profiles measured

farthest upstream on the smooth plate were used to generate these velocity profiles. For the $M = 2.5$ tests the calculated free stream Mach number is found to be 2.46 ± 0.01 with a corresponding velocity of 571 ± 5 m/s (1873 ± 16 ft/s). The free stream Mach number and velocity for the nominal $M = 3.0$ tests are 2.98 ± 0.01 and 624 ± 5 m/s (2047 ± 16 ft/s), respectively. The boundary layer thickness, δ , defined by the distance at which $u/u_e = 0.995$, is 2.7 ± 0.1 cm (1.06 ± 0.04 in) for $M = 2.5$ and 2.9 ± 0.1 cm (1.14 ± 0.04 in) for $M = 3.0$. The values are obtained by linear interpolation between experimental points. Also shown on the plots are the velocity profiles for a $1/7$ power law. The comparison shows the initial experimental profiles to be slightly fuller than the $1/7$ power law profile near the wall.

Turbulent boundary layer profiles for zero pressure gradient flows are usually considered to be represented in terms of two similarity laws, the law of the wall and the law of the wake. The former is written as

$$u^+ = \frac{1}{\kappa} \ln y^+ + c \quad (3-1)$$

where

$$u^+ = \frac{u^*}{u_\tau} \quad (3-2)$$

and

$$y^+ = \frac{yu_\tau}{\nu_w} \quad (3-3)$$

The friction velocity, u_τ , is defined by

$$u_\tau = \sqrt{\frac{\tau_w}{\rho_w}} \quad (3-4)$$

Nominal values of the constants are $\kappa = 0.4$, and $c = 5.1$. Here the Van Driest's generalized velocity [35,36], for an adiabatic wall, is used to account for the compressibility effect, which is given by

$$u^* = \frac{u_e}{\sqrt{\sigma}} \arcsin \left(\sqrt{\sigma} \frac{u}{u_e} \right) \quad (3-5)$$

where

$$\sigma = \frac{[(\gamma - 1)/2] M_e^2}{1 + [(\gamma - 1)/2] M_e^2} \quad (3-6)$$

By adjusting the value of C_f , equation (3-1) was visually curve fitted to the logarithmic part of each profile. A reasonable fit was obtained with skin friction values of 0.00146 for $M = 2.5$ and 0.00132 for $M = 3.0$. The transformed velocity profiles plotted in semi-logarithmic scale are shown in Figure 13-b, and are in good agreement with equation (3-1) represented by the solid line. They exhibit a law of the wall behavior up to about $y^+ \simeq 1000$. The deviation of the first points from the linear curve for $M = 2.5$ is due to the large uncertainty in determining the wall location. It can also be seen that the first data point with the probe touching the wall is already outside the laminar sublayer.

3.1.1 Percentage of Boundary Layer Bleed

Assuming that the incoming boundary layer is two-dimensional, the mass flow through a cross section of width b , equal to the span of the porous plate, is

$$\dot{m}_{bl} = b \int_0^\delta \rho u dy \quad (3-7)$$

The integral is evaluated from the velocity profiles by numerical integration, using Simpson's method, and found to be 0.475 and 0.430 kg/s (0.216 and 0.195 lbm/s) for $M = 2.5$ and 3.0, respectively. The ratio of the total suction mass flow rate, \dot{m}_s , to the mass flow rate through the boundary layer is given by (\dot{m}_s/\dot{m}_{bl}) . The maximum suction ratio was about 0.10 for $M = 2.5$ and 0.09 for $M = 3.0$ at the highest shock generator angle of 8° .

If a flow coefficient is defined as the ratio of the total suction mass flow rate to the mass flow that would pass through an area equal to the porous area at free stream conditions, namely

$$F = \frac{\dot{m}_s}{\rho_e U_e A} = \frac{\overline{\rho_w v_w}}{\rho_e U_e} \quad (3-8)$$

then the maximum flow coefficient would be 0.016 and 0.014 for $M = 2.5$ and $M = 3.0$, respectively. If the average suction mass flow per unit area, $\overline{\rho_w v_w}$, is compared to the growth of the boundary layer mass flow on a flat plate, $(\partial \dot{m}_{bl}/\partial x)$, then another ratio can be defined as

$$F' = \frac{\overline{\rho_w v_w}}{\frac{\partial \dot{m}_{bl}}{\partial x}} = \frac{F}{\frac{\partial \delta^*}{\partial x} \left(\frac{\delta}{\delta^*} - 1 \right)} \quad (3-9)$$

For $M = 2.5$ and $\alpha = 0^\circ$, $F' = 2$, which means that the total suction flow rate is twice the boundary layer mass flow growth. For the other angles, F' is proportional to F . The bleed ratios and flow coefficients are summarized in Table I for all bleed cases.

3.2 Flow in the Absence of Shock Waves

Knowledge of the properties of the flow on a rough and a porous plate with the tunnel empty is necessary to complete information for shock wave/boundary layer interactions. Results on the effect of suction and/or roughness are available for subsonic flows [37-39]; however, only few experiments have been carried out with supersonic flows [40]. Measurements in the empty tunnel were made for the following purposes: 1) to probe the boundary layer in the absence of a shock wave, 2) to determine the effect of roughness and suction on the boundary layer, 3) to determine the extent of any nonuniformity in the flow, and 4) to calibrate the porous material with the free stream parallel to the plate surface. In the following, the results for the rough plate will be presented first, followed by the porous plate results.

3.2.1 Rough Wall Results

a) Mach number 2.5

Figures 14 show the streamwise wall pressure distribution, boundary layer pitot pressure and velocity profiles, and boundary layer parameters along the centerline for the rough plate insert at $M = 2.5$ and unit Reynolds number 1.66 E7/m (5.0 E6/ft). Figure 14-a displays the surface pressure distribution. The origin of the x-abscissa is taken to be the first static tap on the test plate centerline. This zero reference was located 12.05 cm (5.06 in) downstream of the beginning of the test plate. The wall pressures are normalized by the stagnation pressure measured inside the plenum chamber, P_T . It can be seen that the pressure is constant on the smooth solid plate, followed by a slight increase, which appears to be caused by disturbances from the non-flush fitting of the frame with the test plate and of the rough plate with the frame. On the rough plate, we see local perturbations (spatial fluctuations) in the pressure. The amplitude of the oscillations is less than 5% of the pressure value on the smooth wall upstream. These perturbations are believed to be caused by the roughness of the plate and the flow over the rough plate is similar to the flow over a wavy wall of small waviness. The perturbations could also be caused by sound waves from the backed porous sheet, which is similar here to a shallow cavity [41]. On the

smooth region following the rough insert, the pressure becomes constant again. Aside from the local perturbations on the rough plate, the flow proceeds under zero pressure gradient conditions.

The boundary layer pitot pressure surveys, along the plate centerline, are presented in Figure 14-b. The origins of the profiles are displaced along the horizontal axis, in proportion to the distances at which they were measured, to show the axial development of the flow. These origins are identified by tick marks extending below the horizontal axis. The scale of the x-axis is shown below the first profile. The numbers on the profiles serve to identify their axial location (see Figure 7). The first profile was measured on the smooth wall, the next three on the rough plate insert, and the last one on the smooth plate downstream. The first pitot pressure profile is typical of the incoming turbulent boundary layer. The second profile shows a decrease in slope at the wall; this decrease persists for the next two profiles downstream and is caused by the roughness of the plate. For the last profile, the slope at the wall increases slightly due to the transition back to the smooth wall. The profiles become less full as the probe moved downstream on the rough plate and the pitot pressure as measured with the probe touching the wall decreases slightly.

Figure 14-c displays velocity profiles as deduced from the transverse pitot pressures. The velocities are computed assuming static pressure through the boundary layer equal to the local wall pressure and a temperature distribution given by the Crocco-Busemann relation as explained in Appendix A. The profiles are superimposed so that detailed information is revealed. The first profile is typical of the incoming turbulent boundary layer flow. This is not the initial incoming profile shown in Figure 13-a, rather it is located 4.8 cm (2.18 in) farther downstream (see Figure 7). The free stream velocity is 573 m/s (1880 ft/s), corresponding to a Mach number of 2.47. The boundary layer thickness is 2.8 cm (1.1 in). The free stream velocity and boundary layer thickness of this first profile are used to non-dimensionalize the velocities and y-distances respectively for all the other profiles. It can be noticed that the profiles become less full as we proceed downstream on the rough plate. This is in agreement with the results of Hamma reported in reference [38] for subsonic pipe flows and of Voisinet [40] for a flat plate at supersonic conditions. Downstream of the rough plate insert the velocity profile becomes full again and starts to readjust to the

smooth wall condition. Because of the roughness of the rough plate some disturbances (expansion-compression waves) may originate at the surface, but these are probably weak and thus are not revealed on the plots.

A plot of the same profiles with the y -distance and u -velocities non-dimensionalized with the local boundary layer thickness and local free stream velocity respectively is shown in Figure 14-d. The plots tend to collapse on top of each other in the outer part of the boundary layer; however, in the lower region up to $y/\delta \simeq 0.8$, they still show the effect of roughness.

The boundary layer thickness and integral parameters are shown as functions of the streamwise distance in Figure 14-e. They are larger on the rough plate and over the smooth wall downstream of the rough part. Although not shown here, the free stream velocity and mass flow in the boundary layer increase also. This is consistent with the expected boundary layer growth on a flat plate.

The skin friction on a rough plate is difficult to determine from pitot pressure measurements. For accurate skin friction measurements, a skin friction balance is needed. This method was used by Kong and Shetz [30] in subsonic flow for different roughnesses including a Dynapore material and by Voisinet [40] for a screen type roughness at Mach number 2.9. Many empirical equations are available for the correlation of skin friction from wall pitot and static pressure measurements in supersonic flows for smooth wall conditions [42,44]. To the author's knowledge, no such correlations exist for rough walls, and any such correlation would not be universal because of the variety in roughness geometries, pattern, and density. To check the prediction of these smooth wall correlations, the calibration equation of Abarbanel et al [42] is used to deduce the skin friction on the rough surface. It gives a skin friction decrease, which is in contradiction with the well known results of skin friction increase on rough walls. This can be explained in the following way. Since the pitot pressure measurement can only be made to the top of the roughness elements, and because roughness makes the profiles less full near the wall, the axis of the pitot tube, when in contact with the wall, was already outside the laminar sublayer, and hence was subject to a lower impact velocity than in the smooth wall case, and therefore the skin friction would appear to be lower. If the tube diameter were small enough to probe the laminar sublayer, it might have indicated an increase in skin friction.

For lack of a method to correlate the skin friction on a rough surface, no skin friction results will be presented here.

In order to characterize the flow regime on the rough plate, a roughness Reynolds number parameter, which is proportional to the roughness height-sublayer thickness ratio is used [38,40]. It is defined in terms of the shear velocity, u_τ , as

$$Re_k = \frac{ku_\tau}{\nu_w} \quad (3 - 10)$$

k is taken as the RMS roughness height of the Dynapore material used in the present experiments, which is approximately 0.25 mm (0.01 in). Using the value of u_τ and ν_w from the smooth wall velocity profile at $M = 2.5$ ($u_\tau = 22.0$ m/s and $\nu_w = 1.316 \text{ E-4}$ N.s/m²) then $Re_k \simeq 42$. For $M = 3.0$, $u_\tau = 10.5$ m/s and $\nu_w = 2.035 \text{ E-4}$ N.s/m², which gives $Re_k \simeq 31$. These values of Re_k indicate that the flow over the rough wall is in the transitional rough regime ($5 < Re_k < 70$).

b) Mach number 3.0

Figures 15 show the results for $M = 3.0$ and unit reynolds number of 1.85 E7/m (5.6 E6/ft). The wall pressure distribution is similar to the $M = 2.5$ case and shows perturbations that are on the order of 4% of the smooth wall value. The centerline boundary layer pitot pressure profiles exhibit the same characteristics as those for the $M = 2.5$ case. The total pressure near the wall decreases slightly for the profiles on the rough plate. The roughness causes a change in the slope of the pitot pressure profiles at the wall. All velocity profiles show a smooth monotonic decrease from the free stream value to the wall with no apparent external disturbances. The qualitative behavior of the profiles measured on the rough plate insert is somewhat similar to the $M = 2.5$ case. The profiles are less full than the smooth wall profile upstream, and this is consistent throughout most of the boundary layer up to about $y/\delta \simeq 0.8$ after which they tend to collapse on top of each other. The slope of the profiles at the wall decreases as a result of the effect of roughness. The velocity as measured with the probe touching the wall decreases slightly on the rough plate and shows a small increase on the smooth wall downstream.

The boundary layer, displacement, and momentum thicknesses for $M = 3.0$ are shown in curve (e). As for $M = 2.5$, there is a consistent increase of all three

properties with axial distance. There is also an increase in free stream velocity and mass flow within the boundary layer.

3.2.2 Porous Wall Results

Measurements similar to the ones made on the rough plate were performed on the porous instrumented plate at the same operating conditions. In addition to the wall static pressures and boundary layer surveys, the wall temperature and local mass flow through the porous plate were measured.

a) Mach number 2.5

Figures 16 show the results for the tests with suction applied on the porous wall. A suction flow rate of 0.027 kg/s (0.060 lbm/s) representing 5.7% of the incoming boundary layer was obtained. Figure 16-a displays the streamwise pressure distribution. The pressure is constant on the smooth part of the plate, followed by a decrease on the porous wall over a distance approximately equal to one third the porous plate length. This pressure decrease is caused by suction and is equivalent to the pressure drop produced by the expansion fan originating from an expansion corner. Over this length the subsonic part of the boundary layer is progressively absorbed and the roughness elements are still embedded in it, thus making the effect of suction stronger than the effect of roughness. When the subsonic region is absorbed, the effect of roughness then becomes dominant and the wall pressure exhibits perturbations of higher amplitude. The amplitude of the oscillations is about 10% of the smooth wall value. Another phenomenon that may be causing the pressure oscillations is the resonance of the porous wall holes. Repeated measurements were made and showed that the oscillations were always present, but no time dependent measurements were made. Perhaps the use of standard pressure taps in the porous region gives results that are in error due to suction. Furthermore, any such taps may cause nonuniformities in the suction distribution.

The extent of bleed and the pressure inside the bleed plenum chamber are shown on the plot. The pressure inside the bleed plenum was measured with two static taps one on the upstream and the other on the downstream wall of the chamber. The readings from the two taps were found to be within 1% of each other. Since the size of the chamber is large and the flow speed low, it can be assumed that the pressure inside is constant.

Pitot pressure profiles taken upstream of, on, and downstream of the porous plate insert are shown in Figure 16-b. The first profile taken on the porous plate differs significantly from the one taken on the smooth wall. The profile becomes full near the wall as a consequence of suction. The second and third profiles on the porous wall show a further increase of pitot pressure and slope at the wall; they are also fuller than the first bleed profile. The last profile obtained on the smooth wall is less full near the wall than the previous profiles. Near the edge of the boundary layer, the pitot pressure shows small perturbations due to the shock wave, which originates at the end of the porous plate as the flow is turned parallel to the impermeable wall downstream.

The velocity profiles are plotted together in Figure 16-c. The first profile is identical to the one measured with the rough plate except near the wall where it shows some distortion that could be an upstream effect of bleed or due to the error in the y -location of the probe. The free stream velocity is 571 m/s (1873 ft/s) and boundary layer thickness is 2.7 cm (1.063 in). On the porous plate, the profiles become fuller with an increase in free stream velocity and boundary layer thickness. The last profile becomes less full and starts to readjust to the smooth wall condition. The important change to be noted here is the increase in the slope of the profiles near the wall, which is typical of suction. Some wiggles in the profiles can be seen; this is due to the expansion waves generated at the porous plate surface by suction and perhaps also by roughness. The flow visualizations made by Lee and LeBlanc [7,8], for flow conditions at $M = 1.43$, confirm the existence of such expansion waves. They claim that the waves originate at the top of the roughness elements. It is expected that these waves are stronger in the present experiments because of the higher Mach numbers and bleed rates. When the velocities are non-dimensionalized by the local free stream velocity and the y -distances by the boundary layer thickness, the profiles seem to collapse onto one curve from $y/\delta \simeq 0.8$ to the free stream (Figure 16-d); however, below this distance the effect of suction is still very distinct.

The boundary layer thickness and integral properties are shown in Figure 16-e. The boundary layer thickness increases for all profiles on the porous wall and for the last profile on the smooth solid wall. The displacement and momentum thicknesses show an increase at the beginning of the porous plate followed by a

decrease, after which they level to constant values. The integrated mass flow through the boundary layer is found to increase over the porous wall, which can be explained by an entrainment of mass from the external flow into the boundary layer.

The skin friction reduction using the Abarbanel formula gives an increase in skin friction on the porous wall followed by a decrease downstream on the smooth wall. This increase in skin friction is expected because the velocity profiles are fuller near the porous wall than near the smooth wall. The quantitative values are questionable because the correlation formula does not take into account the effects of bleed and roughness.

The mass flow per unit area as obtained from the hot-wire measurements are displayed in Figure 16-f. The bleed distribution is approximately constant over the length of the porous plate. The oscillations observed are expected to occur since the wall pressure showed perturbations also. The mass flux predicted from the porous material calibration equation (equation 3-11) is shown with dashed lines. The prediction is in good agreement with measured values.

The wall temperature distribution is shown in Figure 16-g. The temperature on the smooth part of the plate is 280 °K (504 °R), which is near the adiabatic wall temperature of 283 °K (510 °R). A temperature increase of 12 °K (22 °R) occurs on the porous wall. As mentioned in the experimental technique section, the thermocouples installed on the porous section were mounted on the back of the porous sheet facing the bleed flow. Since the flow through the porous plate may not be isothermal, an increase in temperature may occur. The average wall temperature is near the adiabatic one. The air temperature inside the bleed plenum chamber, as measured by one thermocouple, is shown on the plot and is slightly higher than the wall temperature.

b) Mach number 3.0

The results for $M = 3.0$ and no shock condition are summarized in Figures 17. The amount of boundary layer bleed in this case is 0.021 kg/s (0.046 lbm/s) which is 5% of the incoming boundary layer. The axial wall pressure distribution in Figure 17-a exhibits the same characteristics as those at $M = 2.5$. The wall pressure shows perturbations on the porous plate that are on the order of 10% of the smooth wall value as found earlier at the lower Mach number.

The pitot pressure profiles are plotted in Figure 17-b. As the porous plate is reached, the profiles become fuller from the wall up to the free stream and this is consistent throughout the bleed region. The profiles show no apparent perturbations probably because of the low suction flow rate.

The velocity profiles normalized by the free stream velocity and boundary layer thickness of the first profile just ahead of the porous plate are presented in Figure 17-c. The free stream velocity for this profile is 624 m/s (2047 ft/s) and the boundary layer thickness is 2.9 cm (1.14 in). The profiles on the porous plate exhibit an increase in free stream velocity and are fuller as we proceed downstream. When the profiles are non-dimensionalized with the local conditions, (Figure 17-d), they show no tendency to collapse for most of the boundary layer up to about $y/\delta \simeq 0.8$. Above that they tend to collapse to one curve.

The boundary layer integral parameters presented in Figure 17-e follow to some extent the same trend found for $M = 2.5$. Both boundary layer and displacement thickness show a small increase over the first half of the porous plate, followed by a decrease on the other half. The momentum thickness is, however, constant over most of the porous plate, terminated by a slight decrease over the solid wall downstream. The predicted bleed, using equation (3-11), is shown in Figure 17-f. The total integrated mass flux, assuming a two-dimensional distribution is 0.017 kg/s compared to the measured value of 0.021 kg/s. Although hot-wire measurements were made, the bleed reduction could not be obtained because the measured Nusselt numbers were within a region that was not covered during the hot-wire calibration. The measured values were also below the curve fitted to the hot-wire calibration data. As explained in Appendix B, the flow regime in this case is of a mixed forced and natural convection type.

The wall temperature distribution presented in Figure 17-g shows a 12 °K increase at the beginning of the porous plate, followed by a decrease, and then by an increase over the remaining of the plate. The temperature in the bleed plenum chamber is higher than the wall temperature.

3.2.3 Porous Plate Calibration

The resistance to air flow (pressure drop) through the porous material as a function of flow rate was determined with the flow normal and parallel to the plate surface. The normal flow calibration was made outside the tunnel in a separate apparatus as explained in Appendix C. The parallel flow calibration was made on the porous plate insert used in the experiments. For each Mach number the stagnation pressure inside the settling chamber was changed in order to vary the flow rate through the porous plate.

The results are presented graphically in Figure C3 as the pressure drop coefficient versus the Reynolds number based on the thickness of the porous material, e , (see Appendix C). A least squares fit of the data to the following equation

$$\frac{\Delta p}{\rho V^2} = A + \frac{B}{Re} \quad (3 - 11)$$

where

$$Re = \frac{(\rho v)_w e}{\mu_w}$$

gives $A = 212.7$ and $B = 7588.0$. This equation is used in the numerical calculations as a boundary condition and will serve to determine the local bleed distribution through the porous wall from the difference between the wall pressure and bleed plenum pressure.

3.3 Shock Wave/Boundary Layer Interaction Results

In the absence of a boundary layer, when an oblique shock wave reflects from a solid smooth surface, the pressure jumps with an infinite gradient at the shock impingement point by an amount which depend on the shock strength. In the presence of a turbulent boundary layer, the pressure gradient is finite and the pressure rise takes place over a non-zero length of surface corresponding to the shock reflection. If the boundary layer remains attached, the pressure distribution will rise and reach a final value approximately equal to the inviscid pressure (Figure a). Increasing the shock strength will cause a separation region to form upstream of the shock impingement point with reattachment taking place downstream. When separation is fairly large, two additional inflections will appear in the wall pressure distribution in the region of separation (Figure b). The final pressure value may also be lower than the inviscid

pressure rise. This definition will be used primarily as a means for detecting separation from wall pressure distributions of tests involving the interaction of an oblique shock wave with a turbulent boundary layer.

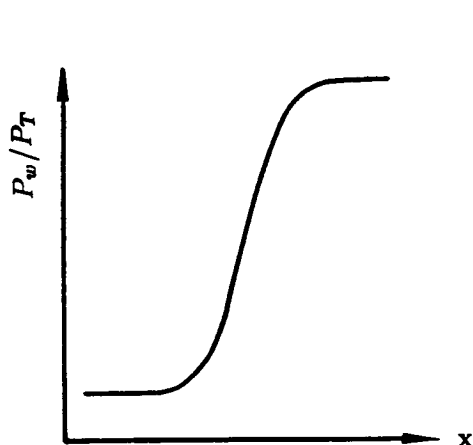


Fig. a Attached Boundary Layer

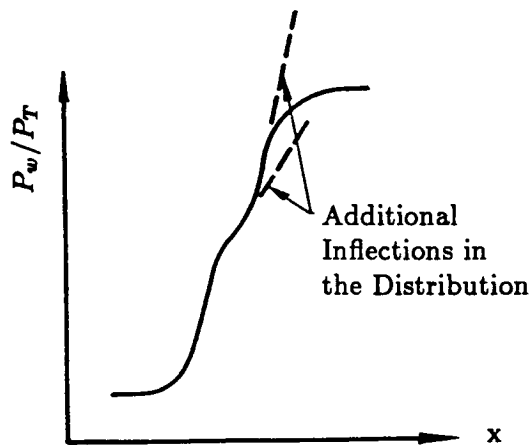


Fig. b Separated Boundary layer

3.3.1 Interactions on the Rough Plate

a) Mach number 2.5

Figures 18 show results for a flow deflection angle of 4° with the oblique shock wave reflecting on the rough plate insert. The surface static pressure distribution (Figure 18-a) has the trend of a non-separated boundary layer. A region of approximately zero pressure gradient exists upstream of the shock impingement point, followed by a monotonic pressure rise caused by the incident and reflected shocks, reaching at the end a constant value. There seems to be a small increase in pressure at the rough plate end which may be caused by perturbations from the junction of the rough plate and the frame-test plate. The inviscid pressure rise determined from the nominal shock angle of 4° and the computed Mach number of 2.46 is also shown on the plot. The final pressure value is slightly higher than that found from inviscid theory. This suggests that the shock wave angle was higher than the nominal value because of the boundary layer build up on the shock generator plate. The pressure rise is spread approximately over one boundary layer thickness.

The pitot pressure profiles, surveyed mainly on the rough surface, are plotted in Figure 18-b. The incident and reflected shocks are evident on the plots; they appear as a band not a single line (smeared shocks) with the reflected shock being broader than the incident shock. The profiles reveal a well defined boundary layer thickness ahead of the incident and downstream of the reflected shock. As the incident shock penetrates into the boundary layer it becomes less apparent on the plots. The pitot pressure ahead of the interaction increases rapidly as the probe moves above the incident shock into a region of lower Mach number. The opposite behavior occurs for the profiles downstream of the point of emergence of the reflected shock, the pitot pressure decreases as the probe moves above the reflected shock into a higher Mach number region.

The profiles show a continuous decrease in slope at the wall until the end of the rough plate, after which the slope increases again. The profiles measured in the interaction region seem to have an inflection point near the wall, which could be explained as follows. First, since the rough plate has interconnected pores, the adverse pressure gradient caused by the incident and reflected shocks may induce flow through the pores from the higher pressure side downstream of the impingement point to the lower pressure side upstream. Second, the probe may be causing the flow to separate. Third, the probe tip is subject to higher pressure gradient and roughness effects causing errors in readings near the wall.

The wall pressure distribution for the 6° flow deflection angle at constant Reynolds number is shown in Figure 19. The wall pressure distribution does not exhibit the usual trend of an attached boundary layer and therefore indicates that separation occurred. The pressure distribution shows a constant pressure region, followed by a pressure rise to a separation point, an additional pressure rise terminated by a change in slope, a pressure rise up to reattachment, and a further pressure rise culminating in a constant pressure region corresponding to the pressure downstream of the reflected shock. The final pressure is slightly lower than the inviscid value. The pressure rise is spread over a distance of two boundary layer thicknesses.

Increasing the shock generator angle to 8° results in a separated interaction as shown in Figure 20. The pressure rise begins farther upstream, almost at the beginning of the rough plate insert. The qualitative picture of the approach to

separation is similar to the 6° deflection angle; however, the size of separation is larger in this case and the length of upstream influence has also increased. Boundary layer separation also causes a reduction in peak pressure to a value below the inviscid pressure rise and the additional inflections became more pronounced. The pressure rise extends approximately over three boundary layer thicknesses.

No pitot pressure surveys were made for the 6° and 8° flow deflection angles because of insufficient tunnel time.

b) Mach number 3.0

For the $M = 3.0$ tests, the shock generator plate was moved forward in the test section so that the shock wave would impinge approximately at the same location as for the $M = 2.5$ case. The results for the 4° deflection angle are shown in Figures 21. The wall pressure distribution (Figure 21-a) shows a typical unseparated interaction. The final pressure value is higher than the inviscid pressure. The distance over which the pressure rise occurs is lower than that observed at $M = 2.5$.

The boundary layer pitot pressure profiles (Figure 21-b) show a development similar to Figure 18-b for a non-separated interaction. The incident and reflected shocks are apparent on the plots.

As previously observed at $M = 2.5$, a wall pressure distribution indicative of separated flow is obtained at $M = 3.0$ for shock generator angles of 6° and 8° (Figures 22 and 23). The pressure rise begins slightly farther downstream and the separation region is smaller. The final pressure reached is lower than the inviscid pressure value and is more pronounced for the 8° flow deflection.

The evidence of extensive flow separation can be seen in Figure 24 which is a photograph of the oil film visualization. The oil on the surface was gathered in the separation region, which spread over a length of approximately 5 cm (two boundary layer thicknesses).

3.3.2 Interactions on the Porous Plate

In all the results to be presented, the bleed region extended upstream and downstream of the shock impingement point.

a) Mach number 2.5

Typical results for the flow deflection angle of 4° are presented in Figure 25. A

suction flow rate of 6.6% of the incoming boundary layer mass flow was obtained. The surface static pressure distribution is shown in Figure 25-a. The pressure on the solid wall and porous plate up to the pressure rise is identical to the one measured with no shock (see Figure 16-a). The pressure rise is slightly steeper relative to the one obtained on the rough plate. It is found that the pressure makes a step-up as the flow passes from the porous plate to the solid smooth wall, after which it decreases slightly. The final pressure value is slightly higher compared to the peak reached with the rough plate insert and is also higher than the inviscid pressure. This increase is caused by the shock wave generated by the flow turning parallel to the solid smooth wall. Perturbations in pressure are apparent in the plots and these were caused by roughness elements and/or sound waves from the bleed chamber as explained earlier (no shock case). A very striking difference from the rough plate tests is a downstream shift in the shock impingement location. As suction absorbs a portion of or all the subsonic layer the shock wave penetrates deeper into the boundary layer and the pressure rise moves downstream. Although with suction there should be a decrease in upstream influence, with the pressure perturbations it is difficult to distinguish such an effect from the plot. The bleed plenum pressure was assumed uniform; its value is indicated on the plot, along with the extent of bleed. Most of the bleed area was upstream of the shock impingement point.

Figure 25-b shows the boundary layer pitot pressure profiles. The first two profiles taken on the smooth wall are identical to the ones taken with the rough plate insert at $M = 2.5$. The effect of bleed on the boundary layer is seen manifested at the fourth profile with an increase in both pitot pressure and slope at the wall. There seems to be no effect of bleed on where the incident shock wave crosses the edge of the boundary layer compared with the interaction on the rough plate; however, there is a noticeable effect on the reflected shock. The reflected shock emerges farther downstream and is broader than the rough plate case. The additional shock from the bleed cut-off can also be seen from the last pitot profile.

The profiles downstream of the bleed region are much fuller than the ones upstream. The last profile shows a decrease in pitot pressure near the edge of the boundary layer, which is caused by the shock wave from the bleed cut-off, and an additional decrease from the reflected shock wave. A decrease in boundary layer

thickness can be seen from the plots. The profiles surveyed on the porous plate show that the pitot pressure remains constant over some distance perpendicular to the wall. In this region the streamlines are curved due to suction and the pitot readings will have errors due to the angle of attack of the flow relative to the probe axis.

The local bleed distribution is shown in Figure 25-c. It shows some scatter, but on the average it is constant before the shock impingement, followed by a slight decrease just before the pressure rise, and then by an increase due to the pressure rise associated with the incident and reflected shocks. It can be said that the local bleed distribution follows the trend of the wall pressure. The total suction flow rate is 0.032 kg/s (0.07 lbm/s). The integrated mass flow, assuming a two-dimensional distribution, is 0.035 kg/s (0.077 lbm/s). The difference is due to the errors in hot-wire readings and total mass flow measurements, and the assumption of two-dimensionality may not be exactly true. The prediction of mass flow distribution using the empirical equation presented in section 3.2 (equation (3-11)) and shown by the dashed line follows very closely the wall pressure variation. The integrated mass flux of this prediction is 0.031 kg/s, which agrees remarkably well with the measured value.

Wall temperature as recorded by five thermocouples is shown in Figure 25-d. The temperature on the smooth wall is 280 °K, followed by a 10 °K increase on the porous wall. The wall temperature increase probably is not caused the shock wave/boundary layer interaction, but rather by the fact that the thermocouples were not mounted flush with the flow surface. The temperature inside the bleed plenum chamber is also shown on the plot and is very near the porous plate temperature.

Figures 26 show results for the 6° flow deflection angle. The static pressure distribution shown in Figure 26-a indicates that the boundary layer remained attached. The pressure rises sharply in this case and the upstream influence is reduced compared to the rough wall. The average pressure downstream of the reflected shock is equal to the inviscid value. The pressure inside the bleed chamber stayed well below the wall pressure ahead of the interaction region so that the pressure gradient along the plate causes no recirculation (rejection) through the porous plate upstream. The final pressure value is essentially unchanged from the non suction case (Figure 22). The difference between the pressure inside the bleed plenum and on the wall ahead of the pressure rise caused by the interaction decreases from the previous case of 4°

flow deflection; however, downstream of the reflected shock the pressure difference increases.

The pitot pressure profiles are displayed in Figure 26-b. The increase in pitot pressure is seen in the fourth profile. The reflected shock wave angle has also increased as can be seen on the 10 th profile where the pressure decrease occurs farther away from the wall. The last profile shows an additional pressure decrease that is caused by the shock wave from the bleed cut-off. The pitot pressure profiles on the porous plate show a constant region perpendicular to the wall, similar to what was seen with the 4° flow deflection angle.

The bleed distribution shows a lot of scatter (Figure 26-c). Variations of $\pm 30\%$ around the mean value are encountered. It is relatively constant before the incident shock and increases at the location of the pressure rise. The total mass flow is 0.038 kg/s (0.084 lbm/s) which corresponds to a 20% increase over the 4° deflection. The integrated mass flux is 0.037 kg/s (0.08 lbm/s). Here again the prediction of bleed flow from the correlation equation follows the wall pressure distribution. It predicts a higher bleed downstream of the reflected shock than the measured one. The integrated total mass flow using the predicted values from equation (3-11) is 0.041 kg/s (0.09 lbm/s).

The wall temperature shows a fairly uniform distribution as can be seen in Figure 26-d. The temperature is in general slightly lower than previously found for the 4° deflection angle. The difference between the plenum temperature and the porous wall temperature increased slightly.

The results for the 8° shock generator angle are shown in Figures 27. The wall pressure distribution shown in Figure 27-a indicates that the pressure rise has moved forward and the pressure peak has increased as a consequence of increase in shock strength. There is no indication of boundary layer separation. The highest pressure reached downstream of the reflected shock is equal to the inviscid pressure rise; however, most of the data points are below it.

The pitot pressure profiles, especially the ones downstream of the interaction region, are fuller on the porous wall because of the increase in suction rate (Figure 27-b). The shock penetrates into the boundary layer farther upstream and the angles of the incident and reflected shocks are higher. The disturbances from the bleed cut-

off are much sharper than with the lower deflections. These are visible in the last three profiles.

The bleed distribution (Figure 27-c) shows less scatter and follows the wall pressure variation. Less mass flow is bled ahead of the pressure rise and more behind it. The total suction mass flow is 0.049 kg/s (0.108 lbm/s) corresponding to a 28% increase over the 6° flow deflection angle case. The integrated bleed flow rate is 0.055 kg/s (0.12 lbm/s), which is 12% higher than the measured value. The prediction of mass removal using equation (3-11) is found to agree with the measured values and is equal to 0.055 kg/s. The rise in bleed distribution using this equation occurs behind the pressure rise. The predicted values are also higher than the measured values. This discrepancy is most likely to be caused by a higher incident shock wave angle during the bleed surveys.

The wall temperature distribution, presented in Figure 27-d, shows a similar distribution to Figures 25-d and 26-d for the lower deflections. Increasing the shock strength and therefore the bleed does not seem to affect noticeably the wall temperature.

b) Mach number 3.0

Results for $M = 3.0$ test cases with suction are shown in Figures 28 through 30. The shock reflections on the porous plate occurred at approximately the same locations as for $M = 2.5$ tests. The results for the 4° deflection angle are presented in Figures 28. The wall pressure distribution (Figure 28-a) is higher than the inviscid pressure value. Since, for the same shock angle, the boundary layer on the rough plate was not separated, the effect of suction on the wall pressure is seen here as an additional increase over and above the inviscid pressure rise. The difference between the pressure peak and the inviscid pressure rise was larger than that at $M = 2.5$. The pitot pressure profiles shown in Figure 28-b are fuller than those measured on the rough plate.

The bleed distribution as predicted from equation (3-11) is plotted in Figure 28-c. The total mass flow is 0.019 kg/s compared to the measured value of 0.22 kg/s. Deducing bleed from the hot-wire measurements and the hot-wire calibration curve was not possible for $M = 3.0$ cases. The corrected hot-wire data was below the calibration curve, in a region of mixed forced and natural convection (see Appendix

B). The wall temperature shows an increase over the beginning of the porous plate, followed by a decrease, and then by a slight increase.

Results of the 6° flow deflection angle are shown in Figures 29. The wall pressure distribution (Figure 29-a) indicates no sign of separation and the rise is sharper than that of the rough wall distribution. As a result of the increase in wall pressure downstream of the reflected shock, the level of pressure inside the bleed plenum pressure has increased. This causes a reduction in upstream bleed and an increase in bleed downstream of the interaction region. The average pressure reached on the reflected shock side is close to the inviscid value. Downstream on the impermeable wall, the pressure is higher than the inviscid pressure. The pitot pressure profiles (Figure 29-b) are much fuller than the ones surveyed on the rough wall under similar conditions. They are also fuller than the profiles for the 4° flow deflection. The fullness of the profiles is a result of both an increase in shock strength and suction. The reflected shock wave and the shock from the bleed cut-off are sharper in this case. In Figure 29-c, the bleed distribution is seen to follow the wall pressure distribution. The predicted total mass flux, using equation (3-11), is 0.029 gk/s which is equal to the measured value.

The results for the flow deflection of 8° are presented in Figures 30. The wall pressure (Figure 30-a) shows a sharp rise in the interaction region, indicating that the boundary layer is attached. The average pressure reached downstream of the interaction region is lower than the inviscid value, while on the impermeable wall, the pressure is higher than that of inviscid theory. The pressure inside the bleed plenum pressure is near the wall pressure ahead of the shock impingement point. The pitot pressure profiles show an increase in incident and reflected shock angles. They are also fuller than the profiles for the 6° flow deflection angle. The total predicted mass bleed using the porous material calibration equation is 0.041 kg/s, which is higher than the measured value of 0.038 kg/s. The wall temperature exhibits a continuous increase on the porous plate.

3.4 Two-Dimensionality

3.4.1 Rough Wall

a) Spanwise wall pressures

The spanwise pressures measured at the six axial locations are plotted together

in Figure 31 for the four shock strengths at $M = 2.5$. The pressures on each row are referenced to the centerline value. The 0° flow deflection (no shock) case shows a maximum deviation of $\pm 4\%$ with respect to the value on the centerline, which indicates that the boundary layer is fairly uniform in the spanwise direction. The 4° deflection case shows scatter of $\pm 10\%$; however, at $x = 17.57$ cm the deviation increases to $+30\%$. This streamwise station is located within the pressure rise region and any slight curvature of the shock will show on the spanwise pressures. Results for the 6° deflection show deviations of $\pm 6\%$. There is no large scatter in the spanwise pressure distributions for this flow deflection angle. For the 8° flow deflection, the deviations are within $\pm 6\%$, except for the location $x = 10.26$ cm, which is within the interaction region.

In Figure 32 the distributions at $M = 3.0$ are presented. The qualitative behavior is similar to the $M = 2.5$ results. Quantitatively, the deviations quoted above have almost doubled.

b) Off-centerline wall pressures

Figures 33 and 34 show superimposed plots of the centerline pressure distribution and the additional lines above and below it for $M = 2.5$ and 3.0 respectively at the four deflection angles. The off-centerline pressures fall exactly on the centerline ones for all deflection angles. This leads one to believe that the interactions on the rough plate insert were two-dimensional at least over a region 2.64 cm (1.04 in) wide. Since these off-centerline static taps were installed only on the downstream half of the rough plate insert, nothing can be said about the 6° and 8° shock angles for which the pressure rise occurs on the forward part of the rough plate. No off-centerline pitot pressure profiles were made for the tests with the rough plate insert.

c) Flow visualization

Figure 24, shown earlier, is an oil film visualization made at $M = 3.0$ for the highest shock angle (8° flow deflection). It shows that the boundary layer is separated and that the separation region is straight, not curved. However, since no details of the separation are revealed from the visualization it does not provide any additional information.

3.4.2 Porous Wall

a) Spanwise wall pressures

Figure 35 shows spanwise surface pressure variations at $M = 2.5$ for the four shock strengths. A substantial scatter in spanwise pressure on the porous plate can be noticed. The maximum deviation is about $\pm 20\%$ of the centerline value. The spanwise pressure distribution for the $M = 3.0$ case is presented in Figure 36. It shows a distribution similar to that of the preceding case but with a slightly higher deviation. The scatter in spanwise pressure for the 0° deflection angle (empty tunnel) suggests that the bleed and therefore the porosity of the plate is not uniformly distributed. Some other possible causes of the large scatter found in this case are due to the non flatness of the porous plate surface. A close inspection of the porous plate revealed undulations of ± 0.13 mm (0.005 in) with respect to the mean in both spanwise and streamwise directions.

b) Off-centerline wall pressures

The off-centerline and centerline wall pressure distributions are compared in Figure 37 for the four deflection angles at $M = 2.5$. The pressure rise due to the incident shock occurs at the same axial location for the three lateral distributions. In general, the off-centerline pressures show a little more scatter. This is expected since we have seen a lot of scatter in the spanwise direction. The distributions for the $M = 3.0$ case are shown in Figure 38. They show similar behavior to that of the $M = 2.5$ cases; however, the scatter is larger. This is in agreement with the spanwise pressure distributions (Figure 36).

c) Off-centerline pitot pressures

The pitot pressures surveyed 3.65 cm (1.44 in) from the plate centerline are compared with the centerline profiles in Figure 39 at $M = 2.5$ for the nonzero deflection angles. The first three profiles taken on the solid wall are exactly the same for both centerline and off-centerline distributions. The same is true for the first profile on the porous plate (fourth profile). The difference starts to show on the profiles affected by the incident and reflected shocks. The pitot pressure increase on the incident shock side occurs at a slightly lower position for the off-centerline profiles. On the reflected shock side, the decrease in pitot pressure for the off-centerline profiles

occurs above that of the centerline profiles. This suggests that the shock wave is slightly curved upstream. In Figure 40, the comparisons at $M = 3.0$ indicate that the departure from the centerline profiles is not large compared to that at $M = 2.5$.

d) Off-centerline bleed distribution

The bleed distribution surveyed 3.0 cm (1.19 in) above and below the porous plate centerline at $M = 2.5$ are compared with the centerline distribution in Figure 41 for the four deflection angles. The off-centerline distributions are within $\pm 10\%$ of the centerline values. The scatter in the data does not show any trend of three-dimensionality. Rather it indicates that measurements with hot-wires in low density and low velocity flows are not too reliable. Part of the scatter could be caused by sound waves inside the bleed plenum chamber and vibrations of the wind tunnel.

An oil flow visualization study was made on the porous plate with suction applied. The oil on the porous area was absorbed and no traces were left on the surface. On the solid smooth wall, before and behind the porous plate insert, the surface streamlines were straight and parallel to the plate centerline (see Figure 14).

From the comparisons presented above, it can be concluded that the interactions on both the rough plate and the porous plate are not extensively two-dimensional throughout the whole span. They may be considered to be so over the central strip of $1/3$ the porous plate and rough plate span. The departure from two-dimensionality on the porous plate can be attributed to three causes, 1) non uniformity of the plate porosity, 2) waveness of plate surface, and 3) curvature of shock wave. All these causes can be present at the same time; however, the results of the empty tunnel comparisons indicate that the nonuniformity of the plate porosity is most likely the major cause of departure from two-dimensionality.

3.5 Comparison of Rough and Porous Plate Results

A summary of the wall pressure distributions along the rough plate and the porous plate centerline with the different shock angles including the empty tunnel measurements are presented in Figure 42 for $M = 2.5$ and in Figure 43 for $M = 3.0$. Tests on the rough plate insert show that, for the weaker shock (4° flow deflection), the boundary layer remained attached. For the stronger shocks the boundary layer was separated and the separation region increased with the increase in shock angle. Suction as high as 10% of the incoming boundary layer eliminates separation. The

pressure rise is sharper and approaches the inviscid case. Suction introduces a favorable pressure gradient at the beginning of the porous plate. The wall pressure exhibits perturbations that are higher than with roughness.

Removal of part of the boundary layer mass flow resulted also in significant changes in the boundary layer pitot pressure profiles as shown in Figure 44 and 45. They are fuller than those for the rough wall and hence are capable of withstanding higher pressure gradients. The effects of roughness on the pitot pressure profiles are relatively small compared to suction effects.

3-6 Comparison with Other Work

The results obtained with the porous plate appear to correlate very well with the experimental results reported by Hingst and Tanji [2]. The test configuration used herein is the same as that used by Hingst and the same flow probing is employed. In their experiment, bleed was applied through discrete holes extending over an area of 12.0 cm span and 5.0 or 2.5 cm length. The wall pressure distributions of their measurements did not show any noticeable disturbances because the static taps were located on solid areas of the perforated wall. It is found in both experiments that suction produces a decrease in pressure over the porous wall and eliminates separation that would have occurred in the case with no bleed. The bleed distribution was found to follow to some extent the wall pressure distribution. No direct comparisons can be made since the extent and amount of bleed are different in the two experiments.

The results are also qualitatively in good agreement with the measurements reported by Lee and LeBlanc [8], who surveyed a shock wave/turbulent boundary layer interaction on a continuous porous wall at $M = 1.43$. In their experiments, the bleed zone was 23.5 cm long. No disturbances were found in the wall pressure distribution because of the small number of static taps used in the bleed zone and low suction rates. Their Schlieren flow visualizations showed clearly the existence of expansion waves originating at the porous wall surface. The bleed distribution was inferred from the difference between the wall pressure and bleed plenum pressure using the Darcy equation. The bleed was found to follow the static pressure distribution. As in the present experiments, suction produced fuller pitot pressure profiles on the porous wall than the ones on an impermeable wall.

CHAPTER 4

NUMERICAL CALCULATIONS

The objective of the numerical calculations is to demonstrate the possibility of using a bleed model to predict the bleed distribution instead of relying on experimental results to provide such information. The calculations were performed using the numerical code developed by Shang [22], which employs the explicit finite-difference scheme of MacCormack [23]. The basic problem is the computation of the steady flow resulting from the interaction of an incident oblique shock wave with a turbulent boundary layer on a flat plate including the effect of suction on the interaction. As indicated in Figure 46, the incoming supersonic flow is deflected by an oblique shock wave generated externally. Boundary layer bleed is distributed along the wall upstream and downstream of the shock impingement point to prevent flow separation.

4.1 Governing Equations

The governing equations are the unsteady, compressible, Navier-Stokes equations for mass-averaged variables written in strong conservation form [22,46]. The two-dimensional form of the equations in cartesian coordinates is

$$\frac{\partial U}{\partial t} + \frac{\partial F}{\partial x} + \frac{\partial G}{\partial y} = 0 \quad (4-1)$$

where the flux vector components are

$$U = \begin{pmatrix} \rho \\ \rho u \\ \rho v \\ \rho e \end{pmatrix} \quad (4-2)$$

$$F = \begin{pmatrix} \rho u \\ \rho u^2 - \sigma_{xx} \\ \rho uv - \tau_{xy} \\ (\rho e - \sigma_{xx})u - \tau_{xy} \cdot v - \dot{q}_x \end{pmatrix} \quad (4-3)$$

$$G = \begin{pmatrix} \rho v \\ \rho uv - \tau_{xy} \\ \rho v^2 - \sigma_{yy} \\ (\rho e - \sigma_{yy})v - \tau_{xy} \cdot u - \dot{q}_y \end{pmatrix} \quad (4-4)$$

The apparent stress components, mean specific total energy, and heat fluxes are given by

$$\begin{aligned}
 \sigma_{xx} &= -p - \frac{2}{3}(\mu + \epsilon)\left(\frac{\partial u}{\partial x} + \frac{\partial v}{\partial y}\right) + 2(\mu + \epsilon)\frac{\partial u}{\partial x} \\
 \sigma_{yy} &= -p - \frac{2}{3}(\mu + \epsilon)\left(\frac{\partial u}{\partial x} + \frac{\partial v}{\partial y}\right) + 2(\mu + \epsilon)\frac{\partial v}{\partial y} \\
 \tau_{xy} &= (\mu + \epsilon)\left(\frac{\partial u}{\partial y} - \frac{\partial v}{\partial x}\right) \\
 e &= C_v T + \frac{1}{2}(u^2 + v^2) \\
 \dot{q}_x &= -C_p\left(\frac{\mu}{P_r} + \frac{\epsilon}{P_{rt}}\right)\frac{\partial T}{\partial x} \\
 \dot{q}_y &= -C_p\left(\frac{\mu}{P_r} + \frac{\epsilon}{P_{rt}}\right)\frac{\partial T}{\partial y}
 \end{aligned} \tag{4-5}$$

Auxiliary relationships included in the system of equations are the equation of state for a perfect gas

$$P = \rho RT = \frac{\gamma - 1}{\rho} \left[(\rho e) - \frac{1}{2}((\rho u)^2 + (\rho v)^2) \right] \tag{4-6}$$

and Sutherland's viscosity law

$$\mu = 1.468 \times 10^{-6} \frac{T^{1.5}}{T + 110.6} \tag{4-7}$$

In the above equations, ρ is the density, u and v are the x - and y -components of velocity, and p is the thermodynamic pressure. The molecular Prandtl number is $P_r = 0.72$ and the turbulent Prandtl number is assigned a constant value of $P_{rt} = 0.9$.

4.2 Turbulence Model

The Cebeci model is used in the present calculations in the form described in reference [18]. It is a two region model in which the eddy viscosity, ϵ , is given by

$$\epsilon = \begin{cases} \epsilon_i, & \text{for } y \leq y_c \\ \epsilon_o, & \text{for } y > y_c \end{cases} \tag{4-8}$$

where y_c is the distance from the wall at which ϵ_o becomes less than ϵ_i .

In the inner region

$$\epsilon_i = \rho k^2 y^2 D^2 \left| \frac{\partial u}{\partial y} \right| \tag{4-9}$$

where k , the Von Karman constant, and D , the Van Driest damping factor, are given by

$$\begin{aligned}
 k &= 0.4 \\
 D &= 1 - \exp\left(-\frac{y^+}{A^+}\right) \\
 y^+ &= \frac{yu_r}{\nu_w} \\
 u_r &= \sqrt{\frac{\tau_w}{\rho_w}} \\
 A^+ &= \frac{26.0}{\left\{ \frac{-p^+}{v_w^+} [\exp(11.8v_w^+) - 1] + \exp(11.8v_w^+) \right\}^{1/2}} \\
 p^+ &= -\left(\frac{dp}{dx}\right) \frac{\nu_w}{\rho_w u_r^3} \\
 v_w^+ &= \frac{v_w}{u_r}
 \end{aligned} \tag{4-10}$$

For a nonporous wall with pressure gradient, A^+ reduces to

$$A^+ = \frac{26.0}{[1 - 11.8p^+]^{1/2}} \tag{4-11}$$

If, in addition, $p^+ = 0$, then $A^+ = 26.0$. In the Cebeci-Smith and the Baldwin and Lomax models, A^+ is assigned the value of 26.0 and no pressure gradient correction term is used.

In the outer region, Clauser's defect law is used

$$\epsilon_o = 0.0168 \rho U_{max} \delta_i^* F_{Kleb} \tag{4-12}$$

where δ_i^* is the kinematic displacement thickness (the basic scaling of the outer layer)

$$\delta_i^* = \int_0^h \left(1 - \frac{u}{U_{max}}\right) dy \tag{4-13}$$

and F_{Kleb} is the Klebanoff intermittency correction given by

$$F_{Kleb} = \left[1 + 5.5 \left(\frac{y}{\delta_i^*}\right)^6\right]^{-1} \tag{4-14}$$

In the Cebeci model, the boundary layer edge velocity is used in equation (4-12) and (4-13), and the boundary layer thickness is used in equation (4-14). The need to determine the boundary layer thickness and edge velocity in the outer formulation constitutes a major disadvantage of this model. This is particularly true for interacting boundary layers because the boundary layer edge is not readily defined. As discussed by Visbal and Knight [19], the boundary layer edge is complicated by the presence of shock waves, which introduce variations in the direction normal to the boundary and by the presence of small spurious oscillations in the numerical solution. In order to remedy to this difficulty, Shang and Hankey [10] used the maximum velocity, u_{max} , instead of u_e and the integration was taken over the height of the computational domain, h . They also dropped the intermittency function claiming that it has no effect on the computations. In the present calculations, it was found that the omission of F_{Kleb} will produce an eddy viscosity that increases monotonically from the wall to the free stream, which is unphysical. When it was retained, using δ_i^* as a length scale, instead of the boundary layer thickness, δ , the eddy viscosity exhibited a maximum in the vicinity of the wall and decreased to a very small value near the boundary layer edge.

4.3 Coordinate Transformation

A coordinate transformation is utilized to map the (x, y) physical space onto a square in the (ξ, η) computational space (Figure 47). A highly nonuniform grid in the physical space is mapped onto a uniform set of grid points

$$\begin{aligned}\xi_i &= (i - 1)\Delta\xi & i &= 1, IL \\ \eta_j &= (j - 1)\Delta\eta & j &= 1, JL\end{aligned}\tag{4 - 15}$$

where IL and JL are the number of grid points in the ξ - and η -directions respectively. The use of such transformation permits the implementation of simple finite difference relationships.

By definition

$$\begin{aligned}\Delta\xi &= 1/(IL - 1) \\ \Delta\eta &= 1/(JL - 1)\end{aligned}\tag{3 - 16}$$

A general transformation of the spatial coordinates of the form

$$\begin{aligned}\xi &= \xi(x, y) \\ \eta &= \eta(x, y)\end{aligned}\tag{3-17}$$

is applied to equation (4-1) which then becomes

$$\frac{\partial U}{\partial t} + \xi_x \frac{\partial F}{\partial \xi} + \eta_x \frac{\partial F}{\partial \eta} + \xi_y \frac{\partial G}{\partial \xi} + \eta_y \frac{\partial G}{\partial \eta} = 0\tag{3-18}$$

where

$$\begin{aligned}\xi_x &= J y_\eta \\ \xi_y &= -J x_\eta \\ \eta_x &= -J y_\xi \\ \eta_y &= J x_\xi\end{aligned}\tag{3-19}$$

and J is the Jacobian of the transformation

$$J = 1/(x_\xi y_\eta - x_\eta y_\xi)\tag{3-20}$$

The metrics can be readily determined if analytical expressions are available for the inverse of the transformation. In the present code, the metrics are computed numerically using central differences.

4.4 Numerical Procedure

The numerical code uses the explicit finite-difference, predictor-corrector algorithm of MacCormack [23] (unsplit version). When the MacCormack scheme is applied to equation (4-1), the following algorithm results :

Predictor

$$U_{i,j}^{\overline{n+1}} = U_{i,j}^n - \frac{\Delta t}{\Delta x} (F_{i+1,j}^n - F_{i,j}^n) - \frac{\Delta t}{\Delta y} (G_{i,j+1}^n - G_{i,j}^n)\tag{4-21}$$

Corrector

$$U_{i,j}^{n+1} = \frac{1}{2} \left[U_{i,j}^n + U_{i,j}^{\overline{n+1}} - \frac{\Delta t}{\Delta x} (F_{i,j}^{\overline{n+1}} - F_{i-1,j}^{\overline{n+1}}) - \frac{\Delta t}{\Delta y} (G_{i,j}^{\overline{n+1}} - G_{i,j-1}^{\overline{n+1}}) \right]\tag{4-22}$$

This scheme is second-order accurate in both space and time. The method first obtains an approximate value $U_{i,j}^{\overline{n+1}}$, at each mesh point using two forward differences

to approximate the two spatial derivatives. The approximate solution is then used in the second equation, using backward differencing, to obtain a new value $U_{i,j}^{n+1}$. To maintain second order accuracy, the x-derivative terms in F are backward differenced while the y-derivatives are approximated with central differences. Likewise, the y-derivative terms appearing in G are differenced in the forward direction, while the x-derivative terms are approximated with central differences.

The method is conditionally stable subject to a CFL time step restriction [22,23,45]. The stability requirement is met if

$$\Delta t \leq (\Delta t)_{CFL} \quad (4-23)$$

where

$$(\Delta t)_{CFL} = 1 / \left\{ \frac{U_\xi}{\Delta \xi} + \frac{U_\eta}{\Delta \eta} + a \left[\left(\frac{\xi_x}{\Delta \xi} + \frac{\eta_x}{\Delta \eta} \right)^2 + \left(\frac{\xi_y}{\Delta \xi} + \frac{\eta_y}{\Delta \eta} \right)^2 \right]^{1/2} \right\} \quad (4-24)$$

where the contravariant velocity components are defined as

$$\begin{aligned} U_\xi &= \xi_x u + \xi_y v \\ U_\eta &= \eta_x u + \eta_y v \end{aligned} \quad (4-25)$$

Since the stability analysis used to determine $(\Delta t)_{CFL}$ does not contain viscous terms, a safety factor, α , is used :

$$\Delta t = \alpha (\Delta t)_{CFL} \quad (4-26)$$

The value used in the present calculations is 0.8. The minimum time step at a fixed j grid points is used to advance the solution for all grid points at that level.

As part of this algorithm, a fourth-order pressure damping term [22,45] is incorporated to suppress numerical oscillations. In essence, artificial viscosity-like terms are implemented in each sweep direction of the form

$$\beta \Delta t (\Delta \xi)^4 \left[|U_\xi| + (\xi_x^2 + \xi_y^2)^{1/2} a \right] \frac{1}{p} \left| \frac{\partial^2 p}{\partial \xi^2} \right| \quad (4-27)$$

$$\beta \Delta t (\Delta \eta)^4 \left[|U_\eta| + (\eta_x^2 + \eta_y^2)^{1/2} a \right] \frac{1}{p} \left| \frac{\partial^2 p}{\partial \eta^2} \right| \quad (4-28)$$

MacCormack [23] recommends damping constant values between 0.5 and 1; however, Shang [22] uses values of β between 2 and 3. The value used in the present calculations

is 0.8. The numerical damping is of significance only in the vicinity of shock waves. It spreads the shock over several grid points.

The governing equations are solved in dimensional units. The S.I. system of units is used for all variables. Since the steady state flowfield solution is obtained by time integration of the Navier-Stokes equations from a given initial condition, a convergence criteria must be specified. The computations were considered to be converged when

$$\max_{i,j} \left| \frac{\rho_{i,j}^{n+1} - \rho_{i,j}^n}{\rho_{i,j}^n} \right| \leq 10^{-4} \quad (4-29)$$

4.5 Computational Domain and Grids

The computational domain, shown in Figure 46, has physical dimensions of 30 cm × 8 cm (approximately $10\delta_o \times 2.3\delta_o$). The inflow boundary is located in a region of no influence from downstream, ahead of the incident shock and the bleed zone. Physically, it corresponds to the station at which the first pitot pressure profile was surveyed in the experimental program. The outflow boundary was placed far enough downstream from the bleed zone to be in a region of zero streamwise flow gradients, but not far enough so that the reflected shock would cross the outflow boundary. The height of the computational domain ($2.3\delta_o$) was chosen so as to obtain free stream conditions along the upper boundary and to ensure the emergence of the shock through the downstream boundary.

For turbulent flows, the high velocity gradients near the wall dictate a fine mesh spacing to achieve adequate numerical resolution. A commonly accepted criteria of a mesh Reynolds number of the order of two is usually used [19]. With shock waves and suction, the normal and streamwise grid spacing are required to be sufficiently fine, particularly within the interaction region and on the porous wall, to resolve the boundary layer development and the computed shock wave structure.

The computational domain is divided into two regions. A stretched fine mesh is used near the wall to resolve the part of the flow where the gradients are high; the rest of the domain is described using a stretched coarse mesh. The grid points in these regions were distributed exponentially as follows :

$$\begin{aligned} \Delta y &= \Delta y_2 [\Delta y_1 / \Delta y_2]^{(J_{in}-J)/J_{in}} & \text{for } 1 \leq J \leq J_{in} \\ \Delta y &= \Delta y_3 [\Delta y_2 / \Delta y_3]^{(J_{max}-J)/(J-J_{in})} & \text{for } J_{in} < J \leq J_{max} \end{aligned} \quad (4-30)$$

In the present study

$$J_{in} = 15$$

$$J_{max} = 100$$

$$\Delta y_1 = 0.001 \text{ mm}$$

$$\Delta y_2 = 0.1 \text{ mm}$$

$$\Delta y_3 = 2.0 \text{ mm}$$

In the streamwise direction, the grid points were clustered at the beginning and at the end of the bleed zone. Ahead of and behind the bleed region, a constant step size is used. For all cases computed, the grid consisted of 200 points in the streamwise direction and 100 points in the normal direction. The shock wave/boundary layer interactions with no suction were computed using 200 equally spaced grid points in the streamwise direction and 100 stretched points in the normal direction.

4.5 Boundary and Initial Conditions

In order to completely define the problem, suitable boundary and initial conditions must be specified. The following boundary conditions are prescribed on each iteration, which consist of sweeps in both the x- and y-directions.

a) Upstream Boundary Conditions

The upstream velocity profile was prescribed as follows. In the laminar sublayer, for $y^+ < 6.0$, the laminar sublayer equation is used

$$u^+ = y^+ \quad (4-31)$$

where u^+ is given by equation (3-2). After rearrangement, The u velocity is then

$$\frac{u}{u_e} = \frac{1}{\sqrt{\sigma}} \sin \left[\frac{\sqrt{\sigma}}{2} \frac{\rho_e u_e y}{\mu_w} C_f \right] \quad (4-32)$$

In the overlap and outer layers, the velocity profile is obtained from the law of the wall-law of the wake for compressible boundary layers [35,36]

$$\frac{u}{u_e} = \frac{1}{\sqrt{\sigma}} \sin \left\{ (\arcsin \sqrt{\sigma}) \left[1 + \frac{1}{\kappa} \frac{u_r}{u_e^*} \ln \left(\frac{y}{\delta} \right) - 1.25 \frac{\pi}{\kappa} \frac{u_r}{u_e^*} \left(1 + \cos \frac{\pi y}{\delta} \right) \right] \right\} \quad (4-33)$$

where σ is given by equation (3-6) and the values of C_f and δ are taken from the experimental velocity profiles on the smooth wall (Figure 13). The incoming velocity

profiles for the computations are compared with the experimental profiles in Figure 48. It shows good agreement, although no experimental data points are within the laminar sublayer. The static pressure is assumed to be constant in the direction normal to the wall; it is determined from the total pressure and Mach number. The temperature is determined from the Crocco-Busemann equation assuming adiabatic wall temperature.

Once T and p are determined, the density, ρ , is obtained from the perfect gas equation. The above inflow variables were held fixed for all subsequent iterations. The normal velocity component of velocity is set equal to zero. The assumption of zero v velocity is not totally justifiable; however, an estimate from the incompressible continuity equation on a flat plate gives a maximum value of v on the order of 1% of the free stream velocity. In some trial runs, extrapolation of v from interior points did not prove to be successful.

b) Wall Boundary Conditions

On the solid wall, the no slip condition is applied tangent to the wall ($u = 0$). The normal velocity on the solid wall is taken equal to zero. In the bleed region, the normal velocity is obtained from the difference between the wall static pressure and a specified bleed plenum pressure, according to the empirical equation presented in section 3-2. When equation (3-11) is rearranged, a quadratic equation is obtained

$$A(\rho v)_w^2 + \frac{B\mu}{e}(\rho v)_w - \rho\Delta p = 0 \quad (4-34)$$

the solution of which is

$$(\rho v)_w = \frac{\frac{-B\mu}{e} + \left[\left(\frac{B\mu}{e}\right)^2 + 4A\rho\Delta p\right]^{1/2}}{2A} \quad (4-35)$$

The density was lagged in time in order to solve the above equation.

The wall temperature is obtained using the assumption of adiabatic condition

$$\left. \frac{\partial T}{\partial y} \right|_w = 0 \quad (4-36)$$

The derivative is differenced using two interior points.

The pressure at the wall is computed from the steady y-momentum equation. Taking into consideration the no slip condition at the wall, this equation simplifies to

$$\begin{aligned} \left. \frac{\partial p}{\partial y} \right|_{y=0} = & \left\{ \frac{\partial}{\partial x} \left[(\mu + \epsilon) \left(\frac{\partial u}{\partial y} + \frac{\partial v}{\partial x} \right) \right] - \frac{\partial}{\partial y} (\rho v^2) \right. \\ & \left. + \frac{\partial}{\partial y} \left[\frac{4}{3} (\mu + \epsilon) \frac{\partial v}{\partial y} \right] - \frac{\partial}{\partial y} \left[\frac{2}{3} (\mu + \epsilon) \frac{\partial u}{\partial x} \right] \right\}_{y=0} \end{aligned} \quad (4-37)$$

Second-order three-point differencing is used to discretize this equation at the wall. After the temperature and pressure are determined, the density is obtained from the equation of state.

c) Downstream Boundary Conditions

Since the flow behind the reflected shock is supersonic, except in a relatively thin subsonic region near the wall, all variables along the downstream boundary are extrapolated from interior points. A second-order extrapolation condition is used.

$$\frac{\partial^2 U}{\partial x^2} = 0 \quad (4-38)$$

A three point backward differencing is used to discretize this equation.

d) Outer Boundary Conditions

The outer boundary conditions for the present analysis consists of two segments. In the region before the incident shock, that is along B-C in Figure 46, the free stream conditions, ρ_e , u_e , T_e , p_e , and zero normal velocity are prescribed. Behind the incident shock wave, along C-D, the post-shock conditions were specified using inviscid oblique shock wave theory. The anticipated reflected shock is permitted to pass through the downstream boundary (segment D-E).

e) Initial Conditions

The time-dependent finite-difference method presented requires a set of initial values for all variables at all grid points. The variables at the incoming boundary were specified at all streamwise locations

$$U(0, x_i, y_i) = U(0, 0, y_i) \quad (4-39)$$

CHAPTER 5

NUMERICAL RESULTS

The numerical code was used to calculate the interaction of an oblique shock wave with a turbulent boundary layer on an adiabatic flat plate with and without suction. The calculations were made at $M = 2.46$ and 2.98 and total pressure of 172.3 kpa and 241.2 kpa (25.0 psia and 35.0 psia), respectively. The total temperature was set at 300°K . Oblique shock waves corresponding to flow deflection angles of 4.5° , 6.5° , and 8.5° with respect to the horizontal crossed the upper boundary of the computational domain at a distance x_{sh} (Figure 46). The flow deflection angles were increased by 0.5° relative to the nominal values to take in consideration the boundary layer growth on the shock generator plate. Table II summarizes the conditions for which the computations were made. For the bleed calculations, the bleed zone starts at 9.0 cm and ends at 22.1 cm extending before and behind the interaction region. The bleed was started and cutoff progressively.

The numerical results are presented in two groups. First, comparisons of predicted and experimental results are shown. In the second group, the features of the computed flowfield are presented in terms of Mach number and static pressure contours. The results demonstrate that the numerical code is capable of accurate prediction of the details of the flowfield structure.

5.1 Interactions on a Solid Wall

5.1.1 Mach number 2.46

Numerical results for a 4.5° flow deflection angle (27.5° shock angle) on a smooth solid wall are compared with the experimental data obtained on the rough wall in Figures 49. Figure 49-a shows the wall static pressure distribution. The overall pressure rise is predicted well, but the location of the initial pressure rise occurs downstream of the measured distribution. The predicted interaction length is smaller than measured experimentally. The final pressure level reached downstream of the reflected shock still shows a very slow increase, while the measured pressure decreases slightly.

The numerical and experimental pitot pressure profiles are compared in Figure 49-b. The pitot pressures are deduced from the computed total pressures and Mach numbers using the Rayleigh pitot formula. The profiles are linearly interpolated between the two closest stations. All important qualitative features of a nonseparated interaction are predicted, e.g., the shock wave reflects on the solid wall as a single broad wave which emerges through the downstream boundary. The predicted and measured profiles are in close agreement before the shock impingement point, but on the reflected shock wave side, the shock angle is lower than the experimentally observed angle. The numerical profiles are also fuller than the experimental profiles within and downstream of the interaction region. The disagreement between the experimental and numerical results found here can be attributed to the fact that the computations are made on a smooth wall and no effect of roughness is modeled in the numerical code.

The predicted skin friction distribution is shown in Figure 49-c. It shows a sudden decrease at the beginning of the domain, followed by a constant region before the interaction, a decrease and then by an increase in the interaction region. Qualitatively, this distribution agrees with previously reported numerical results [13]. The value of the skin friction is positive throughout the whole domain indicating no sign of separation. Some oscillations are seen at the axial location where the incident shock crosses the outer boundary of the computational domain. This is likely to be caused by insufficient grid resolution.

The wall temperature (Figure 49-d) is almost constant before the interaction region, followed by a 20 °K increase downstream of the reflected shock wave.

Figure 49-e presents the static pressure profiles throughout the interaction region. The profiles display the pressure peaks and inflections caused by the incident and reflected shocks. The static pressure is in general constant normal to the wall above and below the shock wave, but increases at the location of the shock. These distributions are in agreement with the numerical results of Wilcox [46] and experimental results of Rose [47]. This points out that the velocity profiles deduced from pitot pressure measurements and the assumption of constant pressure normal to the boundary are in error in the interaction region.

In Figure 49-f, the computed Mach number profiles are presented. These profiles

clearly show the incident and reflected shocks. Comparisons with corresponding profiles deduced from the measured pitot pressure profiles were poor. The discrepancy comes from the difference between the numerical and measured pitot pressure profiles found in Figure 49-b, and the use of constant static pressure normal to the plate surface for the deduction of velocity profiles. The Mach number and pressure contours are presented in Figures 49-g and 49-h, respectively. They show the essential features of a supersonic interacting flowfield.

For the higher shock angles (6.5° and 8.5° flow deflection angles), the calculations could not be carried through. The non-dimensionalized pressure gradient, p^+ , in equation (4-11) is high and the term in the denominator becomes negative. Separated flow could be predicted if the pressure gradient term is dropped; this was the case in reference [10] and [11].

5.1.2 Mach number 2.98

Results for $M = 2.98$ and a flow deflection angle of 4.5° (shock angle of 23°) are summarized in Figures 50. The computed wall pressure is displayed in Figure 50-a, together with the experimental data taken on the rough plate. The calculations were made in this case by dropping the pressure gradient term, p^+ , from the inner eddy viscosity equation (equation (4-11)). If p^+ is kept, the denominator of equation (4-11) becomes negative and the computations stopped.

The computed pitot pressure profiles (Figure 50-b) are in close agreement with the experimental profiles before the interaction, but are fuller farther downstream. As indicated in the discussion of $M = 2.46$ case, the observed differences between the predicted and experimental results may be partially attributed to the neglect of roughness effects. The computed skin friction distribution (Figure 50-c) shows a small separation region. The wall temperature is presented in Figure 50-d; it shows a sudden increase in the interaction region, followed by a decrease. In Figure 50-e, the computed static pressure profiles are seen to provide additional confirmation of the variation of static pressure normal to the wall, which is associated with incident and reflected shocks.

5.2 Interactions on a Porous Wall

5.2.1 Mach number 2.46

Results for a 4.5° flow deflection angle with bleed are shown in Figures 51. In Figure 51-a, the computed surface pressure distribution is compared with experimental data. It shows a decrease at the beginning of the bleed zone, after which it levels off to a constant value equal to the average measured pressure. The decrease in wall pressure is caused by the introduction of the velocity normal to the wall. In the interaction region, the pressure rises sharply and is in agreement with the experimental pressure rise. The final pressure reached downstream of the reflected shock shows some perturbations. It is lower than the measured pressures. There are also pressure oscillations at the foot of the pressure rise. Since the pressure gradient is exceptionally large here, it is possible these discrepancies are caused by insufficient grid resolution in the streamwise direction. An increase in static pressure can be seen at the end of the bleed zone as the flow turns parallel to the impermeable surface. Downstream of the bleed zone, the wall pressure is constant and is higher than the measured data.

The computed and experimental pitot pressure profiles, shown in Figure 51-b, are in good agreement upstream of and within the interaction region, but are slightly fuller than the measured profiles farther downstream. This difference may be caused by the effect of roughness on the measured profiles. The predicted profiles show all important details of the experimental profiles (e.g., location of pressure peaks). Inspection of the profiles shows the existence of expansion waves and shock waves generated at the beginning and the end of the bleed zone.

Figure 51-c compares the computed and measured bleed distributions. The predicted mass flux follows exactly the wall static pressure distribution as expected from equation (4-35). The integrated total mass flux, assuming two-dimensional distribution, is 0.03 kg/s which is 7% lower than the measured value. Considering the simplicity of the bleed model, the prediction is good for engineering applications.

The computed skin friction coefficient distribution is plotted in Figure 51-d. It is constant on the solid wall, followed by an increase, of approximately five times the smooth wall value, at the beginning of the porous wall. At the shock impingement point, the skin friction coefficient exhibits an additional increase as the suction flow

rate increases. Downstream of the reflected shock, it is almost constant up to the end of the bleed region, after which it drops to a value slightly higher than the value on the solid wall upstream of the bleed zone. The skin friction drop occurs over a short distance. The overall skin friction increase is about 20 times the value on the smooth solid wall before the porous plate. Numerical oscillations are present on the plot at the location of the pressure rise.

The predicted wall temperature, shown in Figure 51-e, shows an increase on the porous wall and a decrease toward the end of the bleed area, followed by an increase farther downstream on the impermeable wall. Although the predicted temperatures are slightly higher than the measured values, it seems that the use of the adiabatic wall condition is an acceptable assumption.

The computed static pressure profiles throughout the boundary layer are presented in Figure 51-f. They show that the static pressure is not constant perpendicular to the wall, especially in the interaction region and over the porous area. Deviations of as much as 50% from the wall value are encountered here. In comparison with the solid wall static profiles, it can be seen that in the presence of suction the pressure increase is sharper and the shock wave penetrates deeper into the boundary layer. This is essentially due to the absorption of part of the subsonic layer. These results point out that pressure gradient effects at the surface of a porous wall should be accounted for by use of the y-momentum equation at the wall (equation (4-37)). This also emphasizes that flows under these complex conditions can not be described by boundary layer equations.

The predicted Mach number profiles are plotted in Figure 51-g. There is a decrease in Mach number above the incident shock and an increase above the reflected shock. There are also some wiggles in the profiles indicating the existence of expansion and shock waves from the beginning and end of the bleed region.

Mach number contours are shown in Figure 51-h. The incident and reflected shock waves are clearly seen. As the flow passes over the porous area, an expansion wave is generated at the beginning of the bleed because of the introduction of the velocity perpendicular to the wall. Between the incident and reflected shocks the flow is seen to turn toward the wall. At the end of the bleed zone, a shock wave is produced as the flow turns parallel to the impermeable plate surface and the velocity

normal to the wall becomes zero.

Contours of static pressures are presented in Figure 51-i. Here again the flowfield structure is delineated and the incident and reflected shock waves appear as a band of finite width. The incident shock is seen to be curved near the porous wall. Expansion waves and shock waves from the beginning and end of the bleed zone are also produced. The expansion wave is slightly bent as it crosses the incident shock wave.

Similar comparisons for the 6.5° flow deflection (29.0° shock angle) at $M = 2.46$ are shown in Figures 52. The agreement between the analysis and experiment for all boundary layer properties is still good. The total suction mass flow rate predicted is equal to the measured value of 0.038 kg/s.

In Figures 53, the comparisons between the numerical and experimental results start to deteriorate when the flow deflection angle is increased to 8.5° (shock wave angle of 31.0°). The predicted results exhibit the same characteristics as those found with the smaller deflection angles. The comparisons indicate that the effects of roughness can not be neglected and should be modeled in order to improve the numerical predictions.

5.2.2 Mach number 2.98

Results for $M = 2.98$ and a flow deflection angle of 4.5° (23° shock angle) are summarized in Figures 54. Figure 54-a compares the computed and experimental wall pressure distributions. The comparison is good in the bleed area up to the shock impingement point. The predicted pressure rise is sharper than in the experimental data. Downstream of the reflected shock, the wall pressure is lower than the experimental values. Here again the pressure exhibits oscillations at the foot of the pressure rise.

Comparison of the computed and experimental pitot pressure profiles is shown in Figure 54-b. The agreement is good, except for the last two profiles, where the predicted pitot pressures are slightly lower than the measured values near the edge of the boundary layer. The expansion wave from the beginning of the bleed zone as well as the shock wave from the bleed cutoff are seen from the numerical profiles.

The bleed distribution, skin friction, and wall temperature are presented in Figures 54-c, 54-d, and 54-e, respectively. These distributions are very similar to the distributions obtained at $M = 2.46$ for the same deflection angle.

The static pressure profiles are shown in Figure 54-f. Before the interaction region, the static pressure is constant above and below the incident shock, but increases sharply upon crossing the shock. In the interaction region, the incident shock is seen to reflect near the surface. Farther downstream, the static pressure is fairly constant normal to the wall below the shock, followed by a decrease due to the shock from the bleed end, another decrease from the reflected shock and finally a nearly constant region. Above the reflected shock, the pressure shows a small increase due to the emergence of the expansion wave from the beginning of the bleed zone.

The static pressure contours (Figure 54-i) shows a smeared shock, but as the shock penetrates into the boundary layer, it becomes thinner. The incident and reflected shocks are slightly bent close to the porous surface. The reflected shock and the additional shock from the bleed cutoff coalesce and emerge through the downstream boundary as a single shock. This strengthening of the reflected shock explains the sharp static pressure decrease seen in the static pressure profiles downstream of the interaction region.

The results for the flow deflection angle of 6.5° (24.5° shock angle) are presented in Figures 55. The wall pressure is well predicted before and within the interaction region. Farther downstream, the predicted pressure is much lower than the measured values. The computed pitot pressure profiles are in good agreement with the measured profiles before the shock impingement point. On the reflected shock side, the qualitative features of the flow are predicted; however, the quantitative agreement is poor. The predicted angle of the reflected shock is lower than the angle depicted by the experimental profiles. The bleed distribution follows the wall pressure distribution, giving a total suction mass flow of 0.025 kg/s, compared to the measured value of 0.029 kg/s. The skin friction has increased relative to the previous case of a lower flow deflection angle and is mainly due to the increase in suction. The predicted wall temperature is higher than the measured values. The oscillations produced in the wall pressure distributions are also seen on the bleed, skin friction, and somewhat more on the wall temperature distribution. The remaining flow characteristics are very similar to the 4.5° flow deflection results.

No calculations were made for the 8.5° flow deflection angle because the pressure measured inside the bleed plenum chamber was almost equal to the wall static

pressure upstream of the interaction region. Since the computed wall pressure exhibits oscillations at the foot of the pressure rise that increase in amplitude with the shock strength, the predicted pressure becomes lower than the bleed plenum pressure and the bleed rate can not be obtained from the porous plate calibration equation.

Typical values of computer time required to get a converged solution on the CRAY XMP-2 are 20 minutes of CPU time. The number of iterations required to reach the imposed convergence criteria was around 3000. It should be noted that the numerical code is capable of handling general coordinates transformation, although such flexibility is not needed for the simple geometry considered here. The computer time listed above could be reduced by one half if the code were written for the flat plate geometry.

Considering that the turbulence model was derived for equilibrium boundary layer flows with low suction or injection rates and moderate pressure gradients, it predicts well the overall features of the complex flow studied here.

For computations with large pressure gradients and large suction rates, an extremely fine grid is needed near the wall. If the grid is not refined, the solution becomes unstable and the predicted profiles exhibit oscillations near the porous surface. This model could be improved upon by including the effect of surface roughness. A different formulation for the outer eddy viscosity could also be used to avoid the necessity of determining the edge of the boundary layer.

CHAPTER 6

CONCLUSIONS AND RECOMMENDATIONS

Detailed measurements of mean flow properties through the region of interaction between incident oblique shock waves and turbulent boundary layers on a rough plate and a porous plate with suction were obtained at a number of conditions. The experiments were carried out at free stream Mach numbers of 2.46 and 2.98 and unit Reynolds numbers of 1.66 E6/m and 1.85 E7/m respectively, and flow deflection angles of 0° , 4° , 6° , and 8° . The experimental data gathered served as a test case for the verification of numerical computations.

Two-dimensionality of the flow was documented through quantitative measurements of surface static pressures, boundary layer profiles, and bleed surveys at lateral locations off the plate centerline. The measurements indicate that the interactions were fairly two-dimensional over the central strip of $1/3$ the rough and porous plate width, but the two-dimensionality is less clear beyond that. This can be attributed to the nonuniformity of the porous plate and to the perturbations introduced by roughness.

The effect of roughness resulted in only small changes in the pitot pressure and velocity profiles for the empty tunnel runs. Roughness of the type used herein (transitional roughness) affects the boundary layer profiles primarily very close to the wall; the outer portion of the profiles is not disturbed very much.

It is found that, for the weaker shocks (4° flow deflection angle), the boundary layer remained attached, while, for stronger shocks, a separated region formed. The size of the separation region increases with shock strength and is Mach number dependent. For the higher Mach number, the extent of separation decreased.

Suction has significant effects on the flowfield and boundary layer properties. The primary effect is to provide a higher shear stress boundary layer, which can then undergo a higher pressure rise before separating. Suction results in a decrease in boundary layer thickness accompanied by an increase in the fullness of the velocity profiles. These changes are reflected in reduction in displacement and momentum thicknesses.

Suction introduces a favorable pressure gradient at the beginning of the bleed zone and produces a shock wave at the end of the bleed region which turns the flow parallel to the impermeable wall. It is found also that suction combined with roughness produces perturbations in the wall pressure distribution.

The results of the shock wave/boundary layer interactions show that the use of suction within the interaction region is effective in suppressing boundary layer separation. The pressure rise is sharper and approaches the inviscid case. Suction seems to move the shock impingement point downstream as compared to the rough wall.

The local bleed measurements show that the bleed distribution varies on the porous wall and follows closely the wall pressure distribution, that is, the local bleed rate is primarily a function of the local flow conditions. The bleed variation is caused by the pressure gradient produced by the incident and reflected shock waves. This indicates that numerical computations made with a specified constant velocity or mass flux on a porous wall may be inaccurate for flows with severe adverse pressure gradients such as in the present experiments.

Numerical solutions of the unsteady, compressible, mass averaged Navier-Stokes equations with the Cebeci turbulence model and an empirical bleed boundary condition are compared with experimental measurements of shock wave/turbulent boundary layer interactions on a porous wall. For the variety of conditions studied, the predicted results are generally in good qualitative and quantitative agreement with the experimental measurements.

The following conclusions can be drawn. The surface pressure distributions are generally well predicted. The decrease in pressure due to suction is produced at the beginning of bleed as well as the pressure increase and shock wave at the end of the bleed zone. The pressure level downstream of the reflected shock is slightly underpredicted, most likely because of the lack of grid resolution near the wall. The pressure on the solid wall downstream of the bleed region is overpredicted and stays constant, while the experiments show a decrease. The numerical solutions produce some oscillations, which could be caused by insufficient grid resolution in the area of large pressure gradient and high mass transfer at the wall.

The location and angle of the reflected shock wave is well predicted. The

predicted pitot profiles downstream of the interaction region are slightly fuller than the experimental profiles; this is because the roughness of the porous plate is not modeled. Comparison of the results on a smooth solid wall and a rough wall indicate that neglecting surface roughness, although in the transitional regime, is not entirely valid. The effect of roughness should be modeled in order to improve the predicted results; however, the effect of suction is much stronger than the effect of roughness.

Considering the simplicity of the bleed boundary condition used, the predicted bleed distribution is in fairly good agreement with the measurements. It should be remembered that the uncertainty in hot-wire measurements in low density flows is high. The predicted static pressure profiles indicate that the static pressure normal to the wall is not constant within the interaction region and in the vicinity of shock waves. Variations of up to 40% were found at $M = 3.0$ and flow deflection of 8.5° .

Considering the complexity of the flow and the limitations on the Cebeci turbulence model, the computer code provides a rather accurate description of the flow structure and the details of the shock wave/turbulent boundary layer interaction including the effects of suction. The failure of the model to predict solutions for higher shock wave angles on impermeable walls shows that it is not a suitable model for separated flows. It should be recalled that the model was developed and tested for mild pressure gradients.

Recommendations for Future Work

On the basis of the present study, a number of recommendations can be made. First of all, the effects of roughness and suction in zero pressure gradient supersonic flows should be investigated in order to improve on the turbulence model and the boundary conditions at the wall.

With regard to further experimental investigation of the effect of suction on shock wave/turbulent boundary layer interactions, it is recommended that additional porous materials with different bleed flow rates be tested. Since suction can not be separated from roughness, a useful test would be a smooth porous plate to identify the cause of wall pressure oscillations.

It is further recommended that more pitot pressure profiles with refined y -increments be made in the bleed region to resolve the wave pattern of the reflected shock.

Flow visualizations consisting of schlieren photographs similar to the ones reported in reference [8] would be helpful in revealing additional details of the flow structure.

Extensive calibration of porous plates with the flow parallel to the surface are needed to improve bleed modeling.

Local bleed measurements with hot-wires is a difficult task because of the low velocity and low density inside the bleed plenum chamber. It is recommended that hot-wires be calibrated under conditions similar to those in the experiments.

On the numerical side, one could improve the turbulence model by adding terms to account for surface roughness and try other models. The Cebeci turbulence model was developed with the assumption of asymptotic suction conditions and was verified over a limited range of experimental data. A more realistic turbulence model should be developed for higher suction rates and severe pressure gradients. There is also a need for improvement in the downstream boundary conditions.

REFERENCES

- 1- Strike, W.T. and Rippey J., "Influence of Suction on the Interaction of an Oblique shock with a Turbulent Boundary Layer at Mach Number 3", AEDC-TN-129, October 1961.
- 2- Hingst, W.R. and Tanji, F.T., "Experimental Investigation of a Two-Dimensional Shock-Turbulent Boundary Layer Interaction with Bleed", NASA TM-83057, 1983. Also AIAA paper 83-0135, 1983.
- 3- Seebaugh, W.R. and Childs, M.E., "conical Shock-Wave Turbulent Boundary-Layer Interaction Including Suction Effects", J. Aircraft, Vol.7, No.4, July-August 1970, pp. 334-340.
- 4- Sun, C. and Childs, M.E., "Flowfield Analysis for Successive Oblique Shock Wave-Turbulent Boundary Layer Interactions", J. Aircraft, Vol.11, No.1, January 1974, pp. 54-59.
- 5- Hingst, W.R. and Johnson, D.F., "Experimental Investigation of Boundary Layers in an Axisymmetric, Mach 2.5, Mixed-Compression Inlet", NASA TMX-2902, October 1973.
- 6- Fukuda, M.K., Hingst, W.R. and Reshotko, E., "Control of Shock Wave-Boundary Layer Interactions by Bleed in Supersonic Mixed Compression Inlets", NASA CR-2595, August 1975.
- 7- Lee, D.B., "Etude de l'Interaction Onde de Choc-Couche Limite Turbulente sur Paroi Poreuse avec Aspiration", Doctorat d'Ingenieur Thesis, University of Poitiers, France 1983.
- 8- Lee, D.B. and LeBlanc, R., "Oblique Shock Wave-Turbulent Boundary Layer Interaction with Suction", Aeronautical Journal, November 1984, pp. 416-427.
- 9- Delery, J., Progress of Aerospace Sciences, Vol. 22, 1985, pp. 209-280.
- 10- Shang, J.S., Hankey Jr., W.L., and Herbert Law, C., "Numerical Simulation of Shock Wave-Turbulent Boundary-Layer Interaction", AIAA J., Vol.14, No.10, October 1976, pp. 1451-1457.
- 11- Baldwin, B.S. and Lomax, H., "Thin Layer Approximation and Algebraic Model for Separated Turbulent Flows", AIAA paper 78-257, 1978.
- 12- Peters, G.R., Agarwal, R.K. and Deese, J.E., "Numerical Simulation of Several Shock-Separated Boundary-Layer Interaction Flows Using Zero- and Two-Equation Turbulence Models", AIAA paper 86-0248, 1986.
- 13- Viegas, J.R. and Horstman, C.C., "Comparison of Multiequation Turbulence Models for Several Shock Boundary-Layer Interaction Flows", AIAA J., Vol.17, No.8, August 1979, pp.811-820.
- 14- Knight, D.D., "Numerical Simulation of Realistic High-Speed Inlets Using the Navier-Stokes Equations", AIAA paper 77-146, 1977.
- 15- Abrahamson, K.W. and Brower, D.L., "An Empirical Boundary Condition for Numerical Simulation of Porous Plate Bleed Flow", AIAA paper 88-0306, 1988.

- 16- Knight, D.D., "Calculation of High Speed Inlet Flows Using the Navier-Stokes Equations", AFDL TR-70-3138, February 1980, Volume I: Description of Results.
- 17- Cebeci, T., Smith, A.M.O. and Mosinskis, G., "Calculations of Compressible Adiabatic Turbulent Boundary Layer", AIAA J., Vol.8, No.11, November 1970, pp. 1974-1982.
- 18- Cebeci, T., "Behavior of Turbulent Flow near a Porous Wall with Pressure Gradient", AIAA J., Vol.8, No.12, December 1970, pp. 2152-2156.
- 19- Visbal, M. and Knight, D.D., "The Baldwin-Lomax Turbulence Model for Two-Dimensional Shock-Wave/Boundary-Layer Interactions", AIAA J., Vol.22, No.7, July 1984, pp. 921-928.
- 20- Tassa, Y. and Sankar, N.L., "Effect of Suction on a Shock-Separated Boundary Layer- A Numerical Study", AIAA J. Vol.17, No.11, November 1979, pp. 1268-1269.
- 21- Hanin, M., Wolfshtein, M. and Landau, U.E., "Numerical Navier-Stokes Solution for the Effects of Suction on Shock Wave-Boundary Layer Interaction", in Numerical Methods in Laminar and Tubulent Flows, edited by Taylor c., Morgan, K. and Brebbia, C.A., Proceedings of the First International Conference held at University College Swansea, 17-21 July 1978, John Wiley & Sons.
- 22- Shang, J.S., "Numerical Simulation of Wing-Fuselage Aerodynamic Interaction", AIAA J., Vol. 22, No. 10, October 1984, pp. 1345-1353.
- 23- MacCormack, R.W., "Numerical solution of the Interaction of a Shock Wave with a Laminar Boundary Layer", Lecture Notes in Physics, Vol. 8, Springer-Verlag, 1971, pp. 151-163.
- 24- Skebe, S.A., "Experimental Investigation of Two-Dimensional Shock Boundary Layer Interaction", Ph. D. Dissertation, Case Western Reserve University, August 1983.
- 25- Jurkovitch, M.S., "Flow Visualization Studies of a Tree-Dimensional Shock Wave/Boundary Layer Interaction", Masters Thesis, Case Western Reserve University, May 1982.
- 26- Barnhart, J.P., "Experimental Investigation of Glancing Sidewall Shock/Turbulent Boundary Layer Interactions with Bleed", Masters Thesis, Case Western Reserve University, May 1985.
- 27- Lachmann, G.V., Boundary Layer and Flow Control : Its Principles and Application, Pergamon Press, 1961.
- 28- Pearce, W.E., "Application of Porous Materials for Laminar Flow Control", NASA CTOL Transport Technology Conference, Douglas, 1978 (NASA CP-2036 Part I), Paper No. 6693.
- 29- Reynolds, G.A. and Saric, W.S., "Experiments on the Stability on the Flat Plate Boundary Layer with Suction", AIAA paper 82-1026, 1982.
- 30- Kong, F.Y. and Shetz, J.A., "Turbulent Boundary Layer on Solid and Porous Surfaces with Small Roughness", NASA CR-3612, September 1982.

- 31- Green, J.E. "Reflection of an Oblique Shock Wave and a Turbulent Boundary Layer", J.F.M. Vol. 40, Part 1, 1970, pp. 81-95.
- 32- Reda, D.C. and Murphy, J.D., "Shock Wave/Turbulent Boundary-Layer Interactions in Rectangular Channels", AIAA J., Vol. 11, No. 2. February 1973, pp. 139-140.
- 33- Chew, Y.T., "Shock Wave and Boundary Layer Interaction in the Presence of an Expansion Corner", Aeronautical Quarterly, August 1979, pp. 507-527.
- 34- Squire, J.E., "Interaction of a Shock Wave with a Turbulent Boundary Layer Disturbed by Injection", Aeronautical Quarterly, May 1980, pp. 85-112.
- 35- Maise, G. and McDonald, H., "Mixing Length and Kinematic Eddy Viscosity in a Compressible Turbulent Boundary Layer", AIAA J., Vol. 6, No. 1, January 1968, pp. 73-80.
- 36- Mathews, D.C. and Childs, M.E., "Use of Coles' Universal Wake Function for Compressible Turbulent Boundary Layers", J. Aircraft, Vol. 7, No. 2, March-April 1970, pp. 137-140.
- 37- Kline, S.J., Cantwell, B.J., and Lilley, G.M., The 1980-81 AFOSR-HTTM Stanford Conference on Complex Turbulent Flows : Comparison of Computation and Experiment". Vol. I, pp. 112-129.
- 38- Schlichting, H., Boundary Layer Theory, McGraw-Hill Book Co., New York, 1979.
- 39- Cebeci, T. and Smith, A.M.O., Analysis of Turbulent Boundary Layers, Academic Press, New York, 1974.
- 40- Voisinet, R.L.P., "Combined Influence of Roughness and Mass Transfer on Turbulent Skin Friction at Mach 2.9", AIAA paper 79-0003, January 1979.
- 41- Rockwell, D. and Naudasher, E., "Review-Self Sustaining Oscillations of Flow Past Cavities", J. of Fluid Engineering, Vol. 100, June 1978, pp. 152-165.
- 42- Abarbanel, S.S., Hakkinen, R.J., and Trilling, L., "The Use of Stanton Tube for Skin-Friction Measurements", Fluid Dynamics Research Group MIT TR-57-2, July 1957.
- 43- Allen, J.M., "Evaluation of Compressible-Flow Preston Tube Calibrations", NASA TN D-7190.
- 44- Sigalla, A., "Calibration of Preston Tubes in Supersonic Flow", AIAA J. Vol. 11, No. 10, August 1965, p. 1531.
- 45- Anderson, A.D., Tannehill, J.C., and Pletcher, R.H., Computational Fluid Mechanics and Heat Transfer, McGraw-Hill Book Co., 1984.
- 46- Wilcox, D.C., "Numerical Study of Separated Turbulent Flows", AIAA J., Vol. 13, No. 5, May 1975, pp. 555-556.
- 47- Rose, W., "The Behavior of Compressible Turbulent Boundary Layer in a Shock-Wave-Induced Adverse Pressure Gradient", NASA TN D-7092, March 1973.
- 48- Rose, W., "Comparison of Solutions to the Boundary Layer and Navier-Stokes Equations for the Case of Mass Removal from a Turbulent Boundary Layer", AIAA paper 76-150, 1976.

- 49- Fingerson, L.M and Freymuth, P., "Thermal Anemometers", TSI IFA 100 System, Instruction Manual.
- 50- Boltz, F.W., "Hot-Wire Heat-Loss Characteristics and Anemometry in Subsonic Continuum and Slip Flow", NASA TN D-773, February 1961.
- 51- Collis, D.C. and Williams, M.J., "Two-Dimensional Convection from Heated Wires at Low Reynolds Numbers", J.F.M., No. 6, 1959, pp. 357-384.
- 52- Muskat, M., The Flow of Homogeneous Fluids Through Porous Media, J.W. Edwards, Inc., Ann Arbor, Michigan, 1946.

APPENDIX A

DATA REDUCTION

The pitot data were reduced using the measured wall static pressure and the Rayleigh pitot formula to calculate the Mach number distribution. The static pressure throughout the boundary layer was assumed constant and equal to the wall value. This assumption may not be completely valid in the presence of suction and oblique shock waves and an experimental check could be done. The temperature was obtained from the Crocco-Busemann relation, assuming that the wall temperature was adiabatic. With these assumptions, then, the velocity profiles were obtained and relevant integral properties were calculated using standard formulas and integration techniques.

A.1 Quantities in External Flow

If we assume that the expansion of the flow from the settling plenum to the tunnel test section is isentropic and the static pressure is constant normal to the wall (boundary layer theory), then the local Mach number in the free stream is given by :

$$M_e = \left[\frac{2}{\gamma - 1} (P_{pe}/P_w)^{\frac{\gamma-1}{\gamma}} \right]^{1/2} \quad (A - 1)$$

with $\gamma = 1.4$

$$M_e = 5^{0.5} [(P_{pe}/P_w)^{0.2857} - 1]^{0.5} \quad (A - 2)$$

where P_{pe} is the pitot pressure in the free stream and P_w the wall static pressure. The isentropic flow relationships for the free stream temperature T_e , density ρ_e , and velocity u_e are

$$T_e = \frac{T_T}{1 + 0.2M_e^2} \quad (A - 3)$$

$$\rho_e = \frac{P_w}{RT_e} \quad (A - 4)$$

$$u_e = M_e a_e = M_e \sqrt{\gamma RT_e} \quad (A - 5)$$

The unit Reynolds number per meter is then

$$R_e = \frac{\rho_e u_e}{\mu_e} \quad (A-6)$$

where μ is the viscosity, which is obtained from Sutherland's temperature law

$$\mu_e = 1.468 \times 10^{-6} \frac{T_e^{0.5}}{T_e + 110.6} \quad [\text{N/m}^2 \cdot \text{s}] \quad (A-7)$$

A.2 Variables through the boundary layer

a) Empty tunnel surveys

In order to determine Mach number distribution through the boundary layer from pitot pressure measurements, knowledge of the static pressure distribution is also needed. In boundary layer theory, the static pressure is assumed to be constant normal to the wall. The validity of this assumption for flows with mass removal at the wall is questionable. Rose [48] found, by solving the Navier-Stokes and boundary layer equations, that the static pressure was not constant in the cross-stream direction when bleed was applied, with the variation being higher for increased bleed rate. Despite the uncertainty in the assumption, it was used here and experimental check of its validity is needed. The wall static pressure was then combined with the pitot pressure to form the ratio (P_p/P_w) from which the local Mach number was computed.

For $P_p/P_w \leq 1.893$, the subsonic Mach numbers were computed from the isentropic flow equation

$$\frac{P_p}{P_w} = \left(1 + \frac{\gamma-1}{2} M^2\right)^{\frac{\gamma}{\gamma-1}} \quad (A-8)$$

that is

$$M = \left[\frac{2}{\gamma-1} \left(\frac{P_p}{P_w} \right)^{\frac{\gamma-1}{\gamma}} - 1 \right]^{1/2} \quad (A-9)$$

For $P_p/P_w > 1.893$, the supersonic Mach numbers were calculated by iteration from the Rayleigh pitot formula

$$\frac{P_p}{P_w} = \left(\frac{\gamma+1}{2} M^2 \right)^{\frac{\gamma}{\gamma-1}} \frac{\gamma+1}{(2\gamma M^2 - \gamma + 1)^{\frac{1}{\gamma-1}}} \quad (A-10)$$

The static temperature in the boundary layer was assumed given by the Crocco-Busemann equation

$$T = T_w + (T_{aw} - T_w) \frac{u}{u_e} - \frac{ru^2}{2C_p} \quad (A - 11)$$

where the adiabatic wall temperature is computed, assuming a recovery factor of 0.896, from

$$T_{aw} = T_e + \frac{0.896u_e^2}{2C_p} \quad (A - 12)$$

The velocity distribution is given by

$$u/u_e = \frac{M}{M_e} \sqrt{\frac{T}{T_e}} \quad (A - 13)$$

Since the measured wall temperature showed some scatter and, on the average, was close to the adiabatic temperature, the wall temperature was assumed to be adiabatic.

b) Shock wave/boundary layer interaction surveys

The assumption of constant static pressure normal to the wall in regions of shock wave/boundary layer interactions is not totally justified. For example, Rose [47] found a 40% pressure jump across an oblique shock wave of 9° flow deflection angle at $M = 4.0$. Numerical computations by Wilcox [46] have also shown large variations in pressure normal to the wall. Since there is ample evidence that the static pressure is not constant along the normal to the wall and the effect of bleed and roughness are unknown, no velocity profiles were deduced from the pitot pressure measurements.

APPENDIX B

HOT-WIRE CALIBRATION AND CORRECTION

The procedure followed in obtaining the hot-wire calibration and correction for the effect of Knudsen number are given in this Appendix. The use of hot-wires for mass flow measurements requires calibration before testing. The basic variable measured by a hot-wire sensor is the rate of heat transfer from the wire to the fluid. Since this is not generally the variable of interest, a calibration of bridge voltage vs. flow velocity is made. The calibration was done outside the wind tunnel using a TSI calibrator unit (Model 1125) (Figure B1). The calibrator provides a calibrated chamber flow based on the Bernoulli equation. The hot-wire was placed inside the middle chamber D2 for low velocity calibration and outside nozzle D1 for higher flow velocity. The mass flow rate was varied by the needle and regulator valves. The pressure differential, Δp , across the orifice was measured with a water manometer. The orifice velocity is related to Δp by the following equation

$$V_{or} = \sqrt{\frac{2g\rho_w\Delta h_w}{\rho_a}} \quad (B - 1)$$

where ρ_w and ρ_a are the densities of water and air, respectively. The calibration conditions were the local atmospheric conditions (14.36 psia and 74 °F). Mass flow through the inside chamber D2 is determined via its steady-state relationship to mass flow through the exterior nozzle (D1) by

$$V_{D2} = V_{or} \left(\frac{D_1}{D_2} \right)^2 \quad (B - 2)$$

The most accurate calibration position is end on (outside of D1). However, this is not possible when the calibration is done in chamber D2 or D3, in which cases the probe has to be placed side on and a correction to the readings was applied as suggested by the manufacturer

$$V_{corr} = V_{D2} \cdot K_{sf} \quad (B - 3)$$

K_{sf} is a correction factor that is a function of V_{D2} and wire diameter as shown in Figure B2.

The hot-wire was heated electrically and the power dissipated in it was computed from measurements of the output voltage and wire resistance. The wire resistance at ambient conditions was 6.92 ohms. The wire was operated at an overheat ratio of 1.8. The overheat ratio is defined as

$$a_T = \frac{R_w}{R_a} \quad (B-4)$$

where R_w is the wire operating resistance and R_a is the wire resistance at ambient conditions.

The power dissipated in the sensor is

$$P = \frac{E^2 R_w}{R_w + R_o} = H + K + R \quad (B-5)$$

H represents convection, K , conduction, and R , radiation. E is the voltage across the sensor and $R_o = 10$ Ohms (see Fig. B3). Radiation is usually negligible, in the present case it is on the order of 0.4% of the total power. The quantity of primary interest is the convective heat transfer. For the hot-wire

$$H = N_u \pi l K_f (T_w - T_a) \quad (B-6)$$

where

$N_u = \frac{hd}{K_f}$	Nusselt number
h	heat transfer coefficient
d	wire diameter
K_f	thermal conductivity of the fluid at the film temperature T_f
$T_f = \frac{T_w + T_a}{2}$	
T_w	Wire temperature
T_a	Ambient temperature of the fluid

A general expression for N_u is

$$N_u = f(R_e, P_r, G_r, M, K_n, \gamma, \dots) \quad (B-7)$$

where R_e , is the Reynolds number, P_r the Prandtl number, G_r the Grashoff number, M the Mach number, K_n the Knudsen number, and γ the specific heat ratio. The

results of forced convection investigations have shown that a simple expression exist between the Nusselt number and Reynolds number, often referred to as King's law [49], which is of the form

$$N_u = A' + B' R_e^{0.5} \quad (B - 8)$$

The constants A' and B' are determined from calibration. For low density flow, the most relevant parameter is the Knudsen number, defined as the ratio of the mean free path, λ , to the wire diameter

$$K_n = \frac{\lambda}{d} = \sqrt{\frac{\pi \gamma M}{2 Re}} \quad (B - 9)$$

For air, the value of λ is 6.4×10^{-6} cm at a density corresponding to 76.0 cm of mercury and 15 °C [50]. The value at the same temperature for other pressures is

$$\lambda = 6.4 \times 10^{-6} \left(\frac{76.0}{p} \right) \text{ [cm]} \quad (B - 10)$$

where p is the fluid pressure in cm of mercury.

It is suggested in reference [50] that the regions of the various flows may be classified roughly as follows :

$0 < K_n < 0.015$	continuum flow
$0.015 < K_n < 0.15$	slip flow
$0.15 < K_n < 1$	mixed flow
$10 < K_n$	free-molecular flow

The value of K_n was 0.02 during calibrations. The range of Knudsen numbers during measurements was between 0.4 and 0.5. The difference comes from the fact that the pressure inside the bleed plenum chamber was low. Because of the difference in Knudsen numbers between calibration and measurements, a correction was applied to reduce all measured data to continuum conditions. A correction for temperature jump based on kinetic theory as outlined by Collis and Williams [51] is used.

When thermal conduction takes place between a rarefied gas and a boundary wall, there is a discontinuity in temperature at the wall. If the wall temperature is T_w , and T_s is what the temperature of the gas would be if the temperature gradient along the outward normal, $\partial T / \partial n$, continued right up to the wall, then the discontinuity, or temperature jump, is given by

$$T_w - T_s = -\zeta \left(\frac{\partial T}{\partial n} \right) \quad (B - 11)$$

where ζ is a constant given by

$$\zeta = \frac{2\gamma}{\gamma+1} \frac{1}{P_r} \frac{2-\alpha}{\alpha} L \quad (B-12)$$

α is the accommodation coefficient of the surface for the particular gas. For air, $\gamma = 1.4$, $P_r = 0.72$, and for tungsten in air $\alpha \simeq 0.9$ so that

$$T_w - T_s = -2L \frac{\partial T}{\partial n} \quad (B-13)$$

Here L is defined by the relation

$$L = \frac{\mu}{c\rho\bar{v}} \quad (B-14)$$

and

$$\bar{v} = \sqrt{8RT/\pi} \quad (B-15)$$

where R is the gas constant per unit mass, ρ and μ the density and viscosity respectively, and c is a constant ($c \simeq 0.5$).

If the wire is maintained at a temperature T_w , and q the heat loss per unit area is measured, then the heat transfer coefficient h_w is calculated from the relation

$$q = h_w(T_w - T_a) = \frac{E^2 R_w}{(R + R_w)^2} \quad (B-16)$$

Assuming the measured heat transfer rate is the same as would take place from a cylinder of the same diameter, at a temperature T_s , immersed in a perfectly continuous gas, the continuum heat transfer coefficient would be given by

$$q = h_s(T_s - T_a) = -\left(k \frac{\partial T}{\partial n}\right)_{T_s} \quad (B-17)$$

Combining the last two equations with equation (B-13) it can be shown that

$$\frac{1}{h_s} = \frac{1}{h_w} - 2\left(\frac{L}{k}\right)_{T_s} \quad (B-18)$$

which may be written alternatively as :

$$T_s = T_w - 2\left(\frac{L}{k}\right)_{T_s} \frac{1}{\pi dl} \frac{E^2 R_w}{R_o + R_w^2} \quad (B-19)$$

The correct value of T_s must be obtained by successive approximation, starting with $T_s = T_w$. The continuum Nusselt number can then be determined from

$$N_{uc} = \frac{h_s d}{k_m} \quad (B-20)$$

where k_m is the thermal conductivity of air at the mean film temperature

$$T_m = \frac{T_a + T_s}{2} \quad (B-22)$$

Values of the thermal conductivity were obtained from the Prandtl number formula

$$k = \frac{\mu C_p}{Pr} \quad (B-23)$$

with $Pr = 0.72$, C_p the specific heat at constant pressure, and μ given by Sutherland's viscosity law.

The corrected Nusselt numbers from calibration are plotted against the square root of the Reynolds number in Figure B4. A least squares fit of the data to equation (B-8) gives the constants $A' = 0.66$ and $B' = 0.95$. It is apparent that above a Reynolds number of 0.4, the curve follows a straight line. Below this limit, the data starts to diverge from the linear behavior. According to Collis and Williams, this divergence occurs because natural convection becomes comparable in magnitude to the forced convection (see Figure B5). The wire is then in a mixed natural and forced convection regime. They pointed out that there is a lower limit of velocity which can be measured without ambiguity.

During bleed surveys, the hot-wire was operated at the same overheat ratio as during calibration. The temperature inside the bleed plenum chamber was near the temperature during calibration; however, the pressure and then the density were approximately 10 times lower than calibration. The measured voltages were corrected for the effect of Knudsen number as outlined above. For the $M = 3.0$ tests, it is suspected that the flow velocity was low and thus, the hot-wire readings were lower than the fitted curve given by equation (B-8). This is the reason why the bleed could not be deduced from the hot-wire calibration equation (equation (B-8)).

APPENDIX C

POROUS MATERIAL CALIBRATION

In the present appendix, the flow resistance characteristics of the porous material used in the experiments are reported over a limited range of differential pressures across the material. The flow resistance was determined with the air flow normal and parallel to the porous plate surface.

Although the porous plate is best calibrated under actual tunnel operating conditions, it was not possible to do this during the planning of the experiments. Instead, some preliminary experiments outside of the wind tunnel were done to determine the pressure drop as a function of the flow rate through the porous plate with the flow being normal to the surface. The apparatus used for this calibration is shown in Figure C1. It consists of a 3.175 cm (1.25 in) ID. pipe in which a circular piece cut from the Dynapore material was clamped between two flanges. Flow was induced through the porous material by a vacuum pump. The pressure drop and therefore the volumetric flow rate was adjusted by two valves, one placed 10.16 cm (4.0 in) upstream and the other 10.16 cm downstream of the porous material. The two valves served to maintain a constant pressure on the upstream side of the sample while varying the pressure drop through it. The total mass flow rate was measured by a flowmeter. With this setup, the porous material was calibrated for upstream pressures of 2.0 and 3.0 psia.

During tests in the empty tunnel, the porous plate insert was calibrated with the free stream flow parallel to the surface. It should be remembered that the calibration was made with the porous sheet backed by the honeycomb structure. Since the mass flow rate through the bleed system could not be varied for fixed tunnel operating conditions, and therefore for a constant pressure on the upstream side of the porous material, only one point measurement was possible for each Mach number. However, by changing the stagnation pressure inside the settling chamber, additional data could be obtained. By changing the tunnel stagnation pressure, the pressure on the porous surface changed also. For $M = 2.5$ the stagnation pressures were 20.0, 25.0, and 30.0 psia. Stagnation pressures of 30.0, 35.0, and 40.0 psia were used at $M = 3.0$.

The results are presented graphically in Figure C2 as the pressure drop versus the mass flux per unit area of the porous material. These curves show that the upstream pressure has an effect on the relationship between the mass flow and the pressure drop. Another way of representing these results is by using a pressure drop coefficient versus the Reynolds number based on the thickness of the porous material. The data from Figure C2 is replotted in the above variables in Figure C3. It is seen that the data collapse to one curve with some scatter in the data taken inside the wind tunnel. This can be attributed to the fact that the pressure on the upstream surface of the porous plate showed perturbations and the average of the measured values was used. Another possible source of error is the use of two different instruments to measure the flow rate in the normal and parallel flow calibrations.

A least squares fit of the data to the following equation

$$\frac{\Delta p}{\rho v^2} = A + \frac{B}{Re} \quad (C - 1)$$

gives $A = 212.0$ and $B = 7588.0$. This equation is similar to the one suggested by the manufacturer for normal flow under standard upstream conditions; only the constants A and B are different. According to reference [52], equation (C-1) approximates very well the flow through a variety of porous materials. For some porous materials, the constants may also depend on the pressure on the upstream side.

In the range of the present experimental conditions, the results of the parallel flow calibration show that the pressure drop through the porous material varies approximately with the velocity squared. Although there may be a Mach number dependence, it does not show clearly on the data.

Calibration equations describing the characteristics of the porous materials in parallel flow, such as the one obtained above, are of considerable aid to the designer who wishes to know the amount of bleed needed to prevent separation.

M_e	P_T [kpa]	T_T [K]	α [°]	P_{PL} [kpa]	\dot{m}_s [kg/s]	\dot{m}_{bl}	F
2.5	172.3	300.0	0	4.686	0.027	0.057	0.009
		299.5	4	5.296	0.032	0.066	0.010
		301.5	6	6.385	0.038	0.080	0.013
		299.0	8	7.856	0.049	0.102	0.016
3.0	241.2	300.0	0	3.288	0.021	0.049	0.007
		301.5	4	3.749	0.022	0.050	0.008
		299.5	6	4.527	0.029	0.067	0.011
		299.5	8	5.968	0.038	0.088	0.014

M_e	α [°]	X_G [cm]	Y_G [cm]
2.5	0.0	-18.5	19.4
	4.0	-19.4	20.5
	6.0	-19.8	21.1
	8.0	-20.2	21.6
3.0	0.0	-23.1	19.4
	4.0	-24.0	20.5
	6.0	-24.4	21.1
	8.0	-24.8	21.6

TABLE I Experimental Conditions

M_e	P_T [kpa]	T_T [K]	α [°]	x_{sh} [m]	\dot{m}_s [kg/s]
2.46	172.3	300	4.5	0.050	0.030
			6.5	0.037	0.038
			8.5	0.025	0.055
2.98	241.2	300	4.5	0.015	0.018
			6.5	0.018	0.025

TABLE II Conditions of Calculations

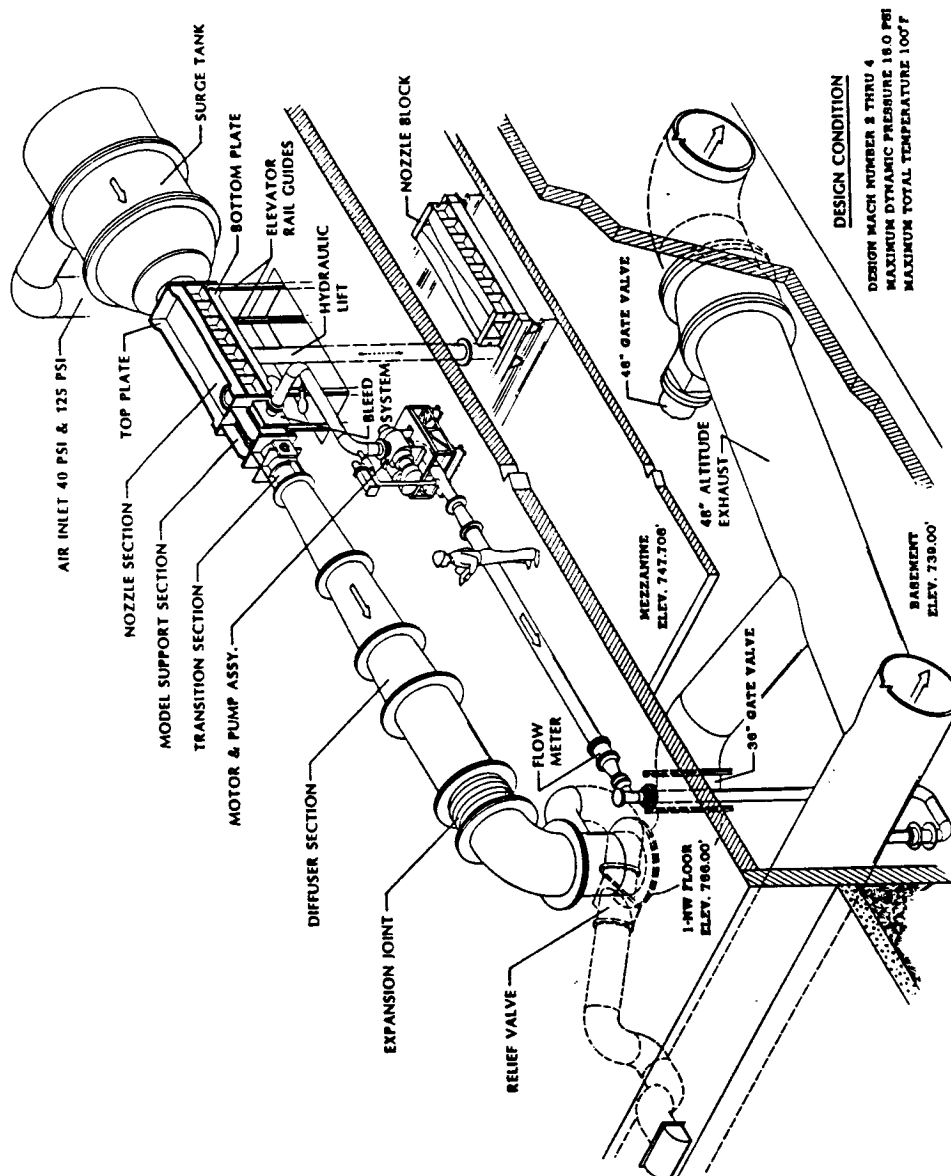


Fig. 1 1ft x 1ft SUPERSONIC WIND TUNNEL

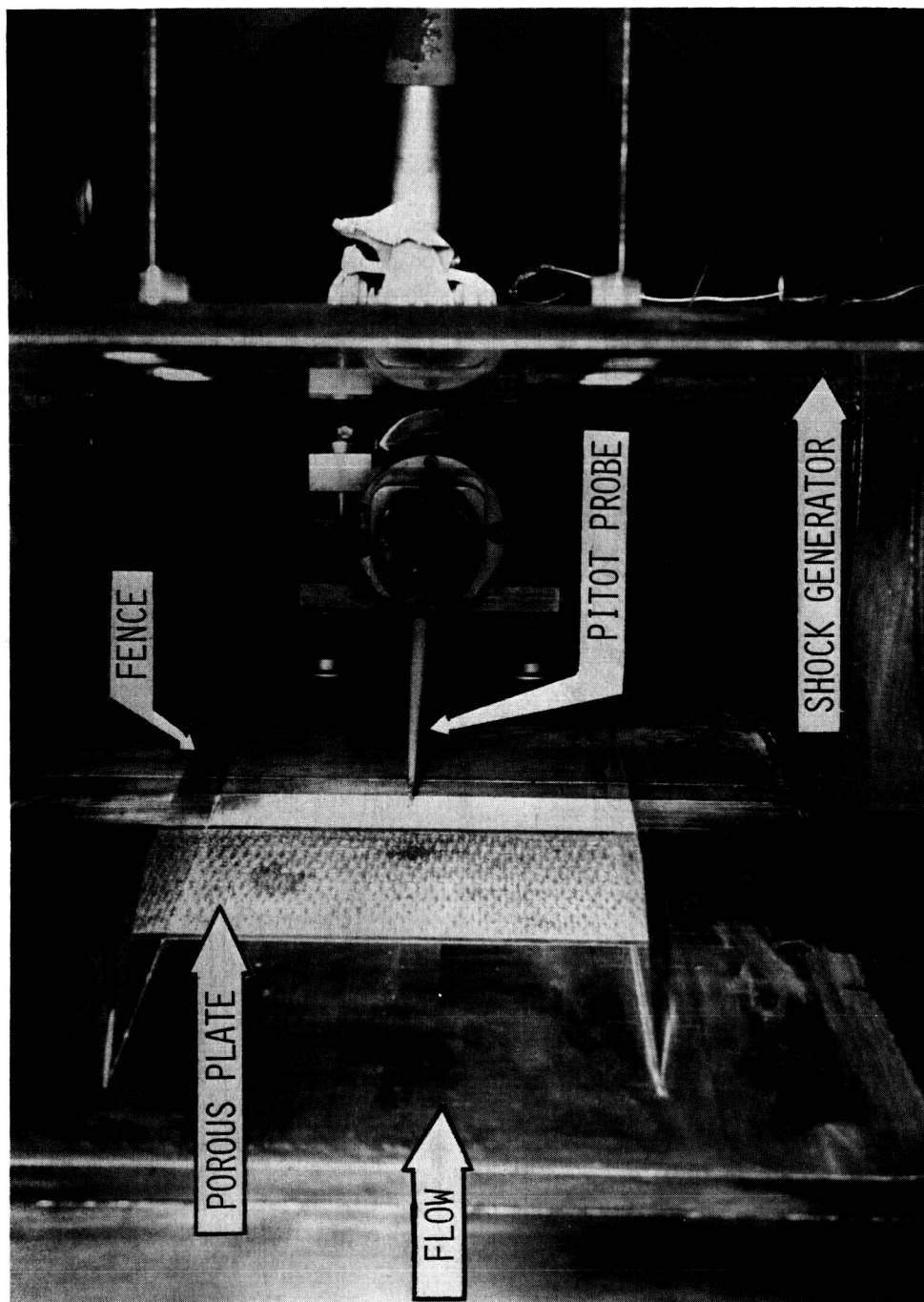


Fig. 2 PHOTOGRAPH OF TEST SECTION

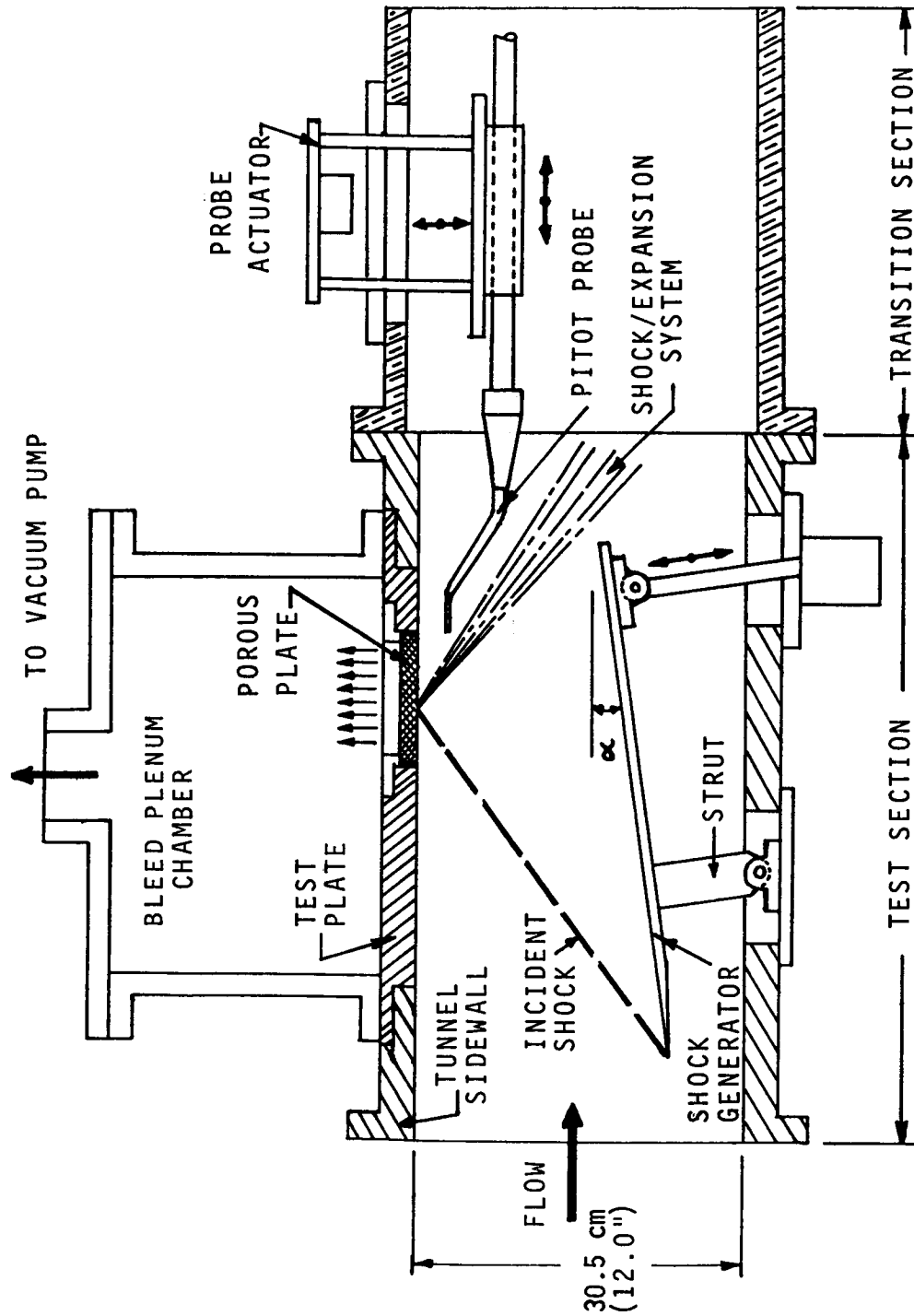


Fig. 3 EXPERIMENTAL CONFIGURATION

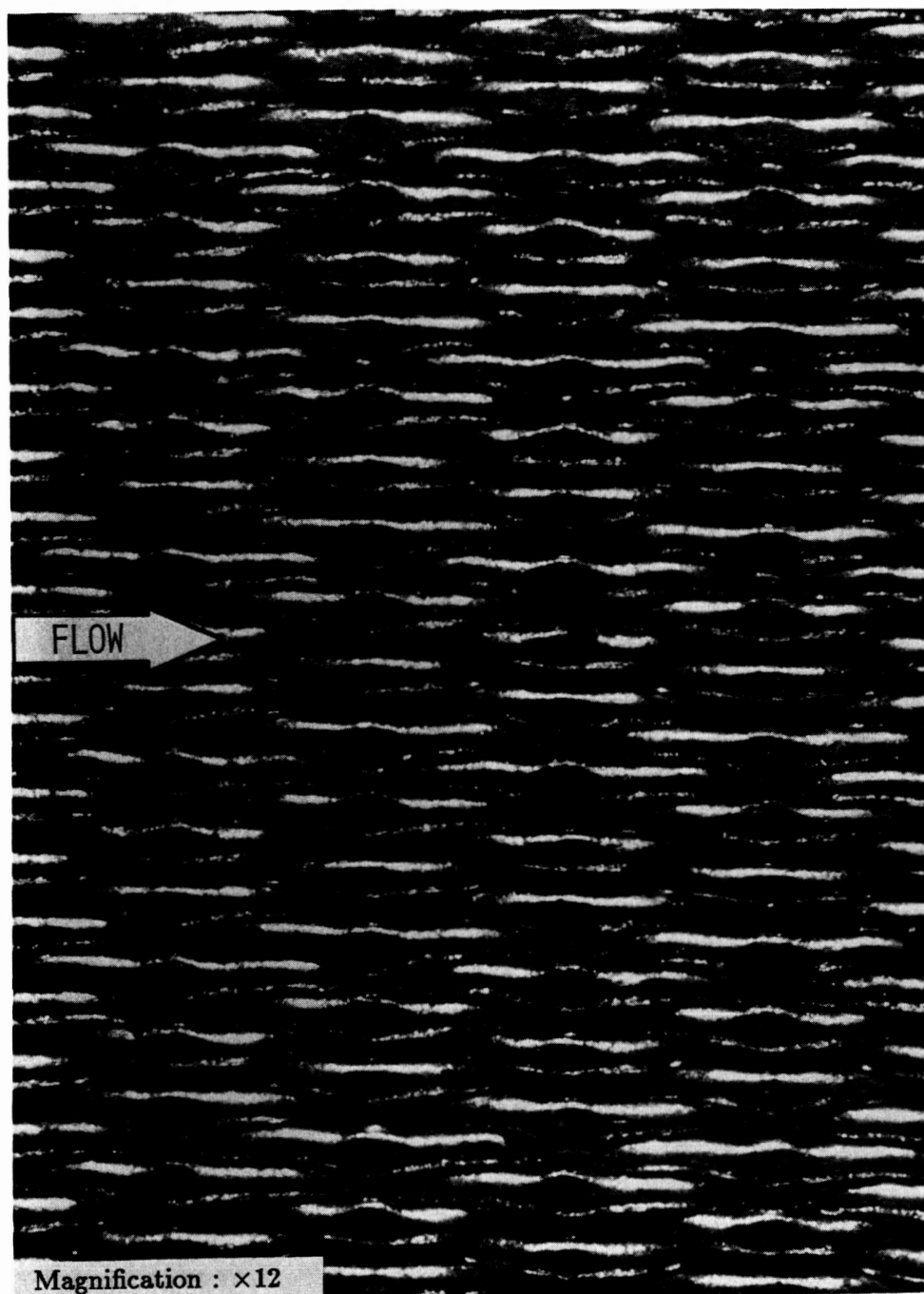
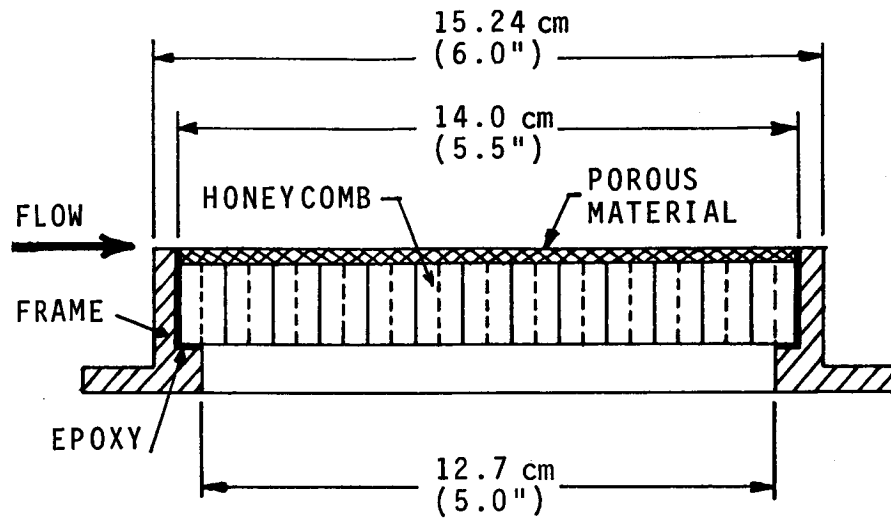
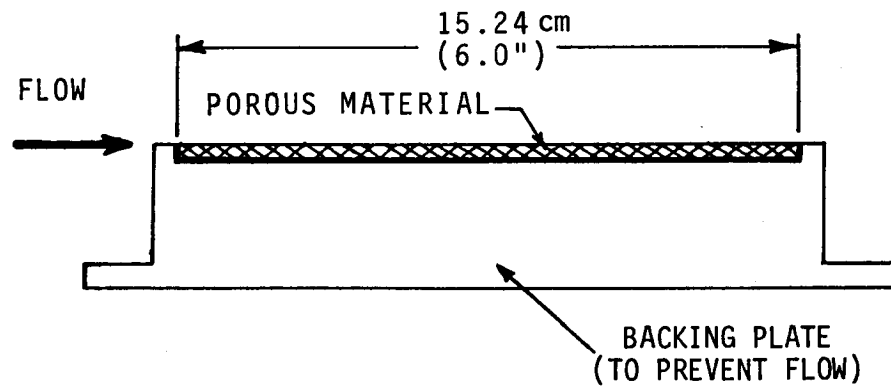


Fig. 4 PHOTOGRAPH OF POROUS MATERIAL



a) Porous plate



b) Rough plate

Fig. 5 CROSS SECTION OF POROUS PLATE
AND ROUGH PLATE

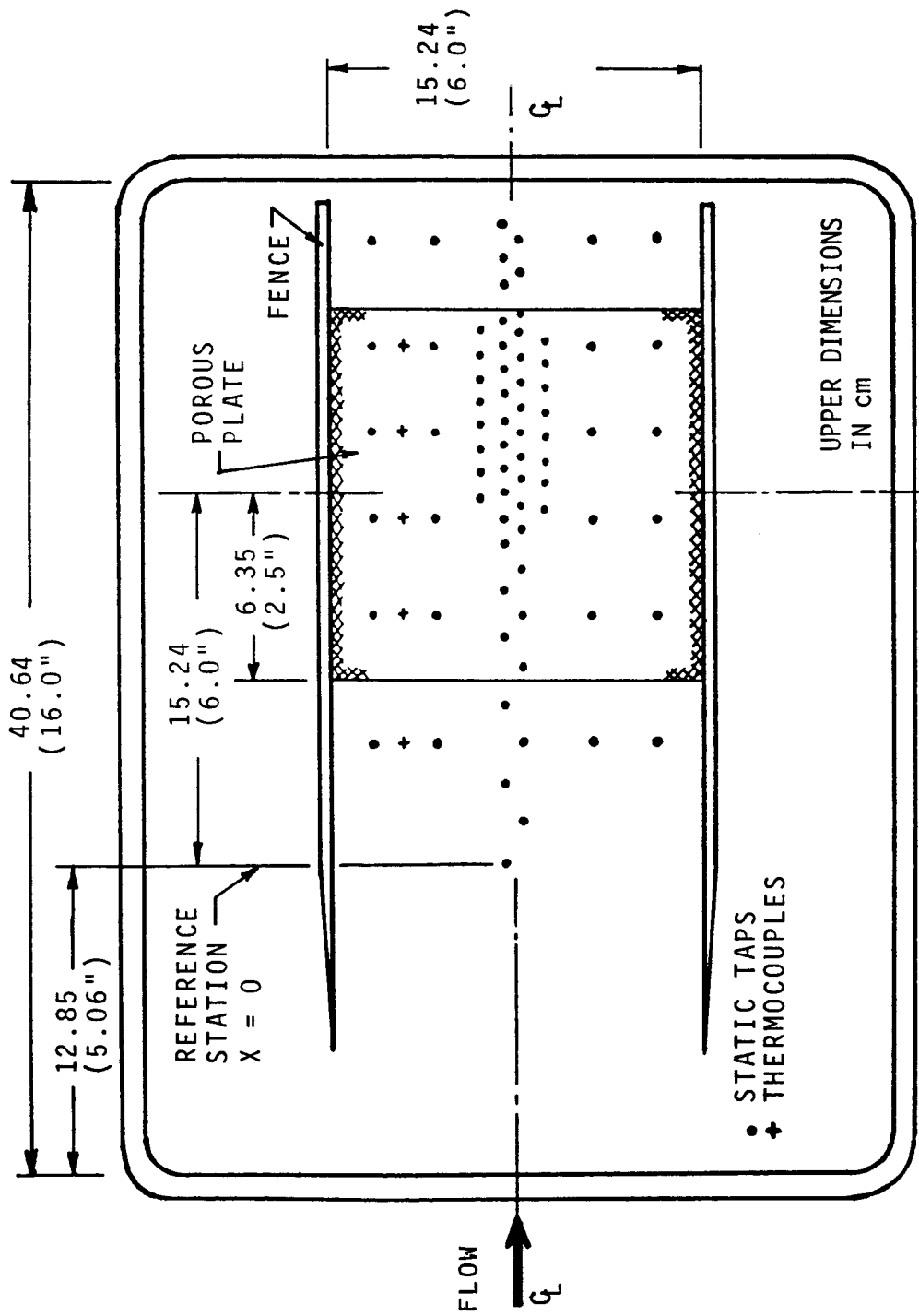


Fig. 6 TEST PLATE INSTRUMENTATION

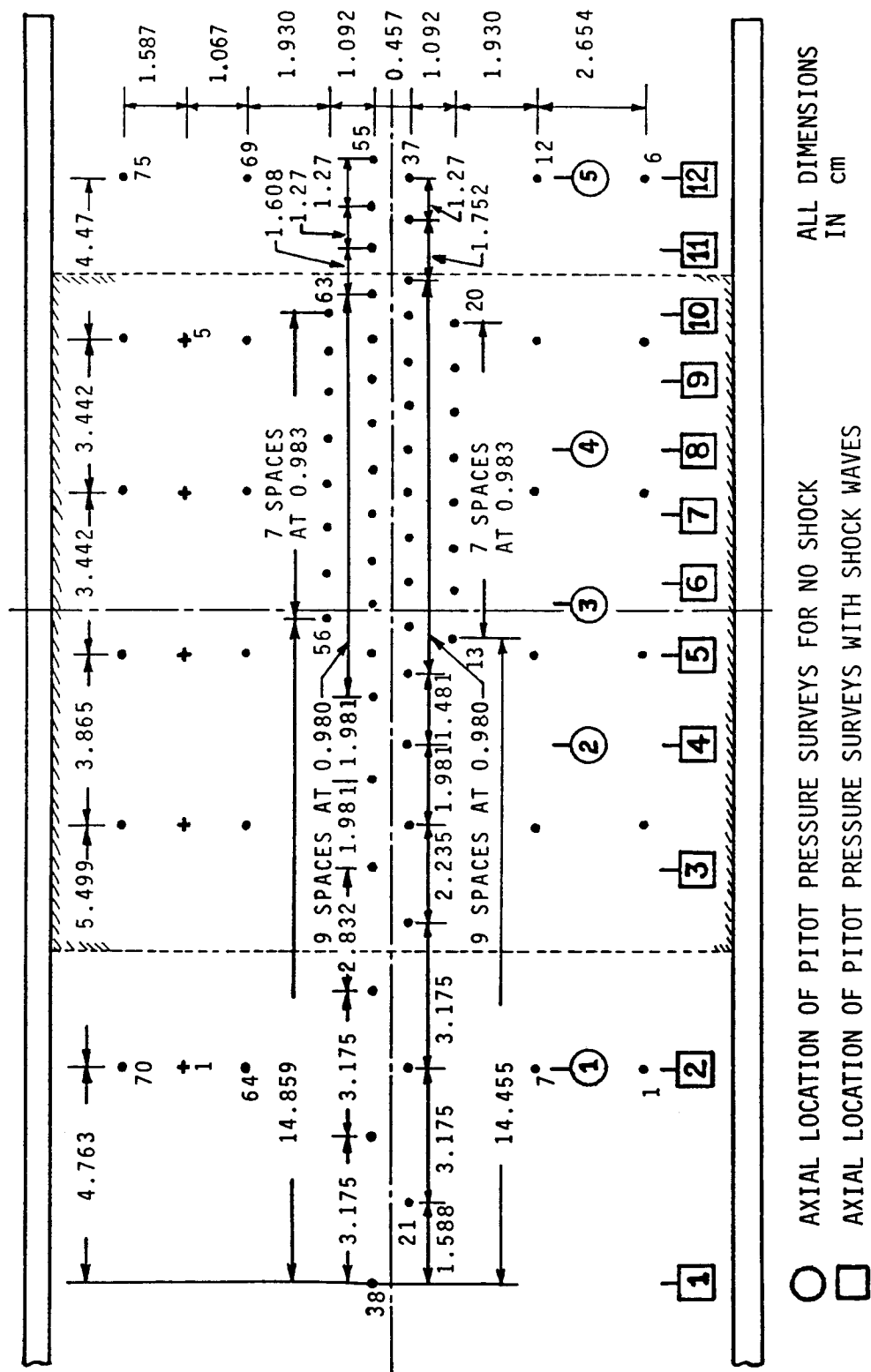


Fig. 7 DETAIL OF TEST PLATE INSTRUMENTATION

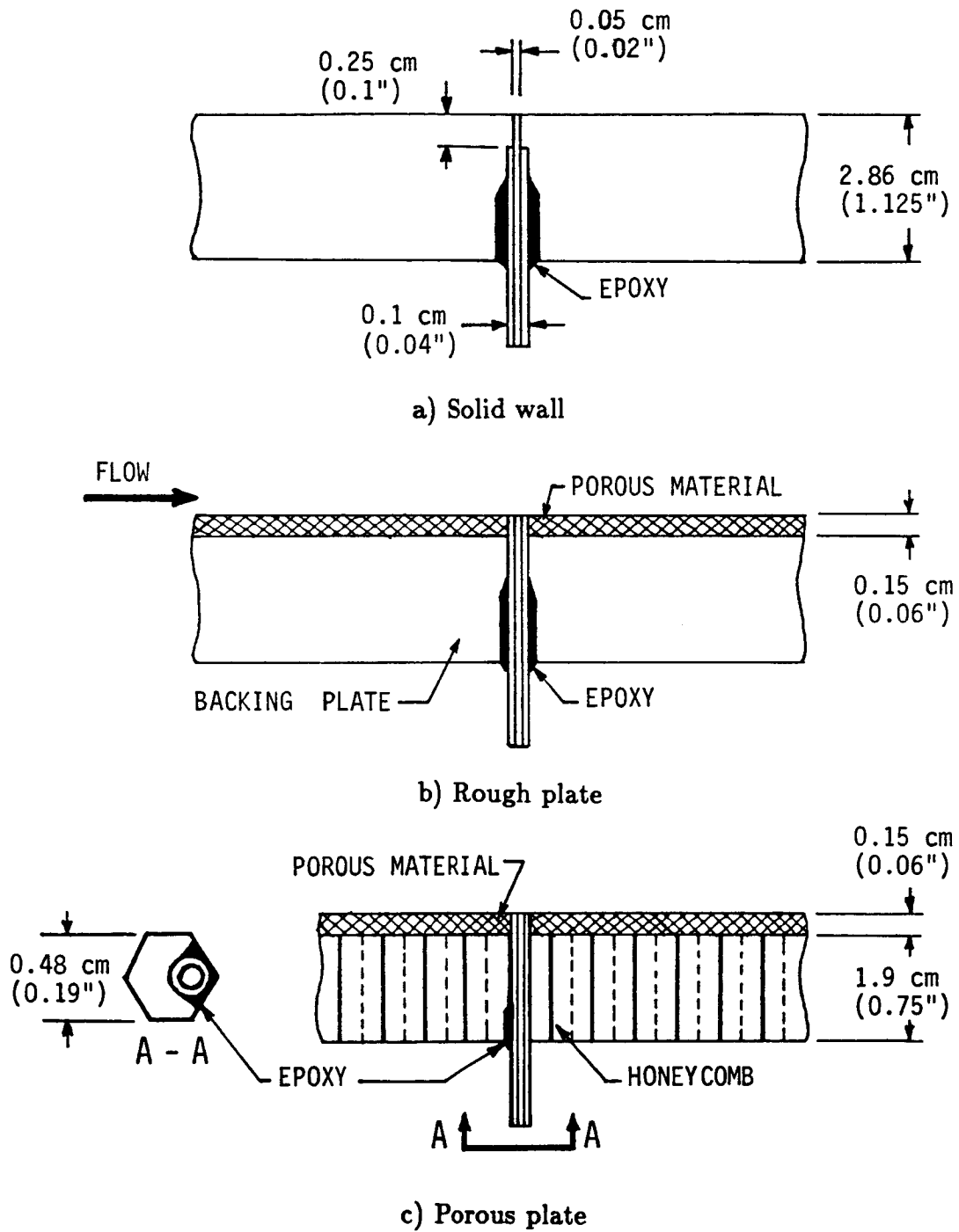
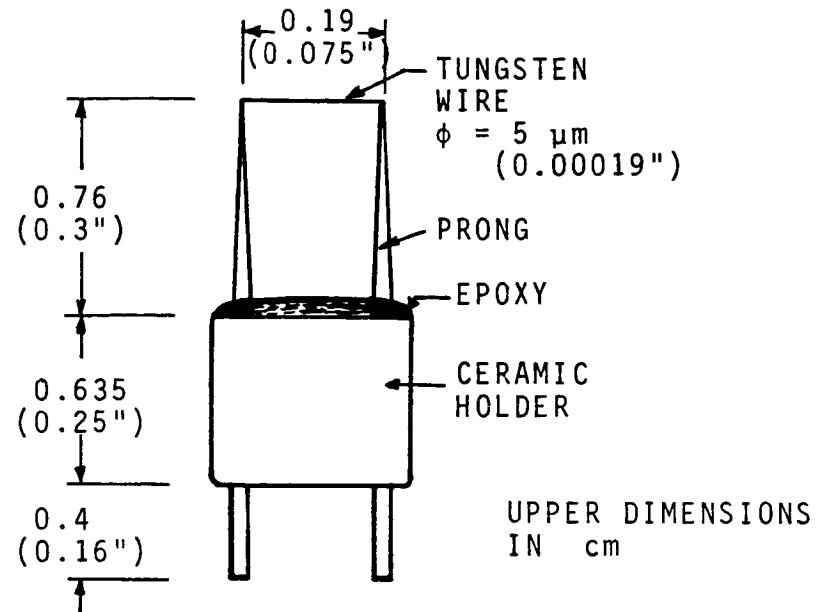
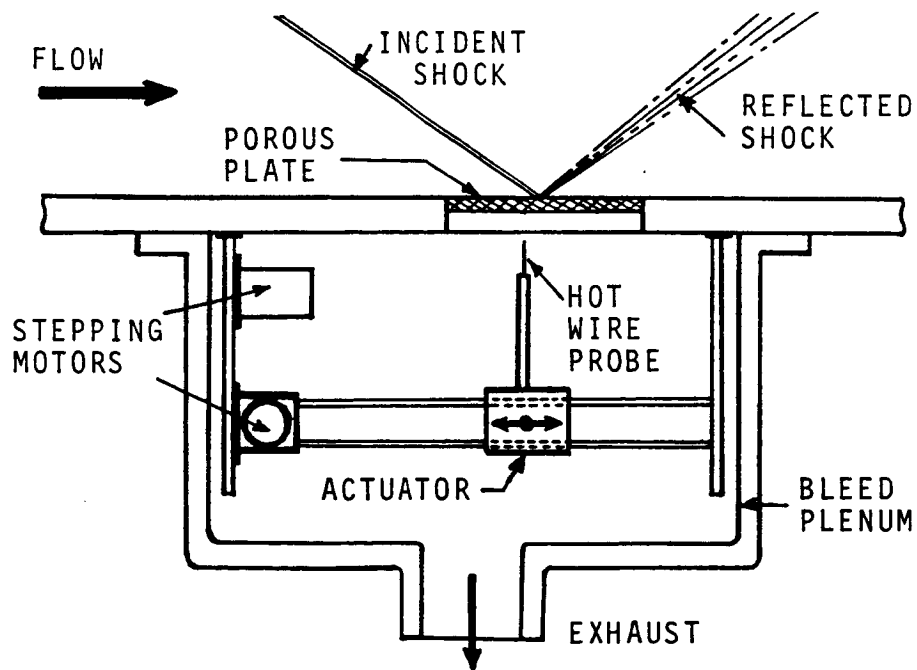


Fig. 8 DETAIL OF STATIC TAPS INSTALLATION



a) Schematic of hot-wire probe



b) Measurement technique

Fig. 10 APPARATUS FOR BLEED MEASUREMENT

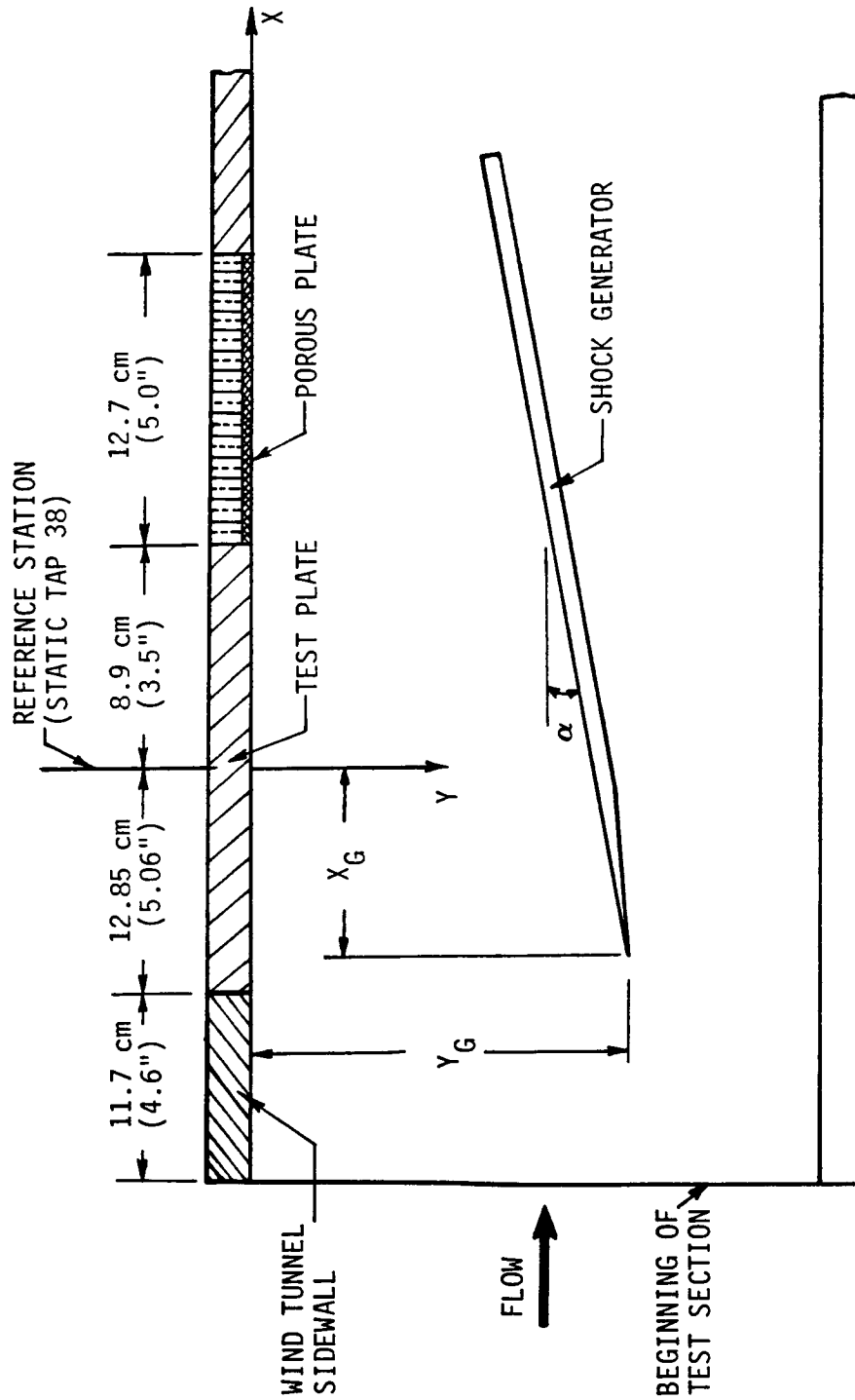


Fig. 11 COORDINATES OF SHOCK GENERATOR

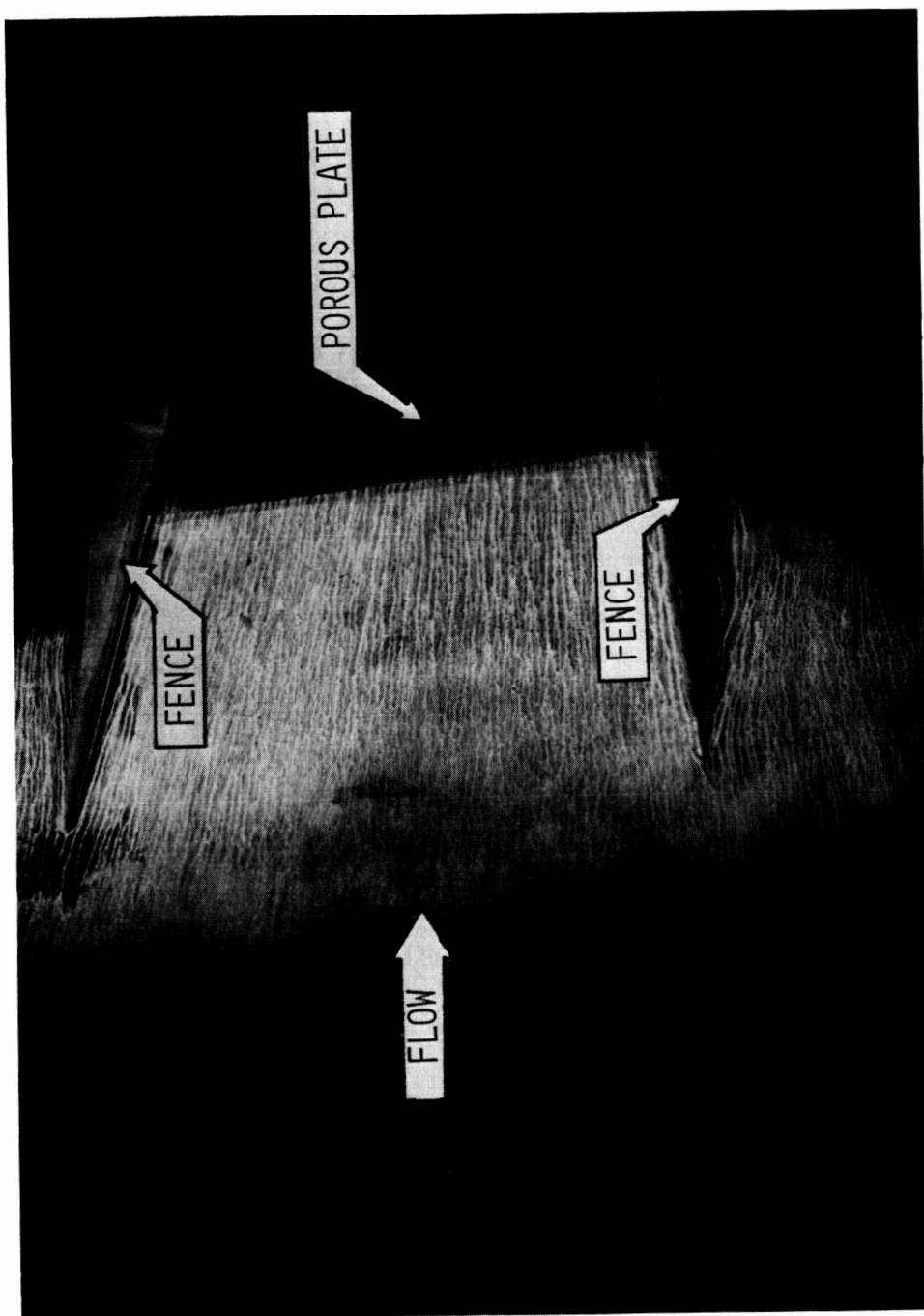


Fig. 12 OIL FLOW VISUALIZATION BETWEEN FENCES

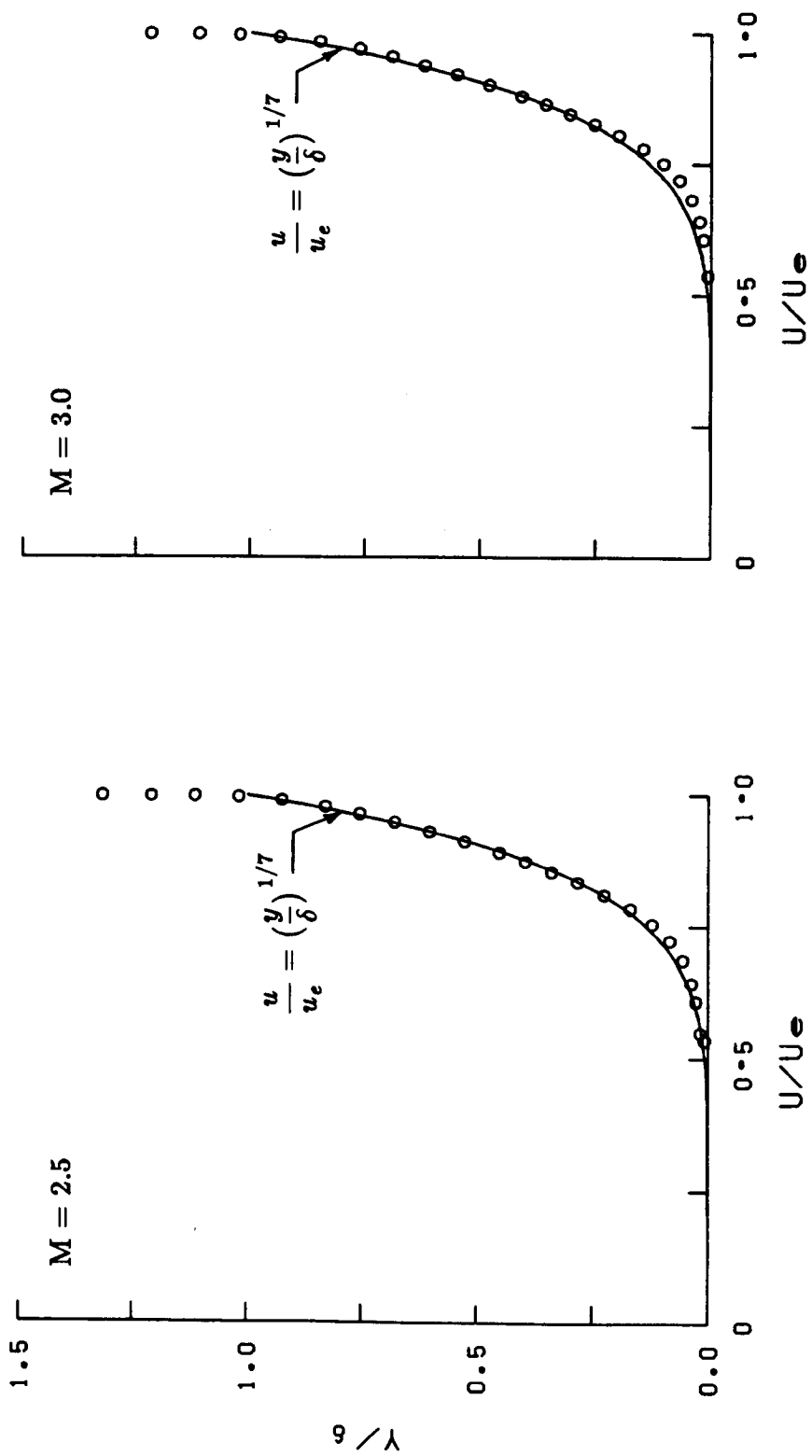


Fig. 13-a INCOMING VELOCITY PROFILES

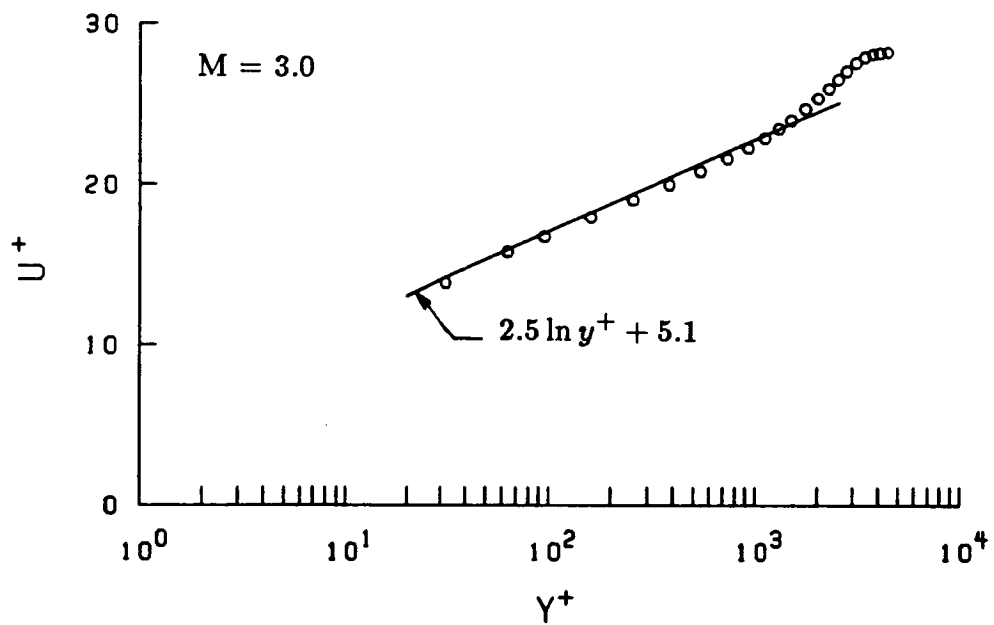
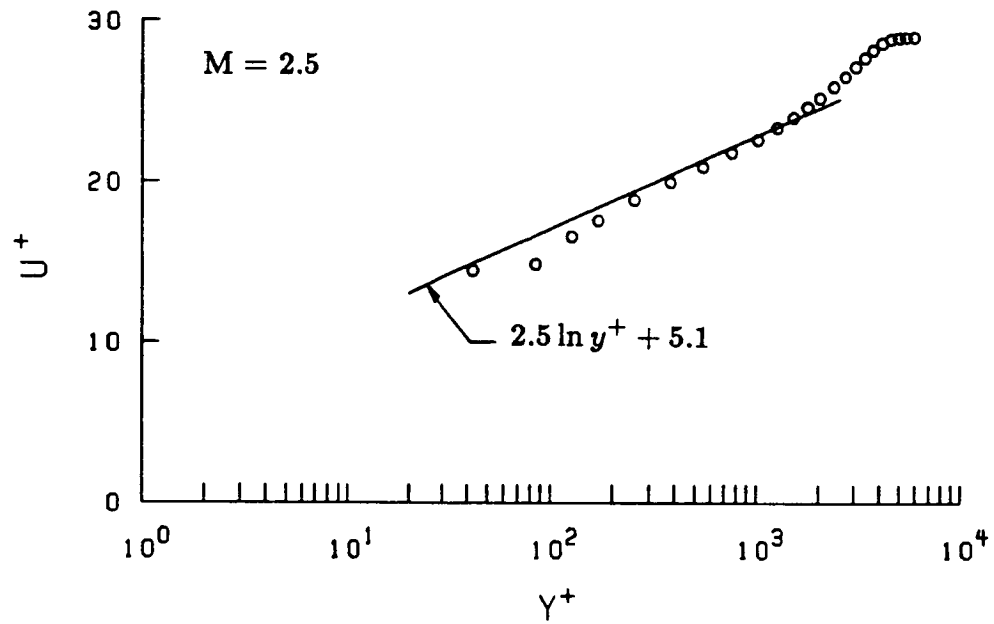
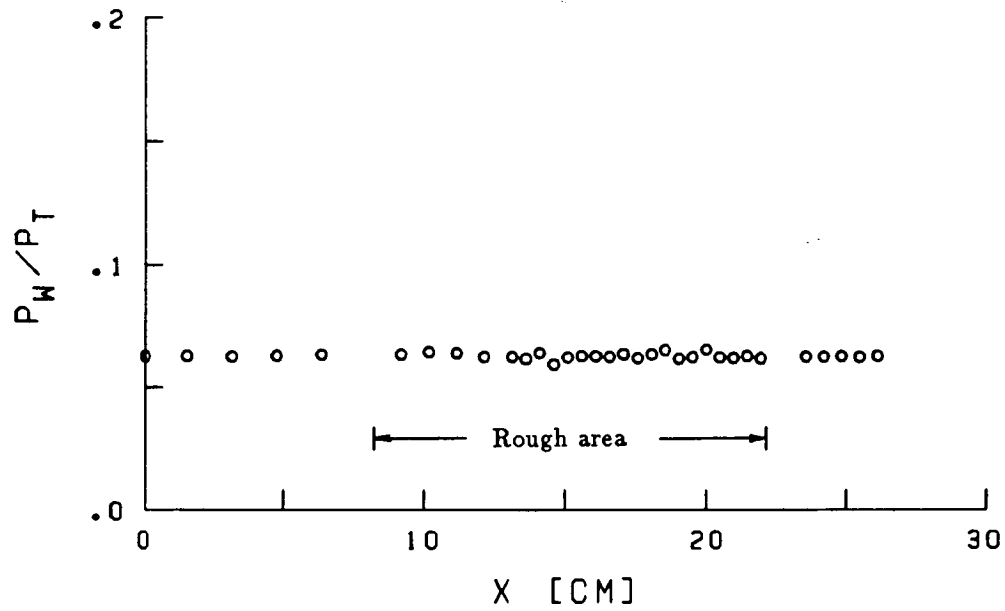
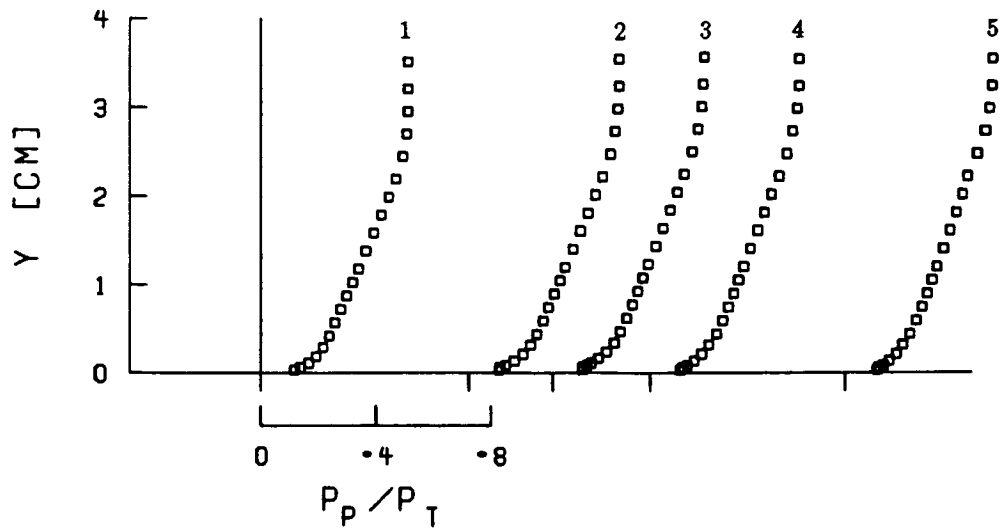


Fig. 13-b SEMI-LOGARITHMIC PLOTS OF
INCOMING VELOCITY PROFILES

02

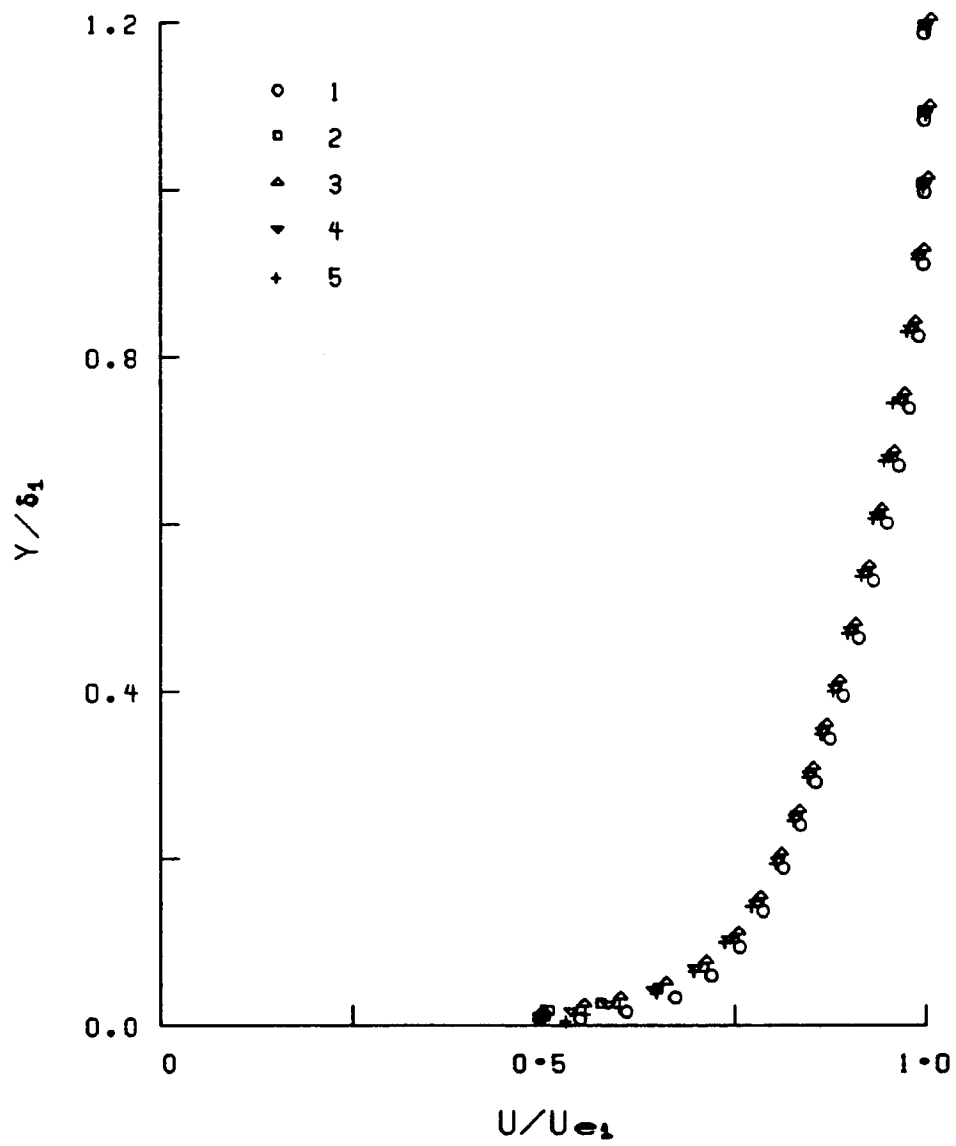


a) Wall pressure distribution



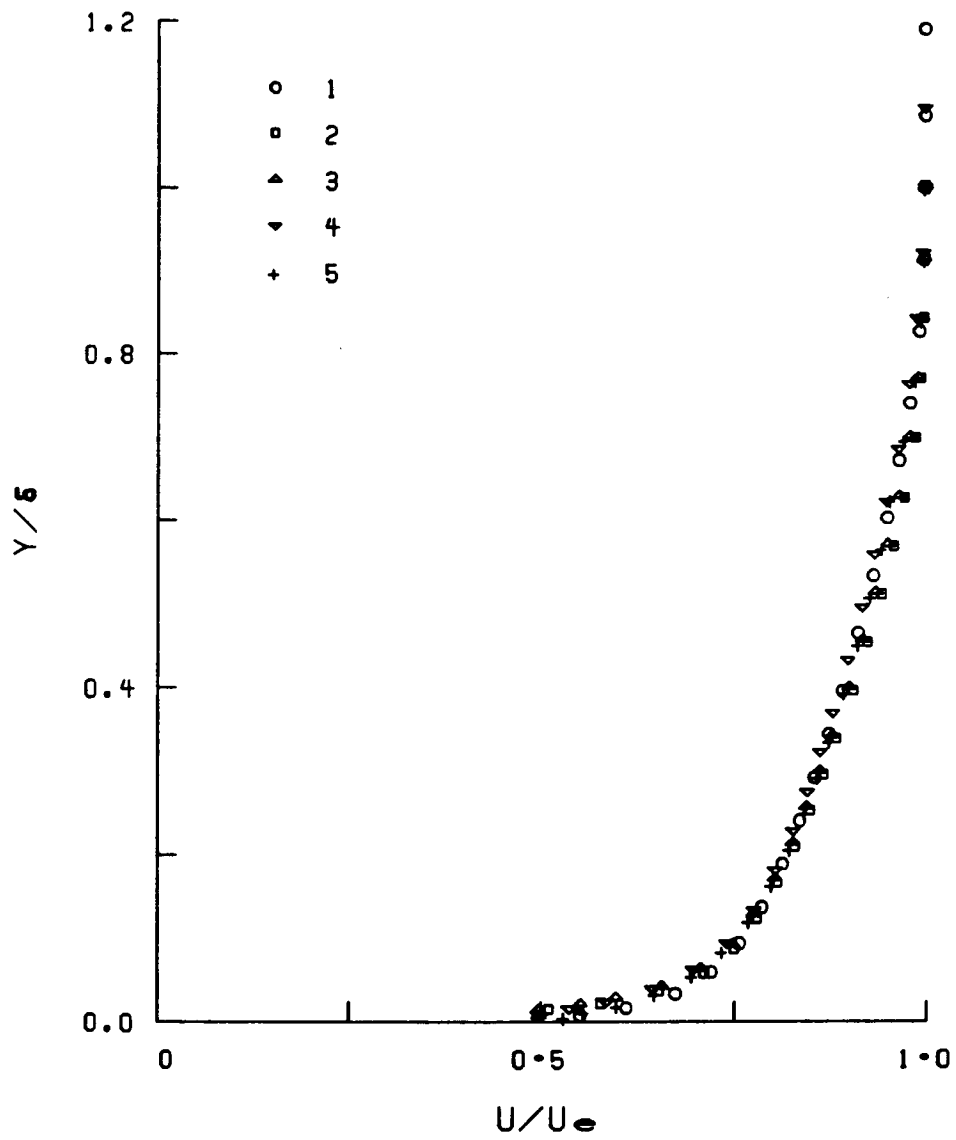
b) Pitot pressure profiles

Fig. 14 MEASUREMENTS ON ROUGH PLATE
AT $M = 2.5$ AND $\alpha = 0^\circ$



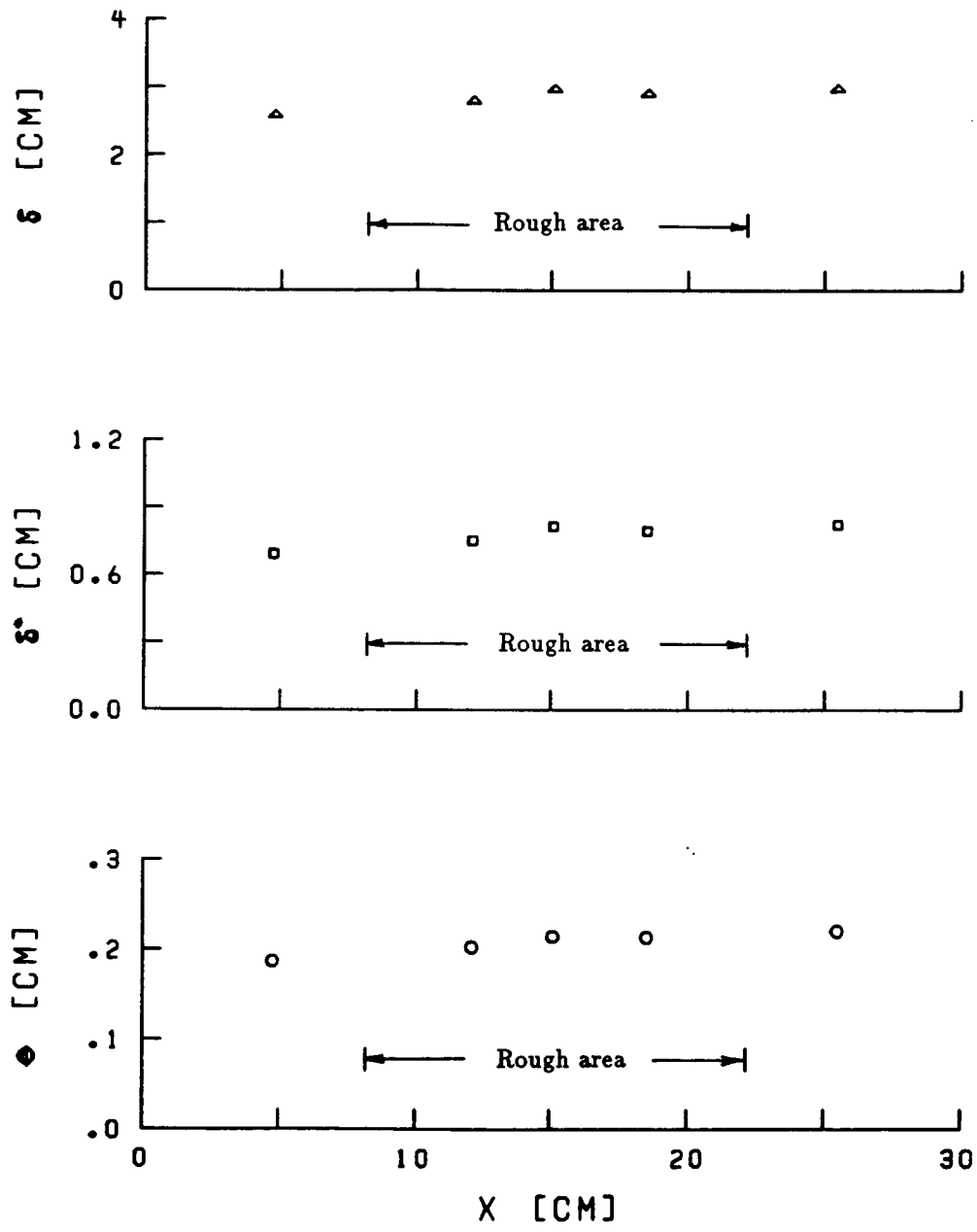
c) Velocity profiles non-dimensionalized
with conditions of first profile

Fig. 14 CONTINUED



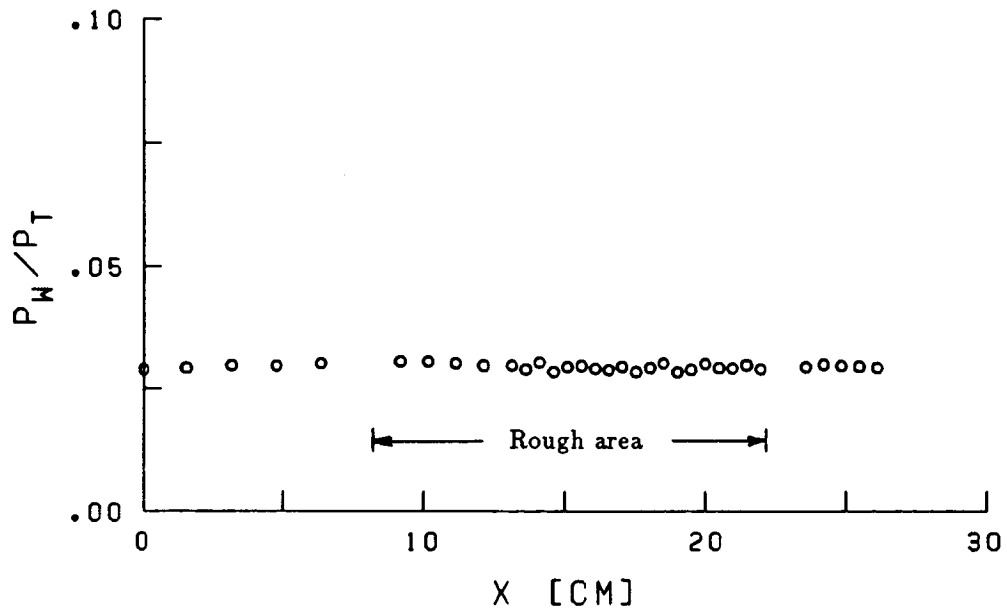
d) Velocity profiles non-dimensionalized
with local conditions

Fig. 14 CONTINUED

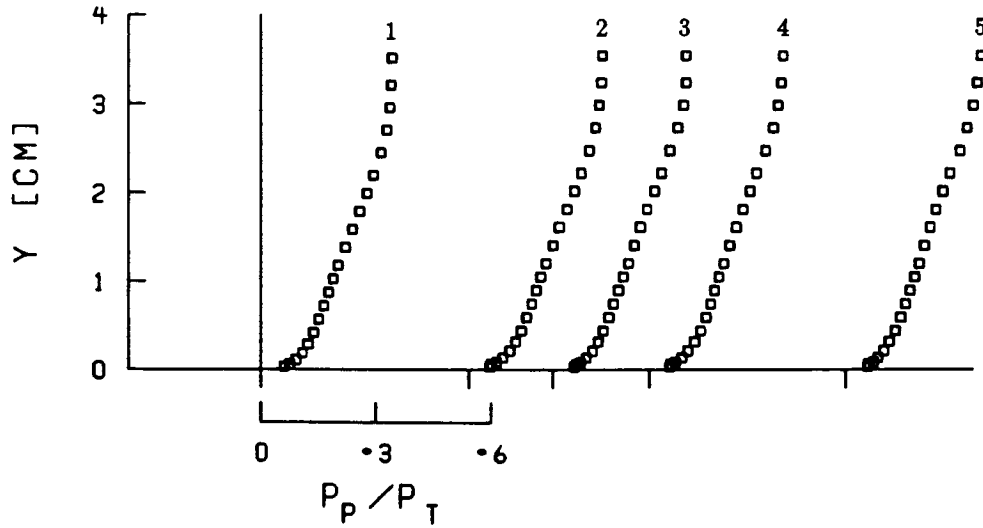


e) Boundary layer parameters

Fig. 14 CONCLUDED

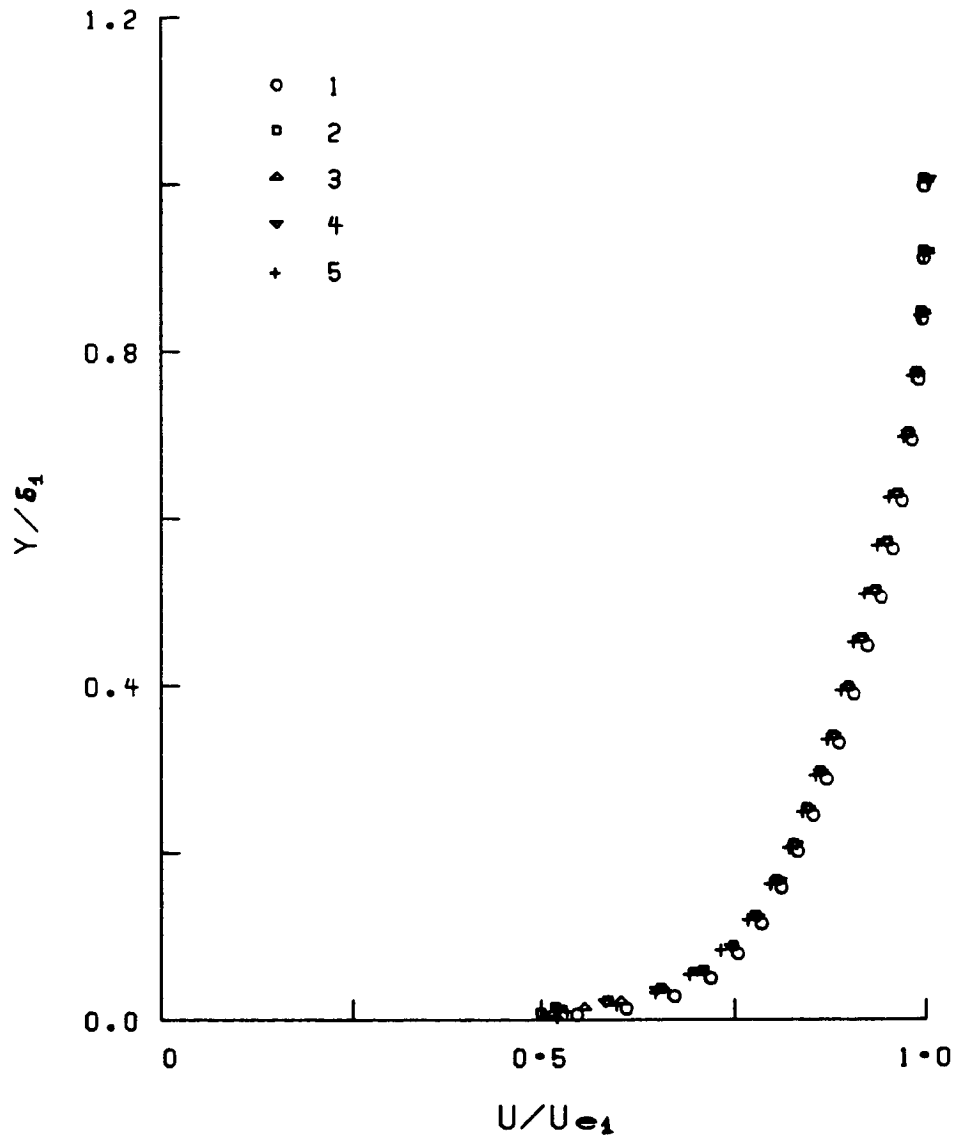


a) Wall pressure distribution



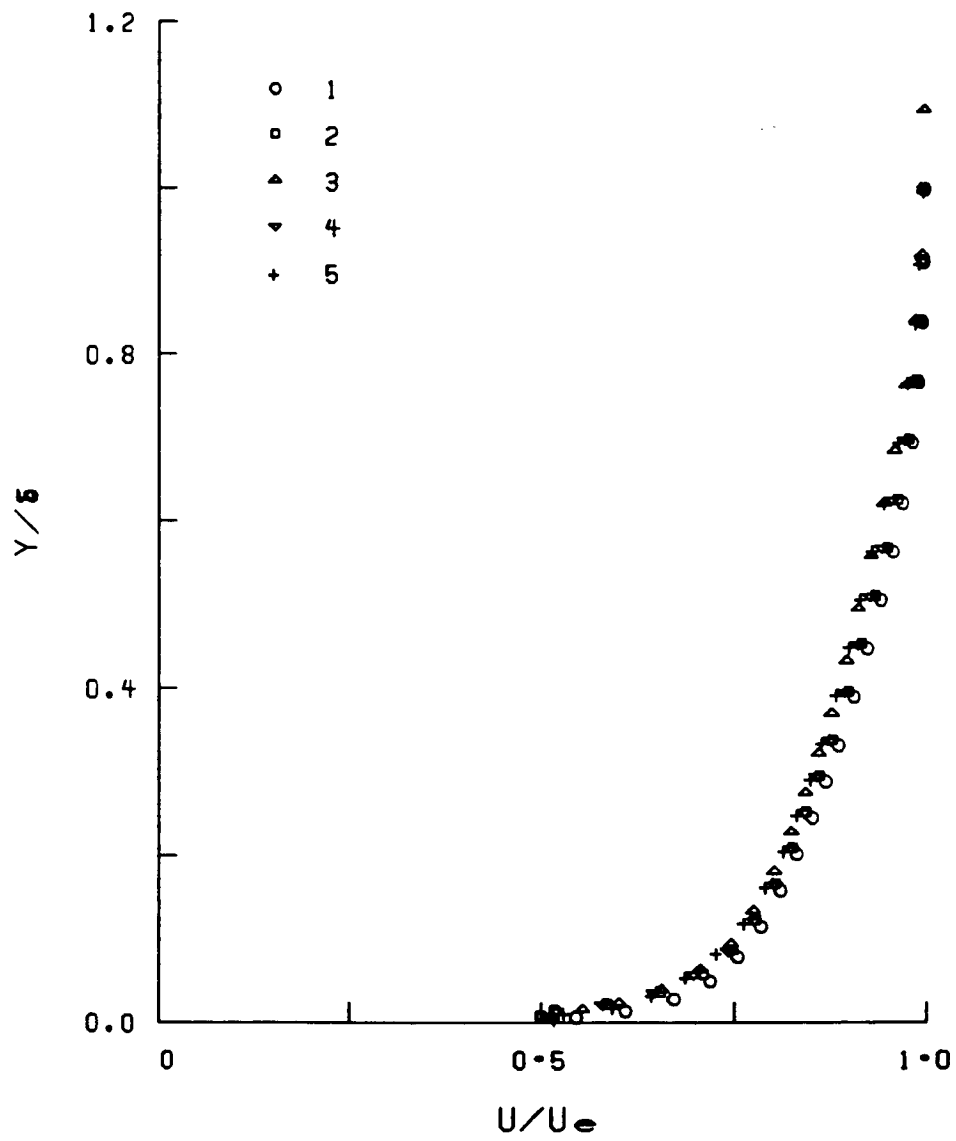
b) Pitot pressure profiles

Fig. 15 MEASUREMENTS ON ROUGH PLATE
AT $M = 3.0$ AND $\alpha = 0^\circ$



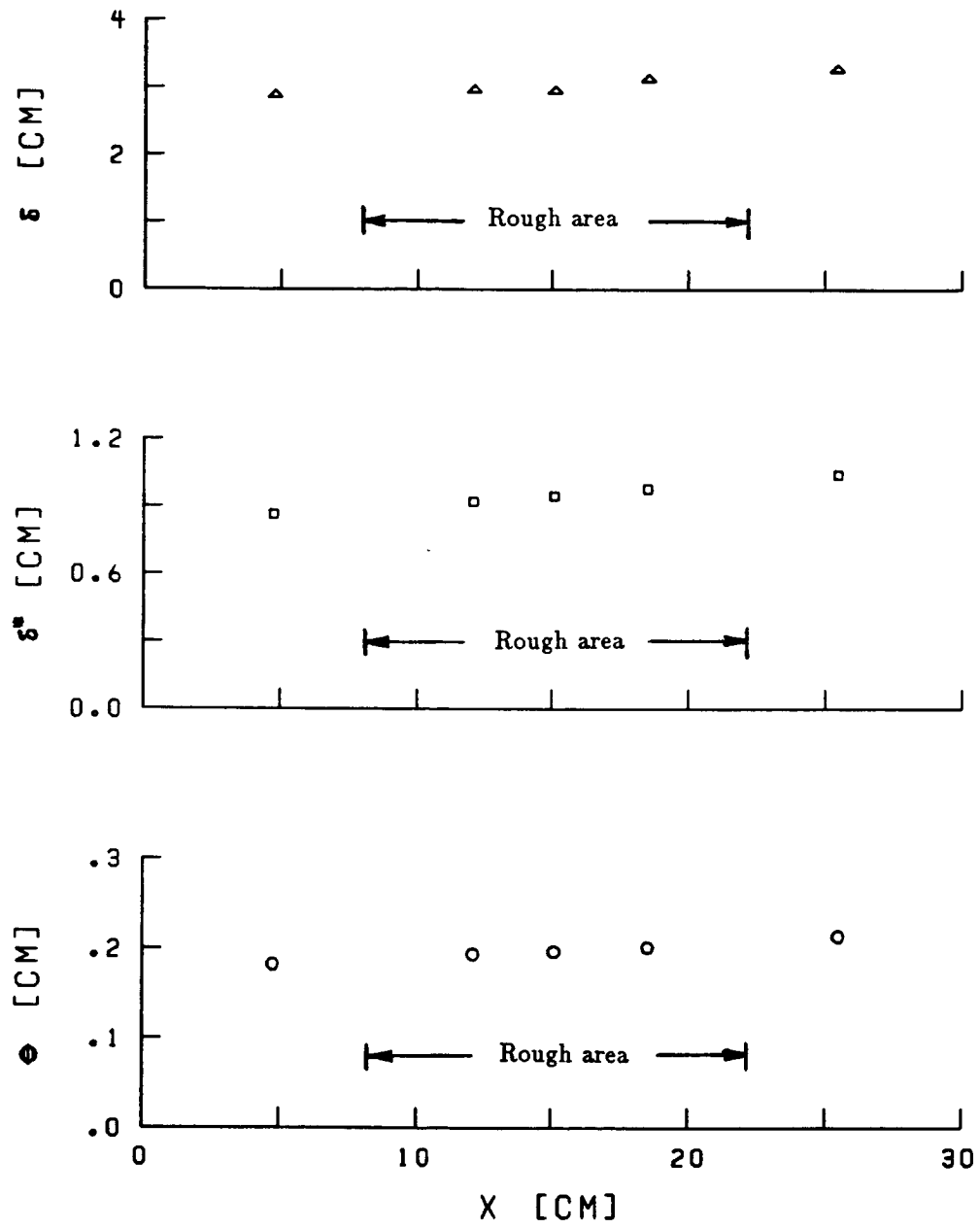
c) Velocity profiles non-dimensionalized
with conditions of first profile

Fig. 15 CONTINUED



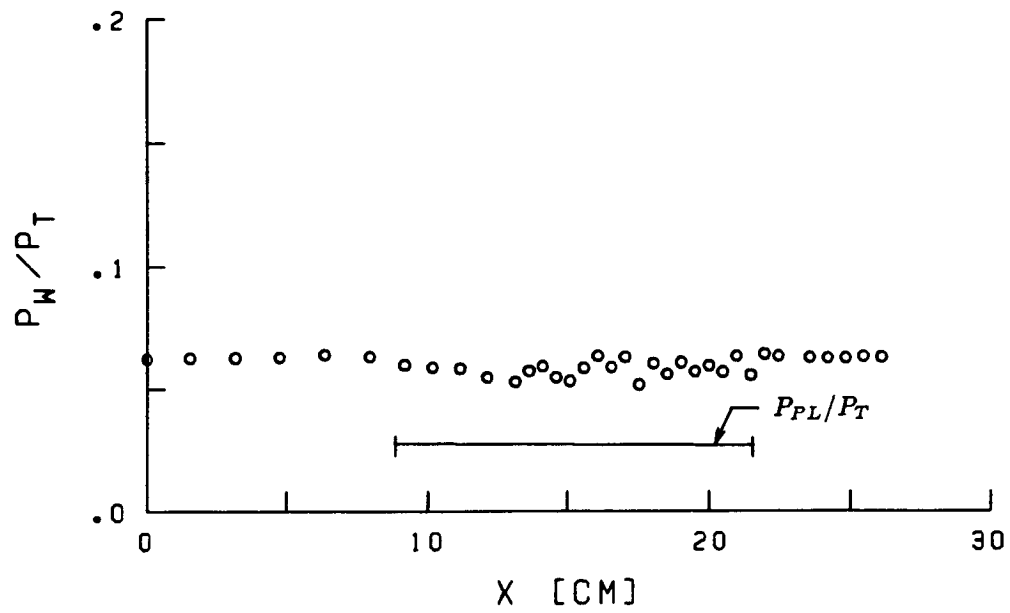
d) Velocity profiles non-dimensionalized
with local conditions

Fig. 15 CONTINUED

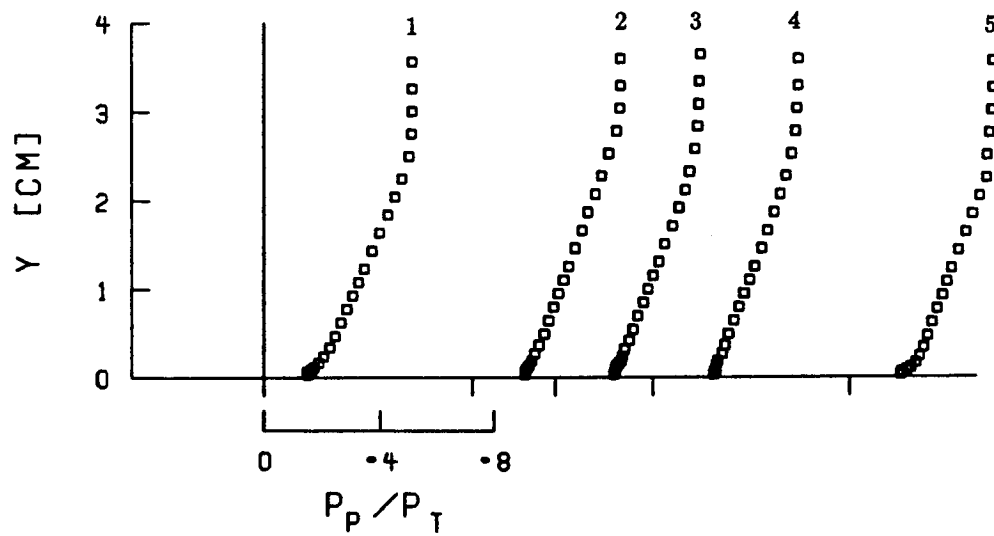


e) Boundary layer parameters

Fig. 15 CONCLUDED

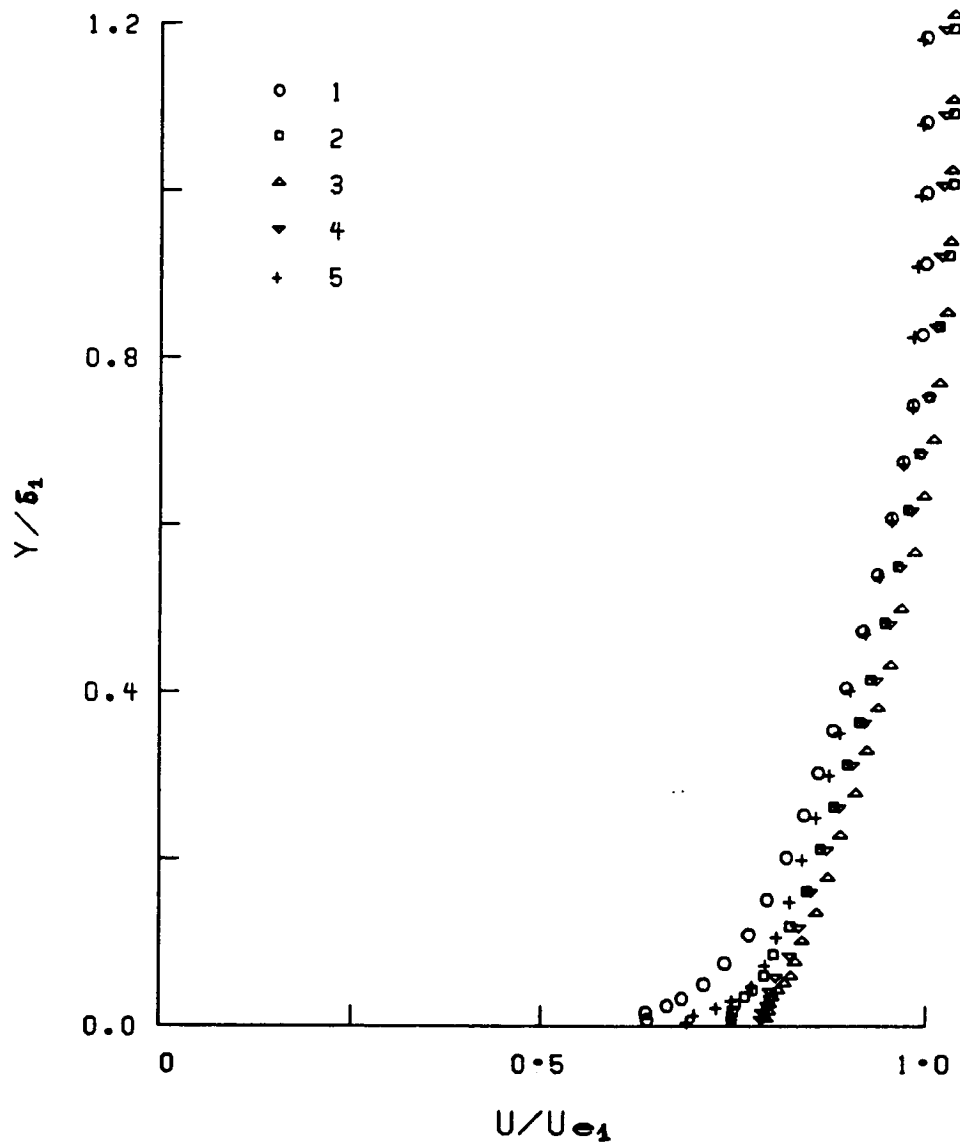


a) Wall pressure distribution



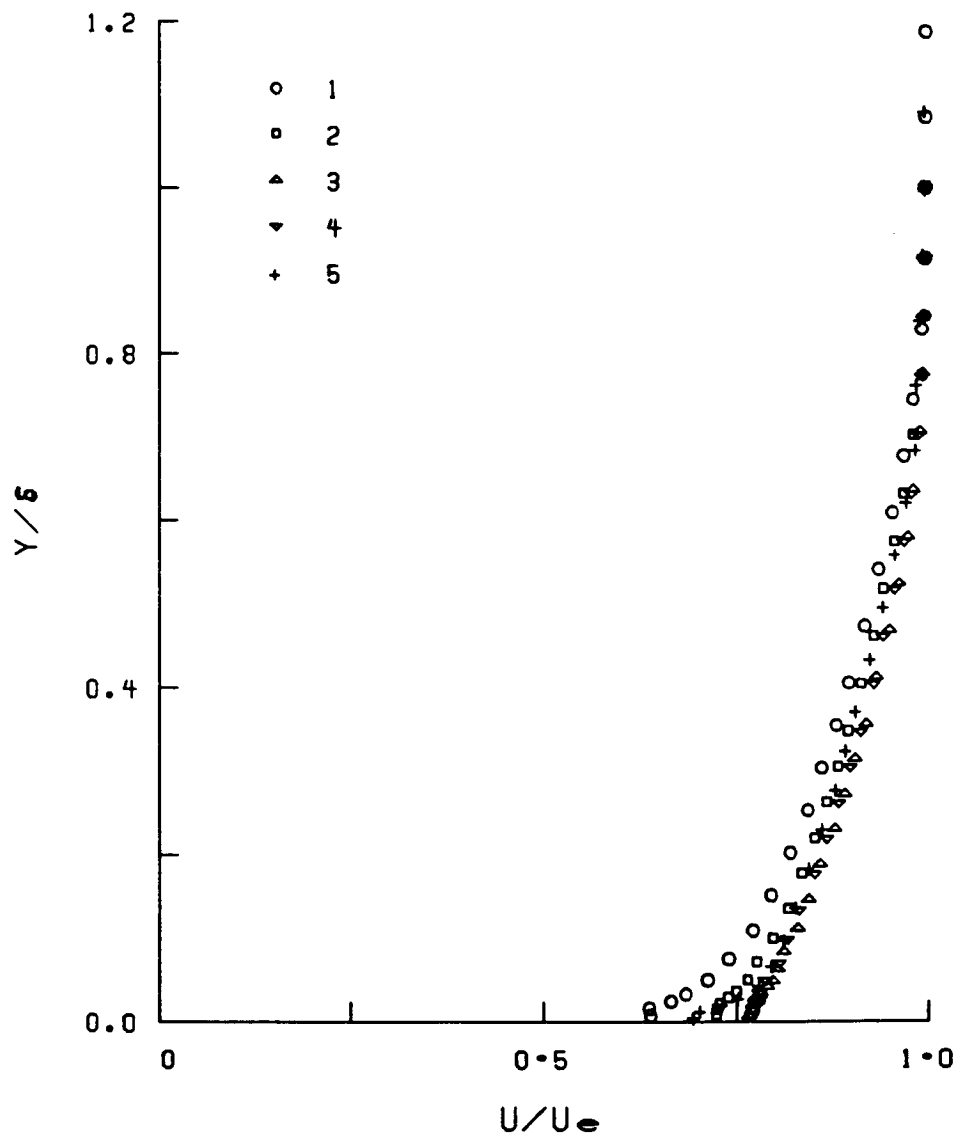
b) Pitot pressure profiles

Fig. 16 MEASUREMENTS ON POROUS PLATE
AT $M = 2.5$ AND $\alpha = 0^\circ$



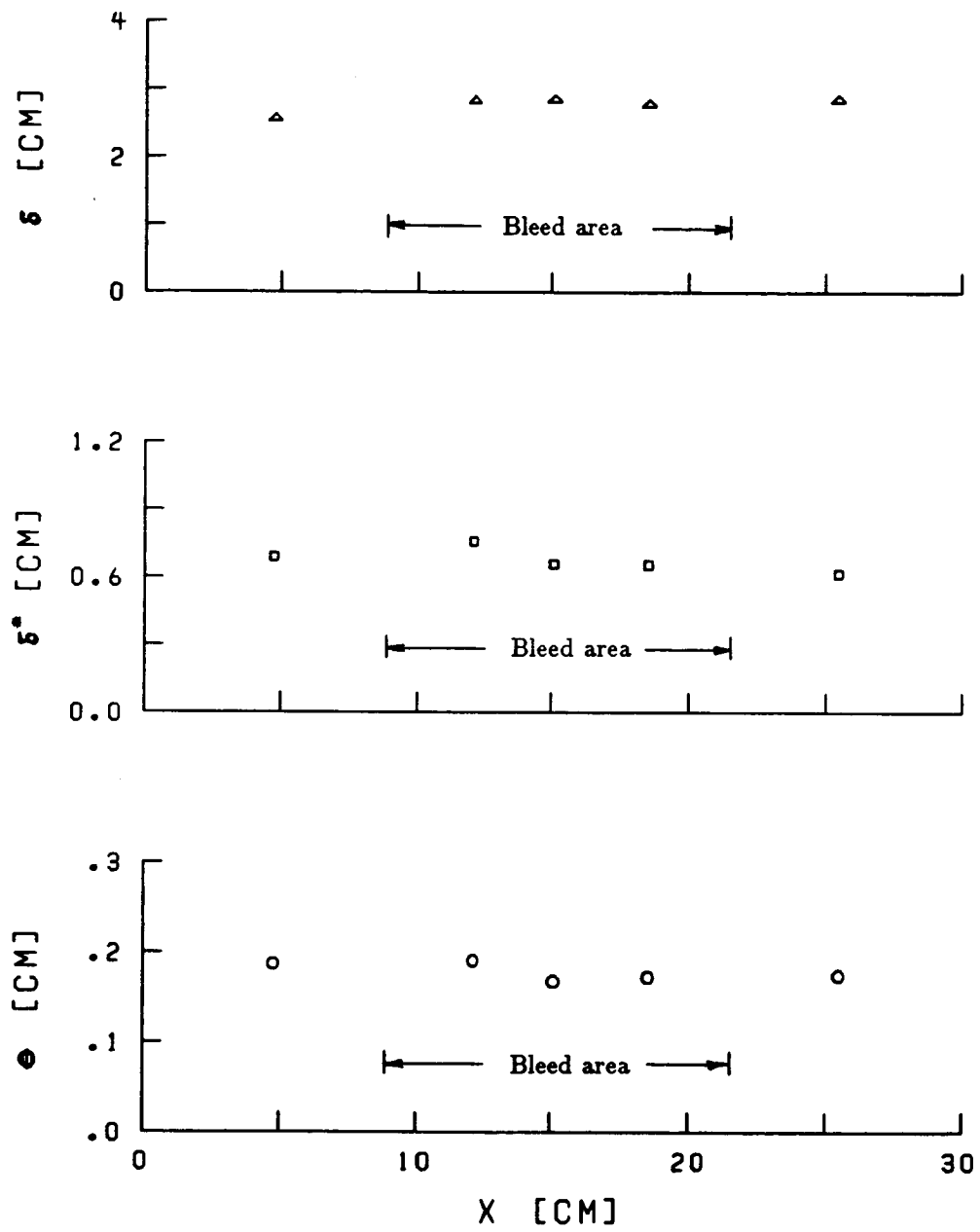
c) Velocity profiles non-dimensionalized
with conditions of first profile

Fig. 16 CONTINUED



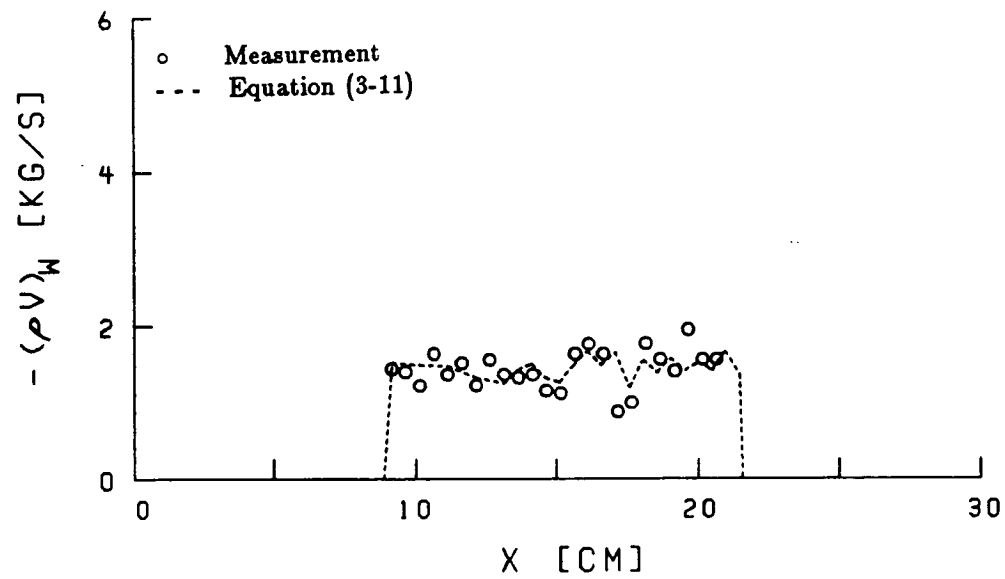
d) Velocity profiles non-dimensionalized
with local conditions

Fig. 16 CONTINUED

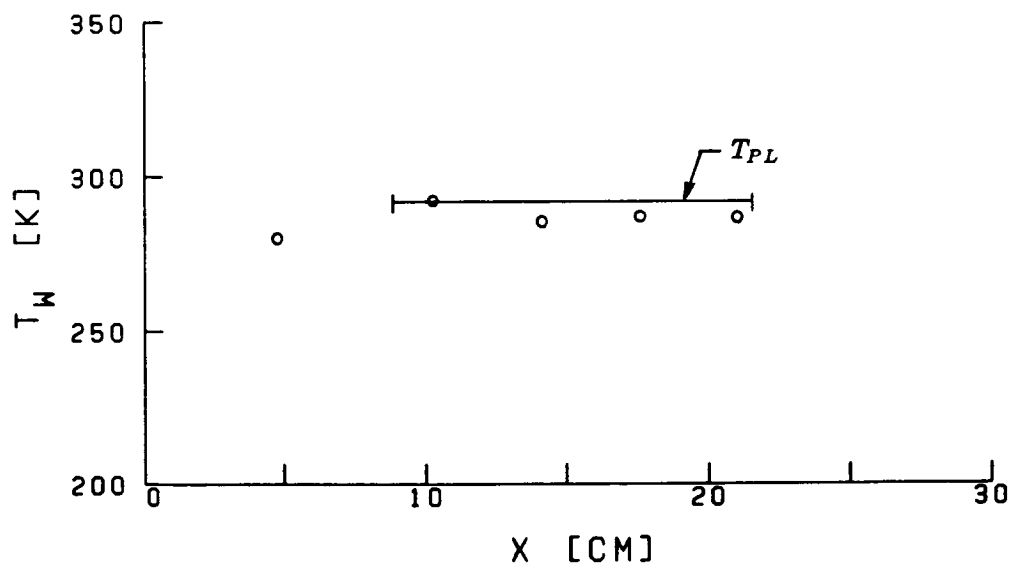


e) Boundary layer parameters

Fig. 16 CONTINUED

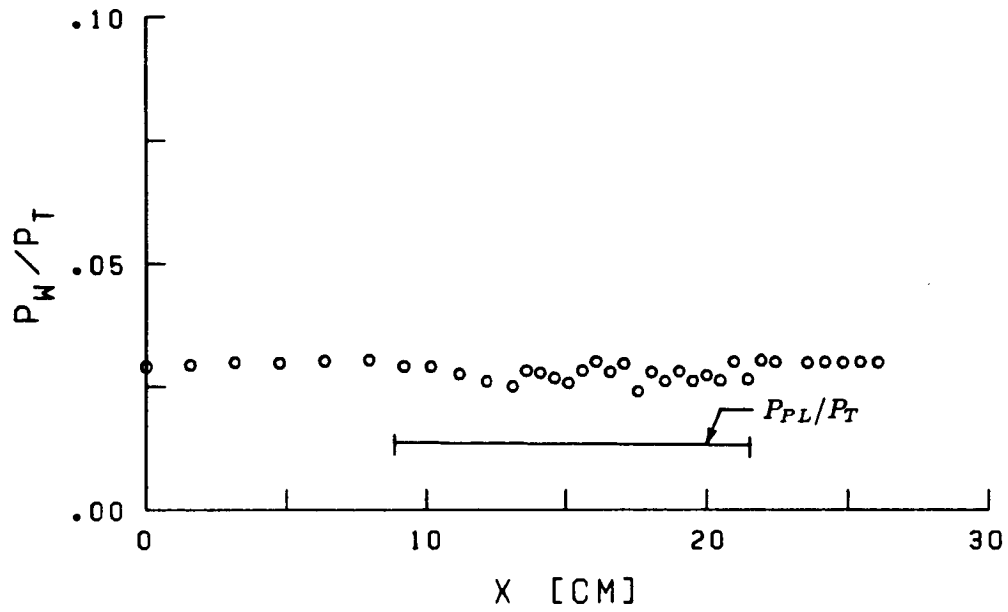


f) Bleed distribution

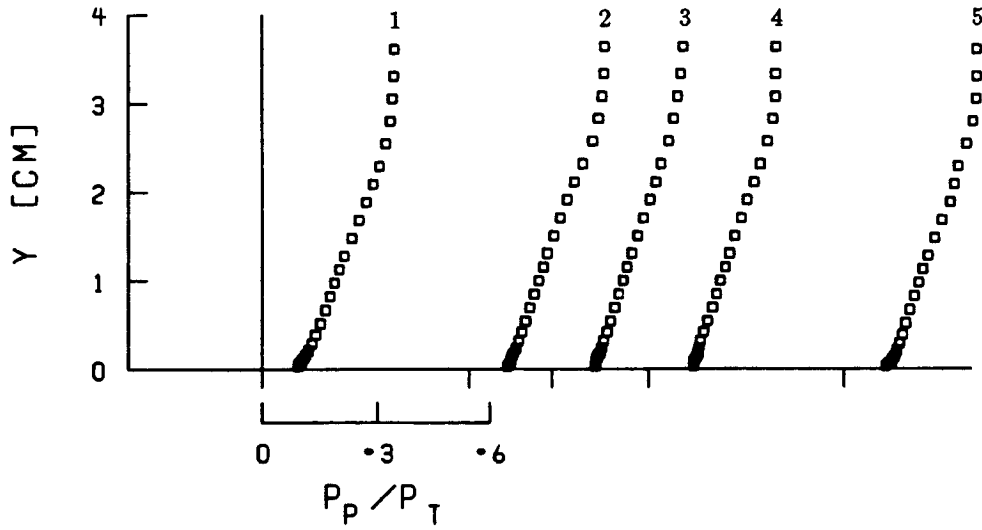


g) Wall temperature

Fig. 16 CONCLUDED

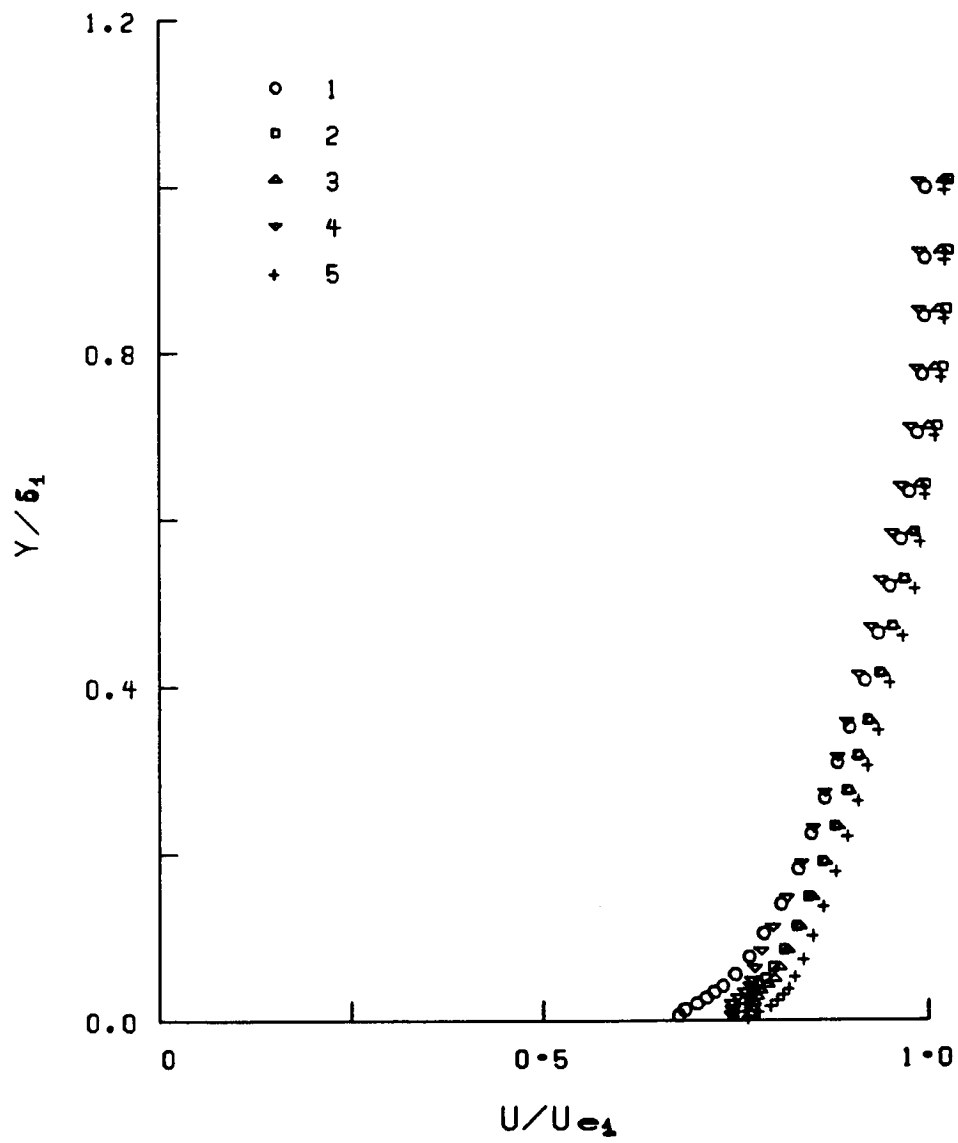


a) Wall pressure distribution



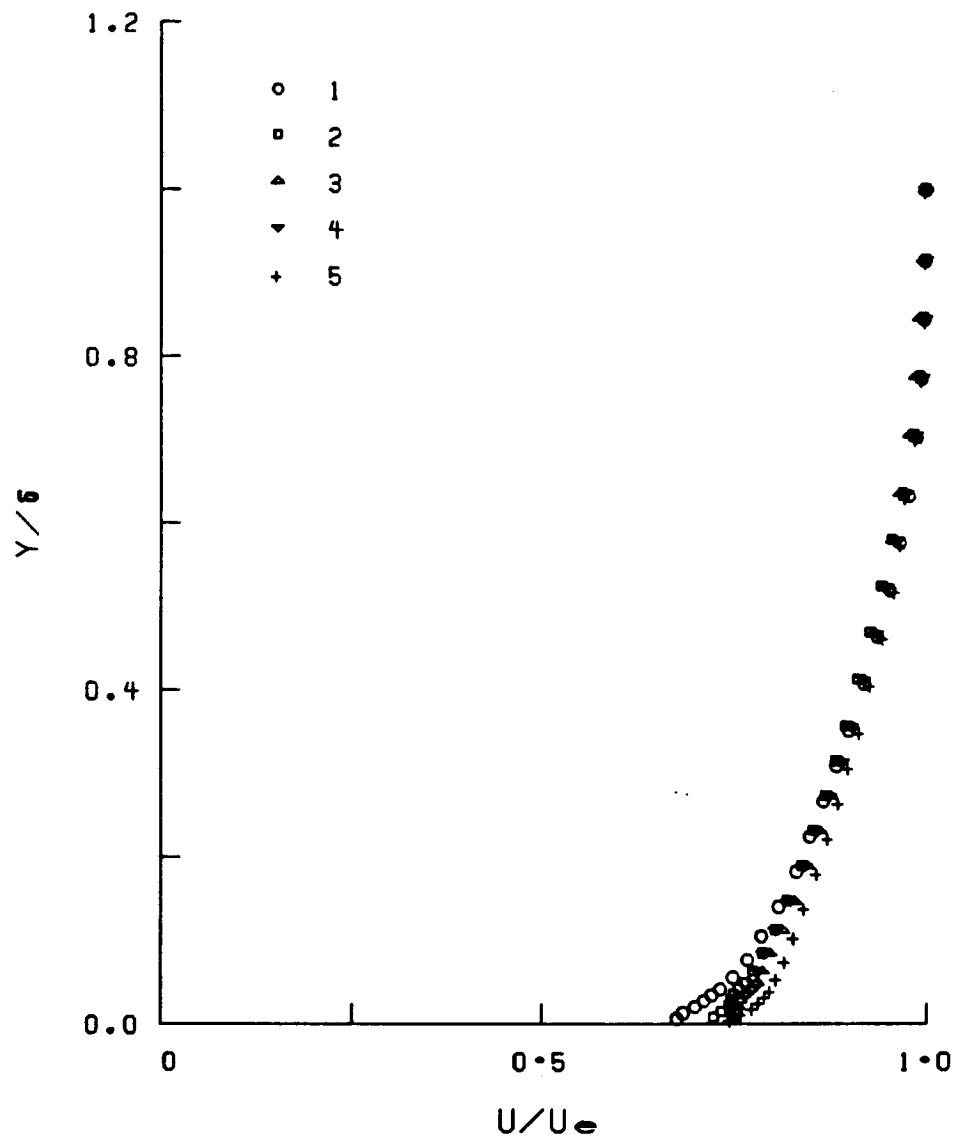
b) Pitot pressure profiles

Fig. 17 MEASUREMENTS ON POROUS PLATE
AT $M = 3.0$ AND $\alpha = 0^\circ$



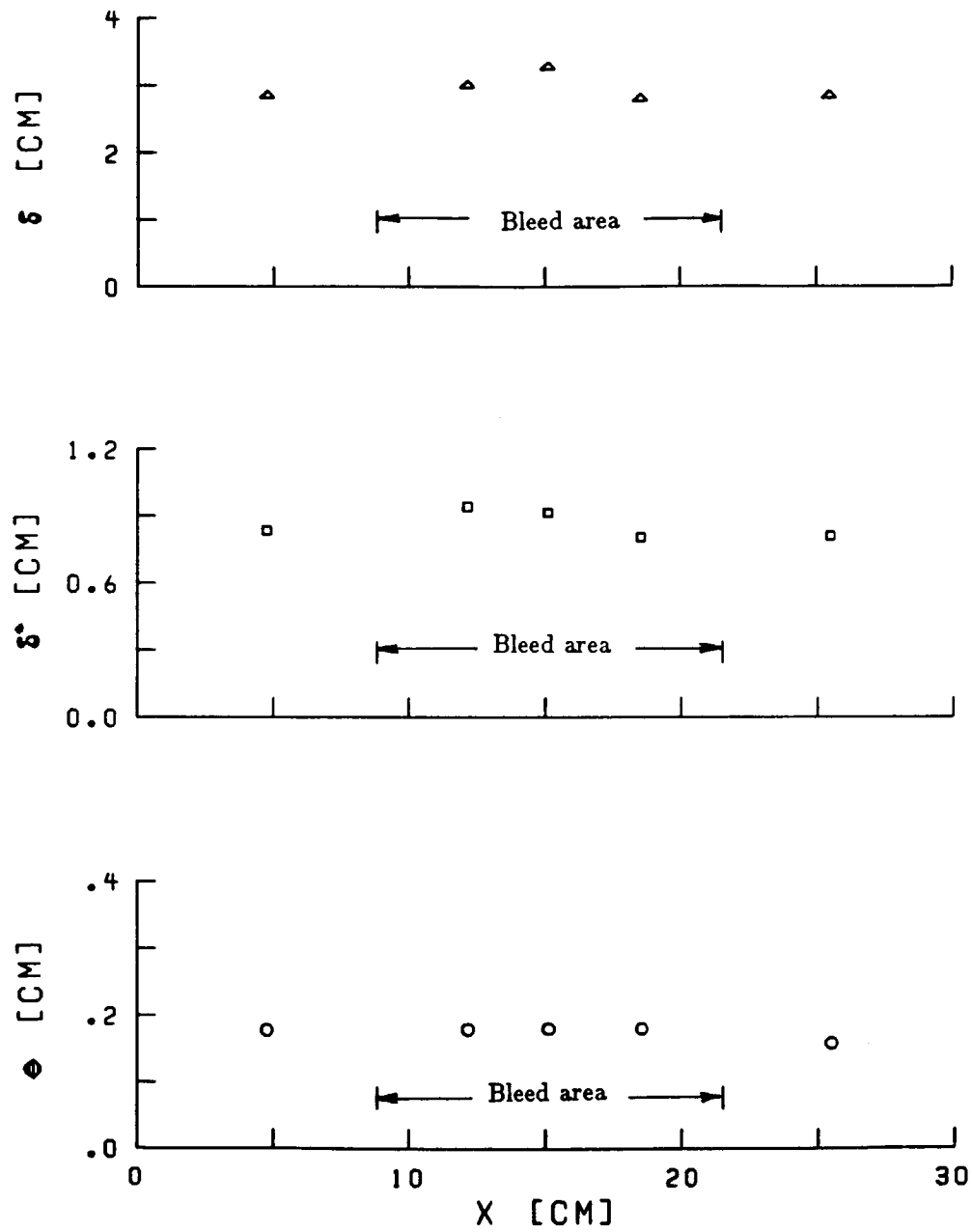
c) Velocity profiles non-dimensionalized
with conditions of first profile

Fig. 17 CONTINUED



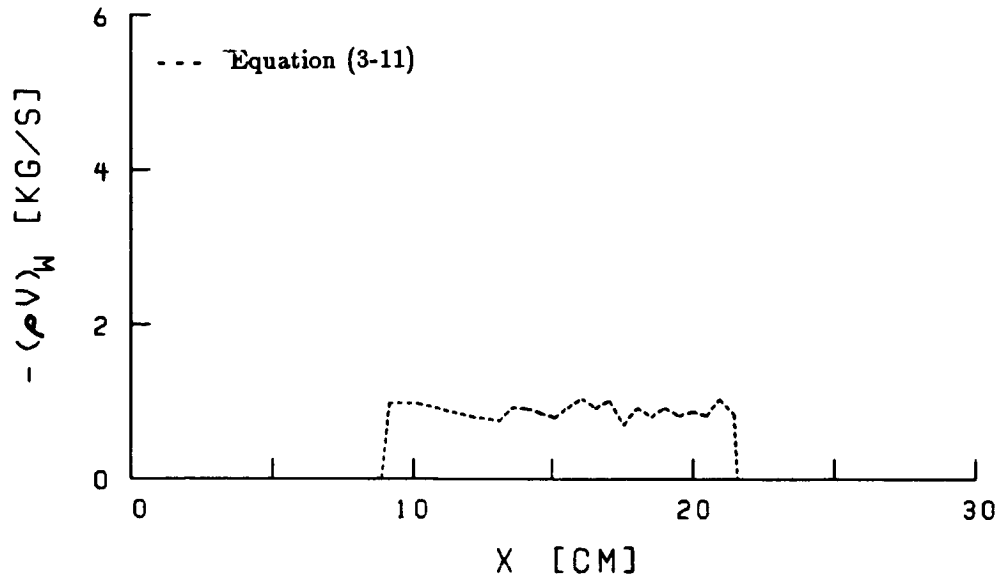
d) Velocity profiles non-dimensionalized
with local conditions

Fig. 17 CONTINUED

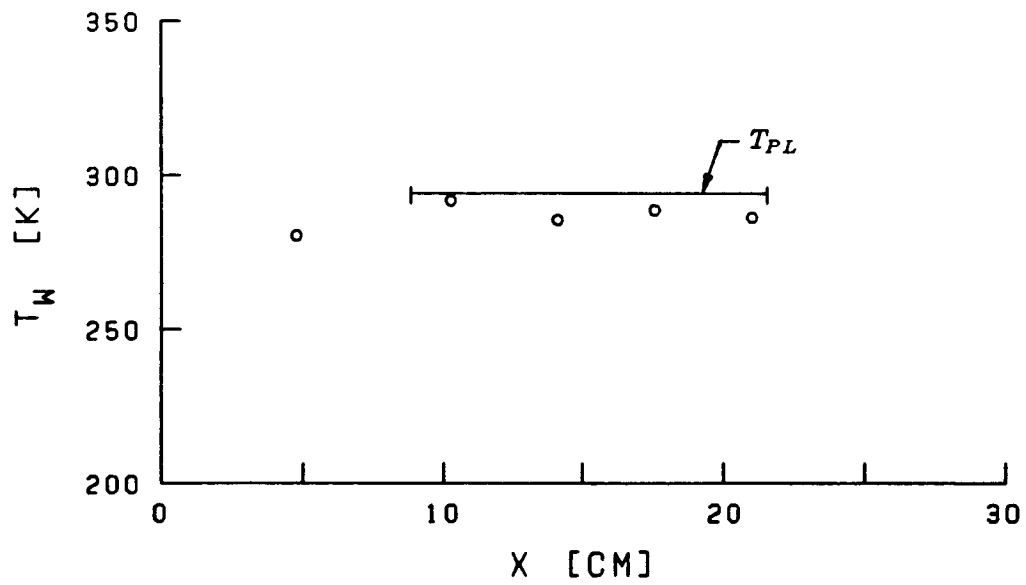


e) Boundary layer parameters

Fig. 17 CONTINUED

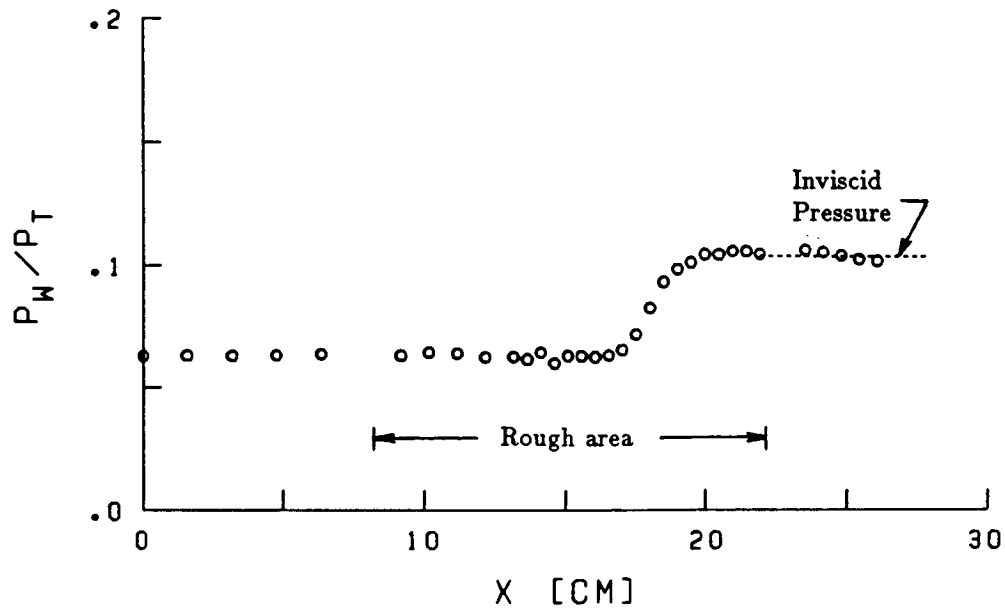


f) Bleed distribution

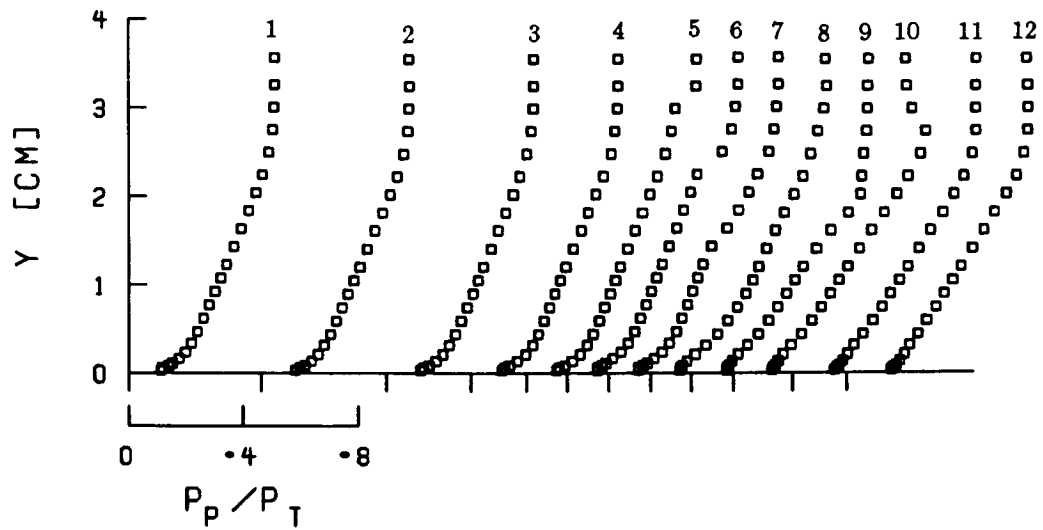


g) Wall temperature

Fig. 17 CONCLUDED



a) Wall pressure distribution



b) Pitot pressure profiles

Fig. 18 MEASUREMENTS ON ROUGH PLATE
AT $M = 2.5$ AND $\alpha = 4^\circ$

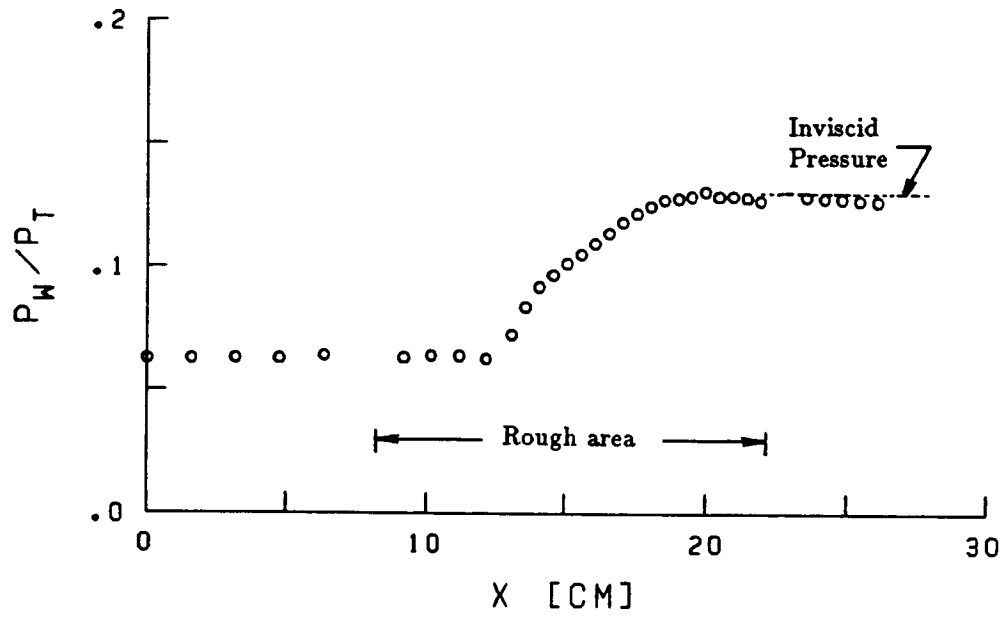


Fig. 19 MEASUREMENTS ON ROUGH PLATE
AT $M = 2.5$ AND $\alpha = 6^\circ$

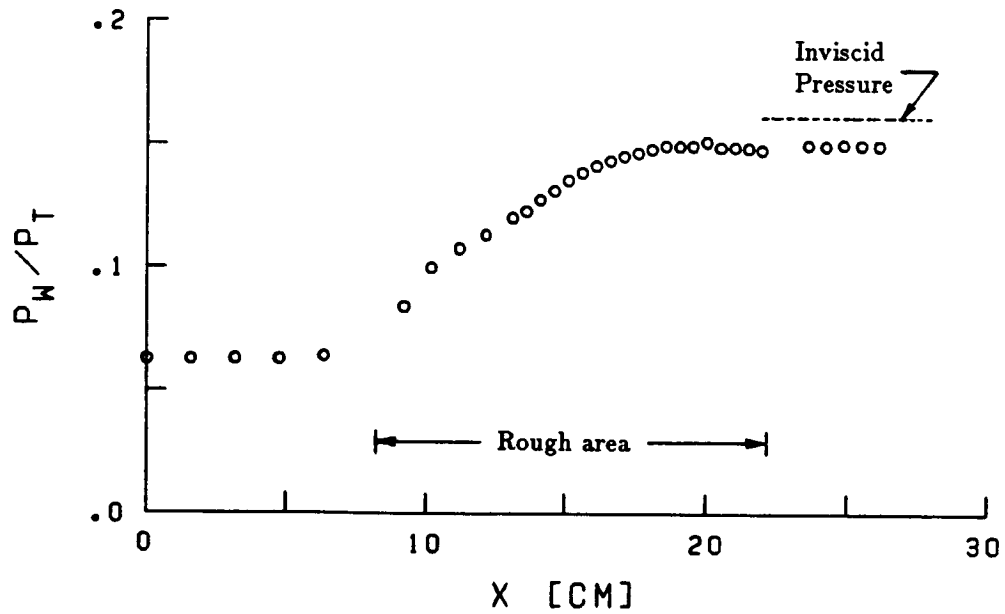
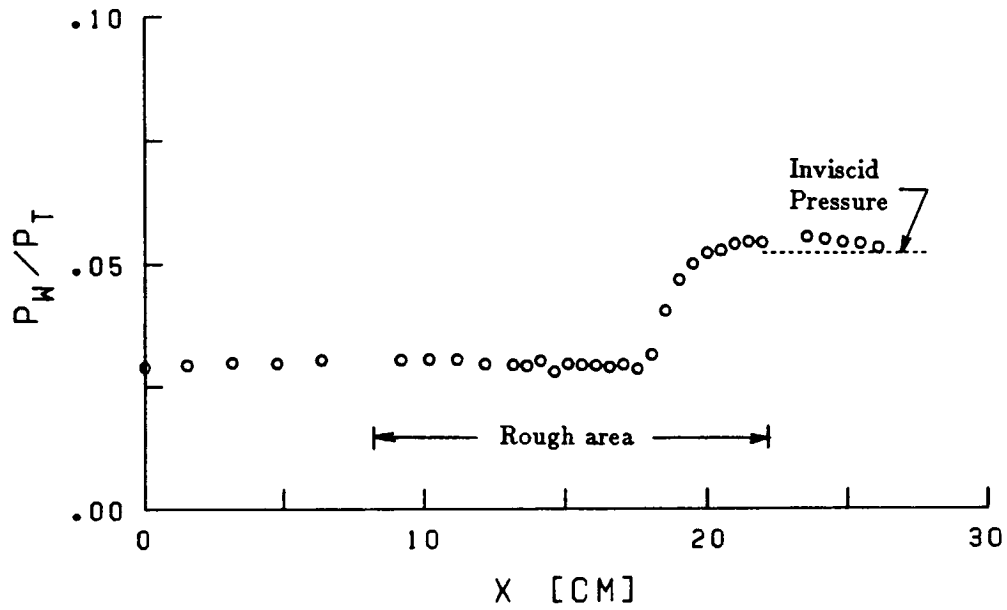
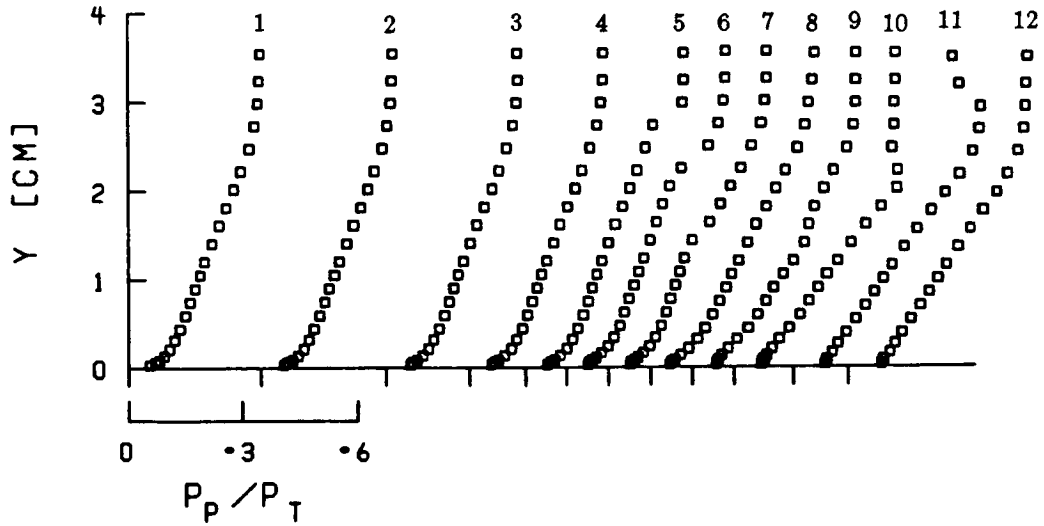


Fig. 20 MEASUREMENTS ON ROUGH PLATE
AT $M = 2.5$ AND $\alpha = 8^\circ$



a) Wall pressure distribution



b) Pitot pressure profiles

Fig. 21 MEASUREMENTS ON ROUGH PLATE
AT $M = 3.0$ AND $\alpha = 4^\circ$

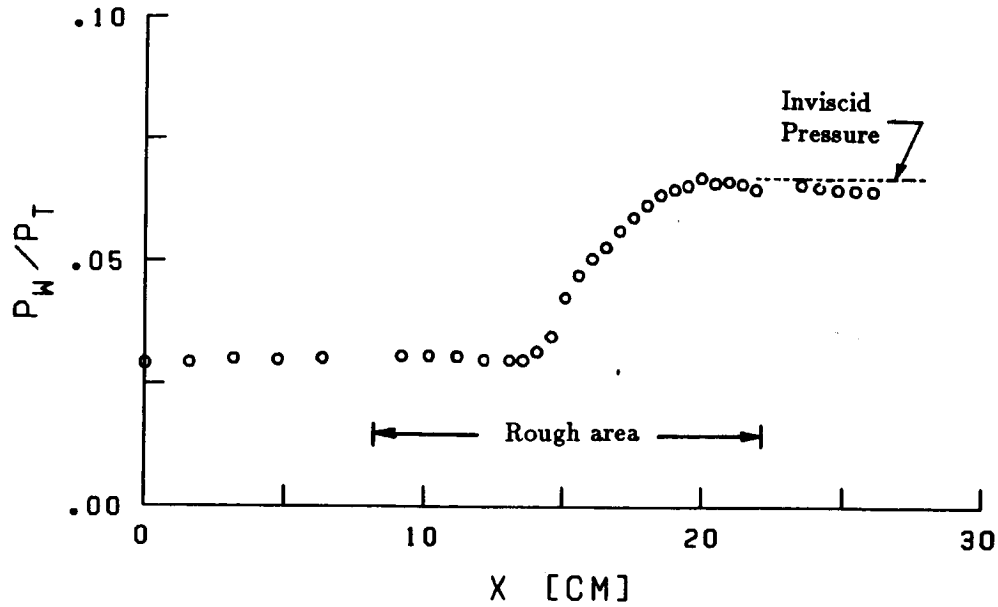


Fig. 22 MEASUREMENTS ON ROUGH PLATE
AT $M = 3.0$ AND $\alpha = 6^\circ$

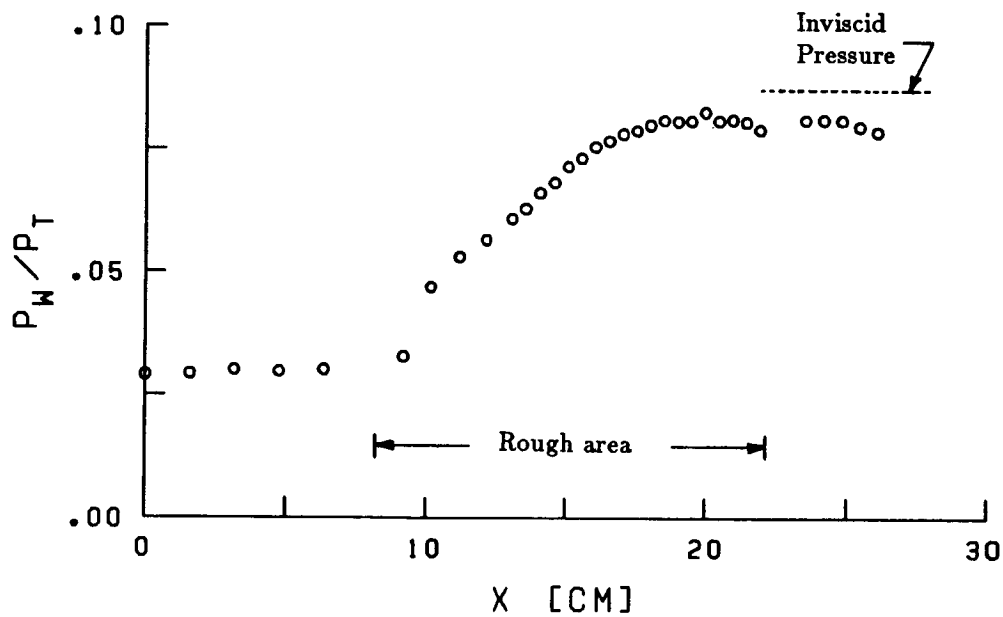


Fig. 23 MEASUREMENTS ON ROUGH PLATE
AT $M = 3.0$ AND $\alpha = 8^\circ$

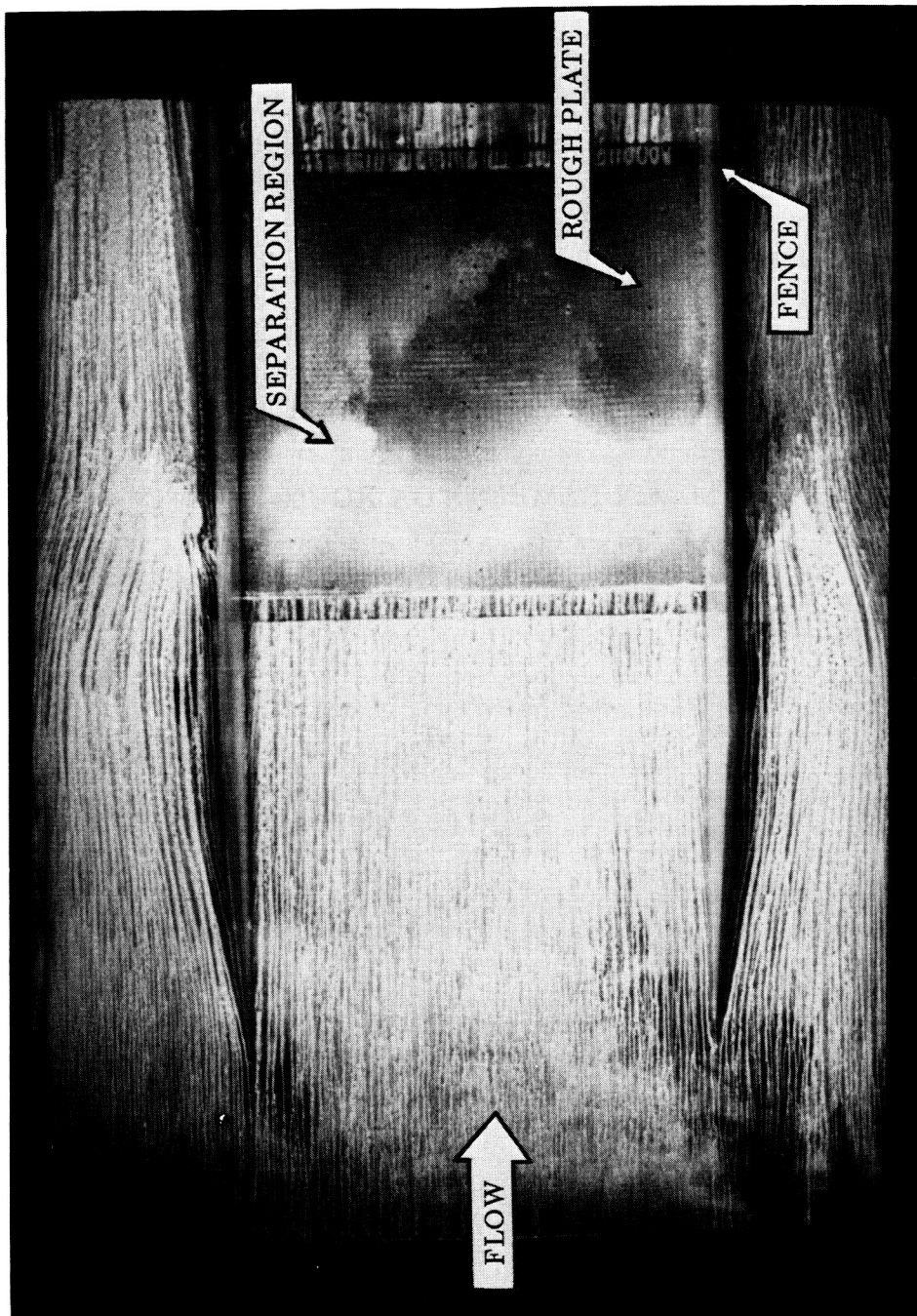
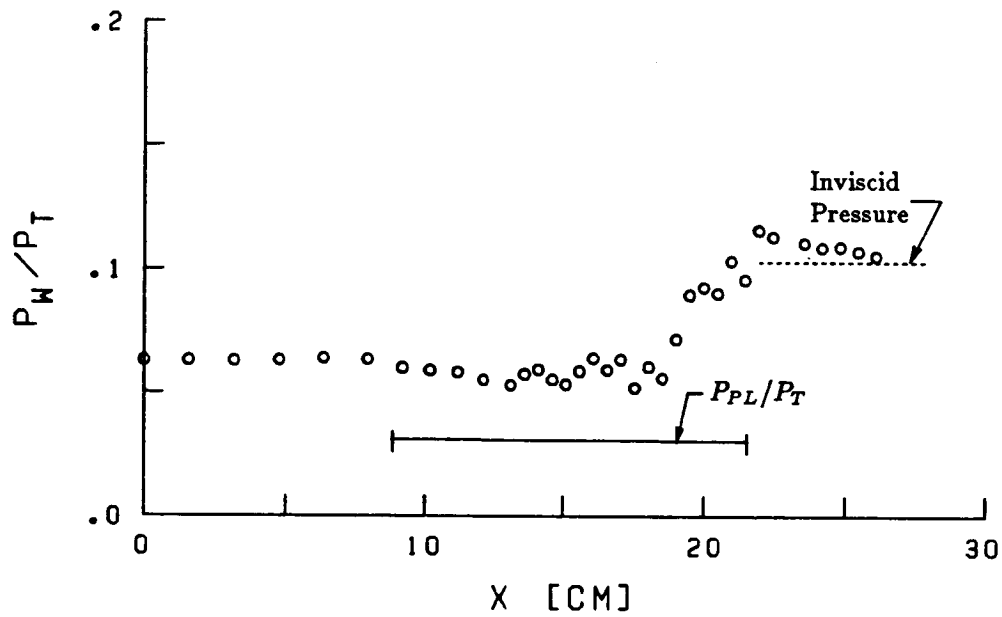
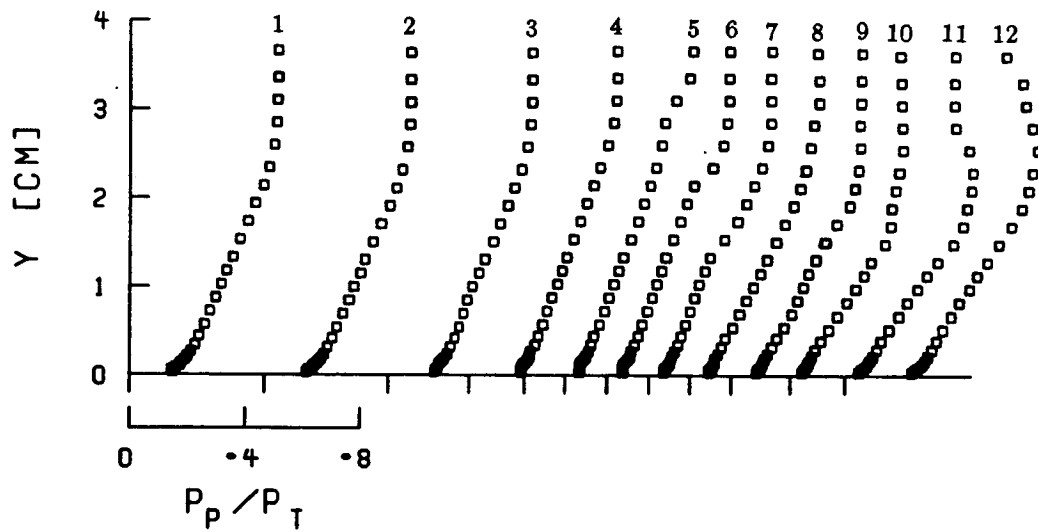


Fig. 24 OIL FLOW VISUALIZATION ON ROUGH PLATE
AT $M = 3.0$ AND $\alpha = 8^\circ$

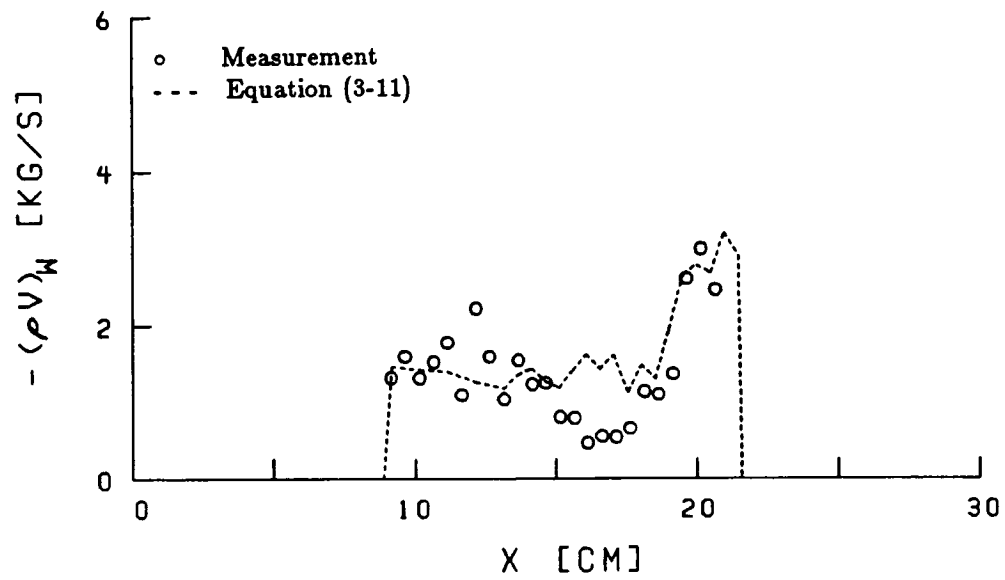


a) Wall pressure distribution

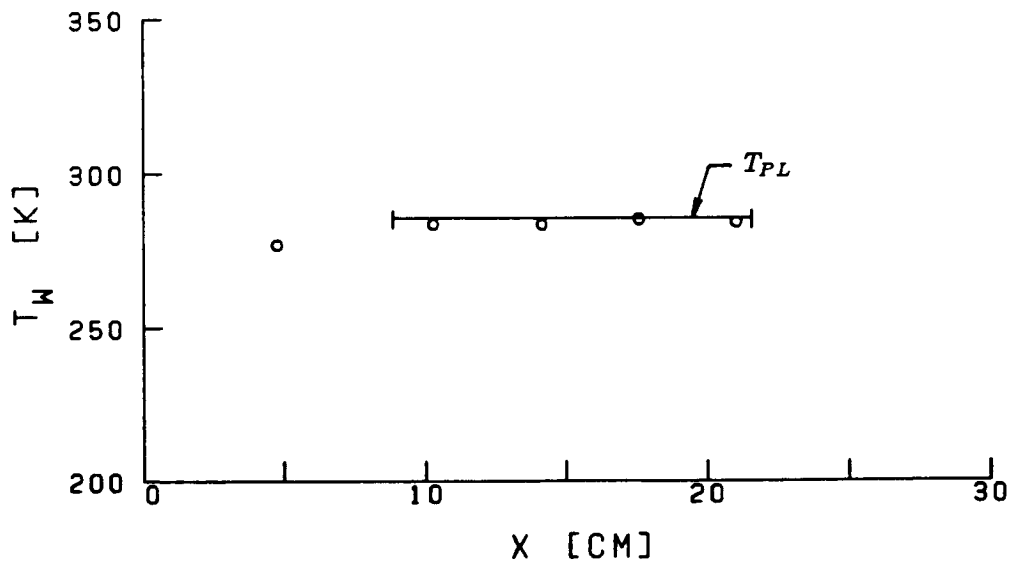


b) Pitot pressure profiles

Fig. 25 MEASUREMENTS ON POROUS PLATE
AT $M = 2.5$ AND $\alpha = 4^\circ$

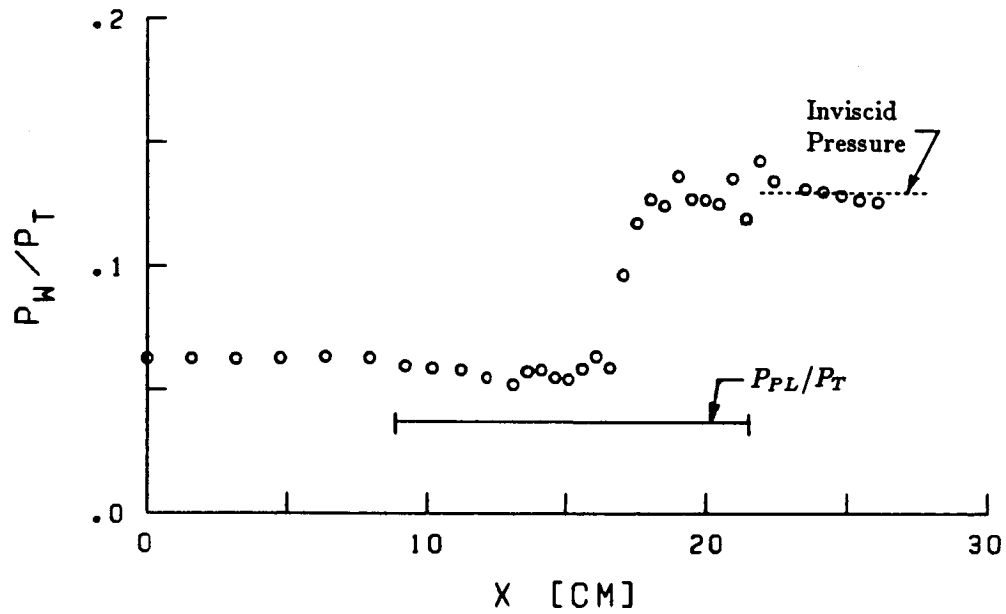


c) Bleed distribution

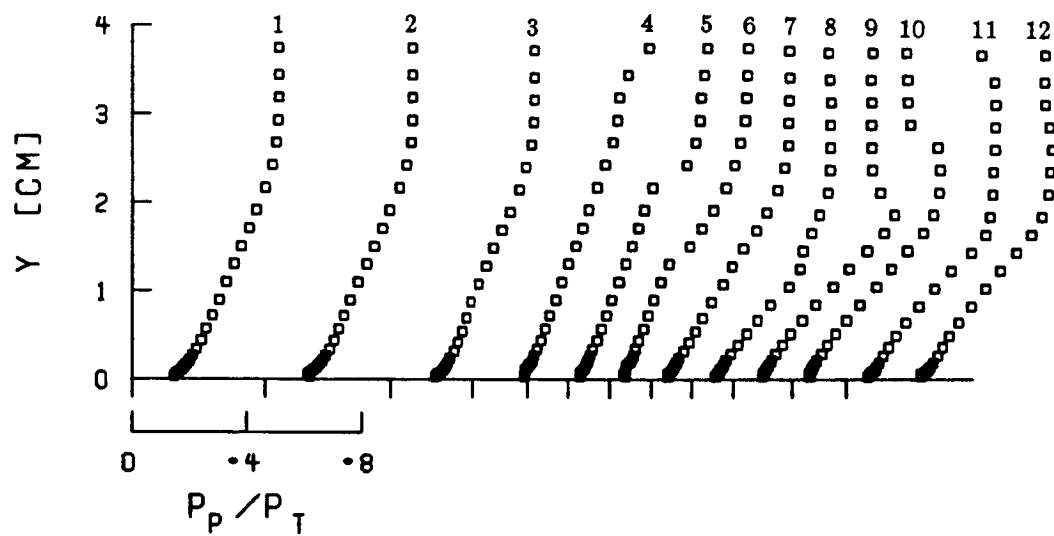


d) Wall temperature

Fig. 25 CONCLUDED

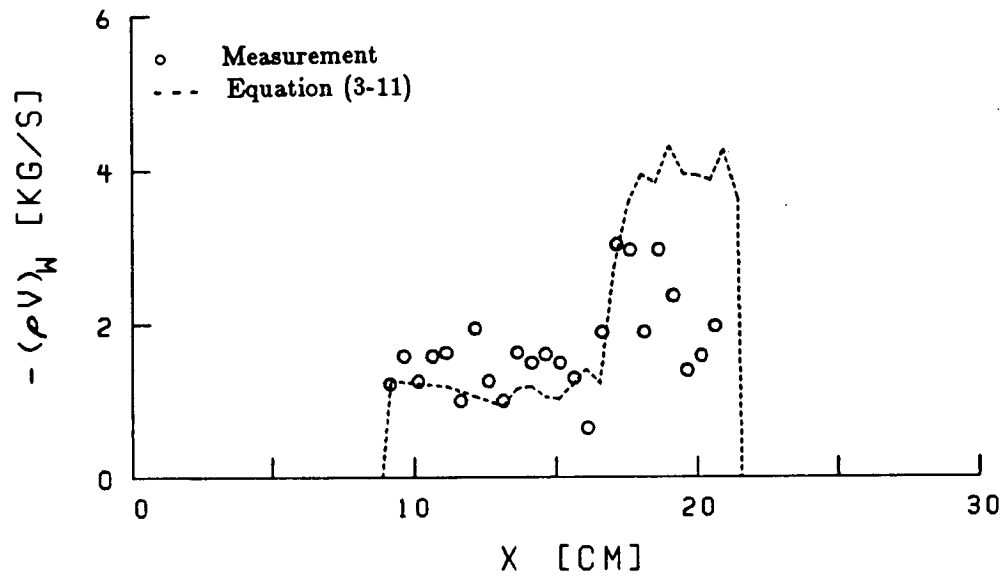


a) Wall pressure distribution

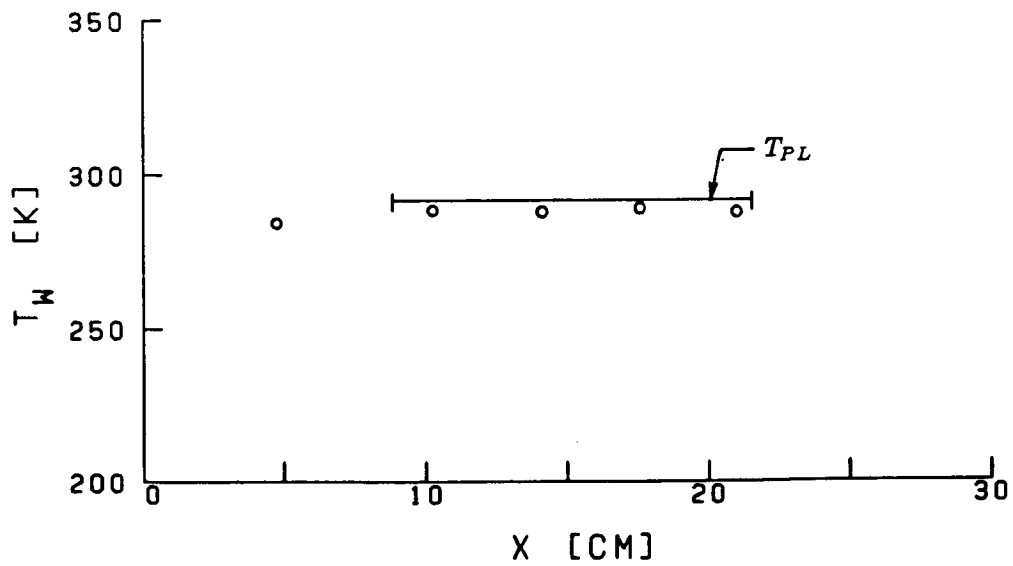


b) Pitot pressure profiles

Fig. 26 MEASUREMENTS ON POROUS PLATE
AT $M = 2.5$ AND $\alpha = 6^\circ$

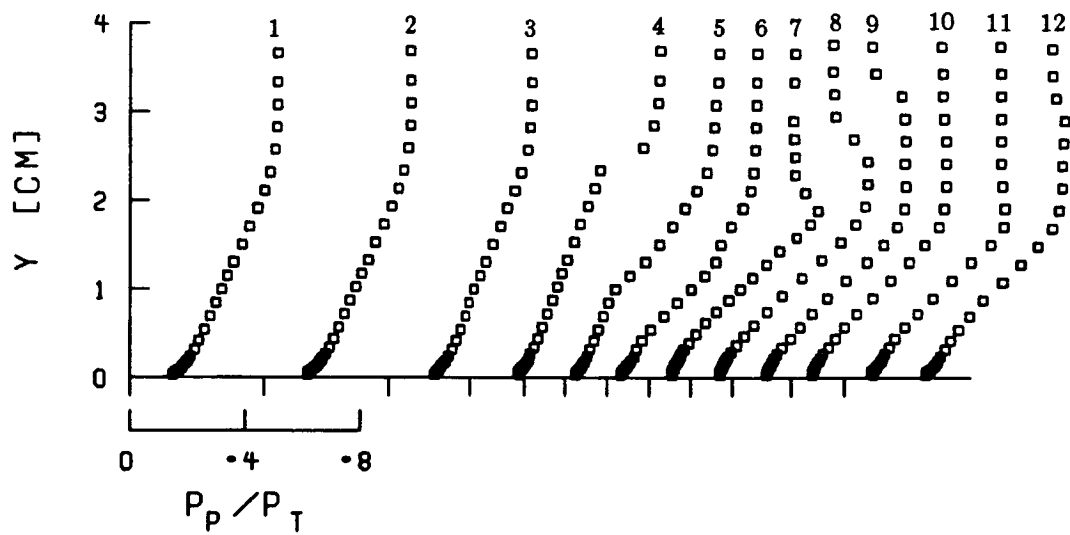
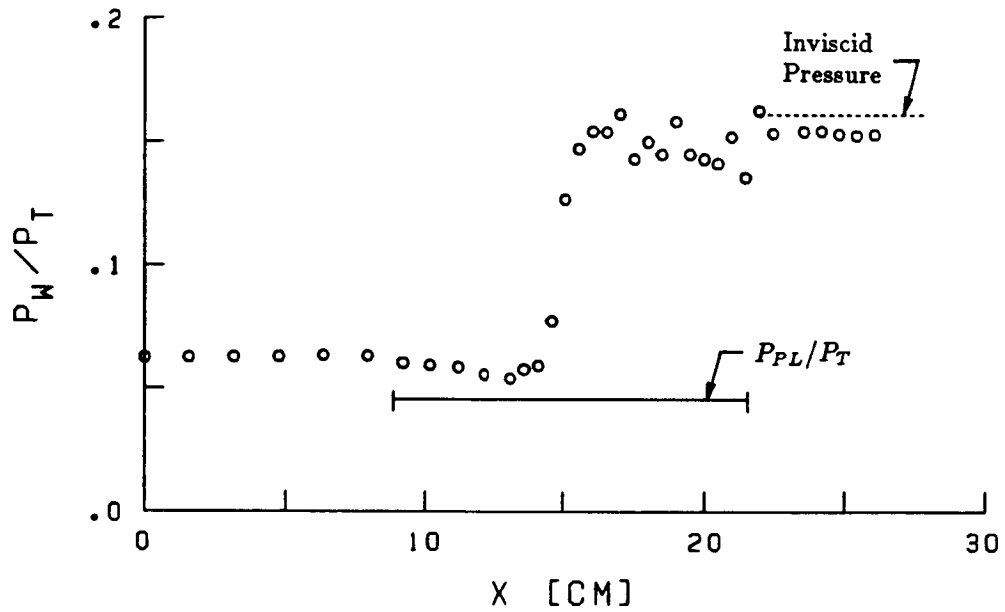


c) Bleed distribution



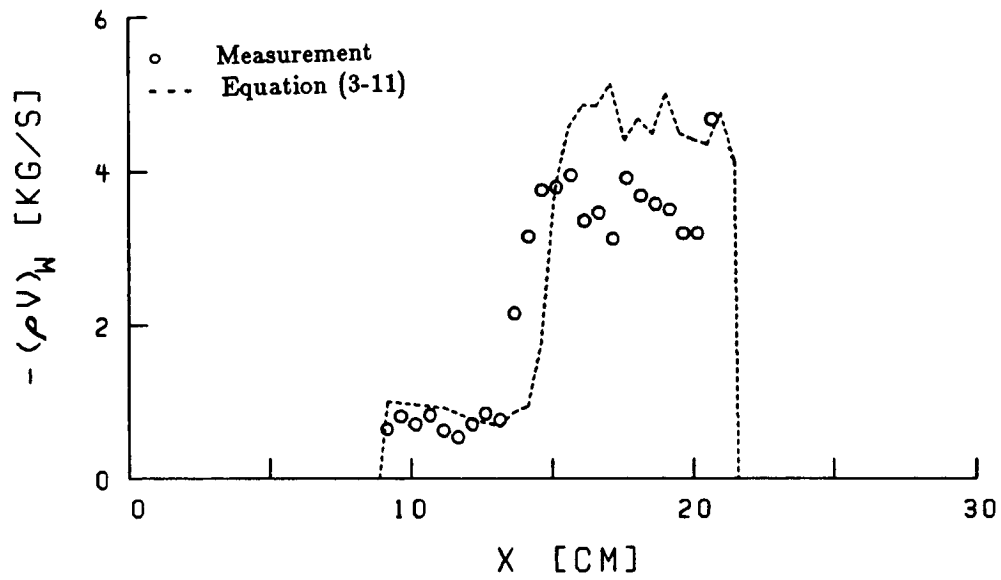
d) Wall temperature

Fig. 26 CONCLUDED

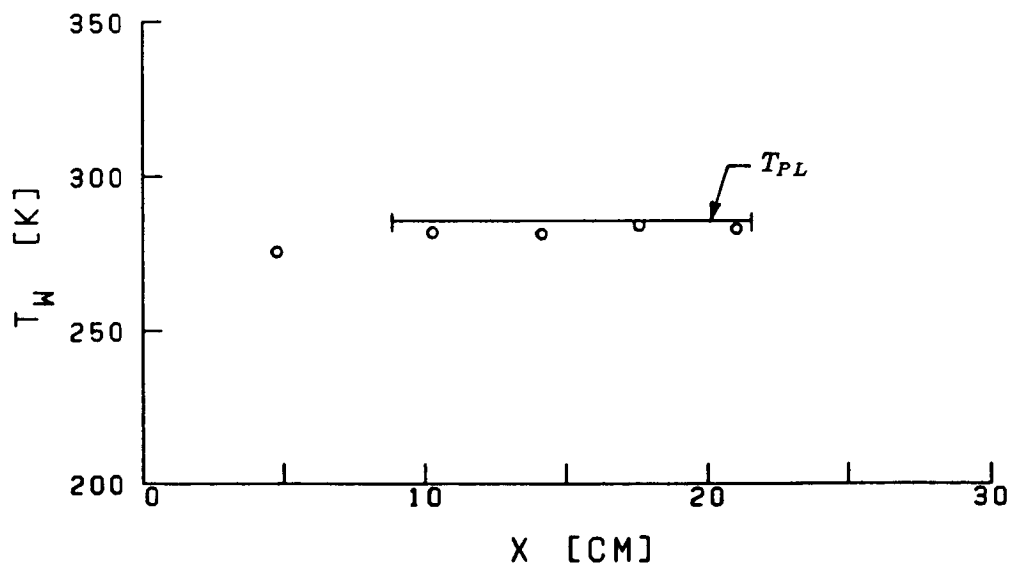


b) Pitot pressure profiles

Fig. 27 MEASUREMENTS ON POROUS PLATE
AT $M = 2.5$ AND $\alpha = 8^\circ$

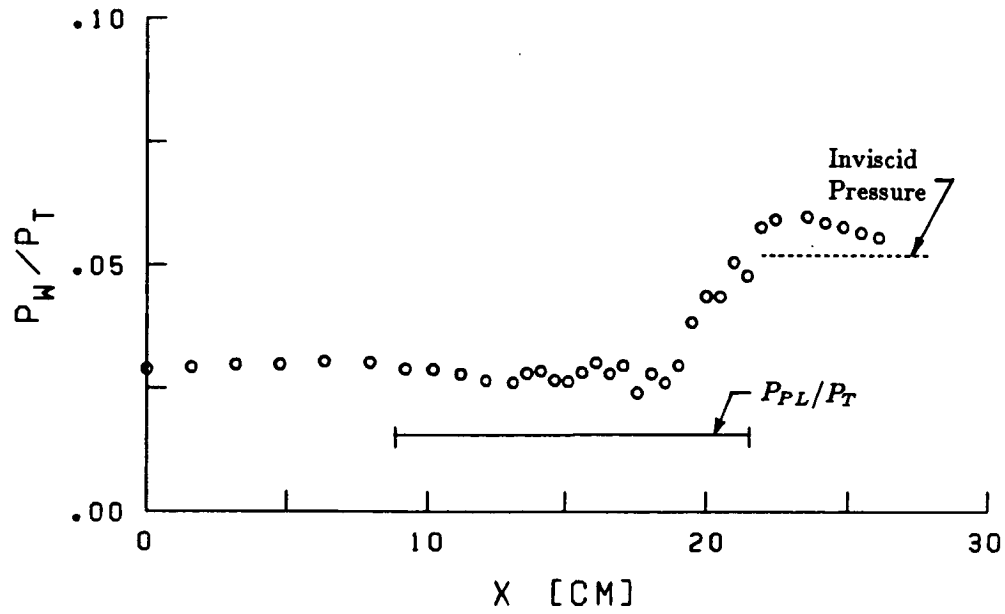


c) Bleed distribution

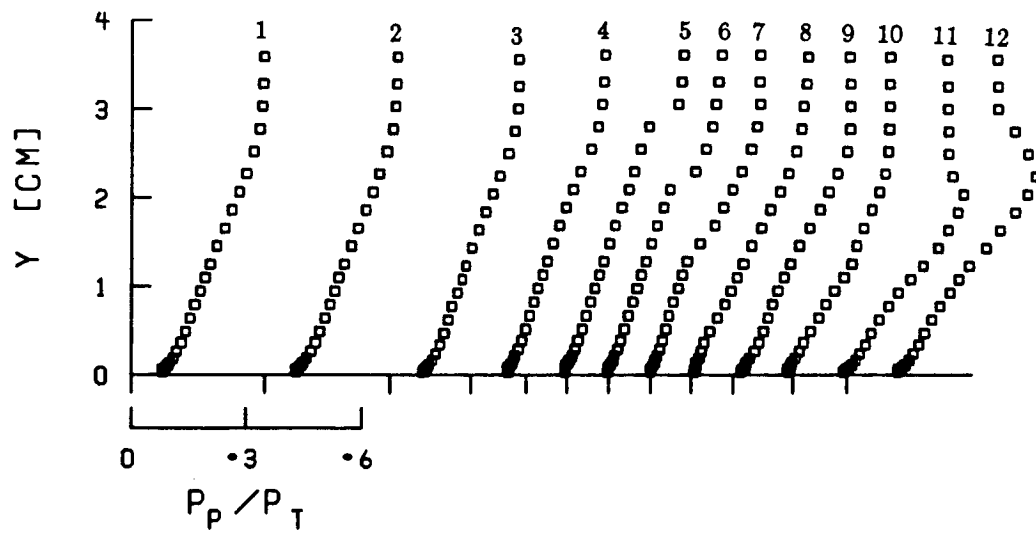


d) Wall temperature

Fig. 27 CONCLUDED

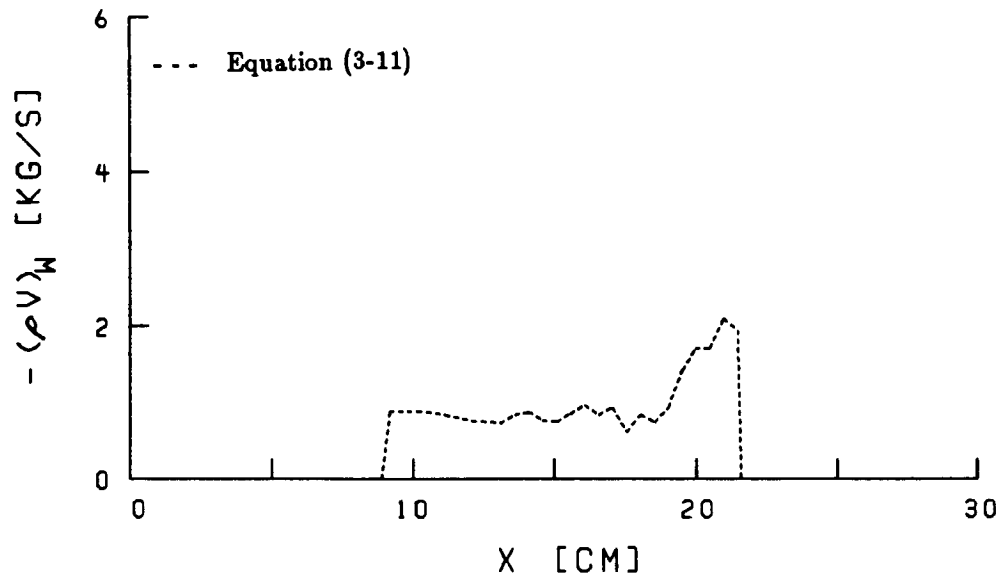


a) Wall pressure distribution

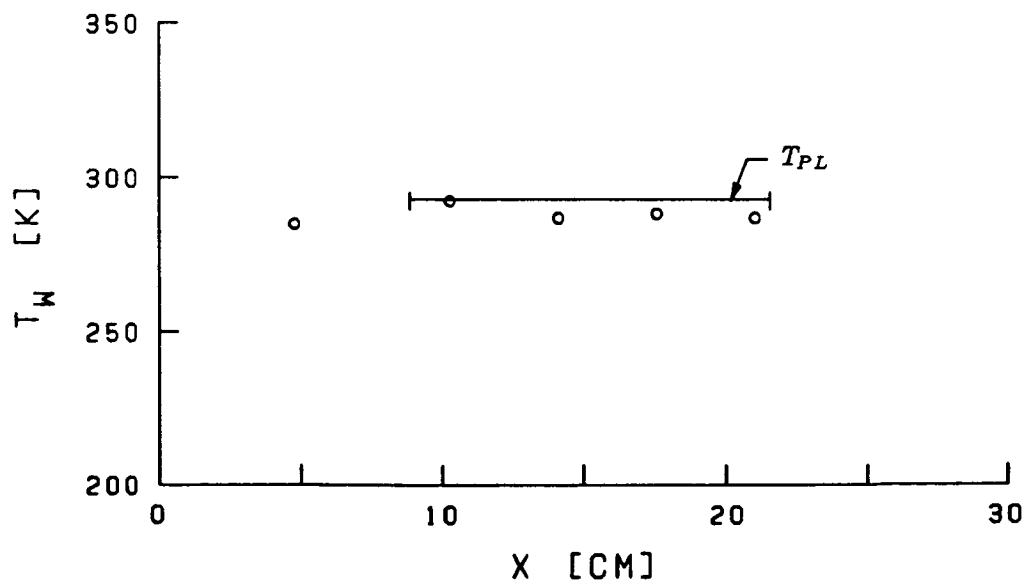


b) Pitot pressure profiles

Fig. 28 MEASUREMENTS ON POROUS PLATE
AT $M = 3.0$ AND $\alpha = 4^\circ$

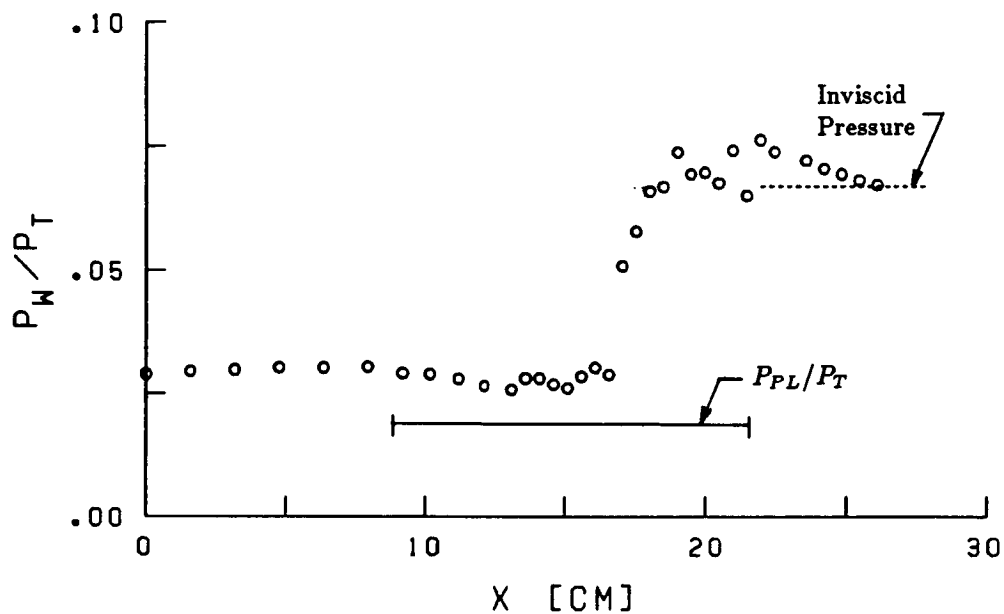


c) Bleed distribution

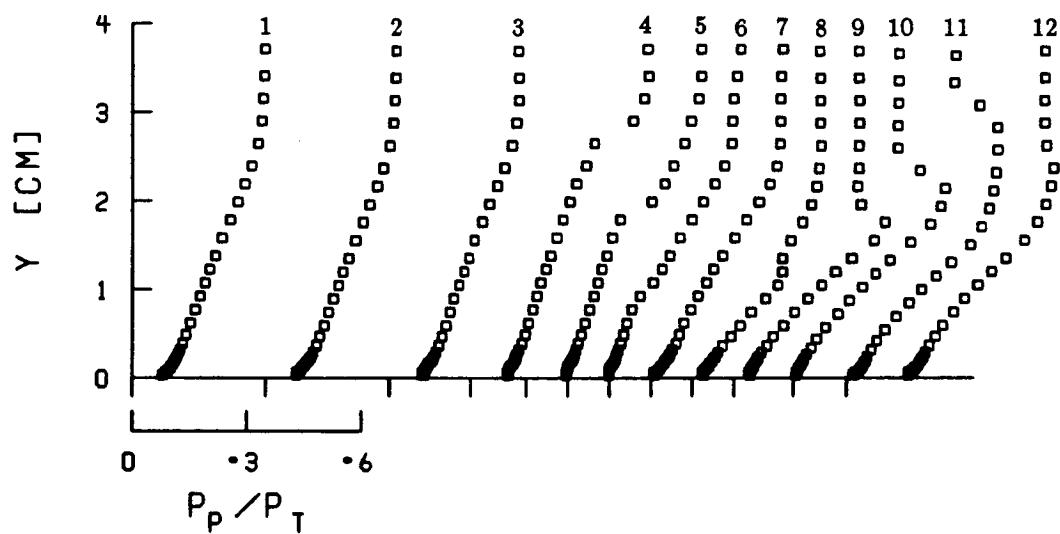


d) Wall temperature

Fig. 28 CONCLUDED

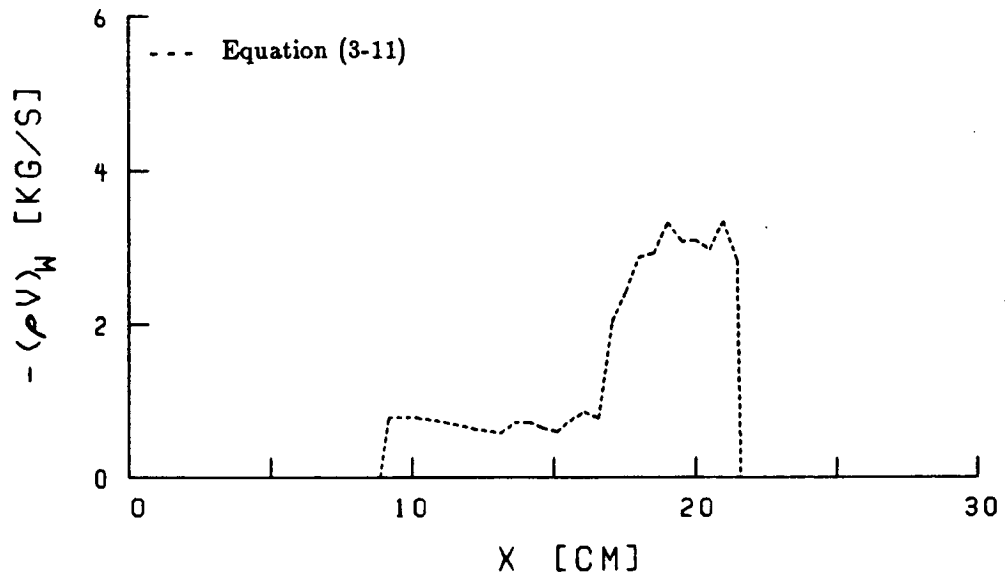


a) Wall pressure distribution

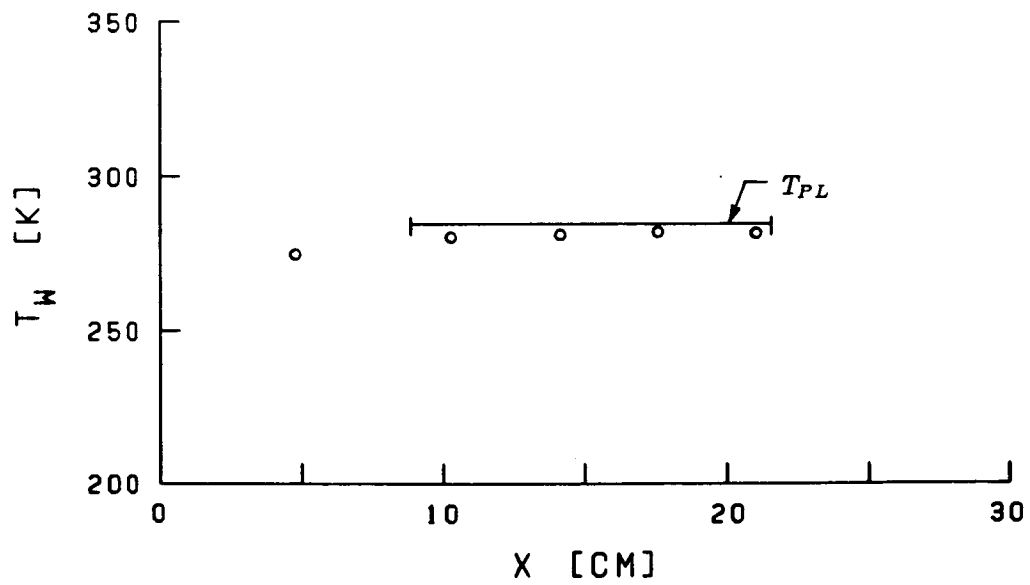


b) Pitot pressure profiles

Fig. 29 MEASUREMENTS ON POROUS PLATE
AT $M = 3.0$ AND $\alpha = 6^\circ$

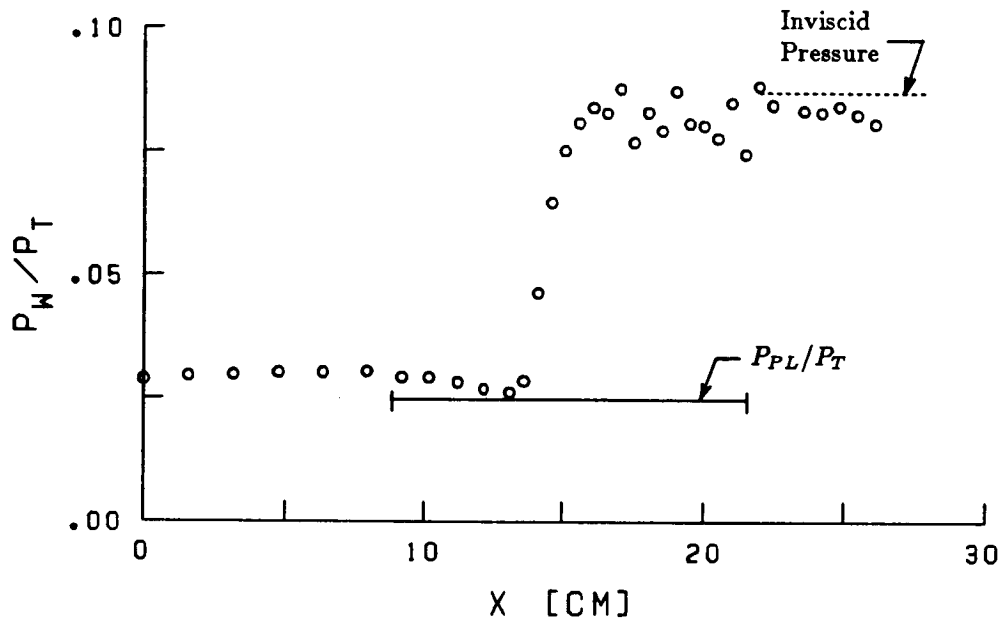


c) Bleed distribution

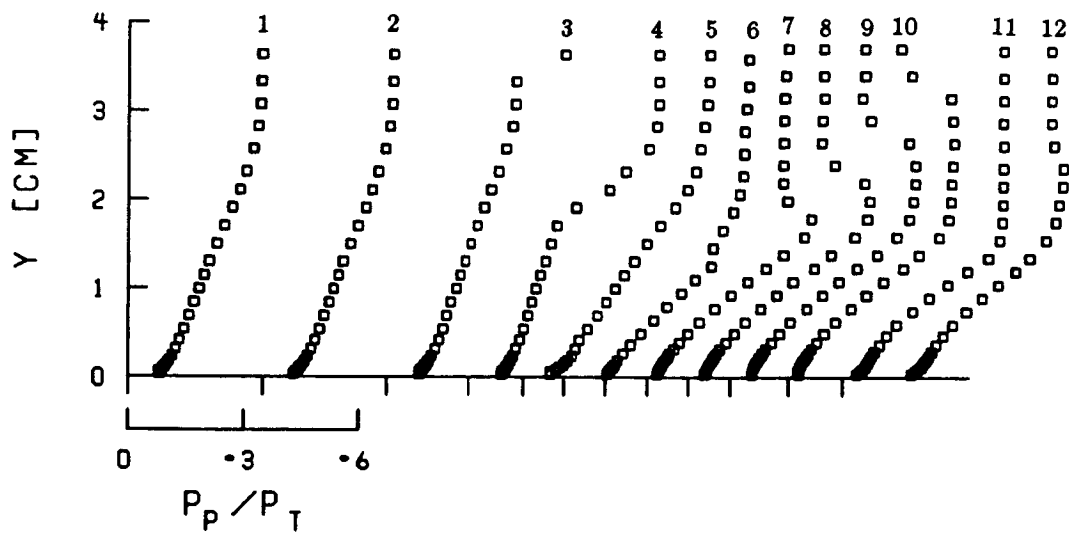


d) Wall temperature

Fig. 29 CONCLUDED

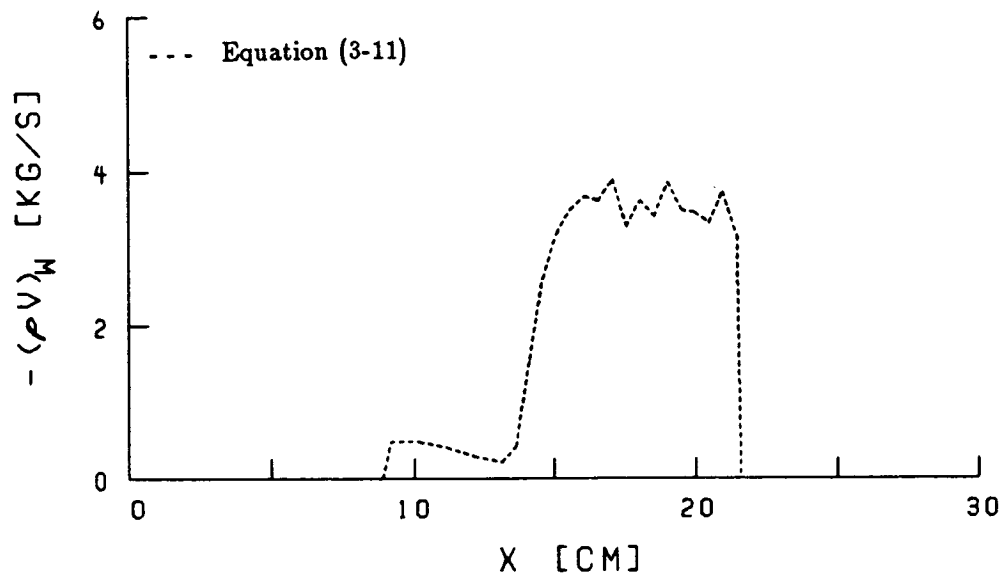


a) Wall pressure distribution

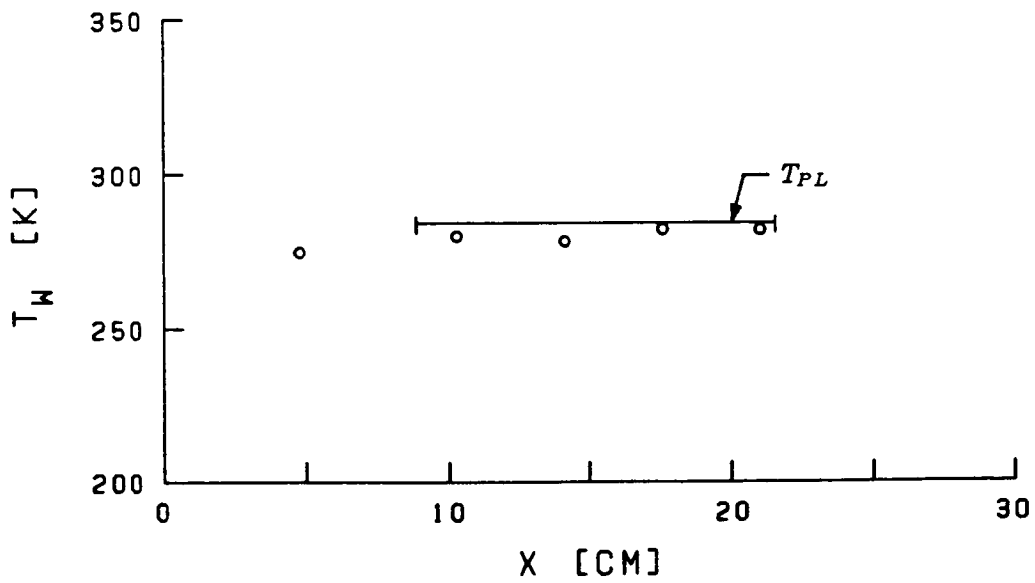


b) Pitot pressure profiles

Fig. 30 MEASUREMENTS ON POROUS PLATE
AT $M = 3.0$ AND $\alpha = 8^\circ$



c) Bleed distribution



d) Wall temperature

Fig. 30 CONCLUDED

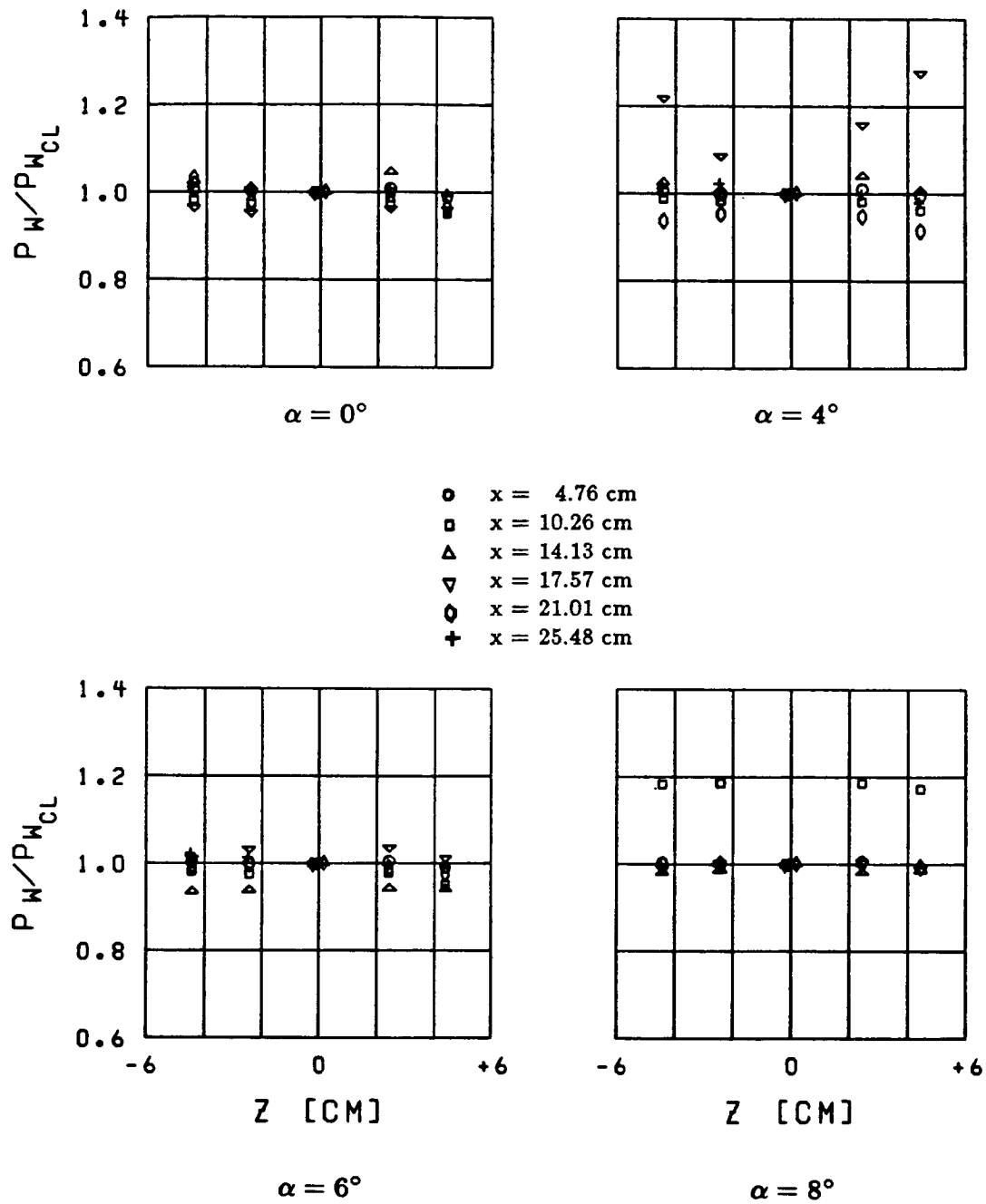


Fig. 31 SPANWISE STATIC PRESSURE DISTRIBUTIONS
ON ROUGH PLATE AT $M = 2.5$

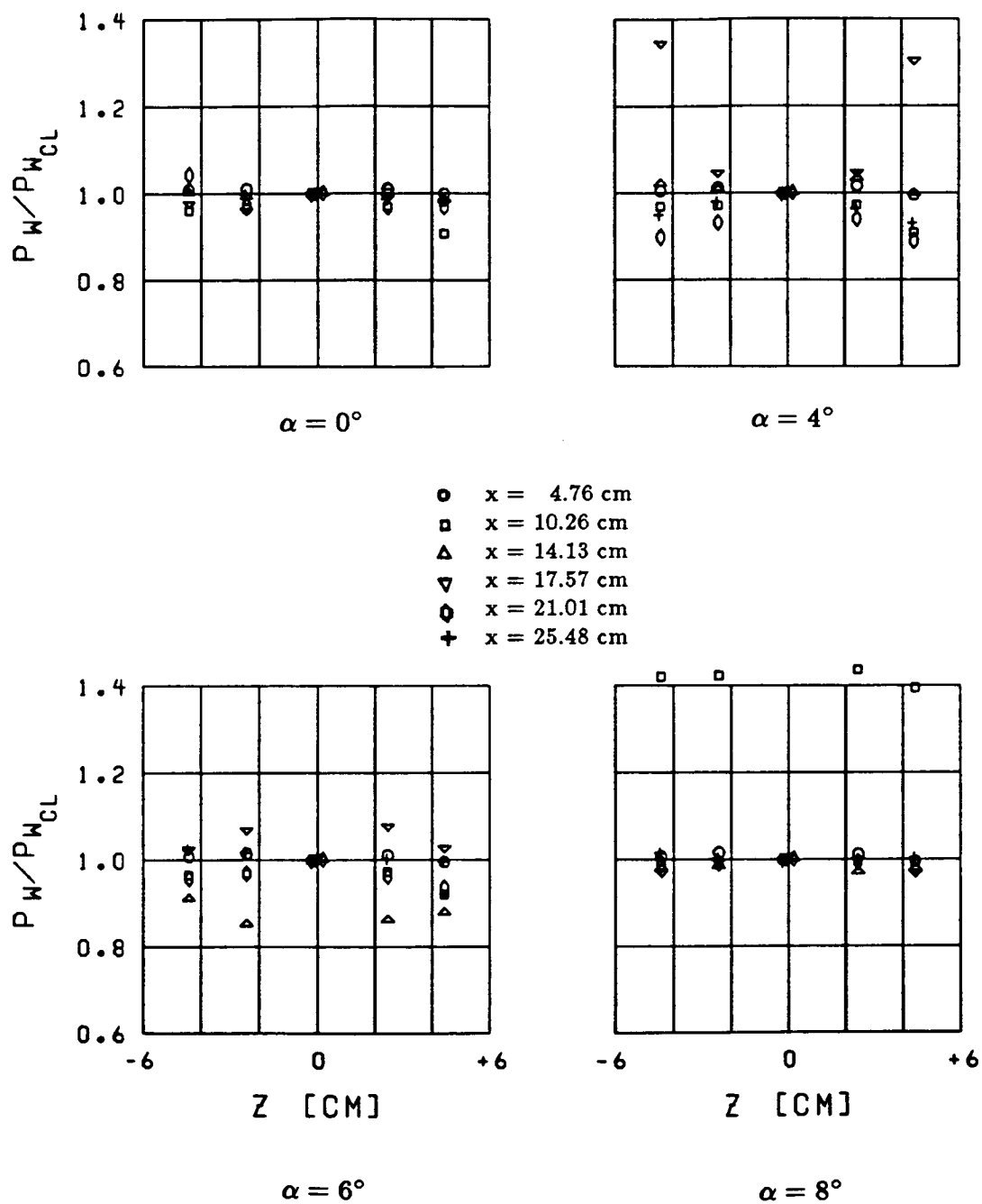


Fig. 32 SPANWISE STATIC PRESSURE DISTRIBUTIONS
ON ROUGH PLATE AT $M = 3.0$

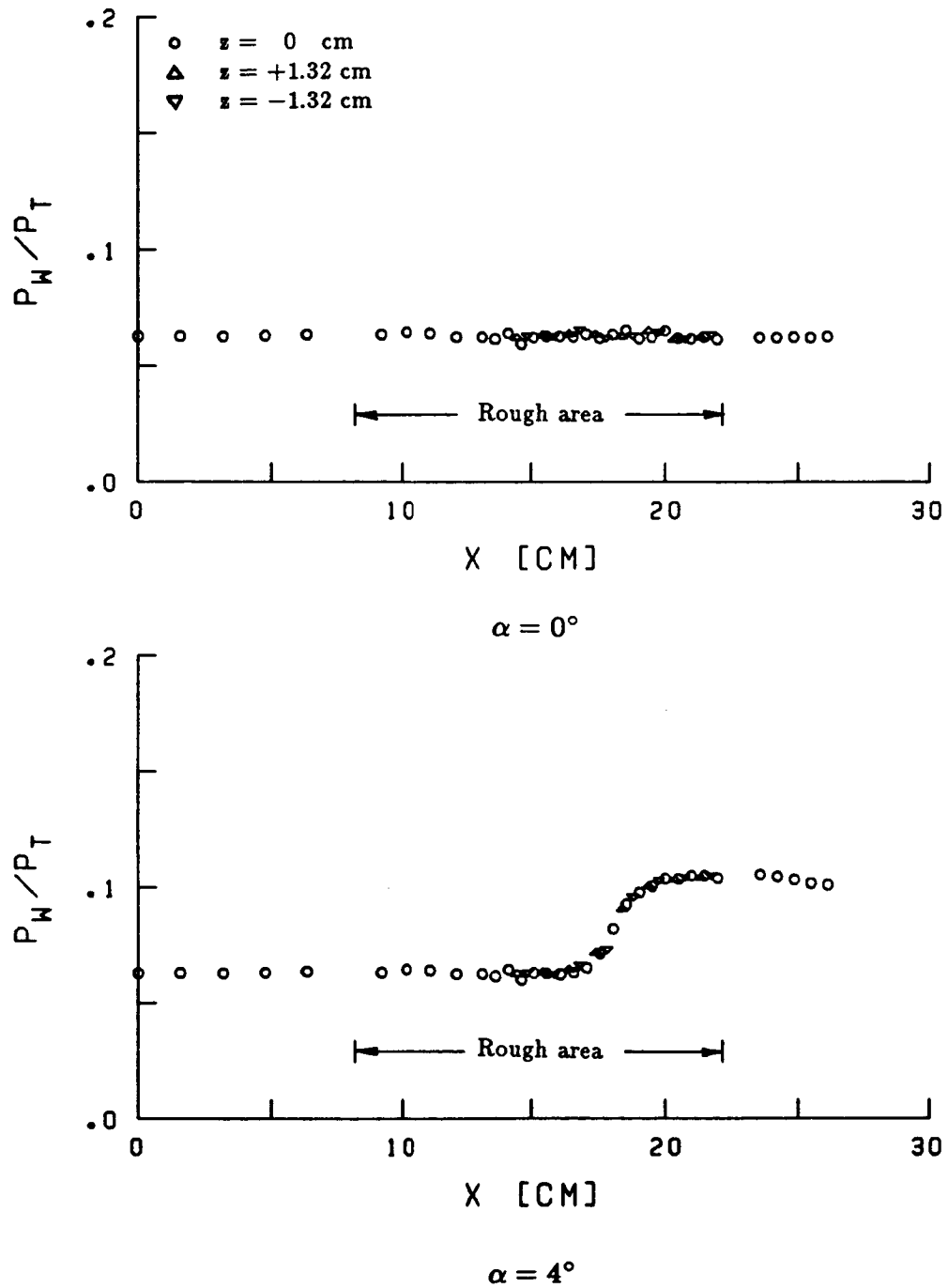


Fig. 33 COMPARISON OF CENTERLINE AND OFF-CENTERLINE PRESSURE DISTRIBUTIONS ON ROUGH PLATE AT $M = 2.5$

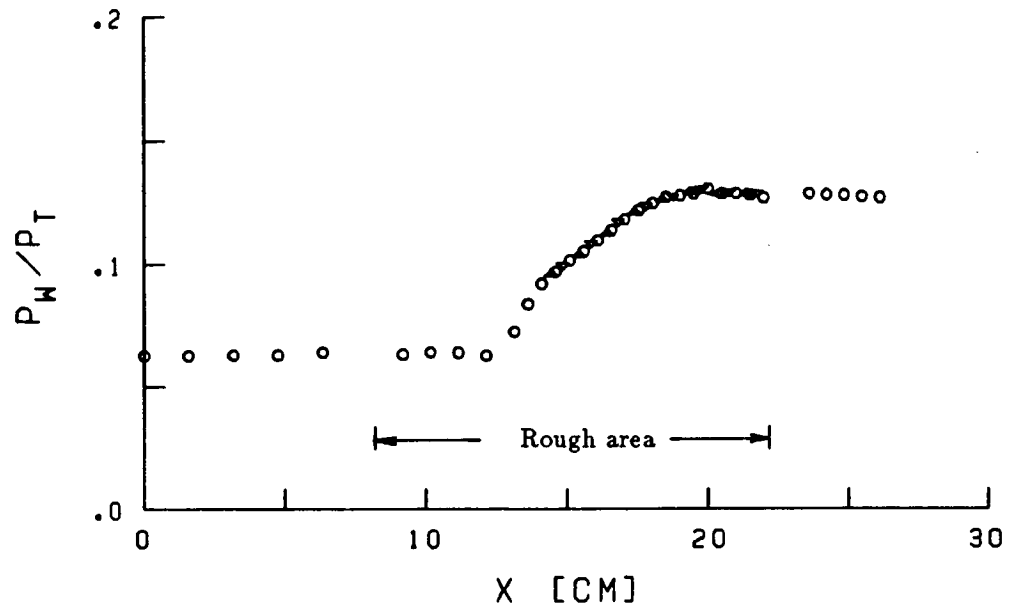
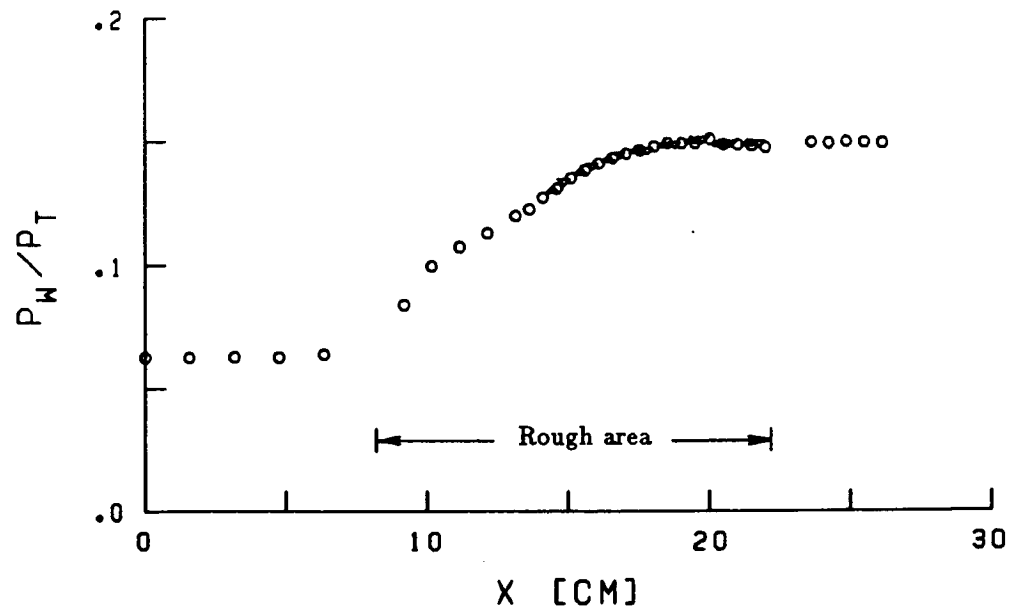
 $\alpha = 6^\circ$  $\alpha = 8^\circ$

Fig. 33 CONCLUDED

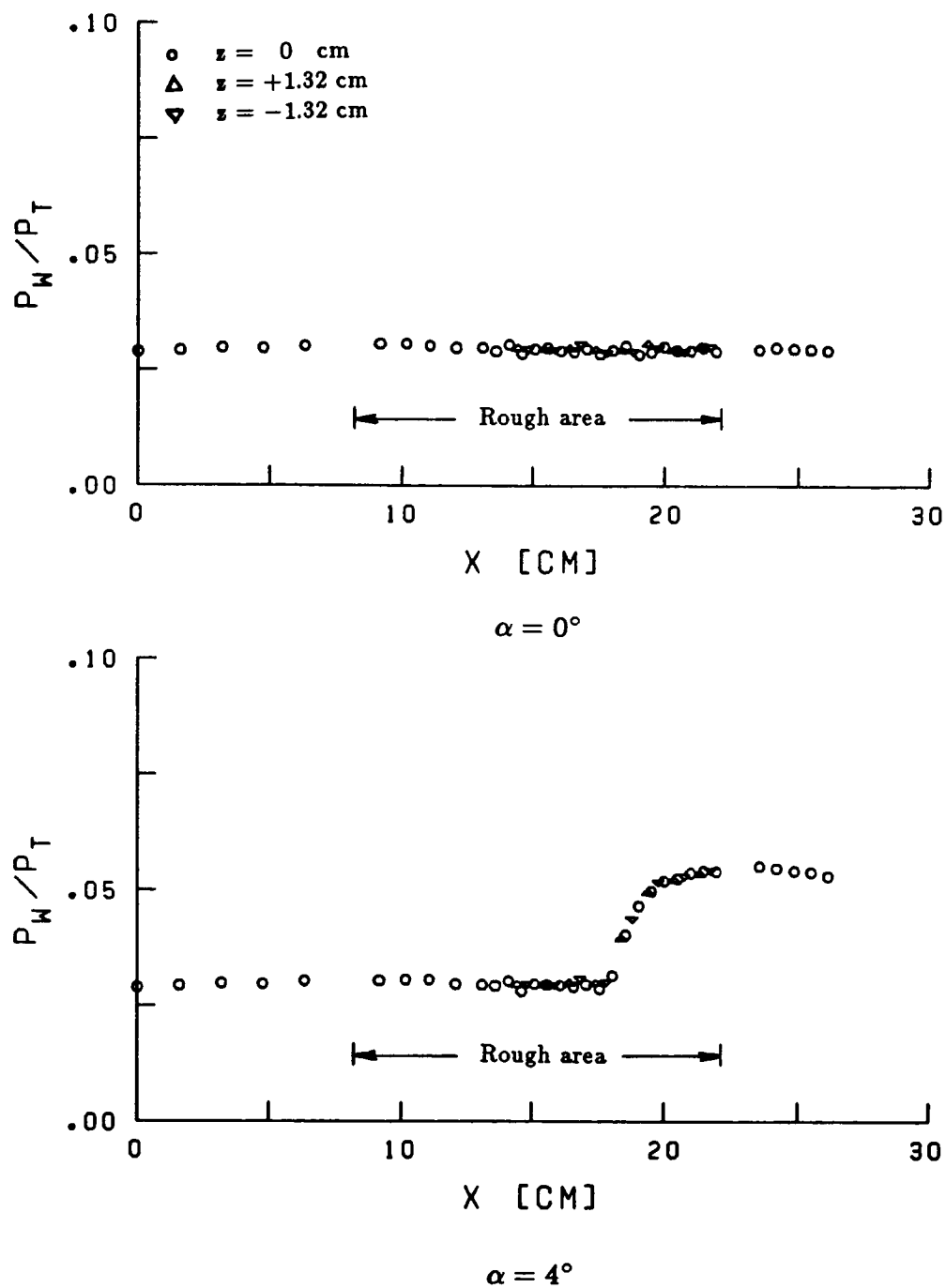


Fig. 34 COMPARISON OF CENTERLINE AND OFF-CENTERLINE PRESSURE DISTRIBUTIONS ON ROUGH PLATE AT $M = 3.0$

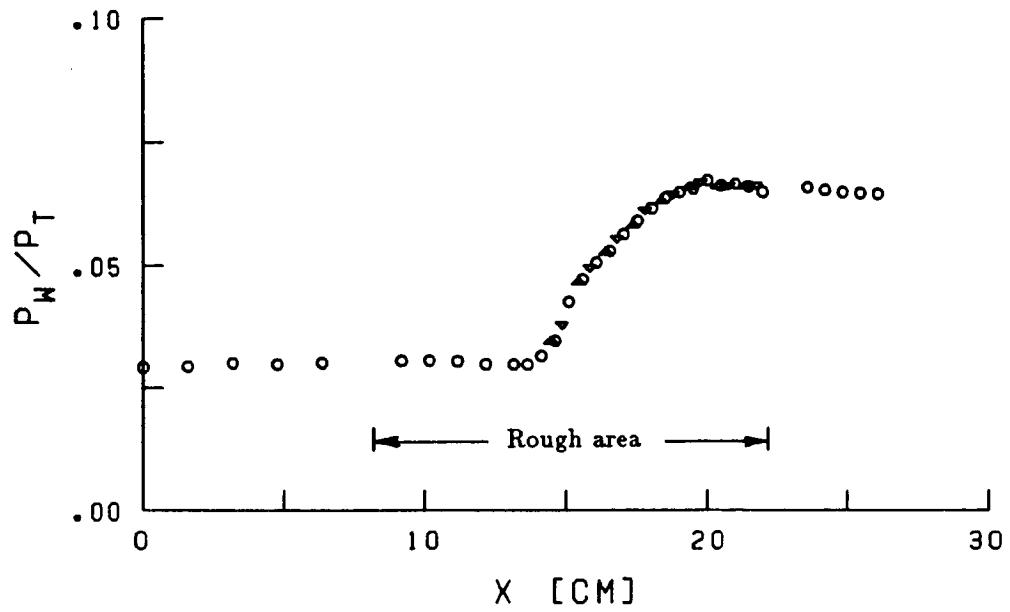
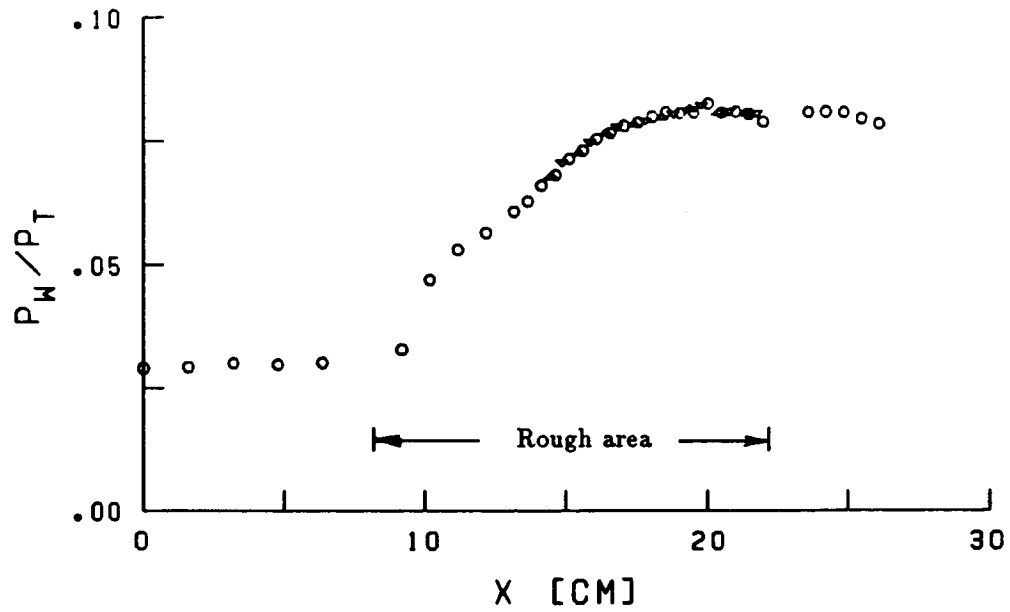
 $\alpha = 6^\circ$  $\alpha = 8^\circ$

Fig. 34 CONCLUDED

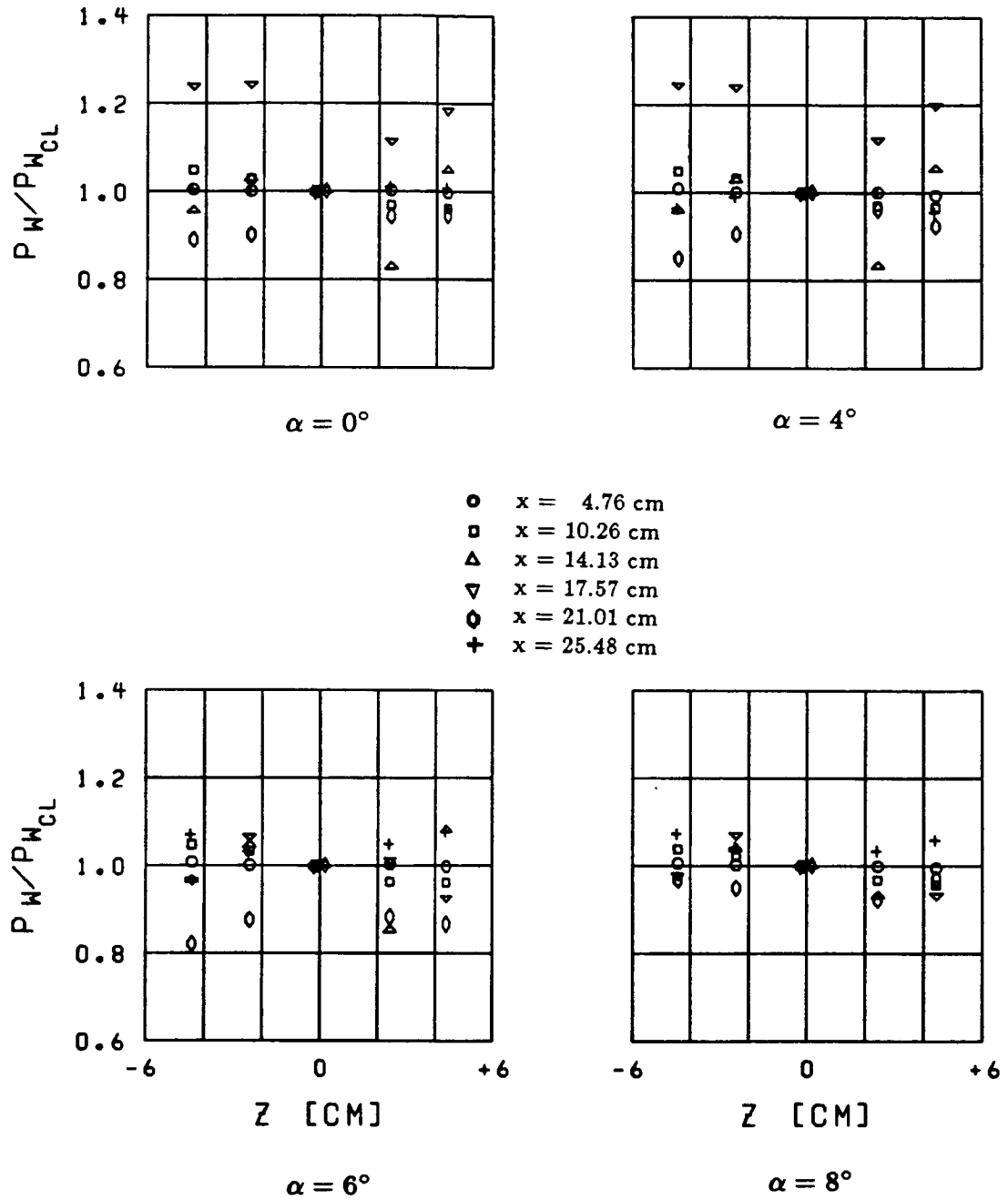


Fig. 35 SPANWISE STATIC PRESSURE DISTRIBUTIONS
ON POROUS PLATE AT $M = 2.5$

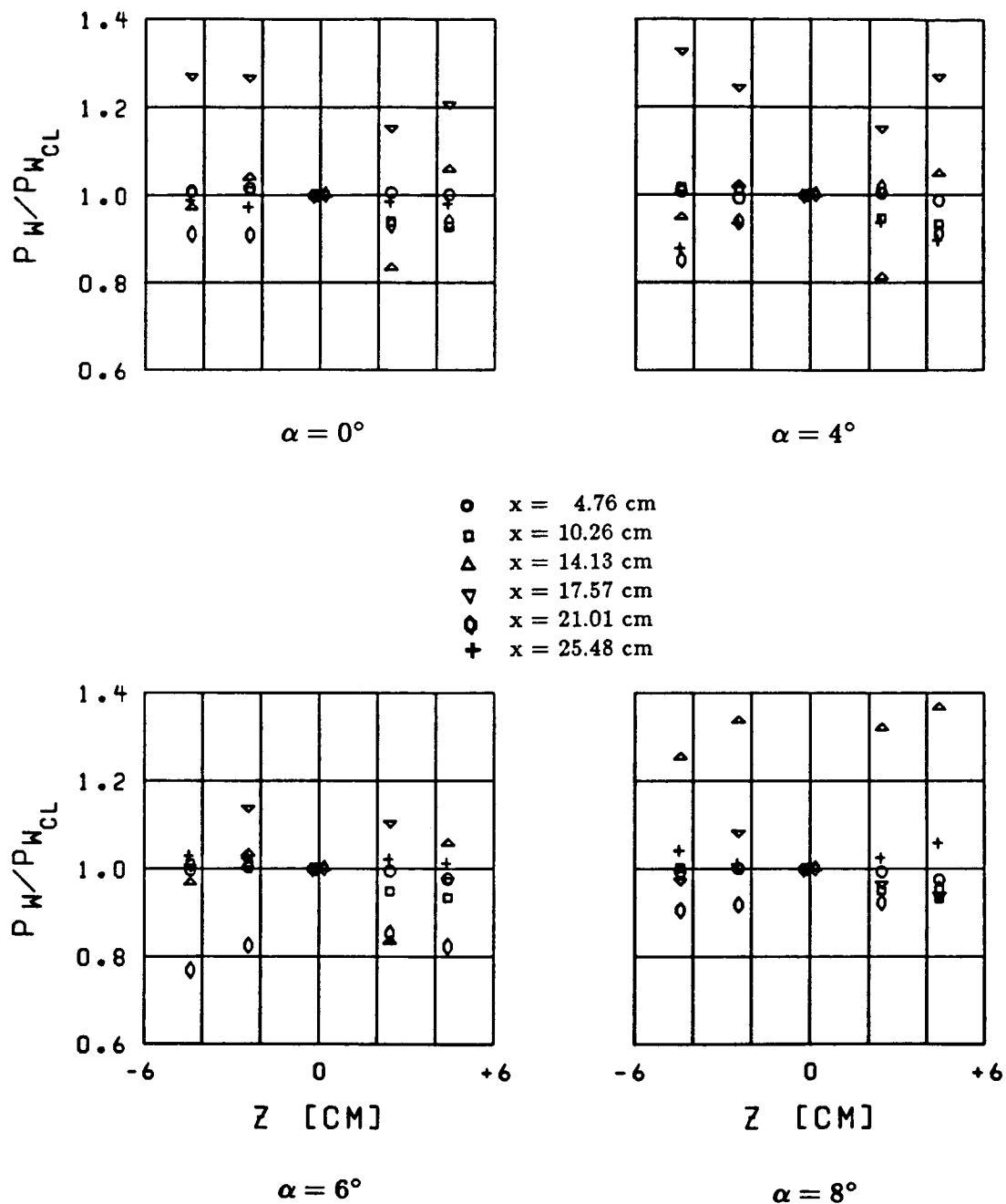


Fig. 36 SPANWISE STATIC PRESSURE DISTRIBUTIONS
ON POROUS PLATE AT $M = 3.0$

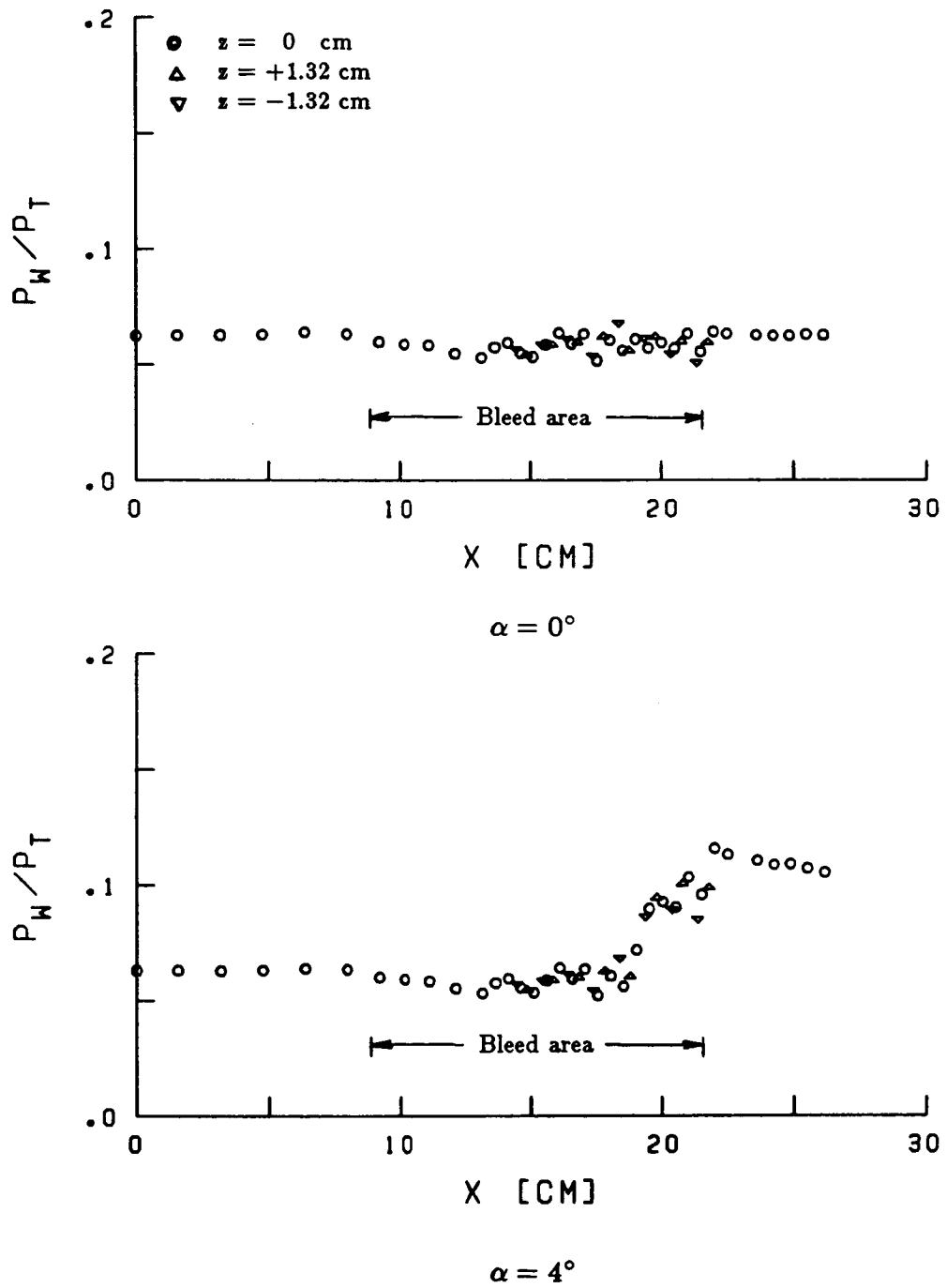


Fig. 37 COMPARISON OF CENTERLINE AND OFF-CENTERLINE PRESSURE DISTRIBUTIONS ON POROUS PLATE AT $M = 2.5$

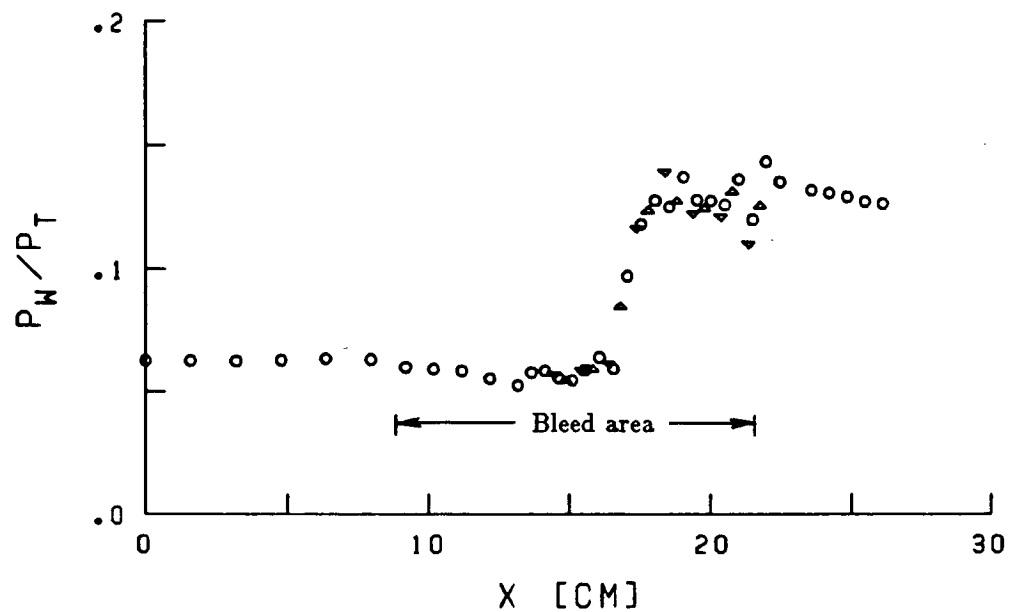
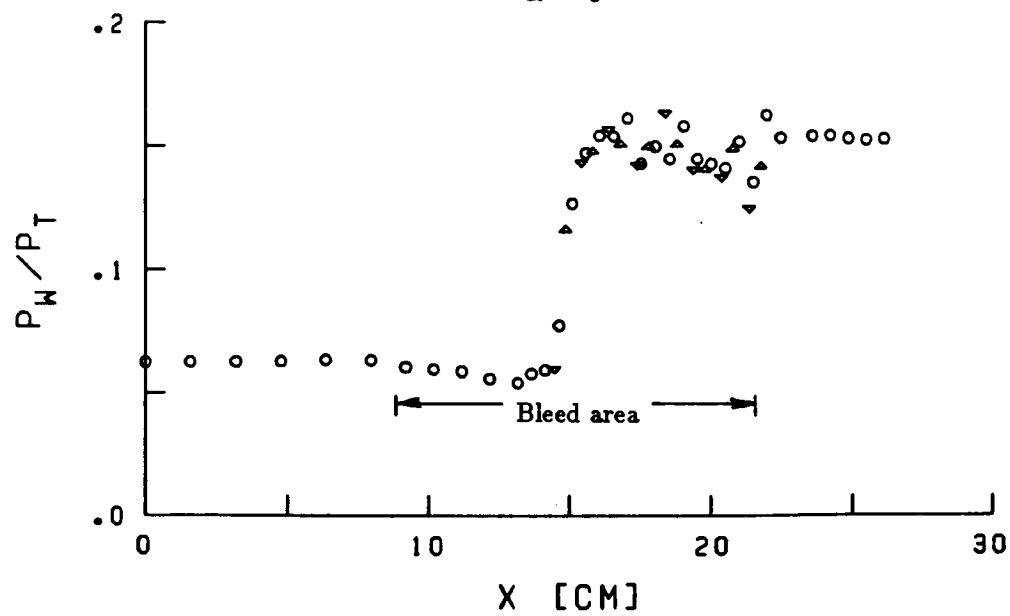
 $\alpha = 6^\circ$  $\alpha = 8^\circ$

Fig. 37 CONCLUDED

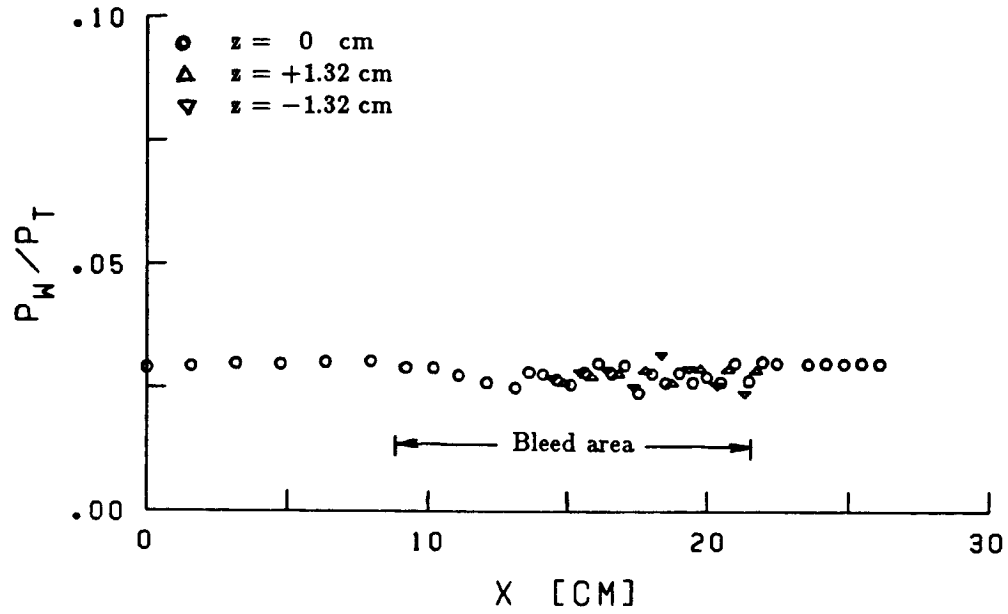
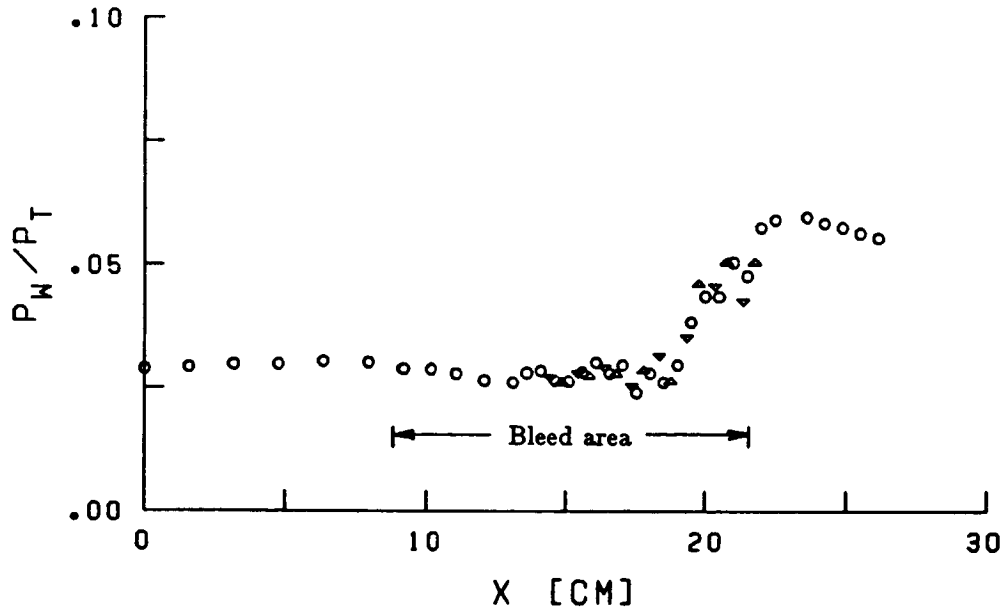
 $\alpha = 0^\circ$  $\alpha = 4^\circ$

Fig. 38 COMPARISON OF CENTERLINE AND OFF-CENTERLINE PRESSURE DISTRIBUTIONS ON POROUS PLATE AT $M = 3.0$

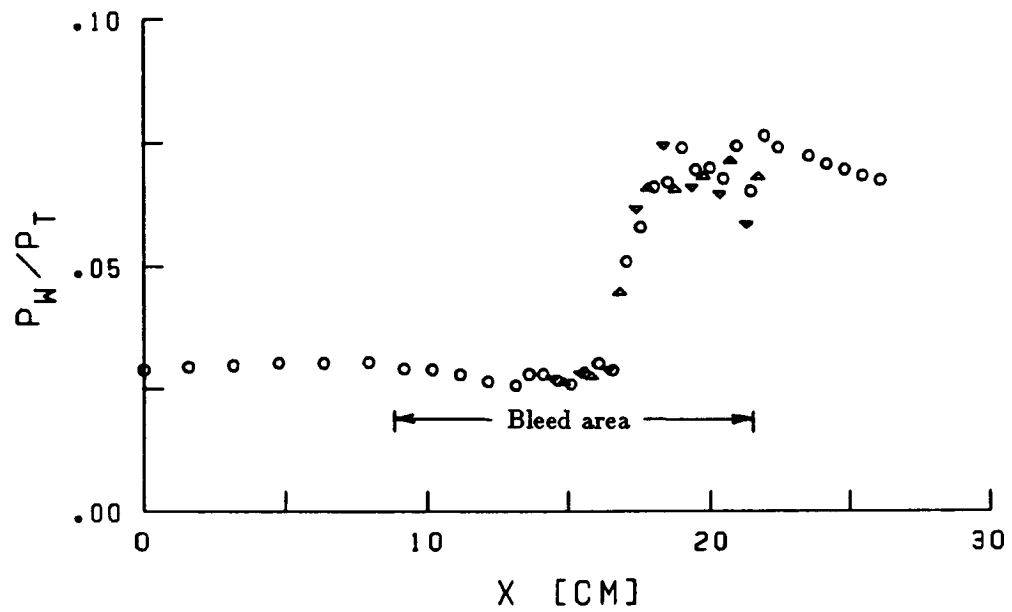
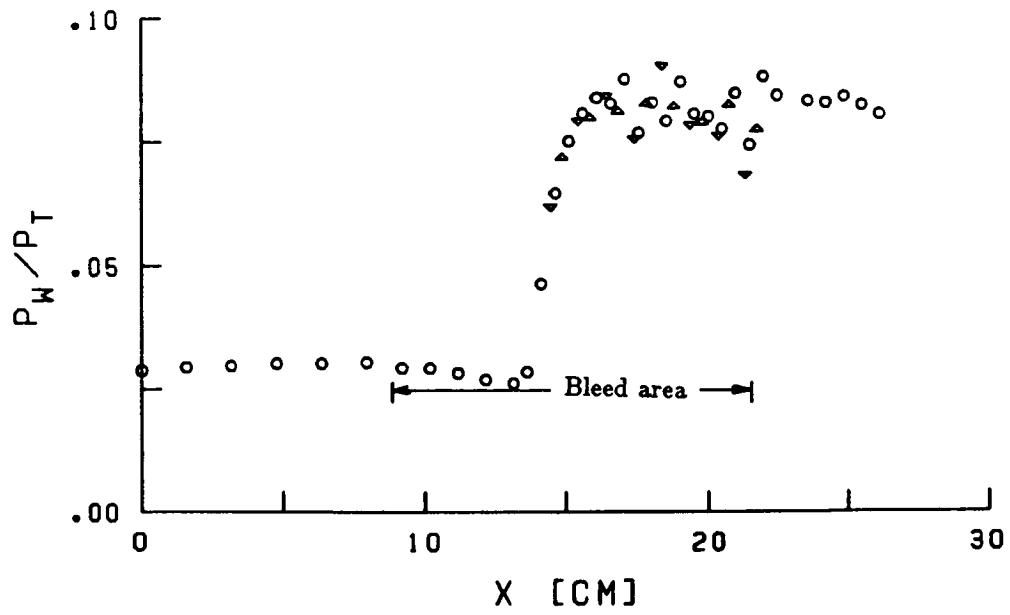
 $\alpha = 6^\circ$  $\alpha = 8^\circ$

Fig. 38 CONCLUDED

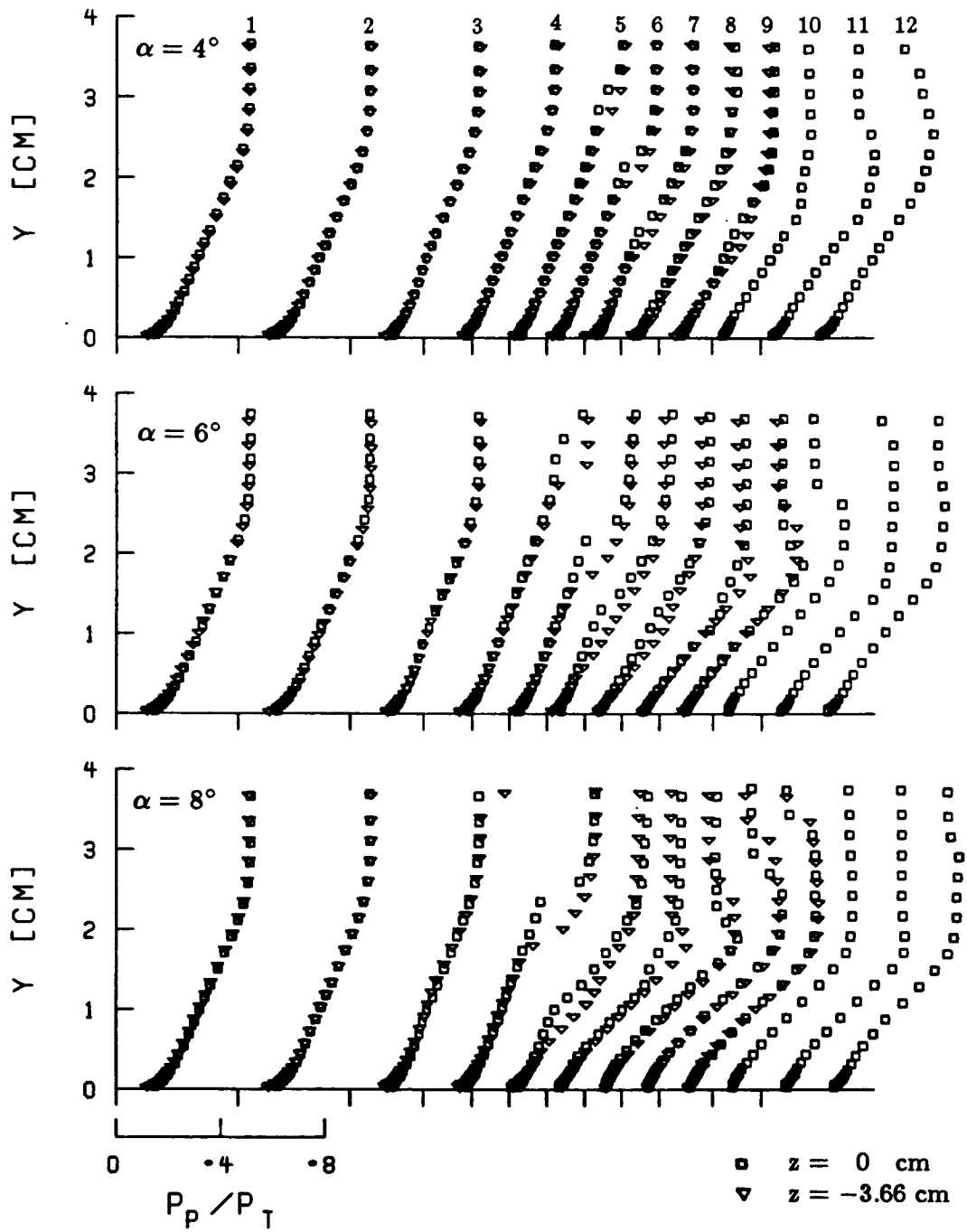


Fig. 39 COMPARISON OF CENTERLINE AND OFF-CENTERLINE PITOT PRESSURE PROFILES ON POROUS PLATE AT $M = 2.5$

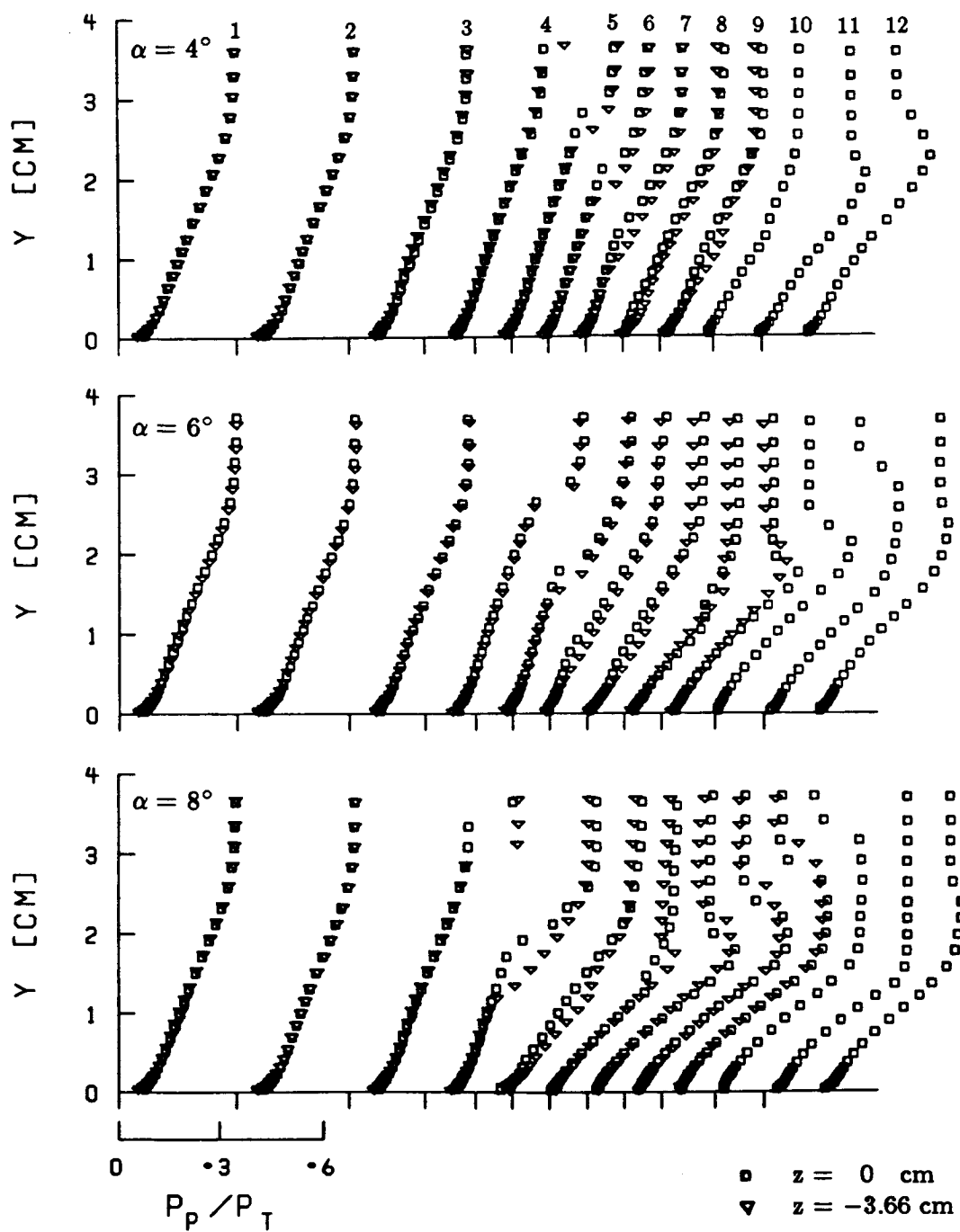


Fig. 40 COMPARISON OF CENTERLINE AND OFF-CENTERLINE PITOT PRESSURE PROFILES ON POROUS PLATE AT $M = 3.0$

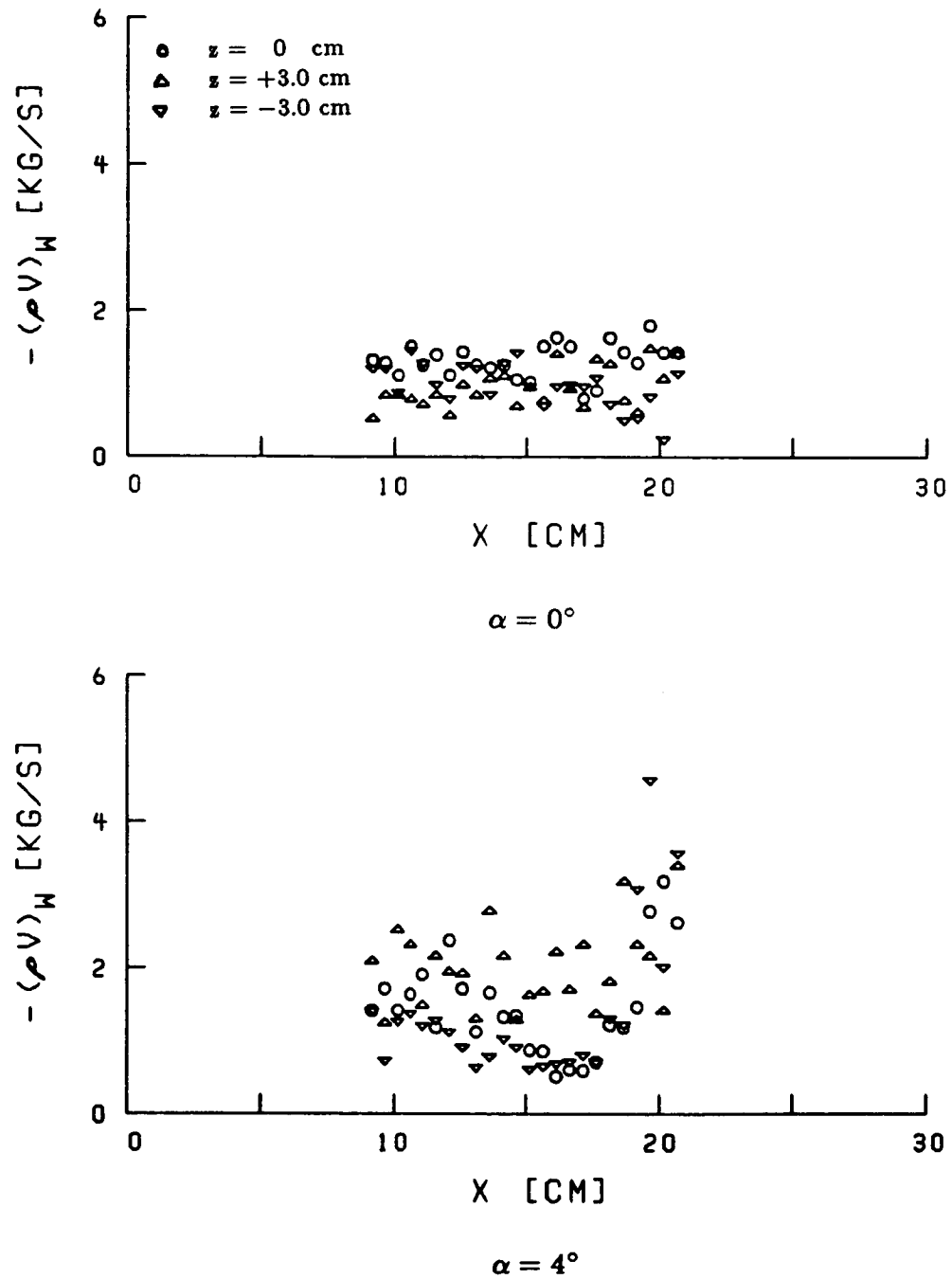


Fig. 41 COMPARISON OF CENTERLINE AND OFF-CENTERLINE BLEED DISTRIBUTIONS AT $M = 2.5$

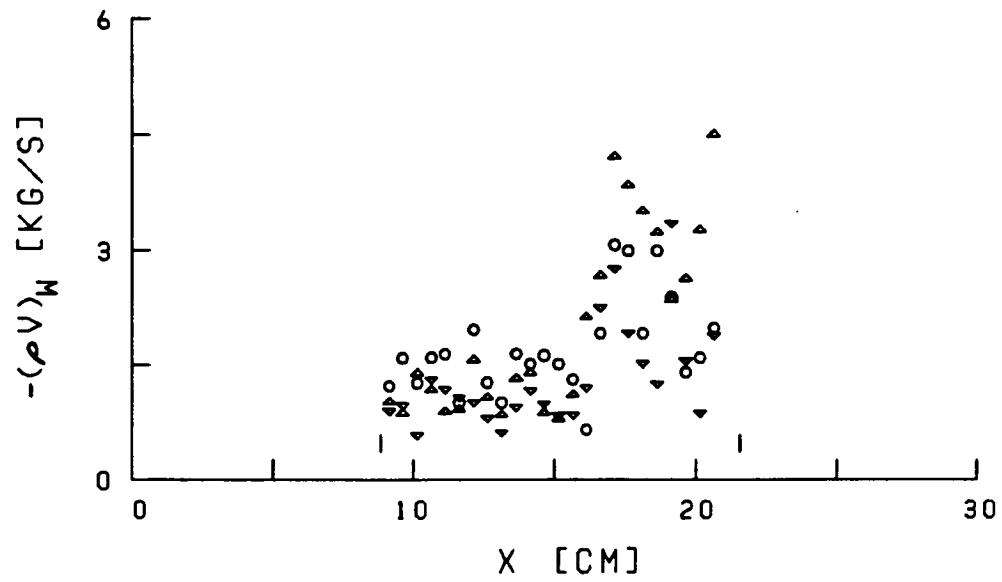
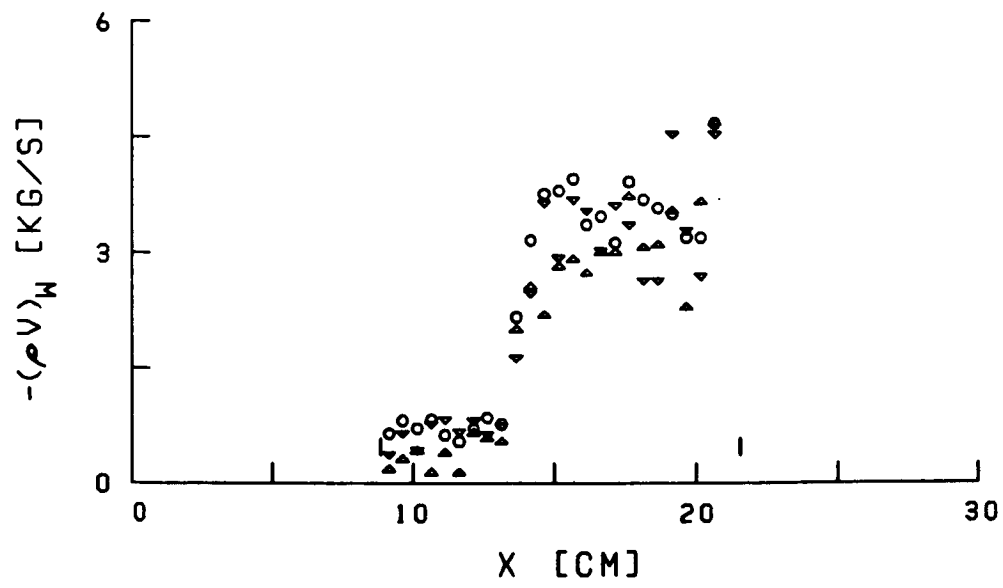
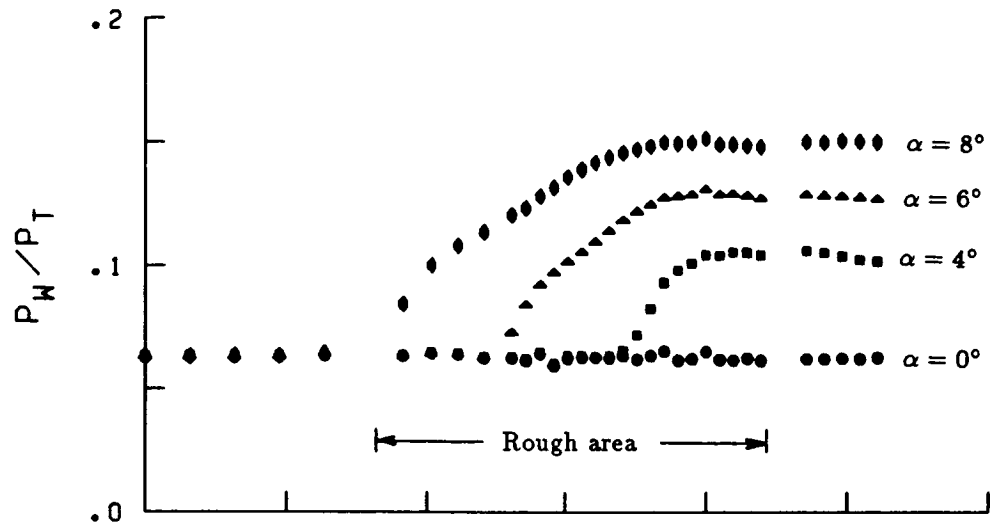
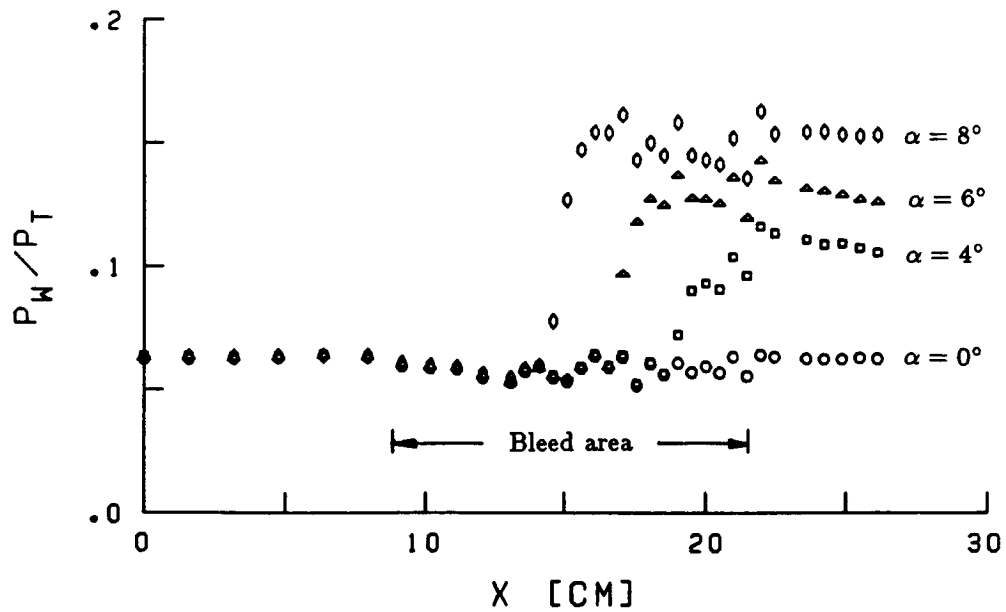
 $\alpha = 6^\circ$  $\alpha = 8^\circ$

Fig. 41 CONCLUDED

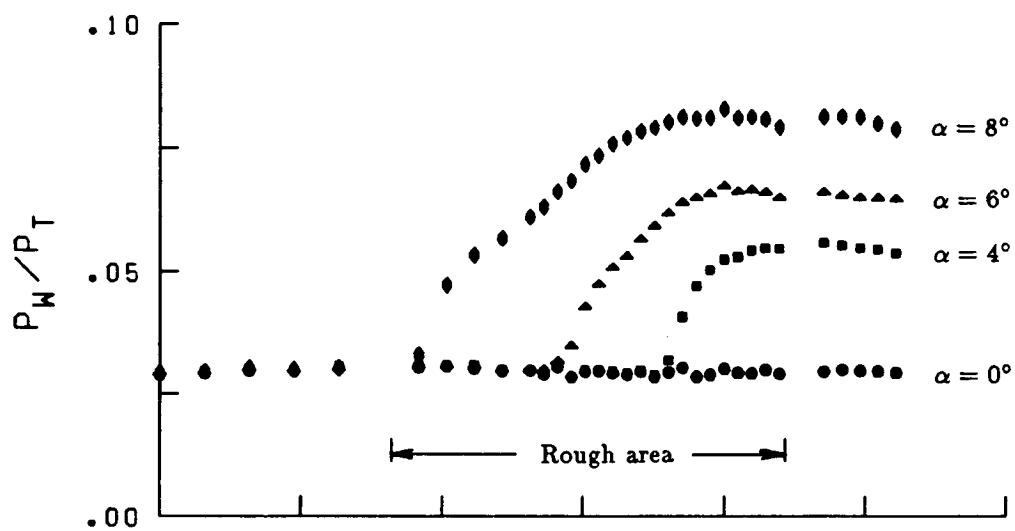


a) Rough plate

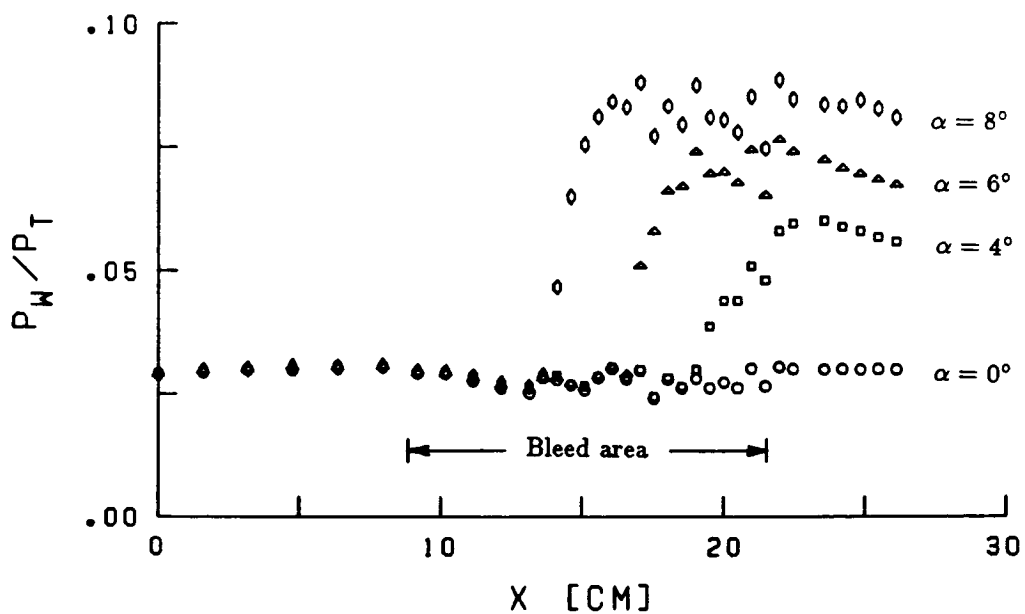


b) Porous plate

Fig. 42 COMPARISON OF WALL PRESSURE DISTRIBUTIONS ON ROUGH PLATE AND POROUS PLATE AT $M = 2.5$



a) Rough plate



b) Porous plate

Fig. 43 COMPARISON OF WALL PRESSURE DISTRIBUTIONS ON ROUGH PLATE AND POROUS PLATE AT $M = 3.0$

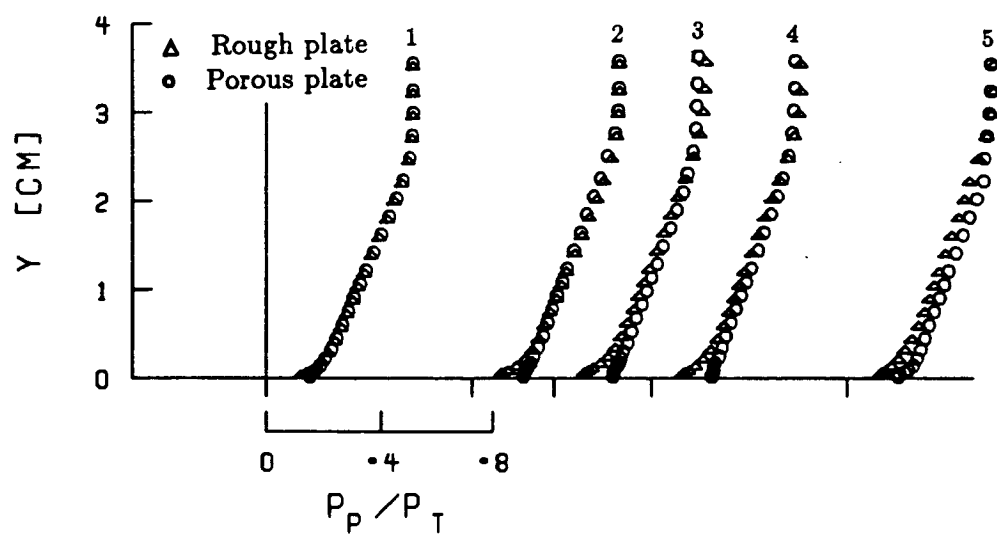
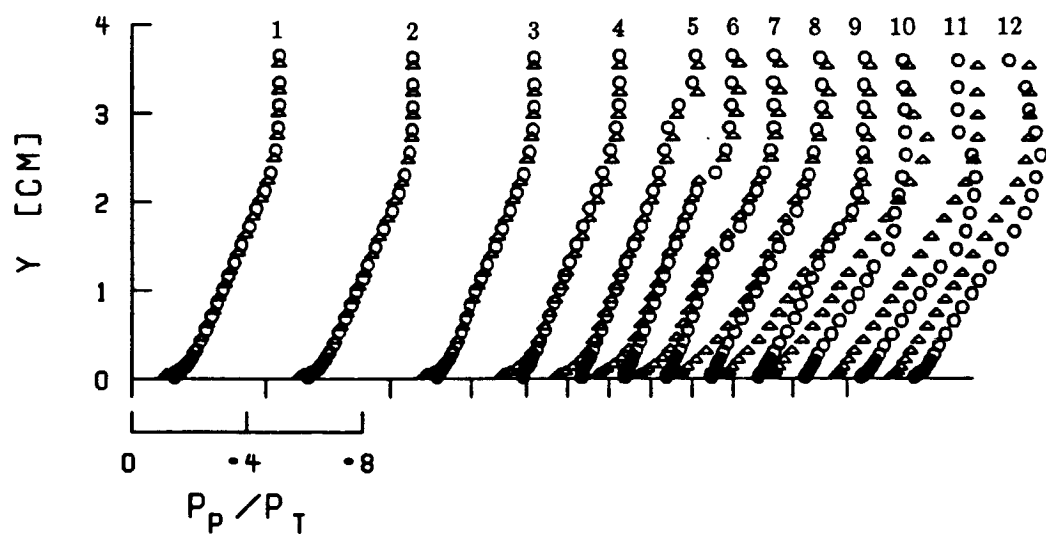
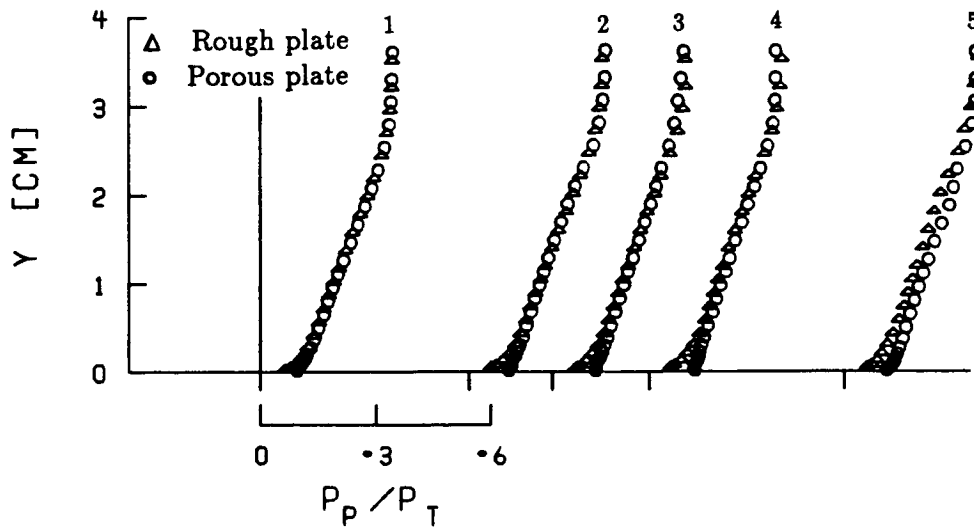
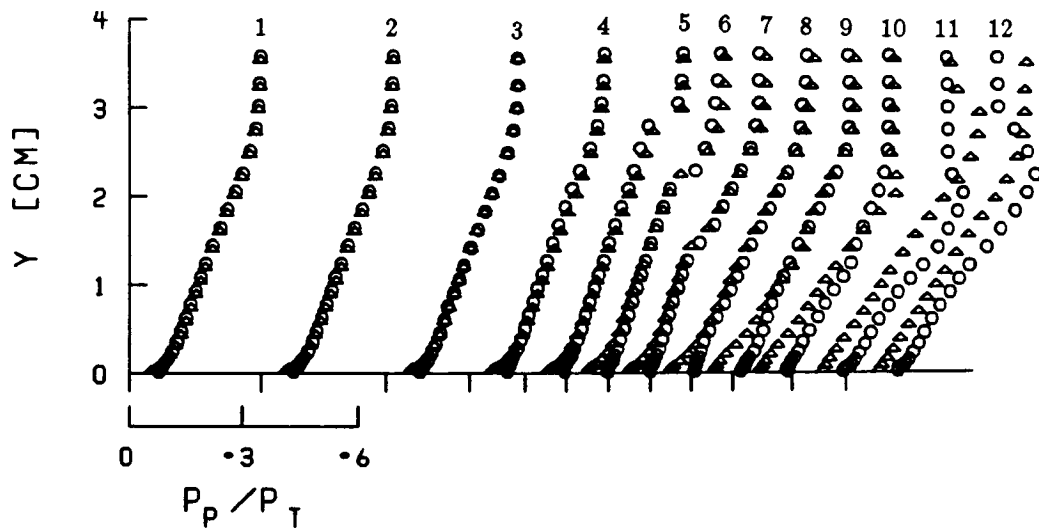
a) $\alpha = 0^\circ$ b) $\alpha = 4^\circ$

Fig. 44 COMPARISON OF PITOT PRESSURE
PROFILES ON ROUGH PLATE
AND POROUS PLATE AT $M = 2.5$

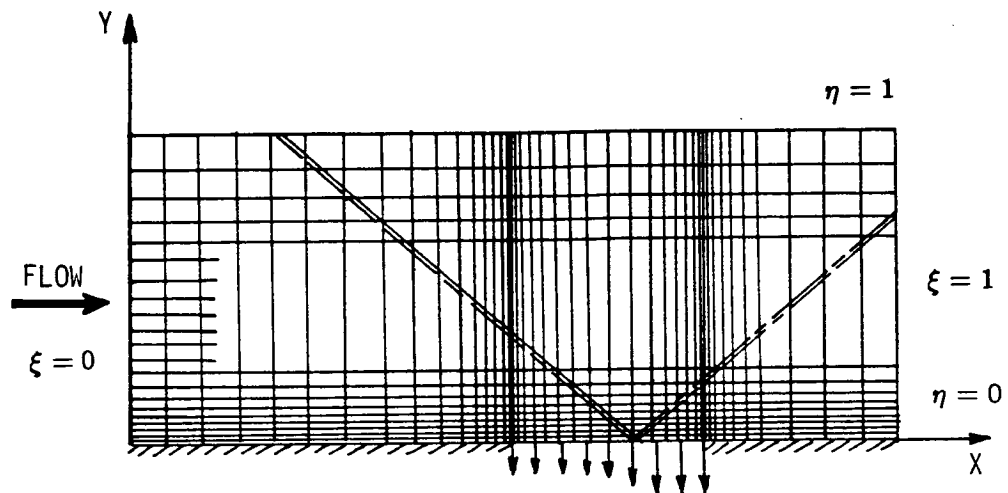


a) $\alpha = 0^\circ$

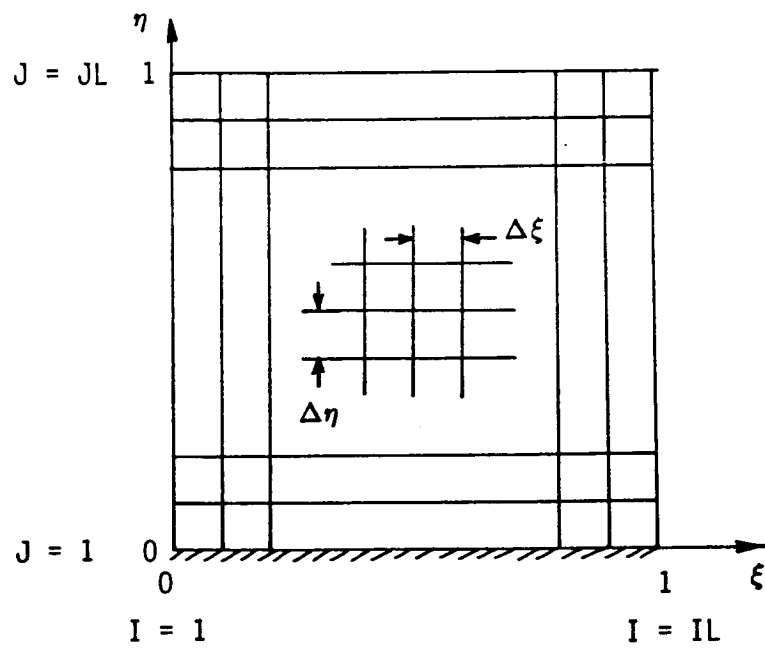


b) $\alpha = 4^\circ$

Fig. 45 COMPARISON OF PITOT PRESSURE PROFILES ON ROUGH PLATE AND POROUS PLATE AT $M = 3.0$



a) Physical plane



b) Computational plane

Fig. 47 MAPPING OF PHYSICAL PLANE
ONTO COMPUTATIONAL PLANE

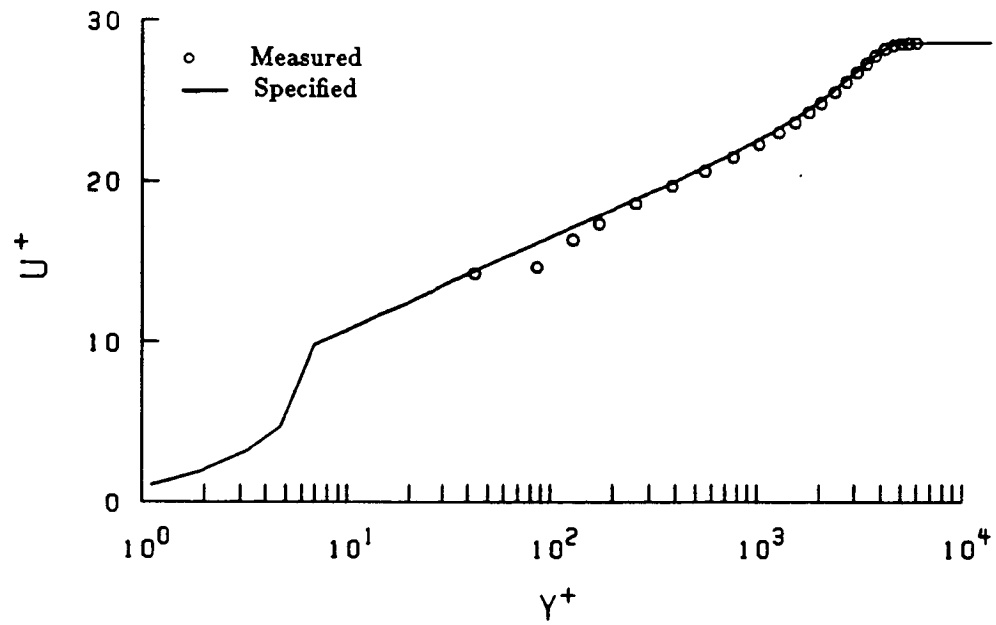
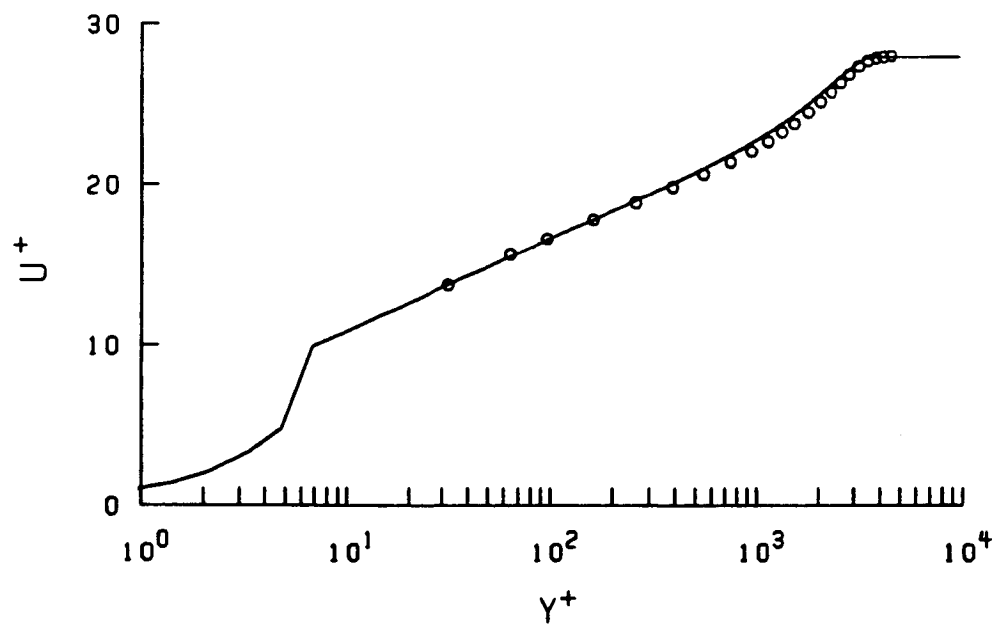
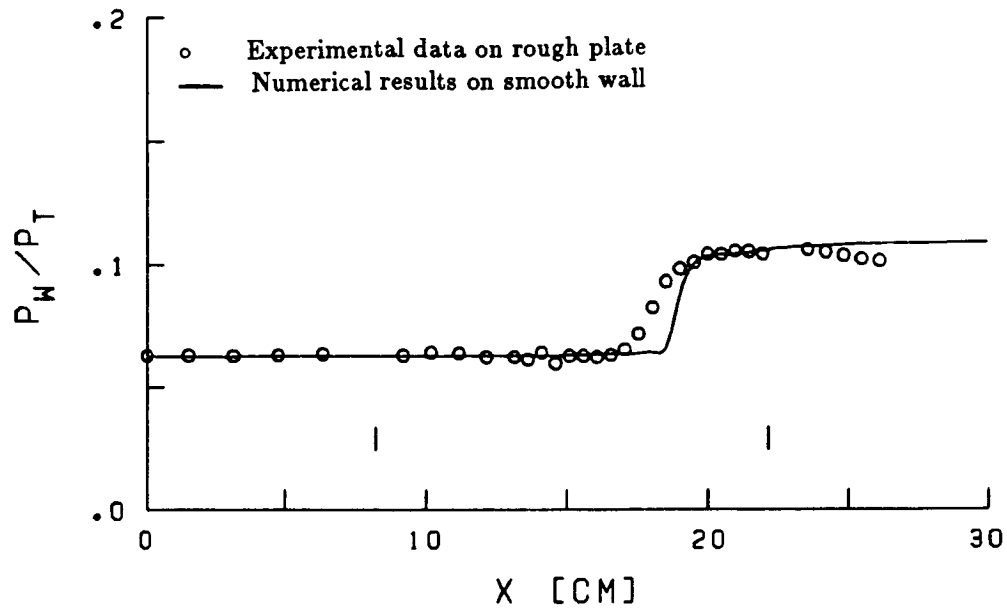
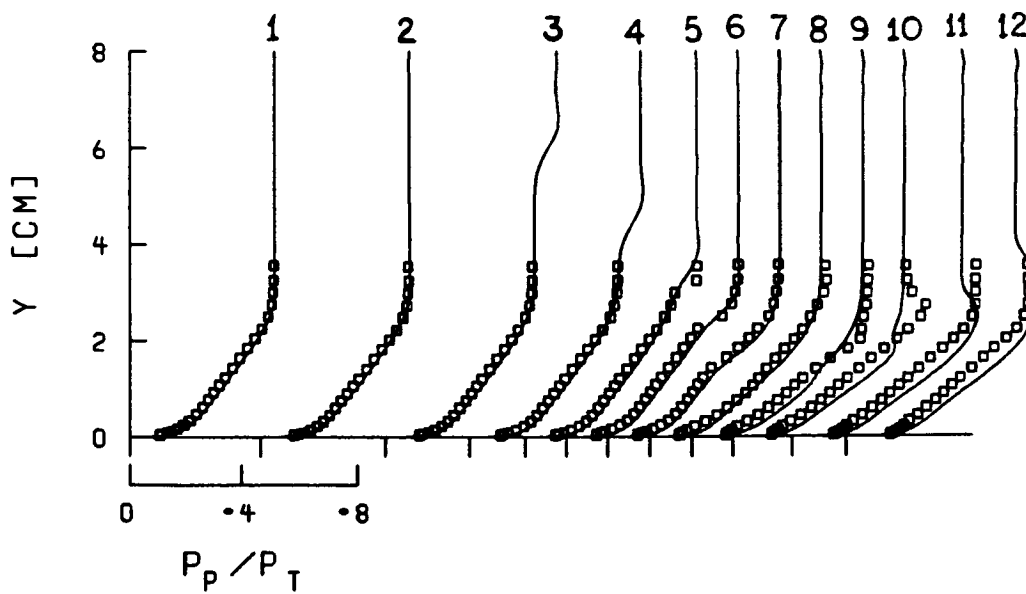
a) $M = 2.5$ b) $M = 3.0$

Fig. 48 COMPARISON OF SPECIFIED INCOMING PROFILES WITH MEASURED PROFILES

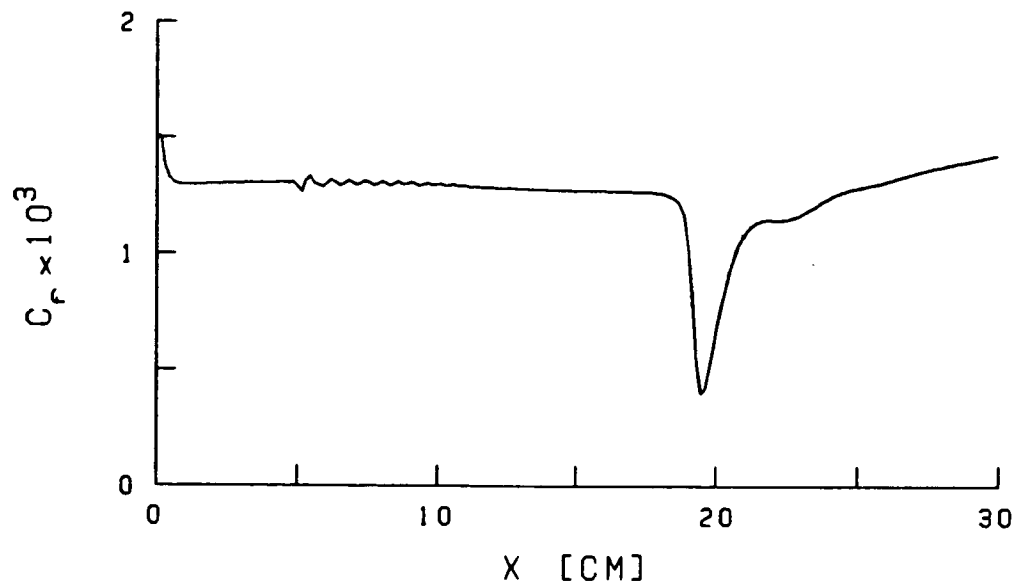


a) Wall pressure distribution

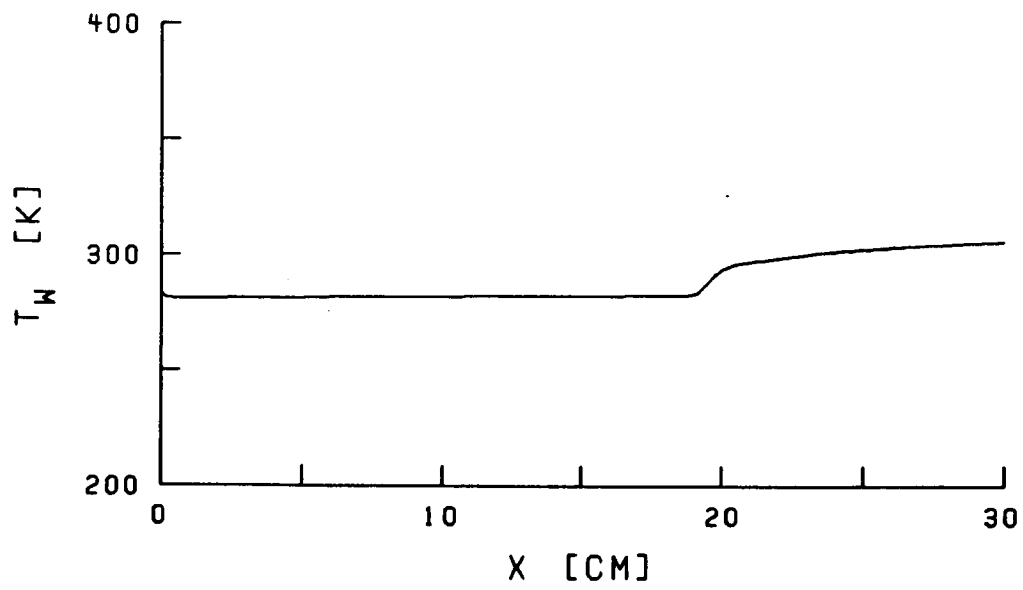


b) Pitot pressure profiles

Fig. 49 COMPARISONS OF COMPUTATIONS
WITH EXPERIMENTAL DATA;
 $M = 2.46$, $\alpha = 4.5^\circ$, AND NO BLEED

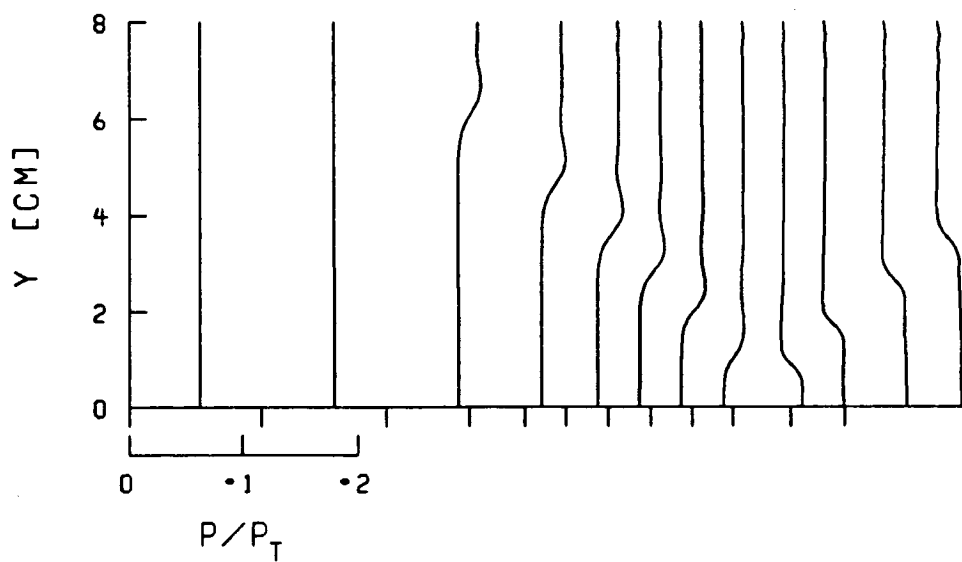


c) Skin friction

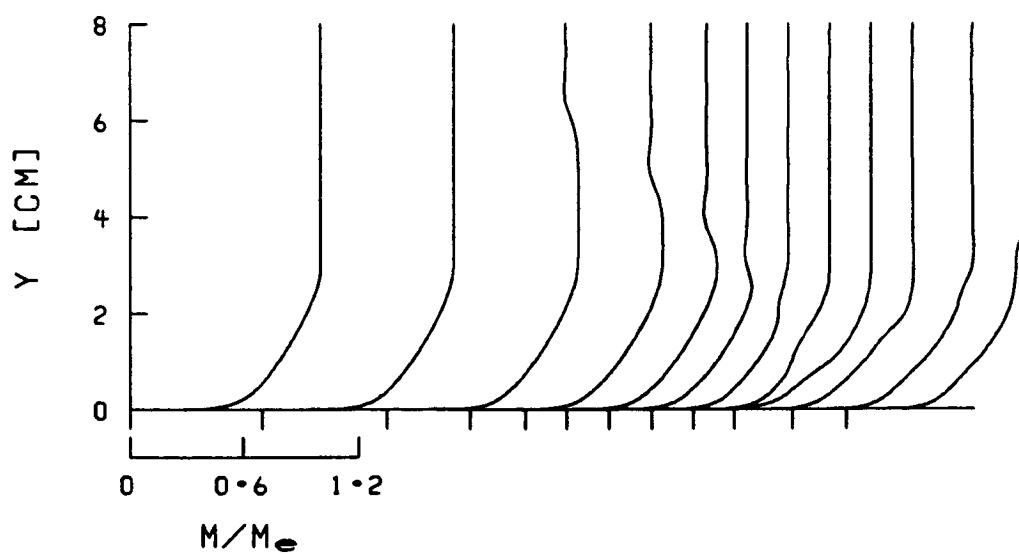


d) Wall temperature

Fig. 49 CONTINUED

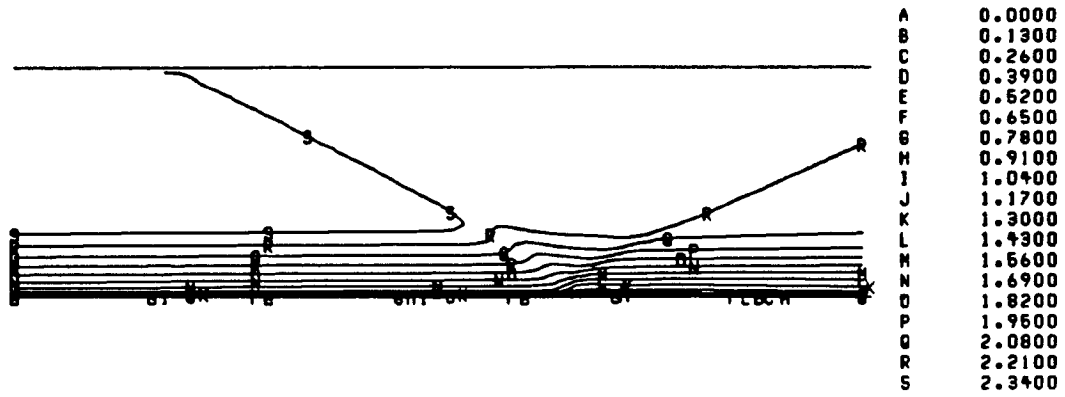


e) Static pressure profiles

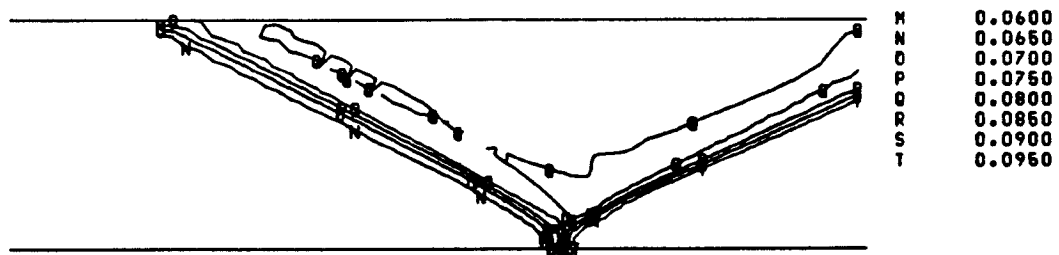


f) Mach number profiles

Fig. 49 CONTINUED

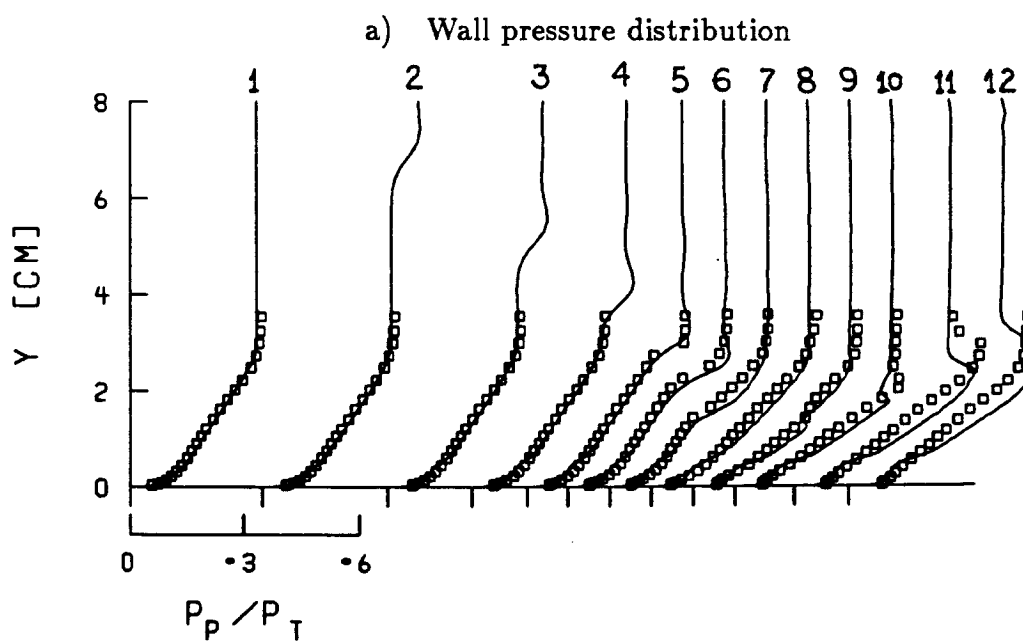
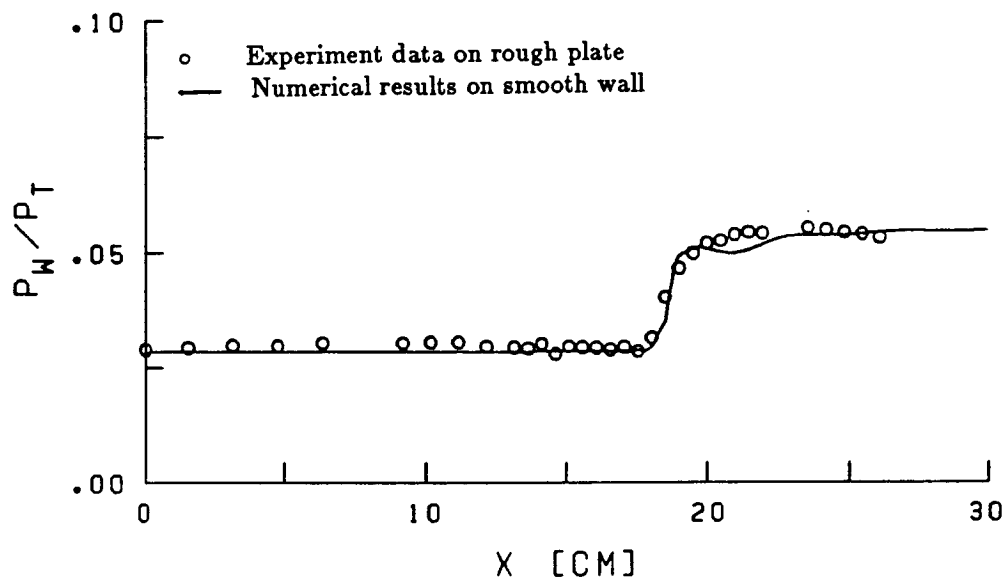


g) Mach number contours



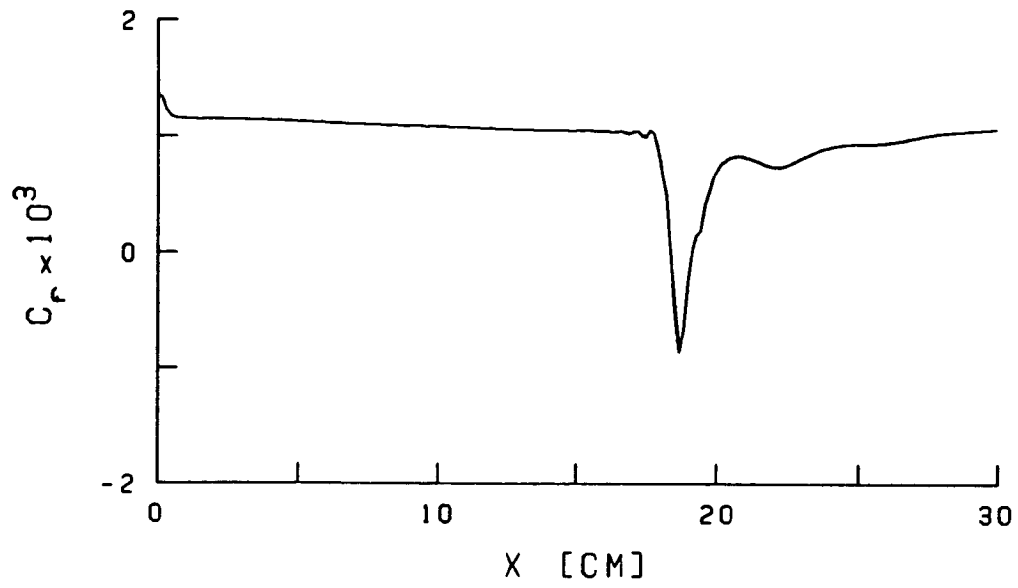
h) Static pressure contours

Fig. 49 CONCLUDED

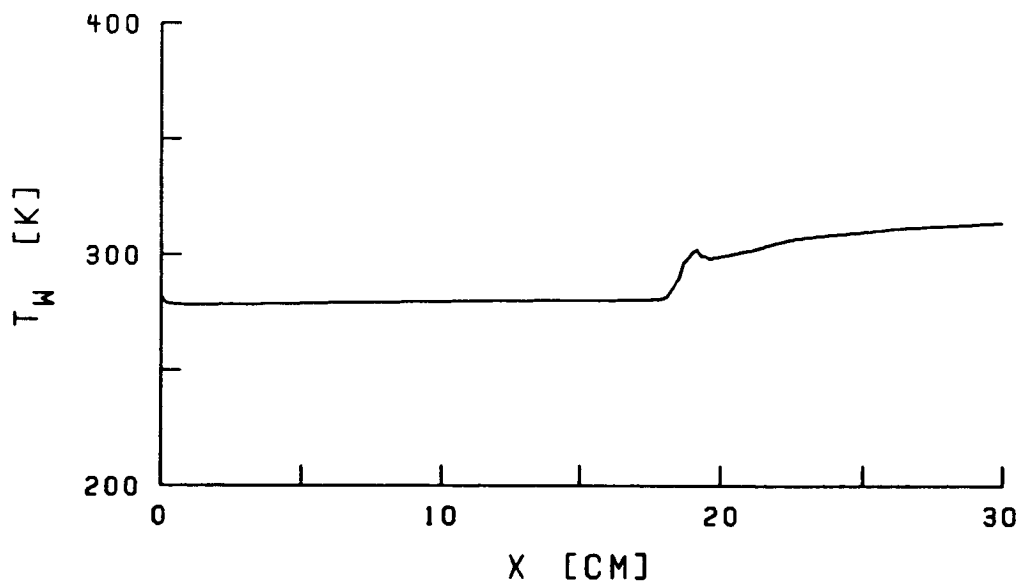


b) Pitot pressure profiles

Fig. 50 COMPARISONS OF COMPUTATIONS
WITH EXPERIMENTAL DATA;
 $M = 2.98$, $\alpha = 4.5^\circ$, AND NO BLEED

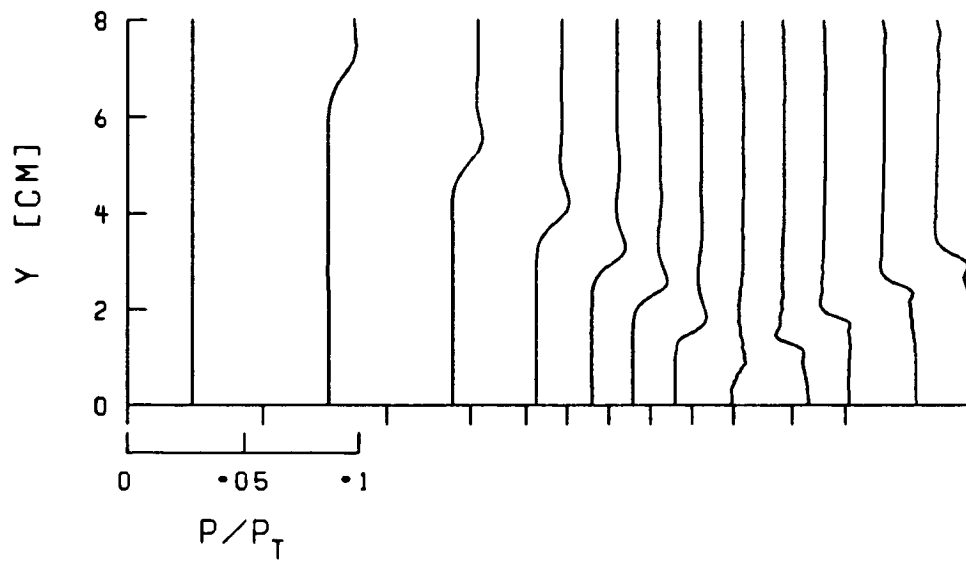


c) Skin friction

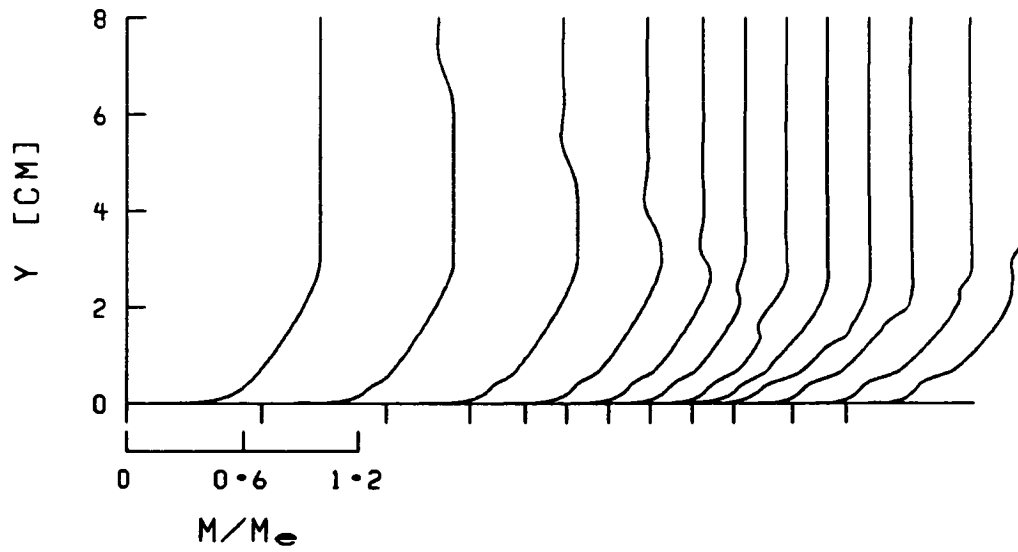


d) Wall temperature

Fig. 50 CONTINUED

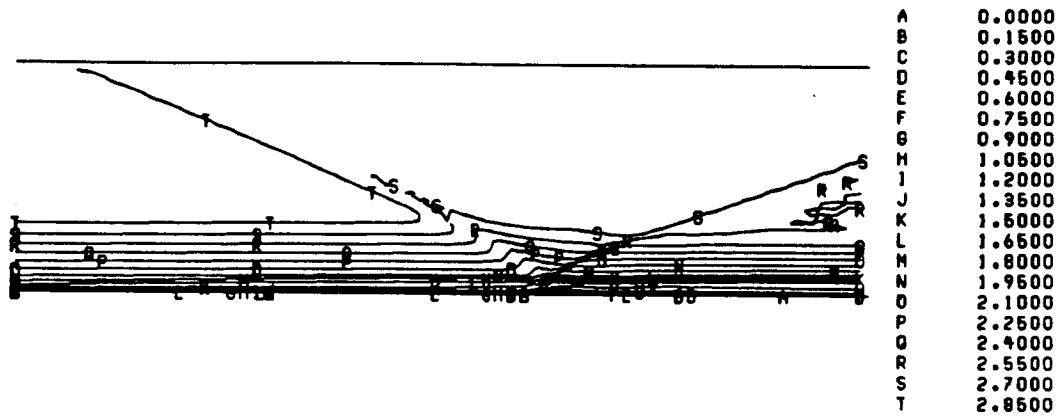


e) Static pressure profiles

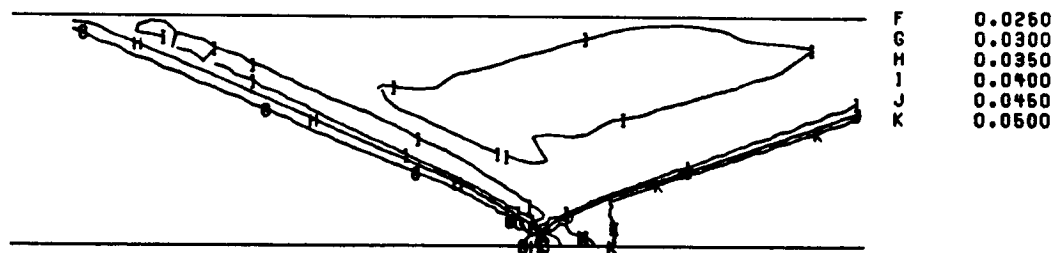


f) Mach number profiles

Fig. 50 CONTINUED

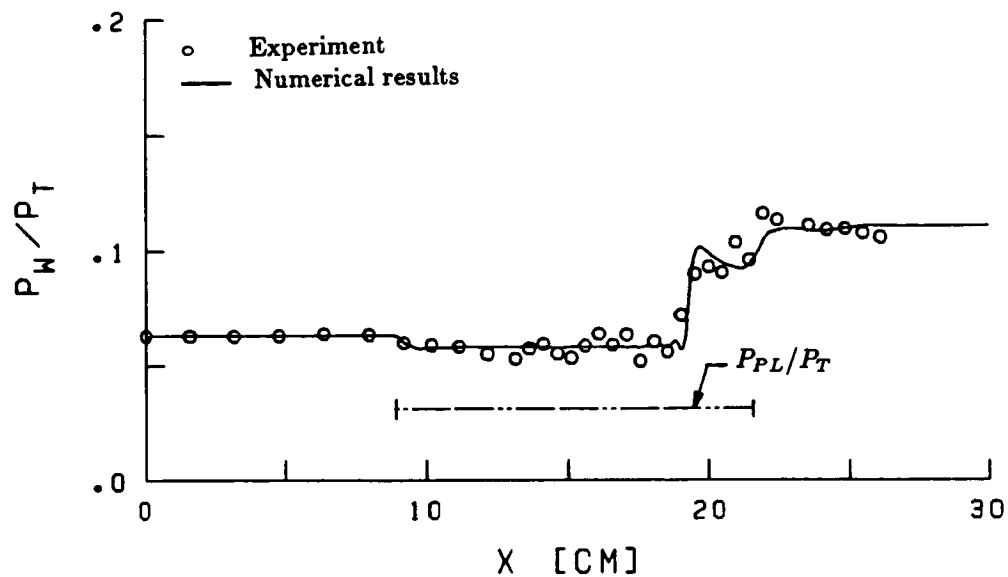


g) Mach number contours

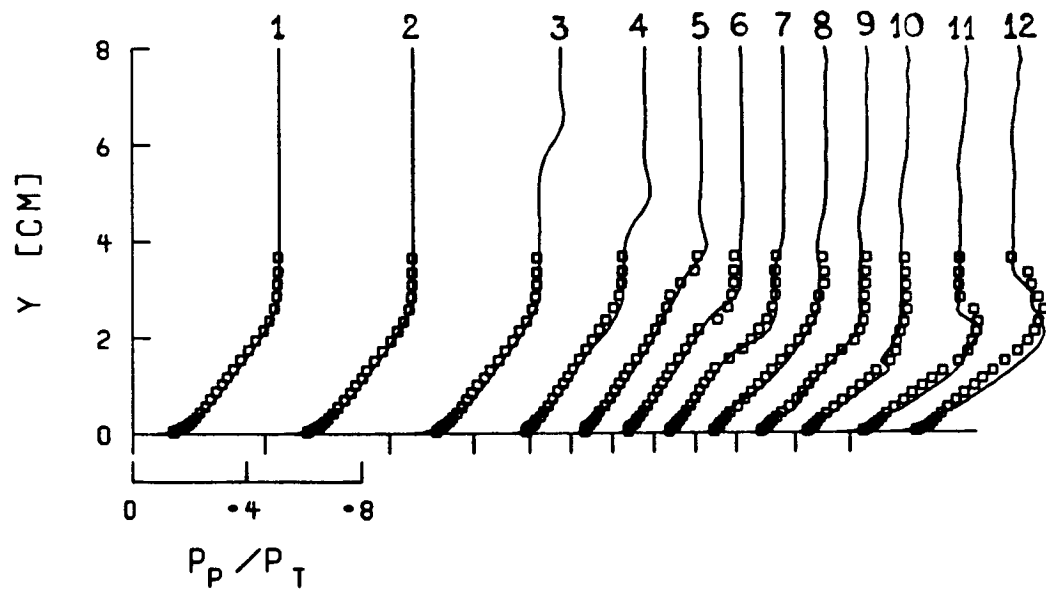


h) Static pressure contours

Fig. 50 CONCLUDED

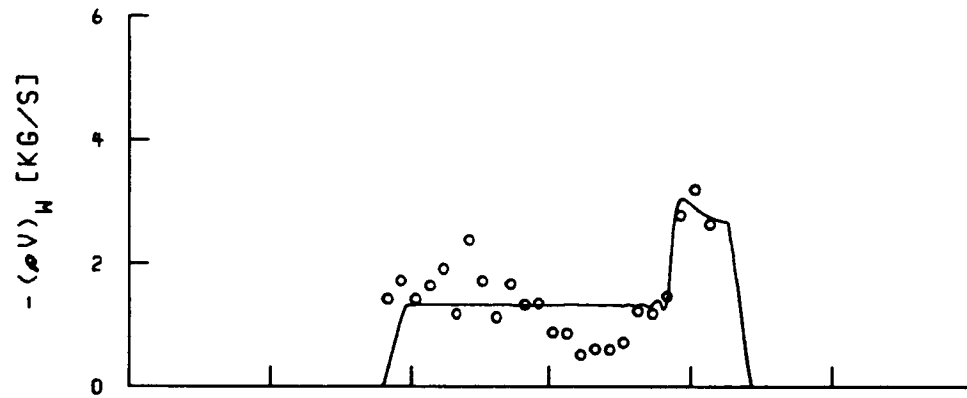


a) Wall pressure distribution

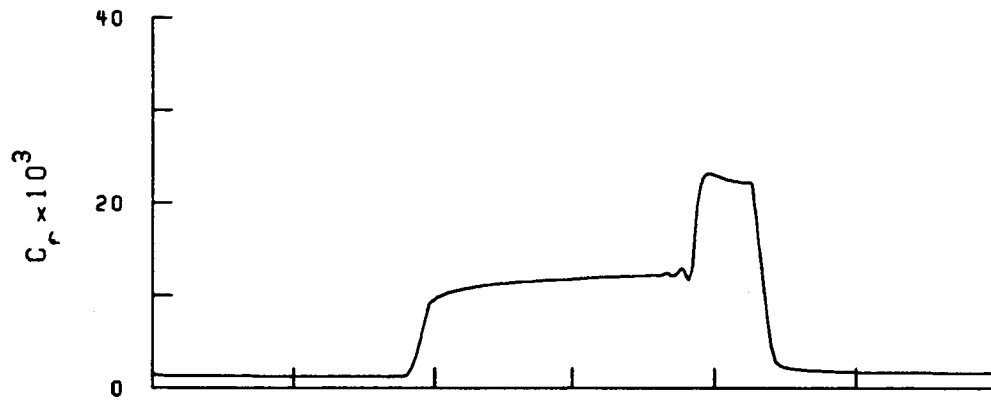


b) Pitot pressure profiles

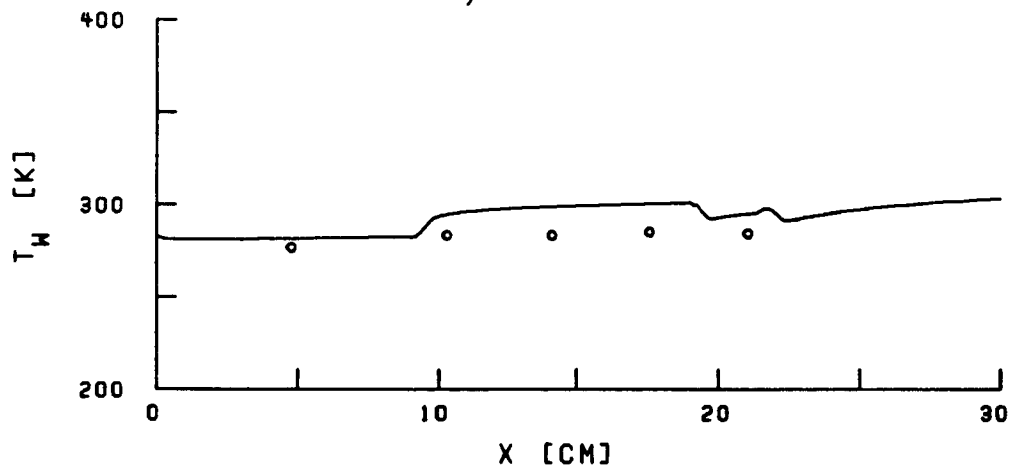
Fig. 51 COMPARISONS OF COMPUTATIONS
WITH EXPERIMENTAL DATA;
 $M = 2.46$, $\alpha = 4.5^\circ$, AND BLEED



c) Bleed distribution

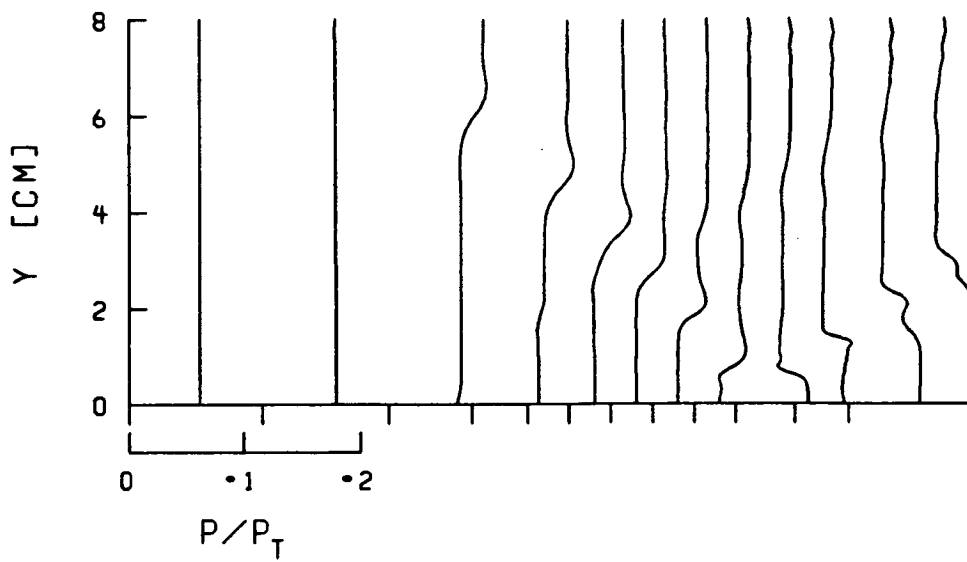


d) Skin friction

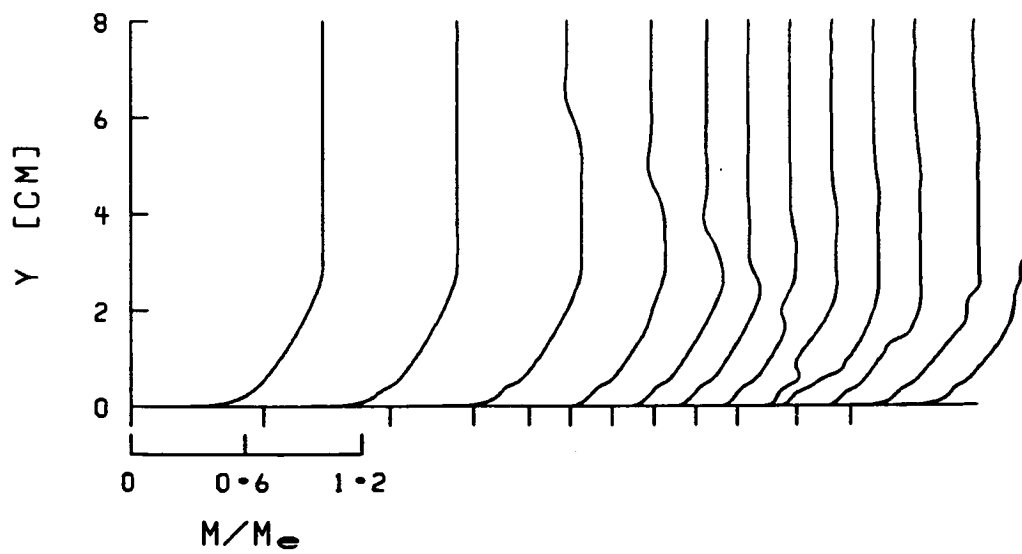


e) Wall temperature

Fig. 51 CONTINUED



f) Static pressure profiles



g) Mach number profiles

Fig. 51 CONTINUED

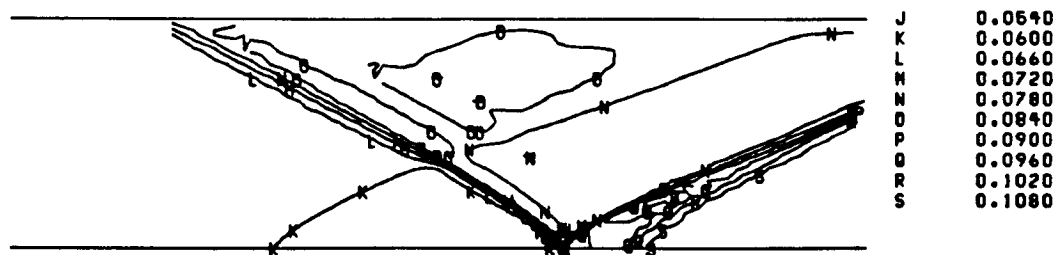
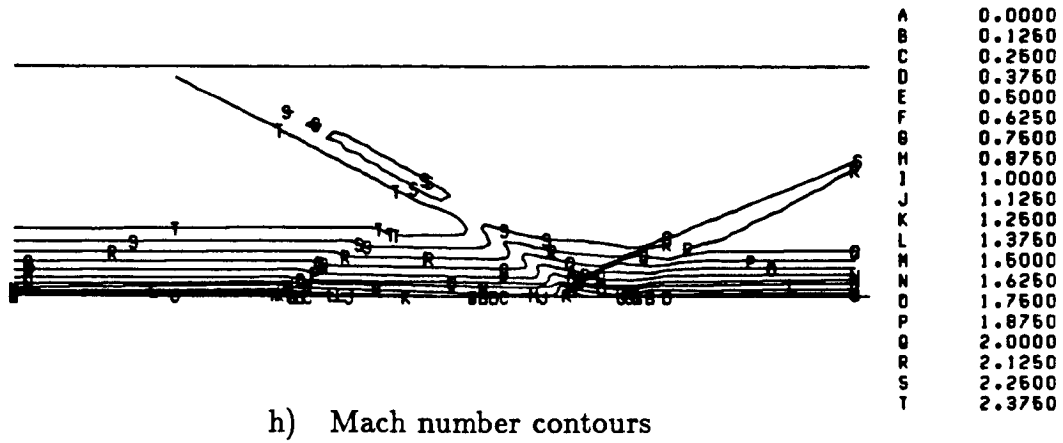
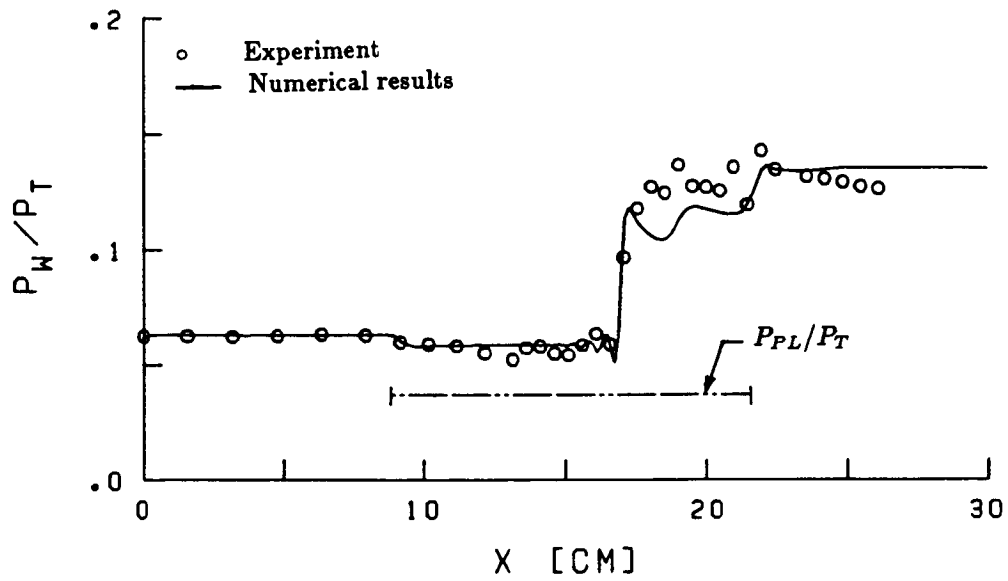
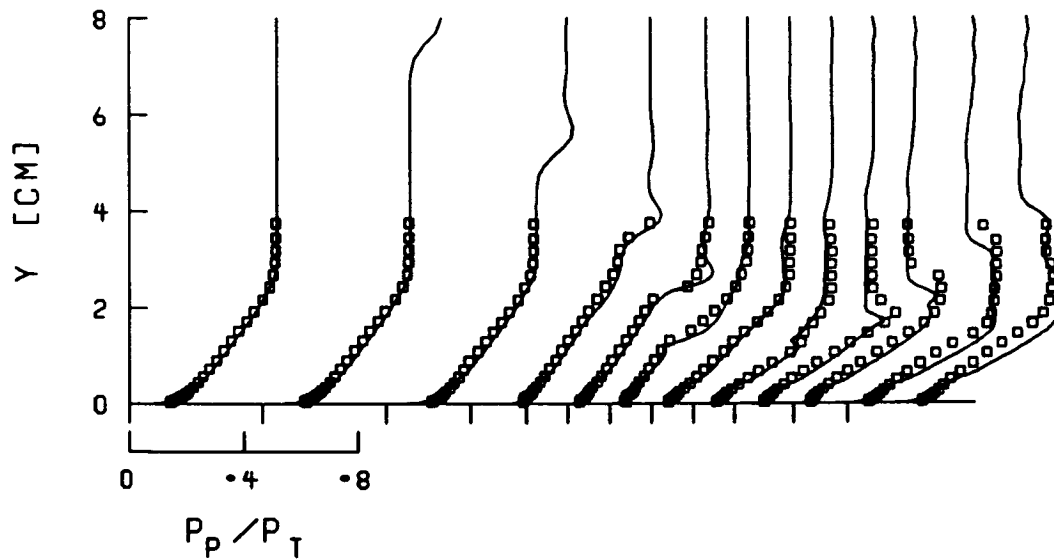


Fig. 51 CONCLUDED



a) Wall pressure distribution



b) Pitot pressure profiles

Fig. 52 COMPARISONS OF COMPUTATIONS
WITH EXPERIMENTAL DATA;
 $M = 2.46$, $\alpha = 6.5^\circ$, AND BLEED

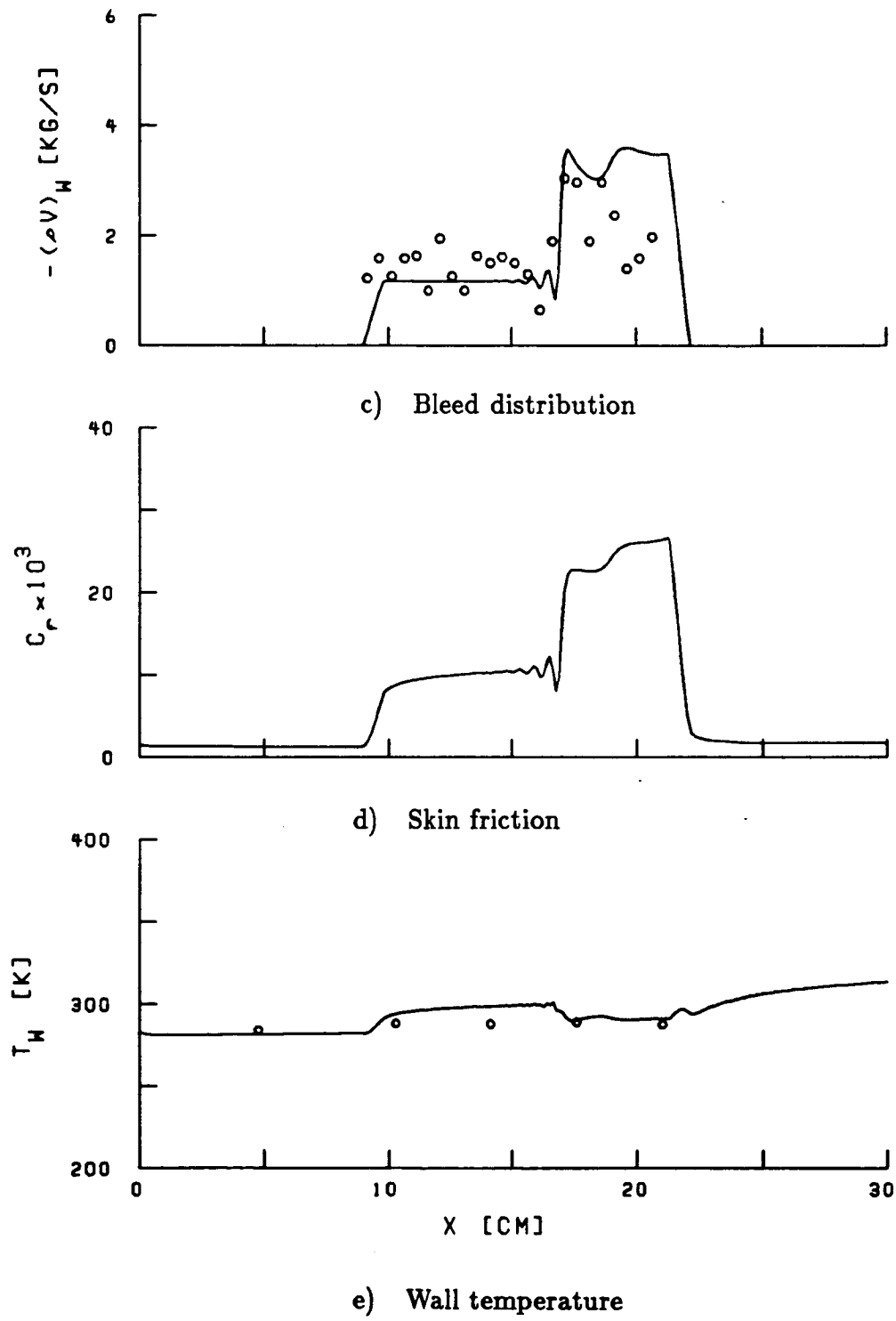
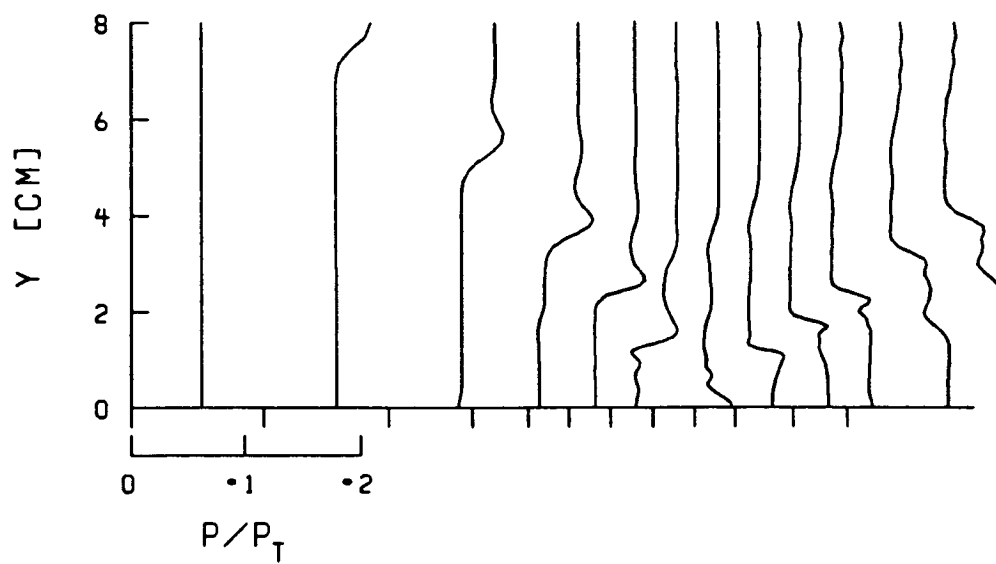
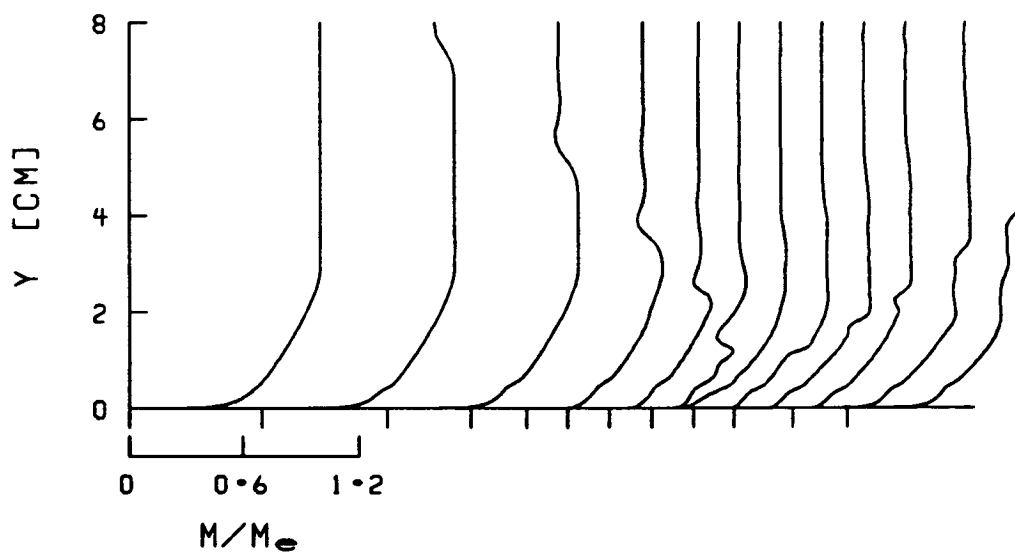


Fig. 52 CONTINUED



f) Static pressure profiles



g) Mach number profiles

Fig. 52 CONTINUED

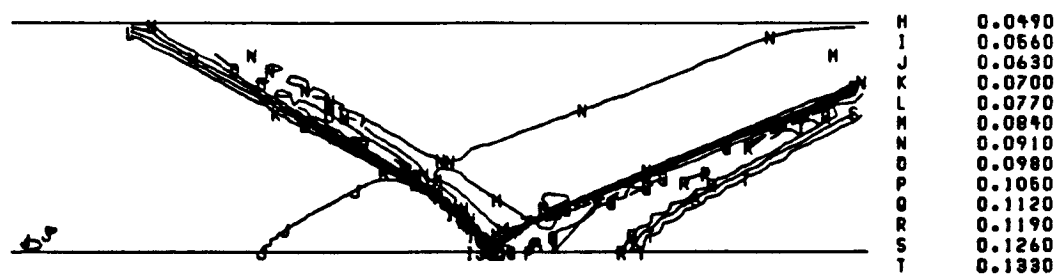
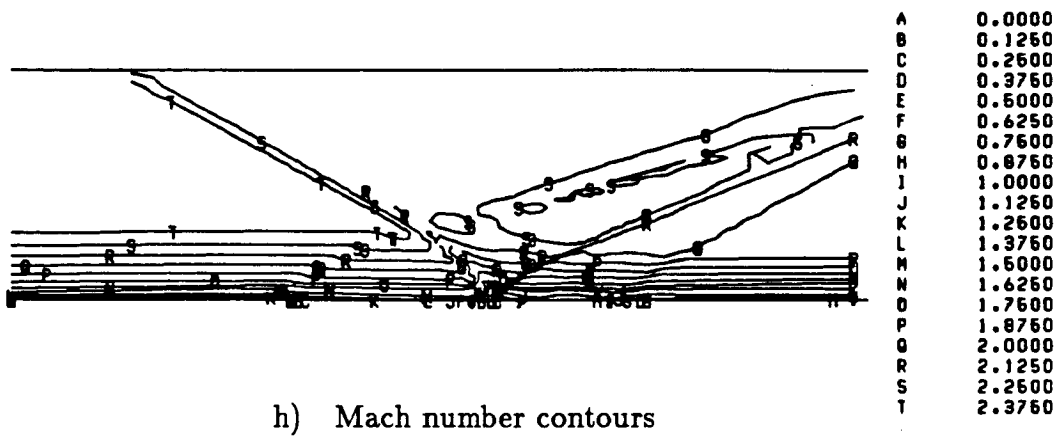
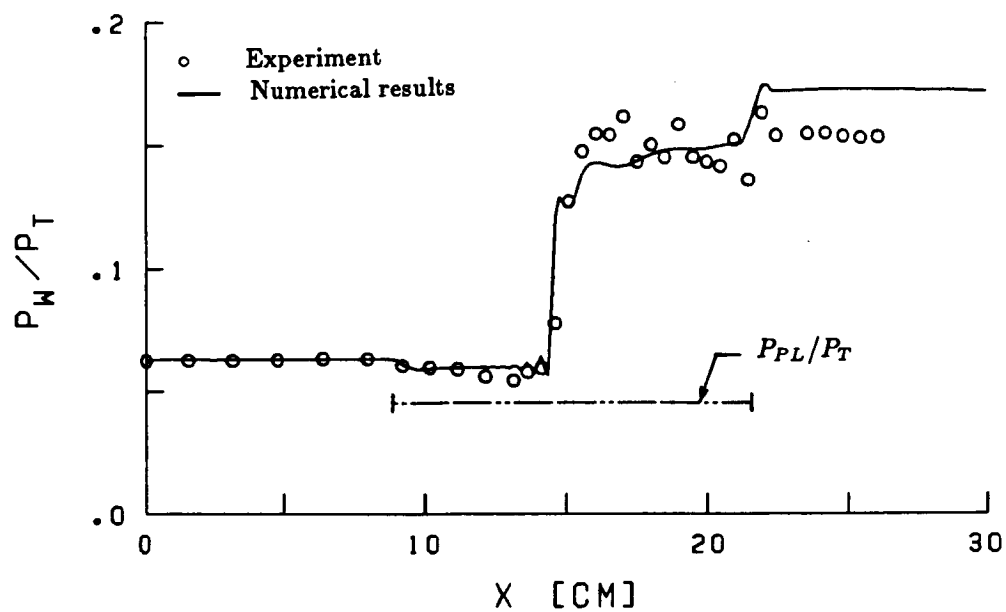
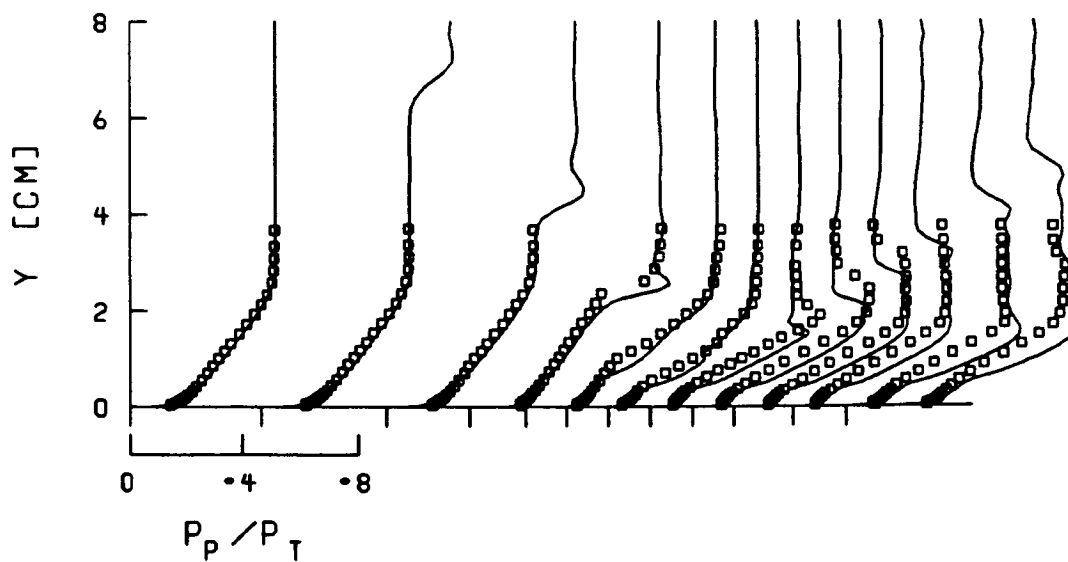


Fig. 52 CONCLUDED



a) Wall pressure distribution



b) Pitot pressure profiles

Fig. 53 COMPARISONS OF COMPUTATIONS
WITH EXPERIMENTAL DATA;
 $M = 2.46$, $\alpha = 8.5^\circ$, AND BLEED

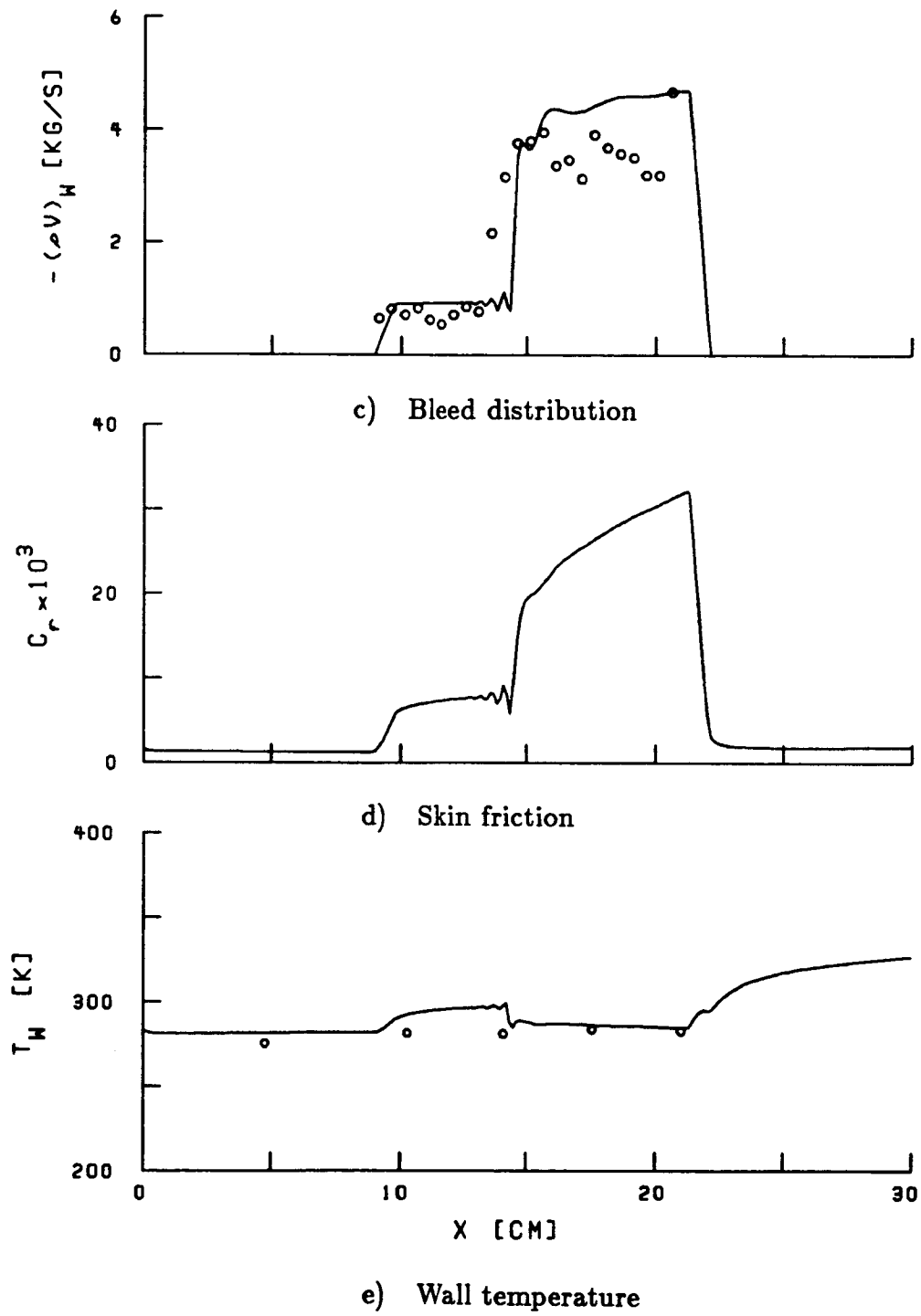
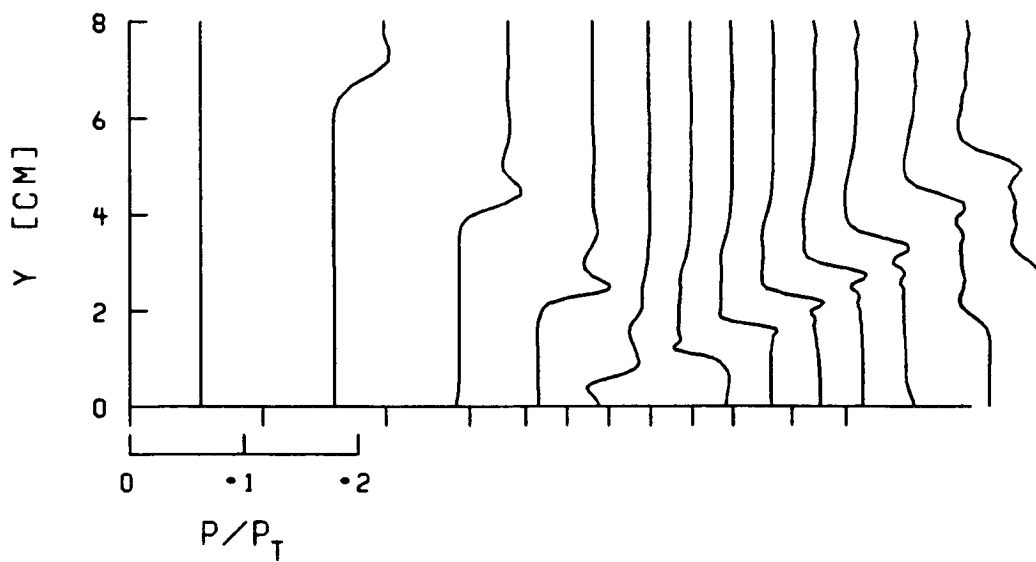
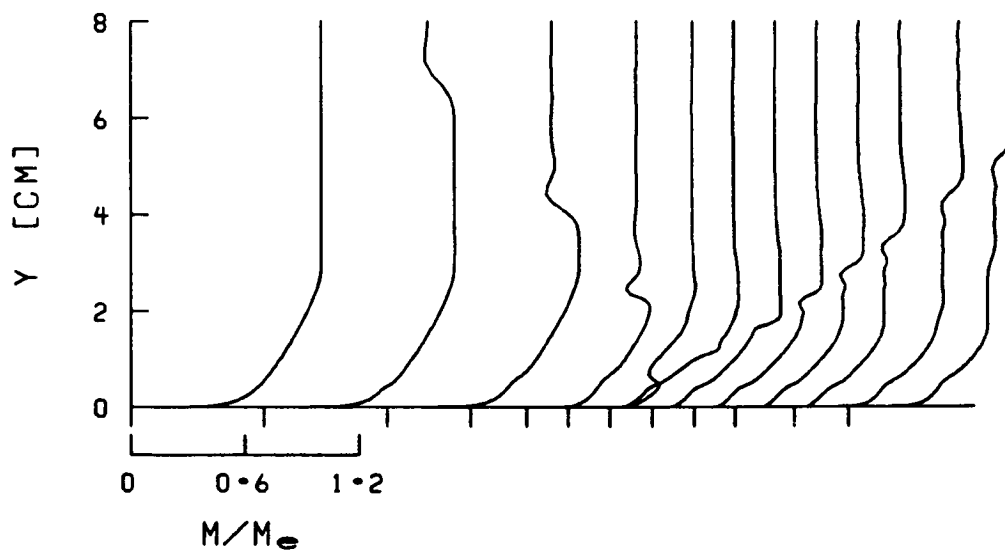


Fig. 53 CONTINUED



f) Static pressure profiles



g) Mach number profiles

Fig. 53 CONTINUED

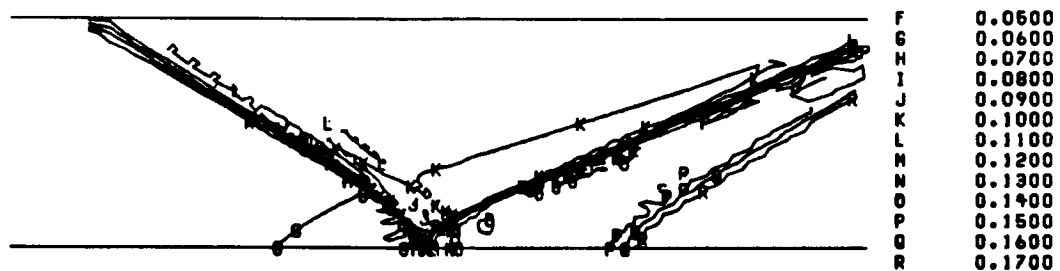
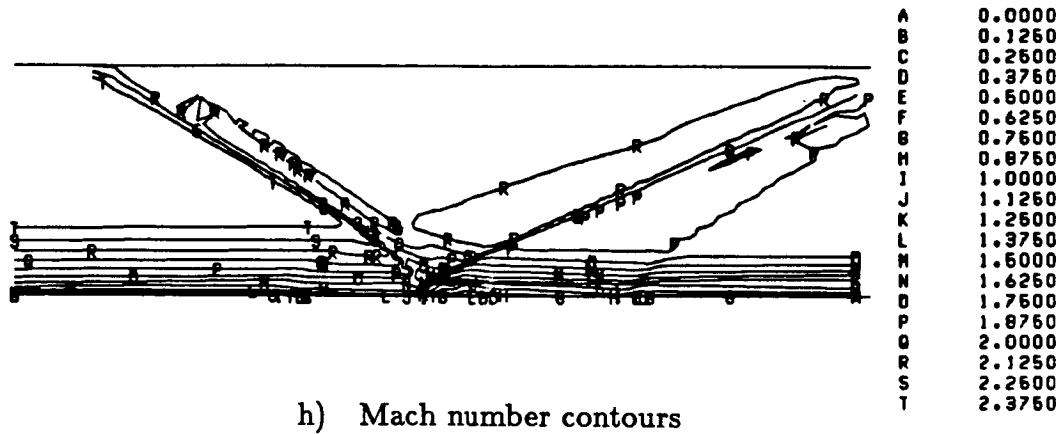
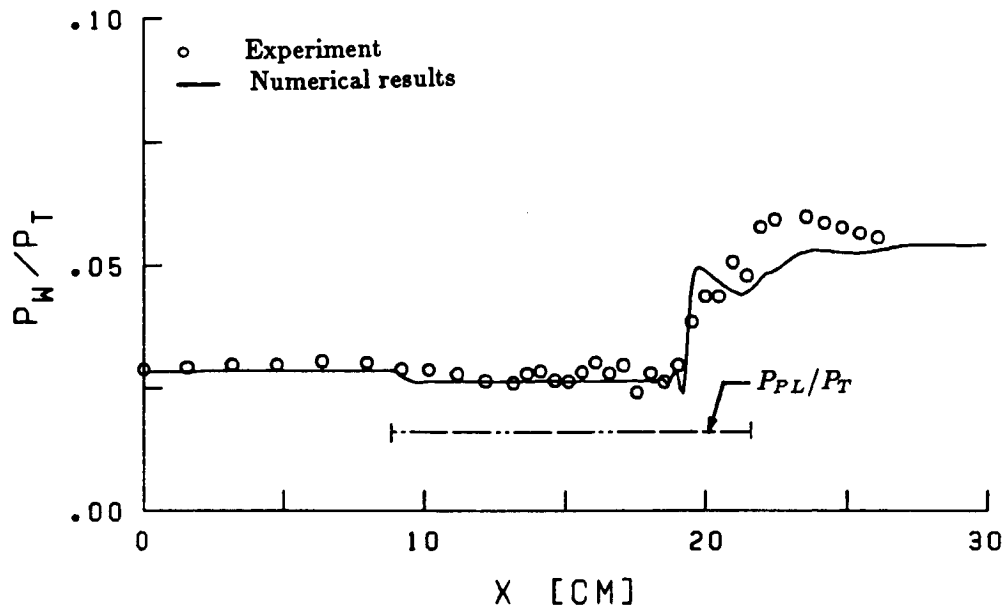
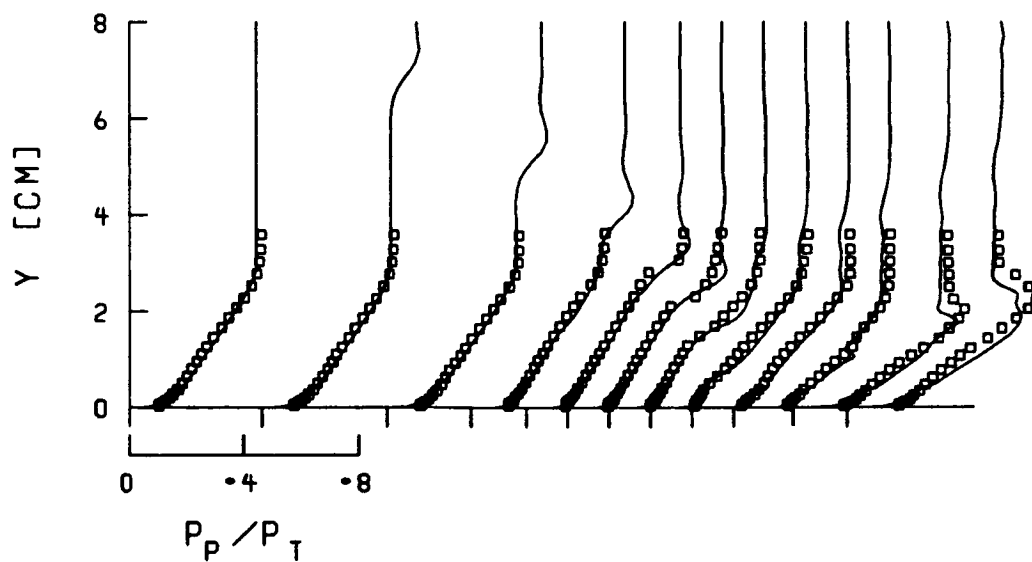


Fig. 53 CONCLUDED



a) Wall pressure distribution



b) Pitot pressure profiles

Fig. 54 COMPARISONS OF COMPUTATIONS
WITH EXPERIMENTAL DATA;
 $M = 2.98$, $\alpha = 4.5^\circ$, AND BLEED

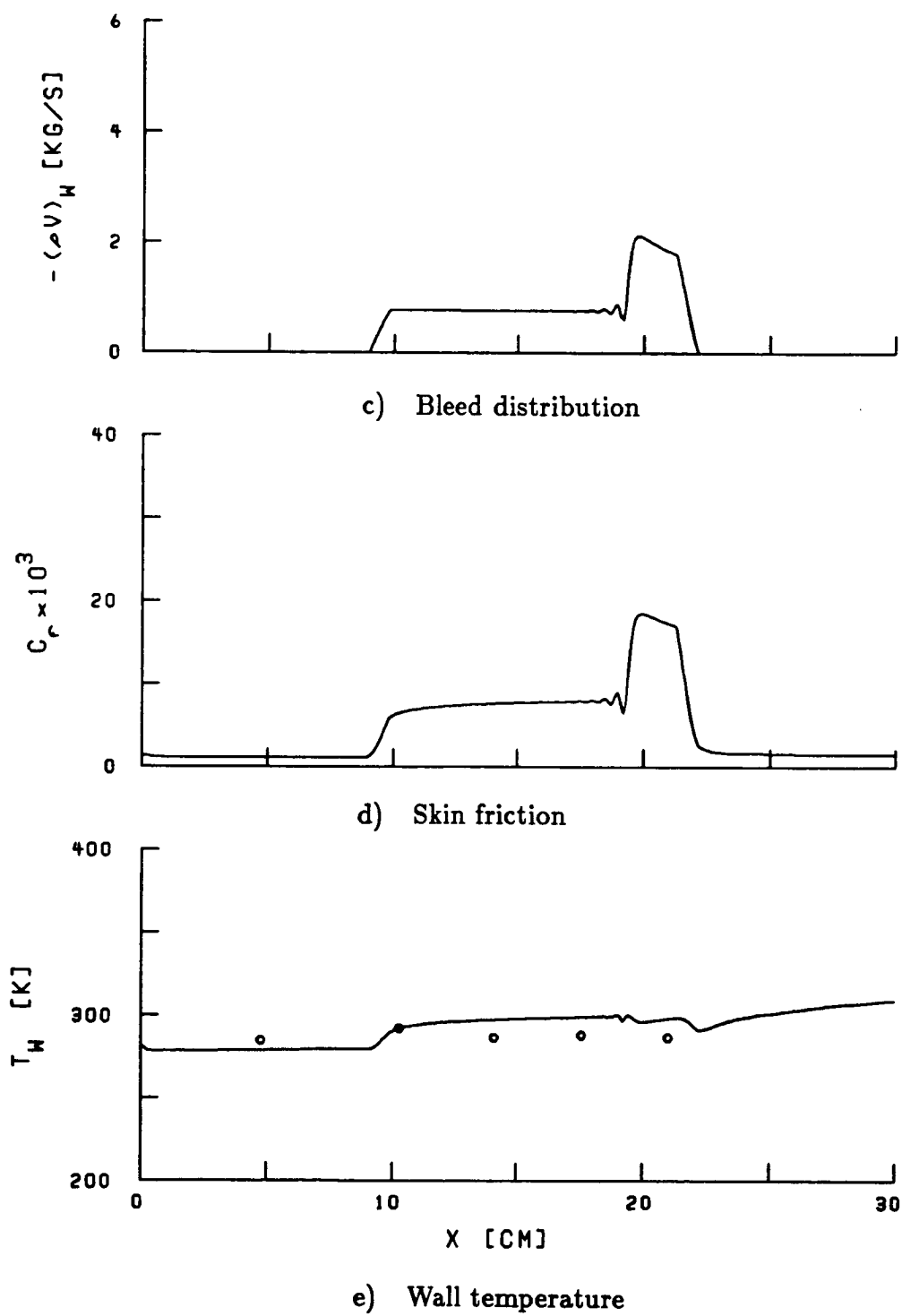
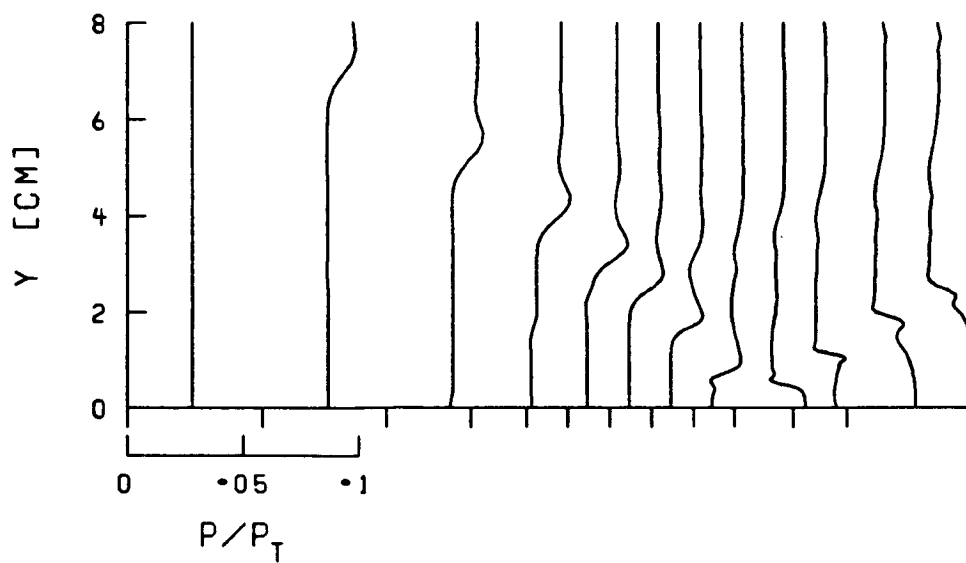
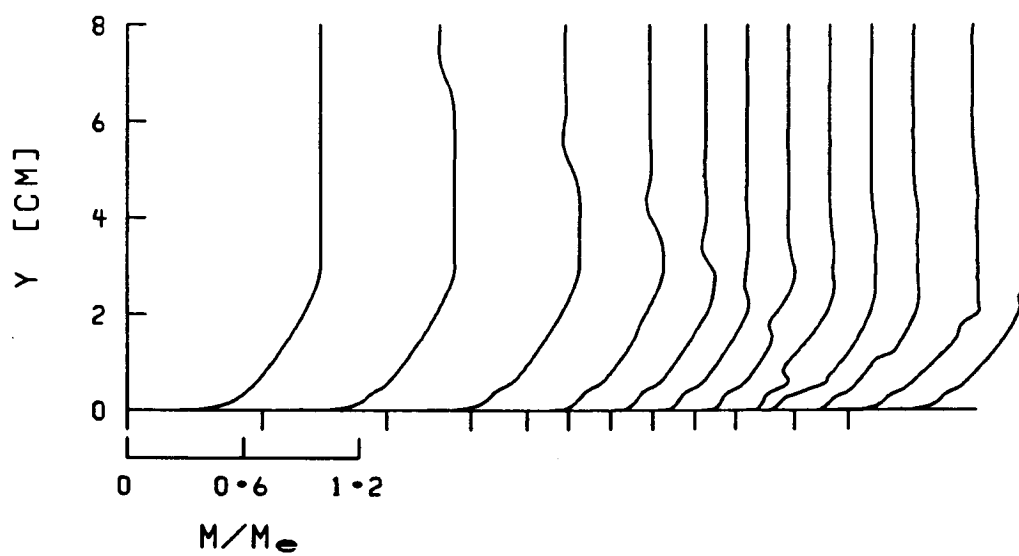


Fig. 54 CONTINUED



f) Static pressure profiles



g) Mach number profiles

Fig. 54 CONTINUED

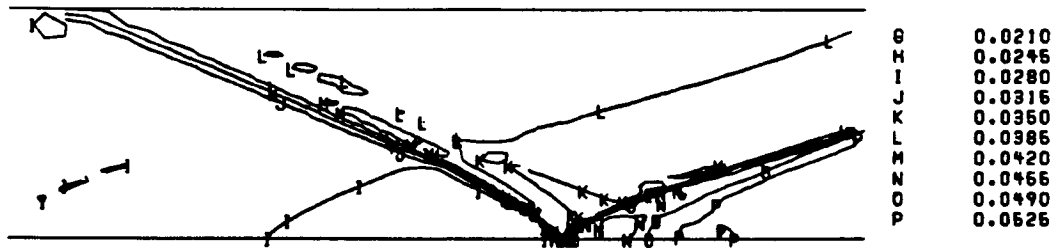
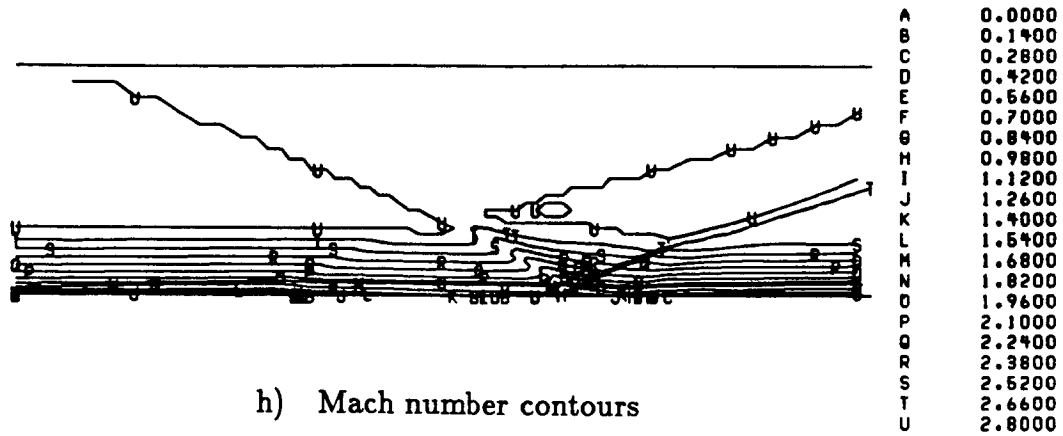
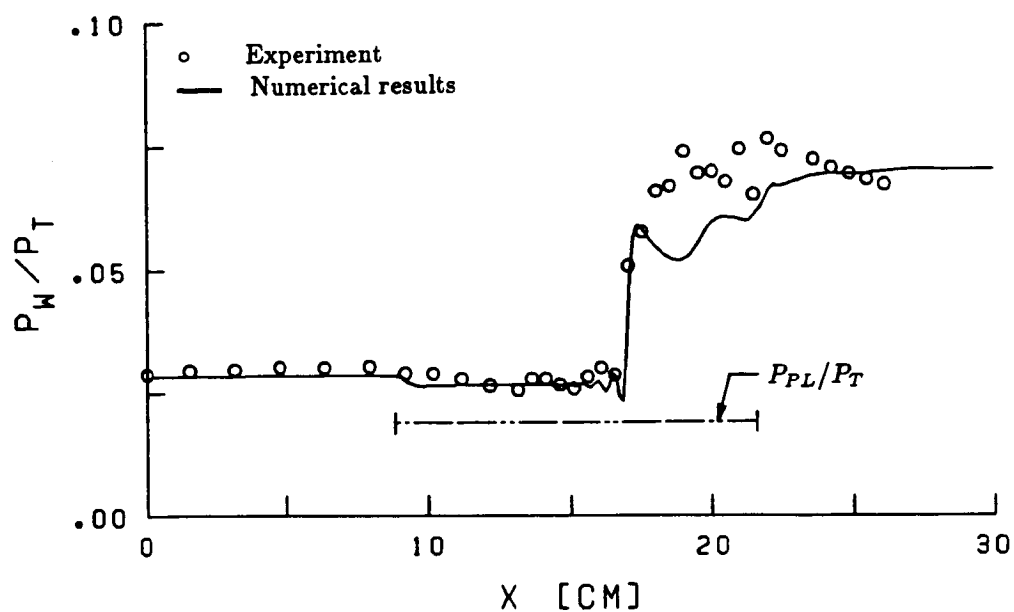
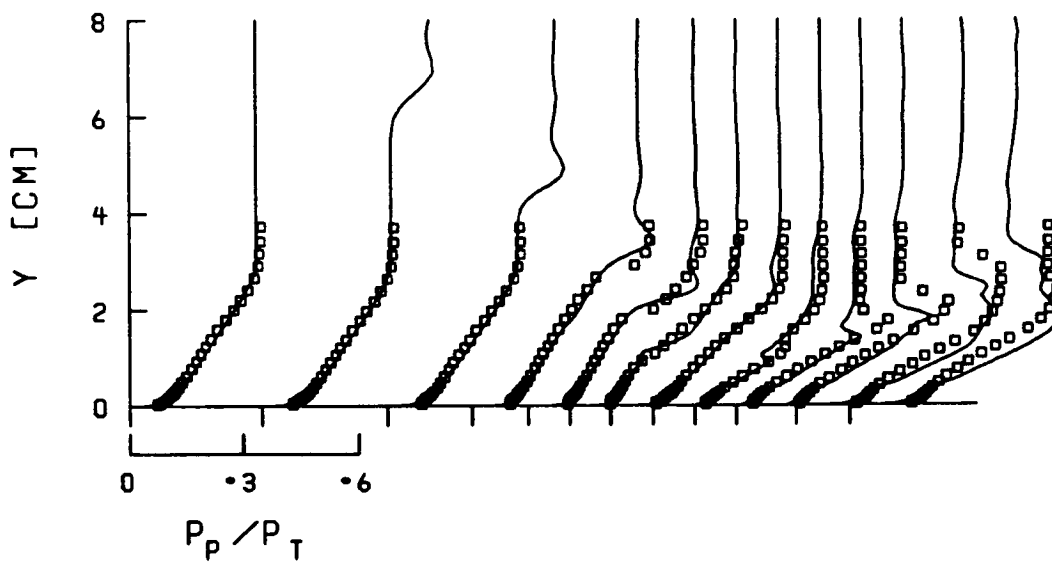


Fig. 54 CONCLUDED

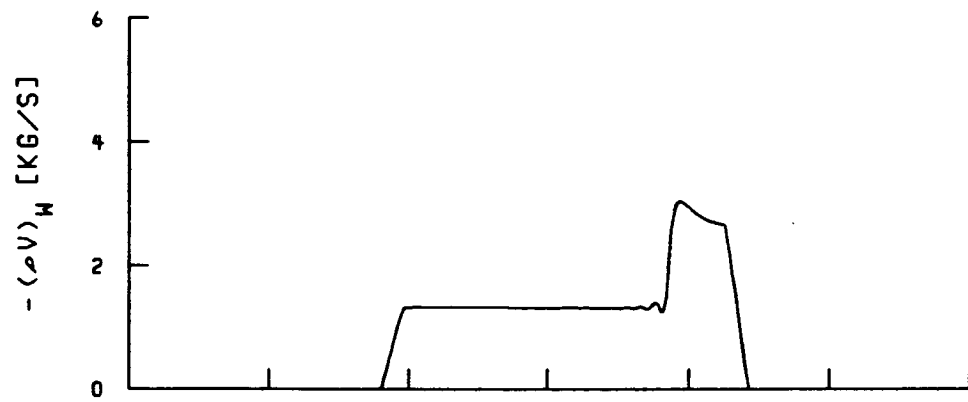


a) Wall pressure distribution

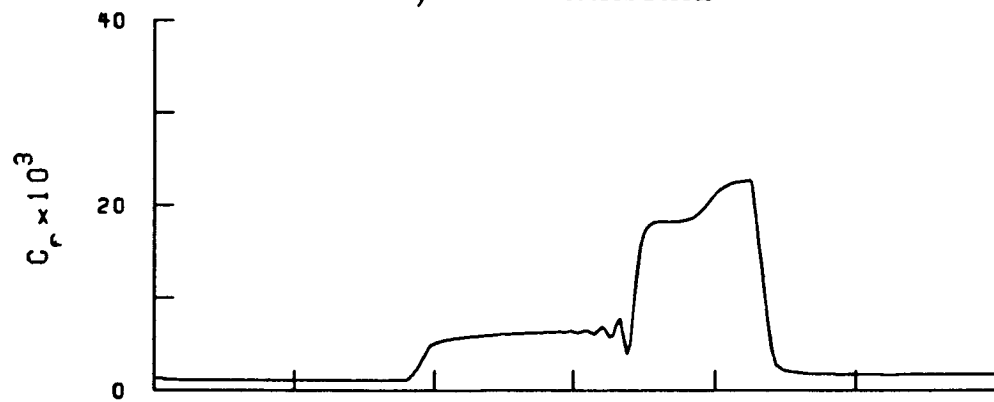


b) Pitot pressure profiles

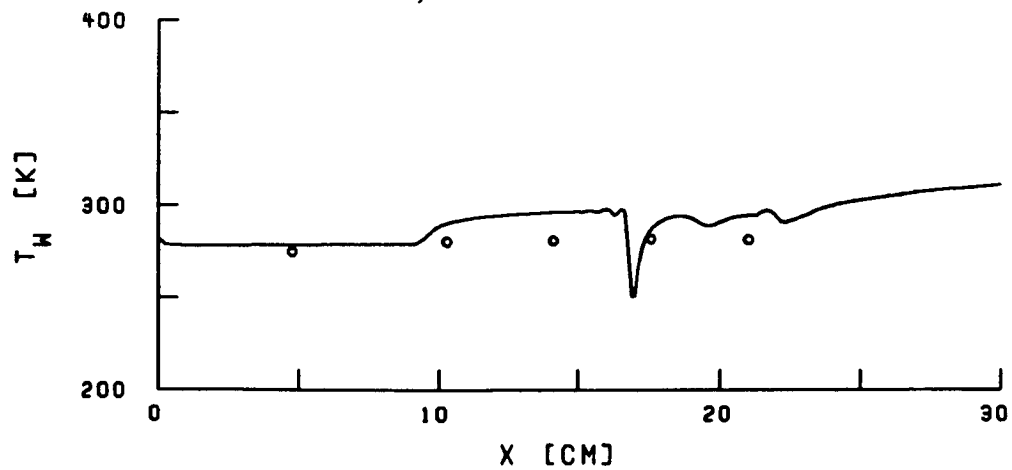
Fig. 55 COMPARISONS OF COMPUTATIONS
WITH EXPERIMENTAL DATA;
 $M = 2.98$, $\alpha = 6.5^\circ$, AND BLEED



c) Bleed distribution

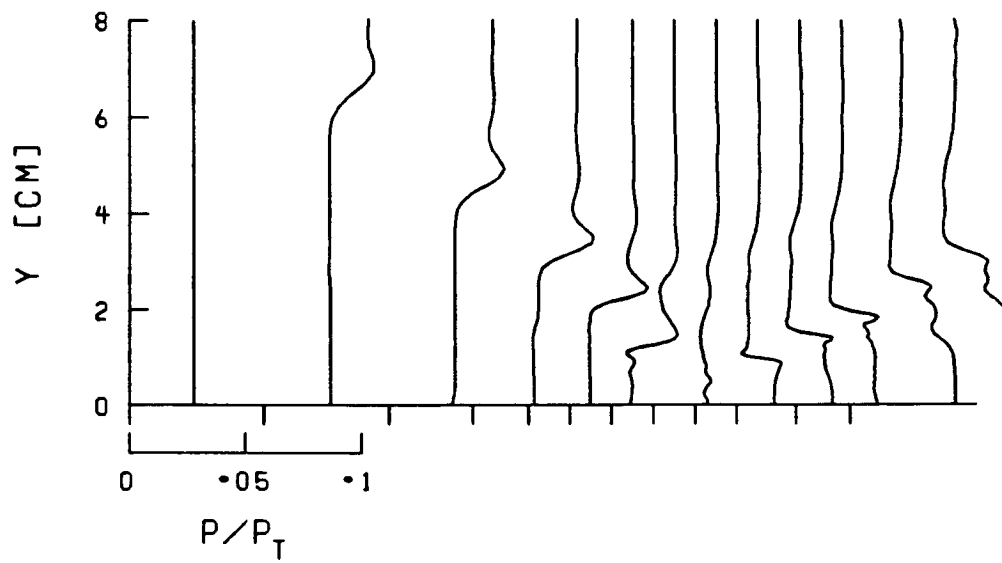


d) Skin friction

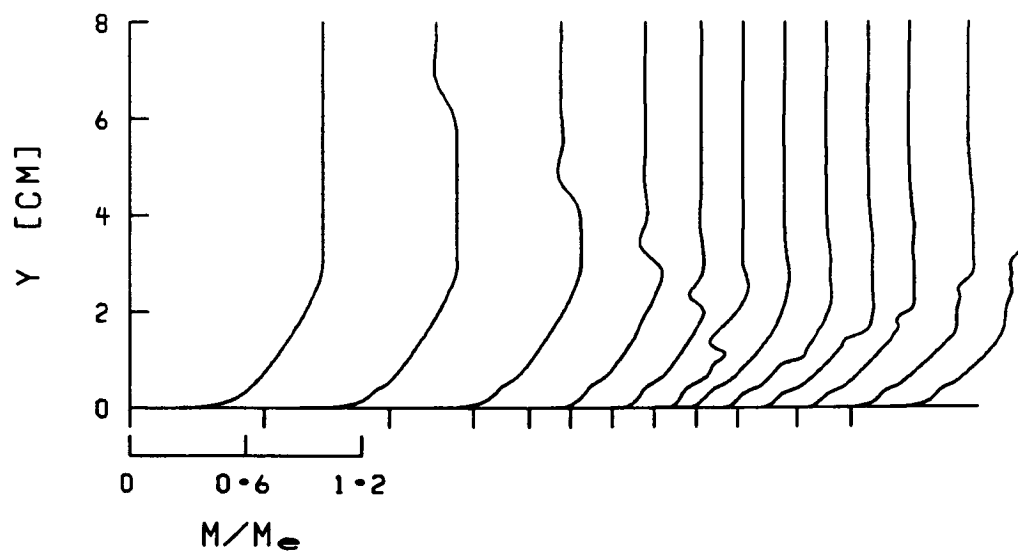


e) Wall temperature

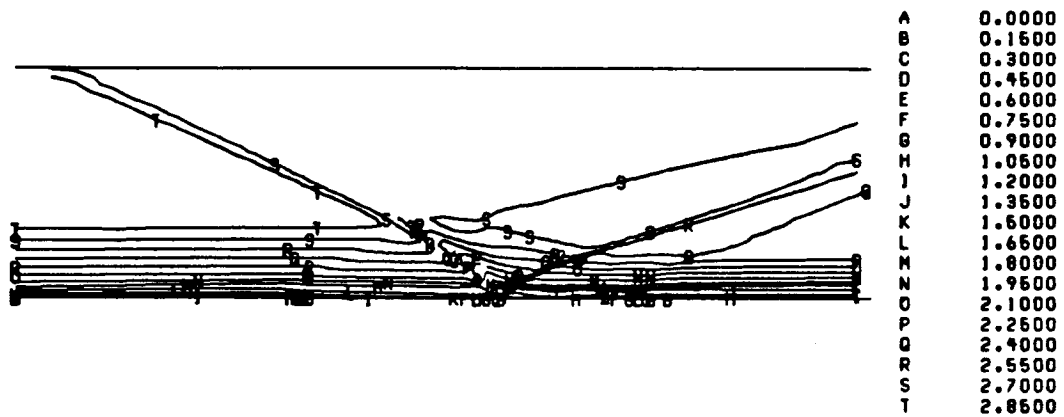
Fig. 55 CONTINUED



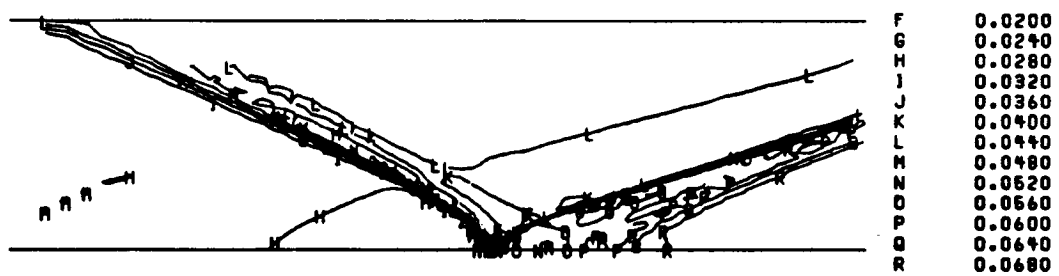
f) Static pressure profiles



g) Mach number profiles



h) Mach number contours



i) Static pressure contours

Fig. 55 CONCLUDED

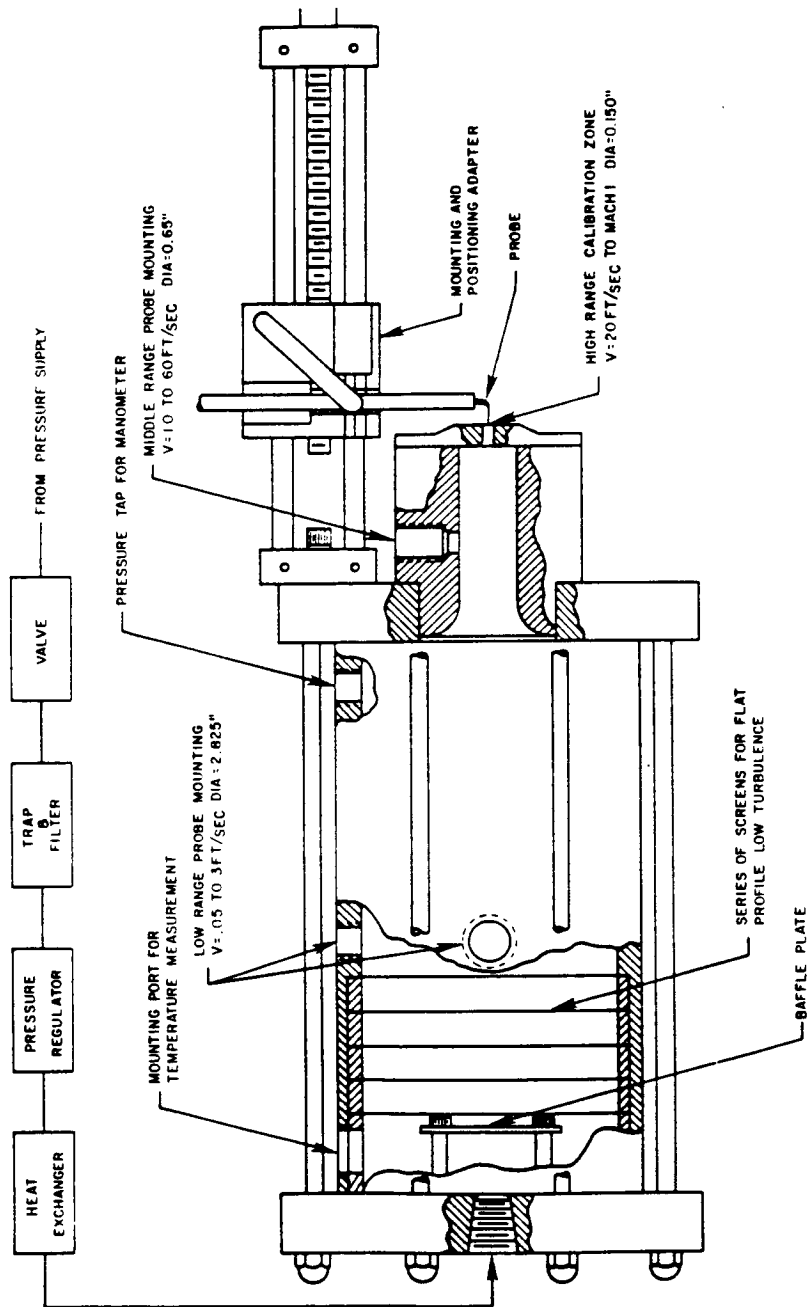


Fig. B1 HOT-WIRE CALIBRATION SYSTEM

ORIGINAL PAGE IS
OF POOR QUALITY

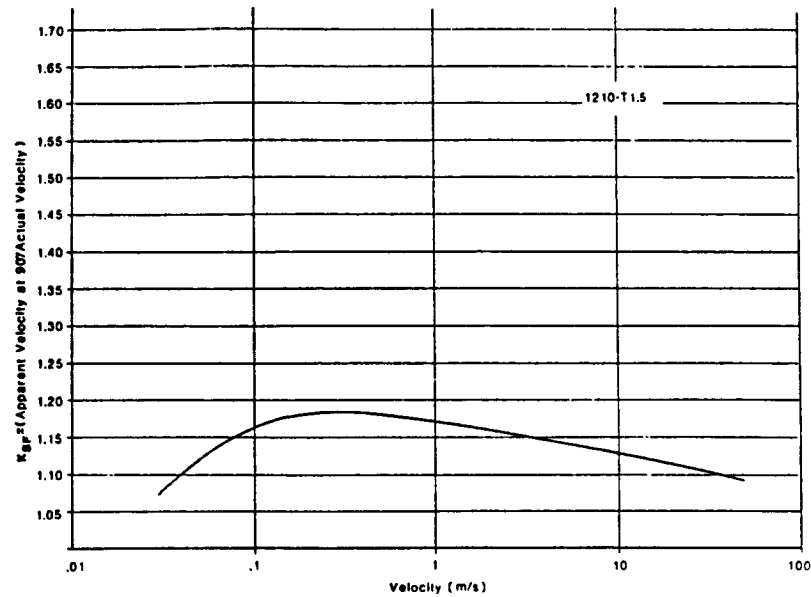
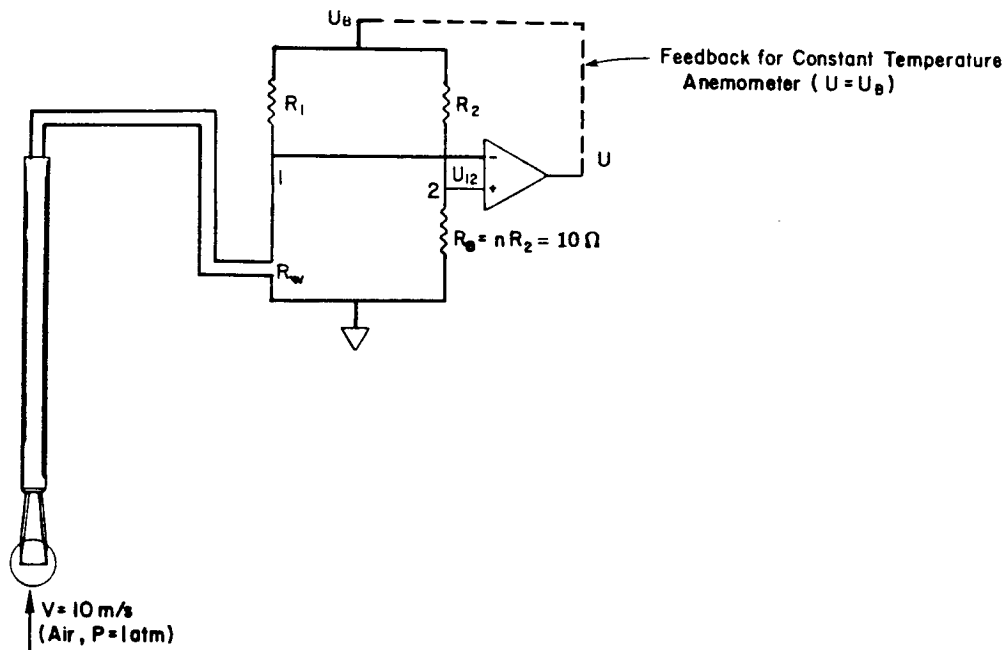


Fig. B2 PITCH CORRECTION FACTOR

Fig. B3 BASIC ELEMENTS OF A
HOT-WIRE ANEMOMETER

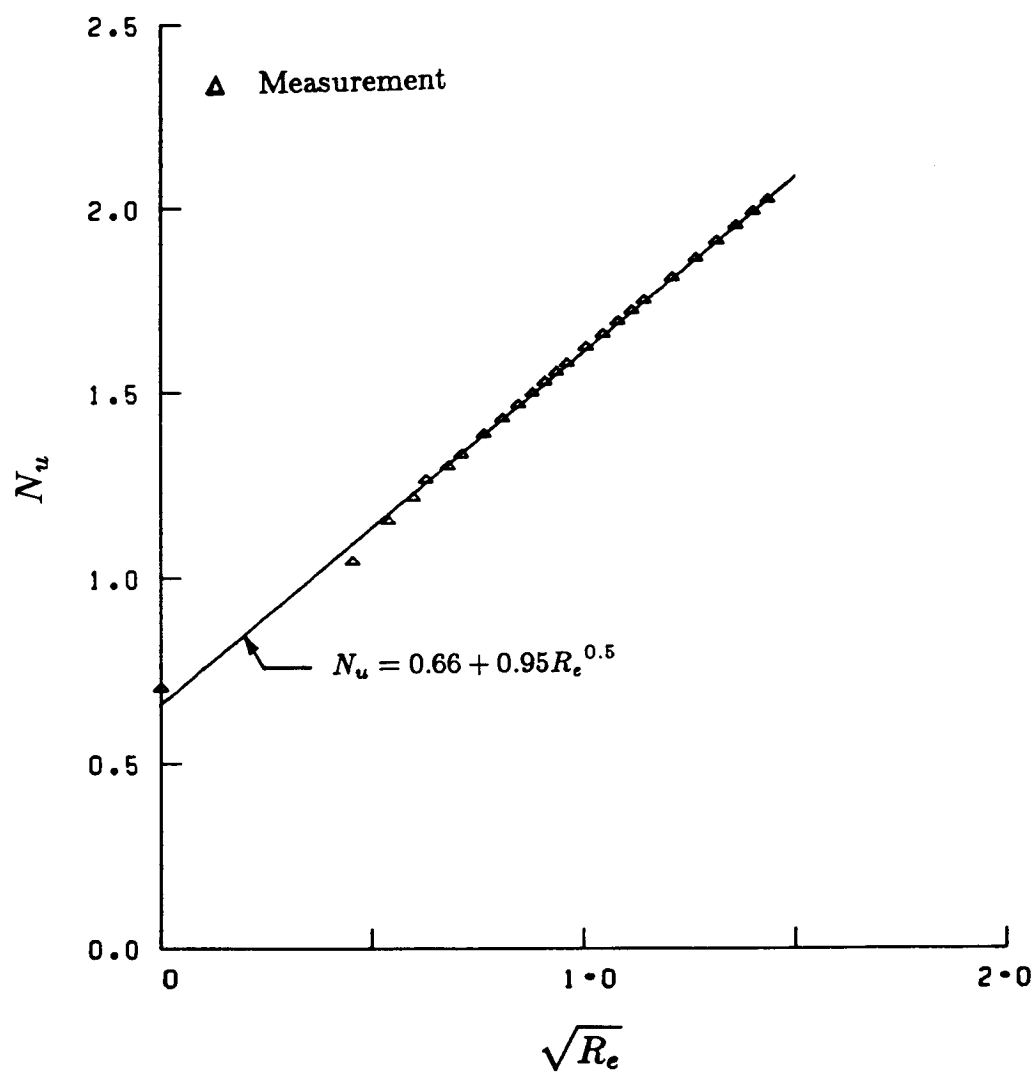


Fig. B4 HOT-WIRE CALIBRATION CURVE

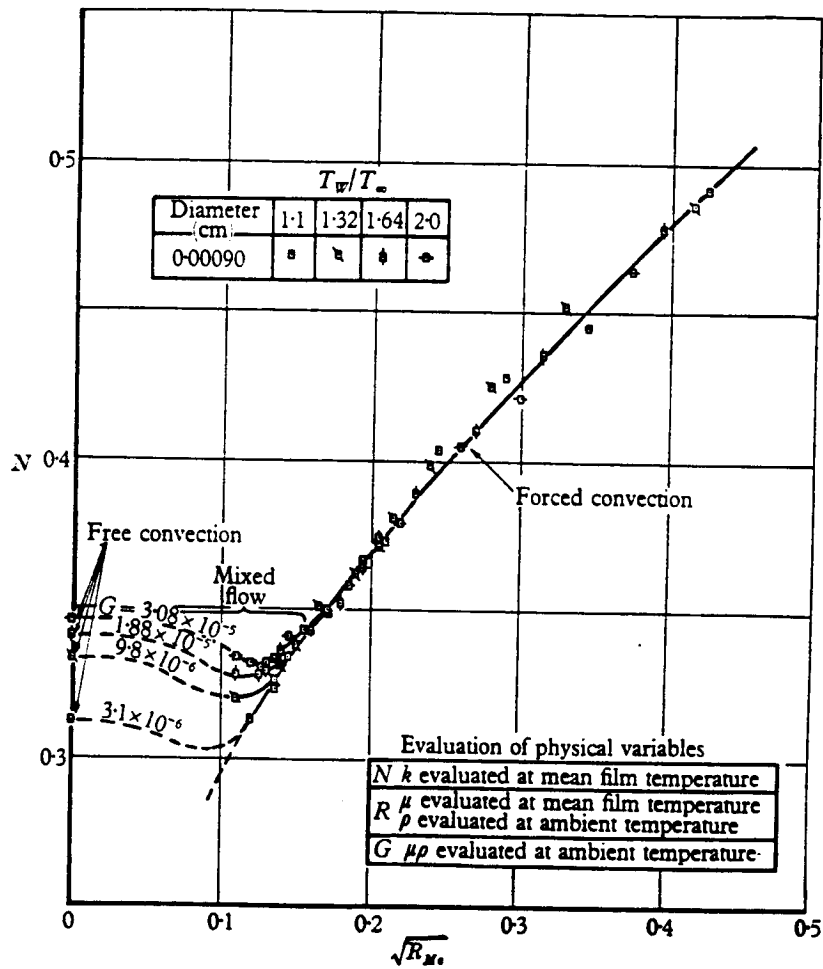


Fig. B5 INTERACTION OF FREE AND FORCED CONVECTION (REF [51])

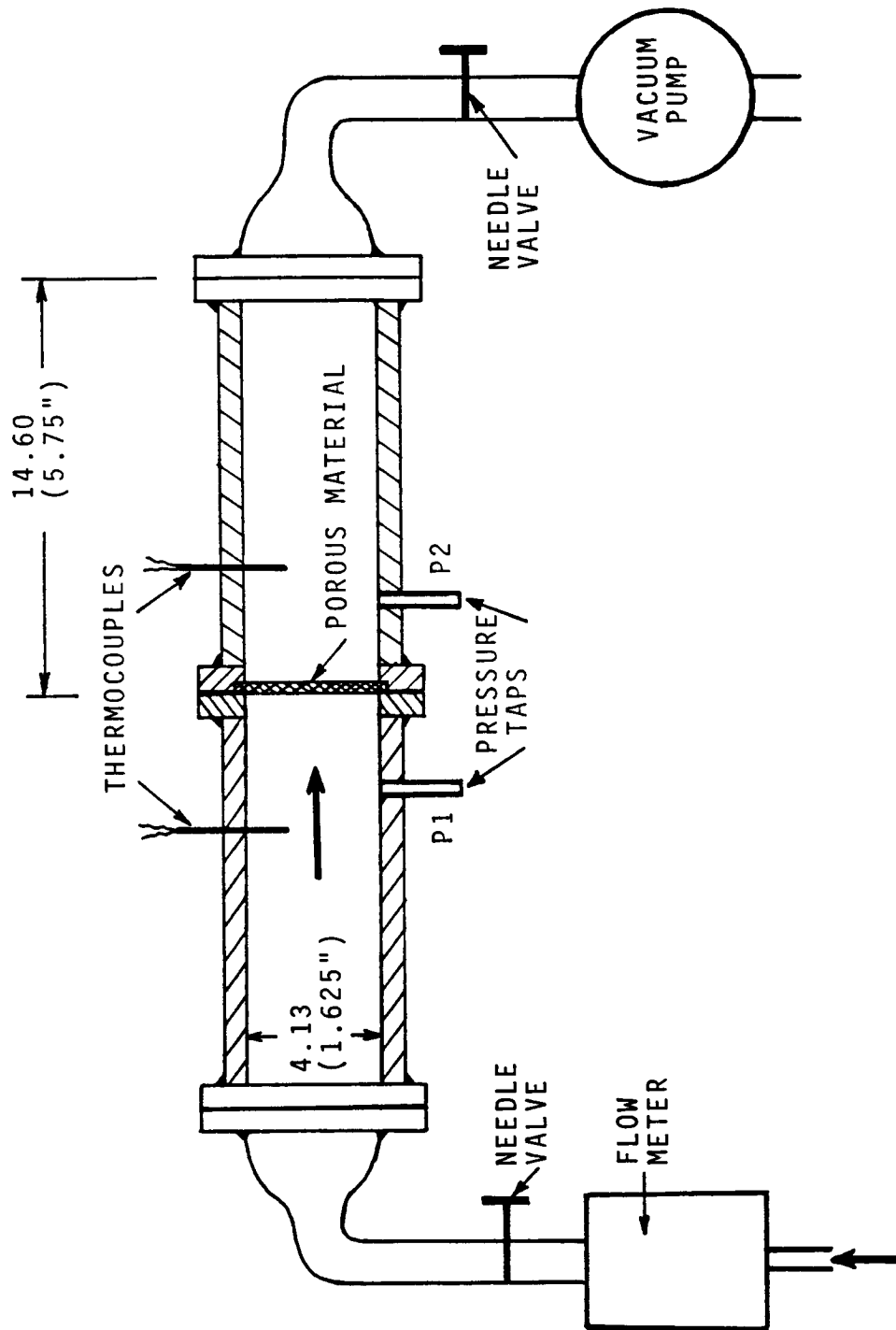


Fig. C1 NORMAL FLOW CALIBRATION APPARATUS

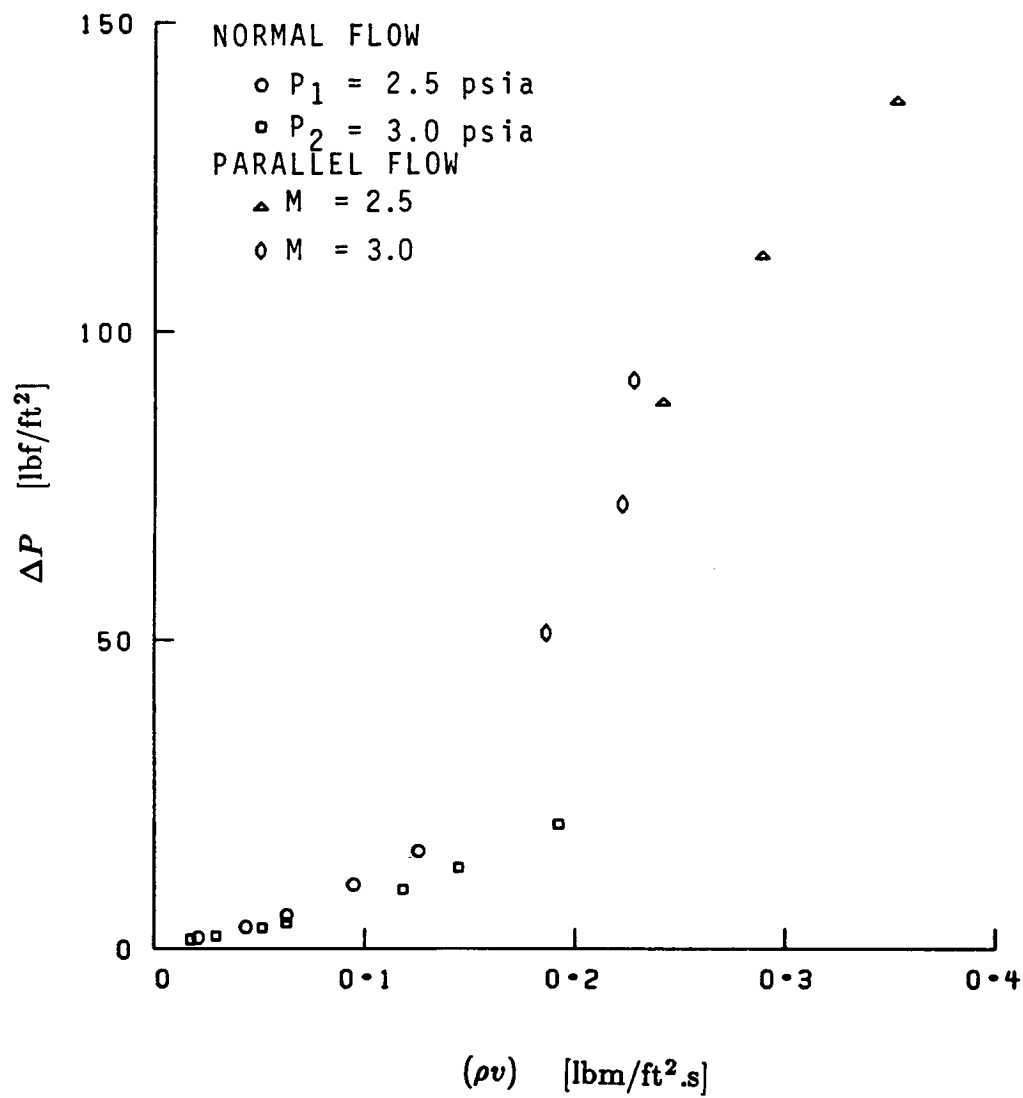


Fig. C2 PRESSURE DROP V.S. MASS FLUX

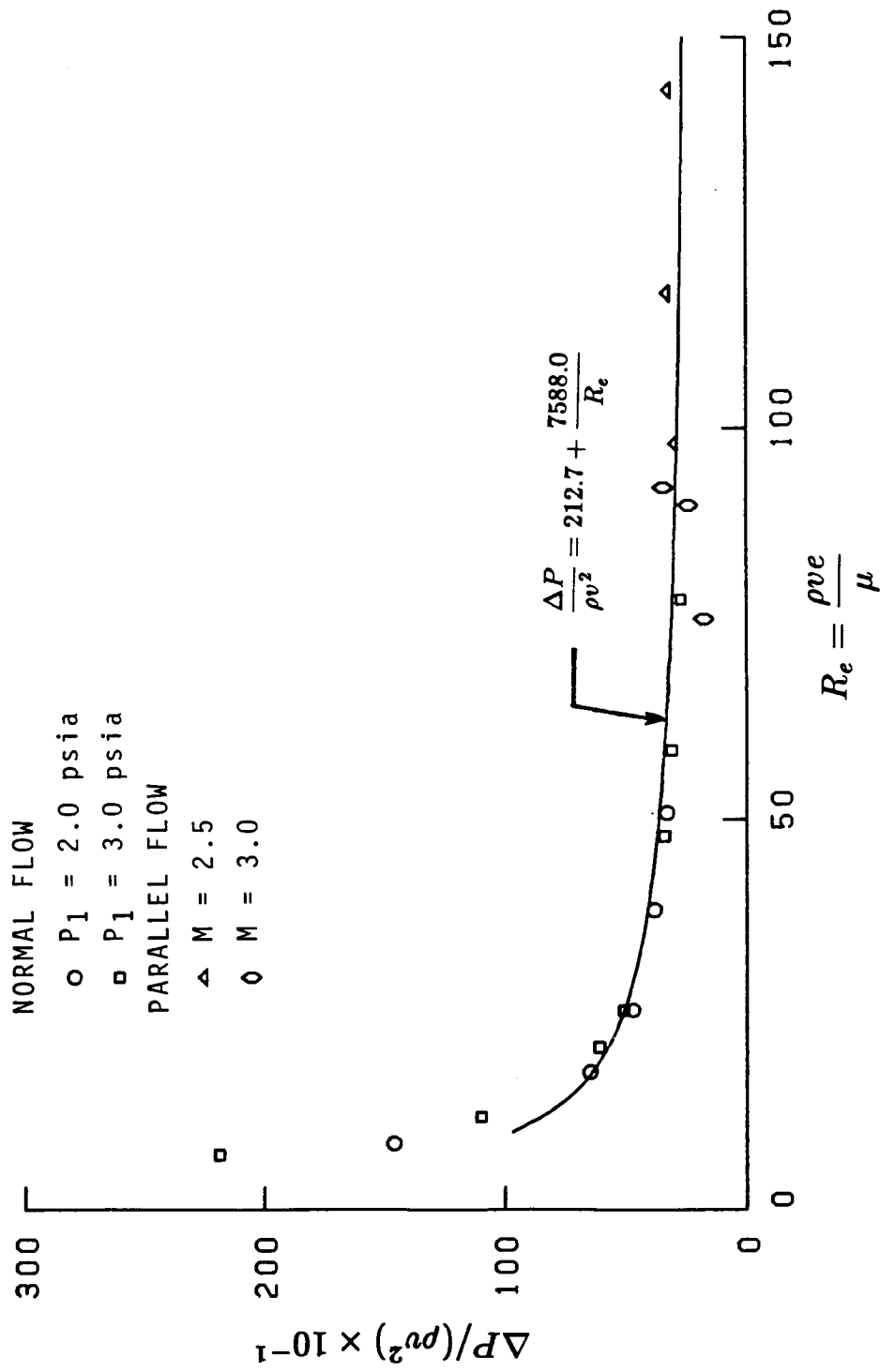


Fig. C3 PRESSURE DROP COEFFICIENT
V.S. REYNOLDS NUMBER

1. Report No. NASA TM-101334		2. Government Accession No.		3. Recipient's Catalog No.	
4. Title and Subtitle Experimental and Numerical Investigation of the Effect of Distributed Suction on Oblique Shock Wave/Turbulent Boundary Layer Interaction				5. Report Date August 1988	
				6. Performing Organization Code	
7. Author(s) Driss Benhachmi, Isaac Greber, and Warren R. Hingst				8. Performing Organization Report No. E-4349	
				10. Work Unit No. 505-62-21	
9. Performing Organization Name and Address National Aeronautics and Space Administration Lewis Research Center Cleveland, Ohio 44135-3191				11. Contract or Grant No.	
				13. Type of Report and Period Covered Technical Memorandum	
12. Sponsoring Agency Name and Address National Aeronautics and Space Administration Washington, D.C. 20546-0001				14. Sponsoring Agency Code	
15. Supplementary Notes Driss Benhachmi and Isaac Greber, Case Western Reserve University, Dept. of Mechanical and Aerospace Engineering, Cleveland, Ohio 44106; Warren R. Hingst, NASA Lewis Research Center. Work was funded through NASA Grant NAG 3-61. This report was submitted as a thesis in partial fulfillment of the requirements for a Doctor of Philosophy degree from Case Western Reserve University.					
16. Abstract A combined experimental and numerical investigation of the interaction of an incident oblique shock wave with a turbulent boundary layer on a rough plate and on a porous plate with suction is presented. The experimental phase involved the acquisition of mean data upstream of, within, and downstream of the interaction region at Mach numbers 2.5 and 3.0. Data were taken at unit Reynolds numbers of 1.66×10^7 and 1.85×10^7 respectively, and for flow deflection angles of 0° , 4° , 6° , and 8° . Measured data include wall static pressures, pitot pressure profiles, and local bleed distributions on the porous plate. On the rough plate, with no suction, the boundary layer profiles were modified primarily near the wall, but not separated for the 4° flow deflection angle. For the higher deflection angles of 6° and 8° , the boundary layer was separated. Suction increases the strength of the incident shock required to separate the turbulent boundary layer; for all shock strengths tested, separation is completely eliminated. The pitot pressure profiles are affected throughout the whole boundary layer; they are fuller than the ones obtained on the rough plate. It is also found that the combination of suction and roughness introduces spatial perturbations in the wall static pressure. The numerical investigation consisted of solving the two-dimensional, unsteady, compressible, mass averaged Navier-Stokes equations in conjunction with the Cebeci turbulence model that includes terms for pressure gradient and suction to predict the experimentally observed features of the flow. An empirical equation relating the mass flow through the porous wall to the difference between the wall static pressure and a specified bleed plenum pressure is used as a boundary condition on the porous wall. The present boundary condition has the advantage of being able to predict the mass flux distribution and account for bleed variation produced by the streamwise pressure gradient. Calculations for 4.5° flow deflection on a smooth wall, with no suction, are slightly in disagreement with the experimental results of the rough plate because the effect of roughness is not modeled. For the 6° and 8° flow deflections, the flow is separated and therefore the numerical code failed. For the bleed cases, computations were made for the 4° , 6° , and 8° flow deflections. The numerical results are in fairly good agreement with the experimental data. The empirical bleed model is capable of predicting the correct bleed distribution through the porous wall.					
17. Key Words (Suggested by Author(s)) Shock wave Boundary layer Suction			18. Distribution Statement Unclassified - Unlimited Subject Category 34		
19. Security Classif. (of this report) Unclassified		20. Security Classif. (of this page) Unclassified		21. No of pages 192	
				22. Price* A09	